POROUS TITANIUM DIOXIDE NANOMATERIALS FOR PHOTOCATALYTIC AND PHOTOVOLTAIC APPLICATIONS

By

Yan Li

A DISSERTATION

Submitted to
Michigan State University
in partial fulfillment of the requirements
for the degree of

Chemical Engineering – Doctor of Philosophy

2016

ABSTRACT

POROUS TITANIUM DIOXIDE NANOMATERIALS FOR PHOTOCATALYTIC AND PHOTOVOLTAIC APPLICATIONS

By

Yan Li

The huge demand for fossil fuels and the risks of the environmental crisis have spurred an interest in renewable energies. Using the clean and abundant solar energy, semiconductor photocatalysis and photovoltaics have evoked tremendous interest. Titanium dioxide (titania, TiO_2) has been the focus of the research trend because of its excellent crystallinity, photoreactivity, chemical and thermal stability, and low cost. The research objective presented in this dissertation is to fabricate titania nanomaterials with tunable porosities, large surface area, unique morphologies, and enhanced capacities of adsorption, electron transport, diffusion, and then apply them in photocatalysis and photovoltaics.

A modified non-hydrolytic sol-gel system with calcium carbonate templating was developed to create macro/micro/nano porous anatase titanium dioxide. The hydrolysis rate was lowered by chelating ligands of valeric acid for slow and sufficient precursor coating. $CaCO_3$ was completely removed via acidification, resulting in titania powders with a surface area ranging from 197 to 239 m^2/g. The templated TiO_2 with a surface area of 239 m^2/g and pore diameters of 6-109 nm showed a promising 27% photocatalytic improvement compared to commercial particles, and a 180% increase compared to template-free TiO_2. This increase is attributed to the increased catalyst loading capacity and active photocatalytic sites.

From hard templates to soft biodegradable natural templates, the rate-controlled sol-gel method was combined with homogenized micro/nano-fibrillated cellulose (MFCs) with an average diameter below 50 nm. Cellulose was removed completely by thermal treatment, and an *in-situ* coating technique created thin titania films on substrates with a porous structure. The degradation efficiency of the photocatalytic films was related to film thickness and to the Ti(IV)-to-cellulose ratio. Photocatalyst on film eliminated the post separation treatment related to powder catalyst and simplified the purification process. The sol-gel/MFCs precursor was also coated *in-situ* as the photoanode for dye-sensitized solar cells. It was found that the thickness of the anode film was a dominant factor to the overall performance and efficiency. The 6-layer cell showed a ~40% increase in solar-to-electricity efficiency (1.75%) compared to commercial paste at the same thickness under a simulated solar light irradiation of 100 mW cm^{-2} (AM 1.5).

From non-hydrolytic to hydrolytic, a modified liquid phase deposition (LPD) approach was combined with MFCs. An optimized solvent composition of isopropanol/water ratio of 4 to 1 was found to yield coatings with uniform spherical TiO_2 possessing a chain-like morphology oriented along the axis of the decomposed cellulose fibers. The average rate constant and degradation percentage were 0.72±0.09 min^{-1}, 95% for TiF_4-cellulose-4IPA-1Water films, which increased by 1.88 times over the film prepared without cellulose templates due to the beneficial surface area, pore size, and the unique morphology. The three-dimensional web structure with pseudo one-dimensional sphere-chain could retard the recombination of photogenerated electron-hole pairs and improve the charge transport.

ACKNOWLEDGEMENTS

I would like to express my heartiest gratitude and sincere appreciation to my advisor, Prof. Lawrence T. Drzal, for his wisdom and guidance through my whole graduate school life. Prof. Drzal has been impressing me with his enthusiasm for research, his attitude to life and work, and his kindness and patience to every student and scholar. I really appreciate how he cared and understood during my time of injury, surgery, and recovery in 2015. I am grateful for his help on my career development in 2016. I was lucky to be a part of his 30-year devotion to composites research celebration. I would like to thank my entire committee members: Prof. Richard Lunt, Prof. Thomas Hamman, Prof. Ilsoon Lee, for their help during my completion of courses, research, and all my questions and ideas. I am very grateful for your providing of equipment regarding photovoltaic testing and measurements. It is very kind of Prof. Tim Hogan to join my thesis defense. I would like to thank Professor McCusker and his student Dr. Lisa Harlow, from Department of Chemistry, for their generous support as well.

I would like to acknowledge Dr. Per Askland, Ed Downey, Brian Rook, Mike Rich for teaching me about microscopes, spectroscopies, and all the other equipment in the Composite Materials and Structures Center. Per deserves special mention for his knowledge, kindness, patience, humor, and friendship. I would like to say thank you to our diligent administrators, Karen and Shirley, for everything they accomplished for students, professors, and the composite center.

Next, I would like to thank all my colleagues, previous or present, Pat, Xian, Jinglei, Anchita, Deb, Dee, Markus, Keith, Nick, Zeyang, Mariana for your company in the office,

your help in labs, and the inspiring conversations we had about research and everything else. I also appreciate my roommate, and all my friends I got to know at Michigan State University. Your support always gave me encouragement and motivation to carry on.

In the end, I would like to thank my parents and sister, who have been in China for the past few years, for their endless love and support. I can never thank them enough for the powerful words and insights they brought to me. I am lucky to have a family like them. I appreciate their belief in me, which has and will always be influencing my future life.

TABLE OF CONTENTS

LIST OF TABLES

LIST OF FIGURES

KEY TO SYMBOLS

TiO_2	Titanium Dioxide
DSSC	Dye-Sensitized Solar Cell
MFC	Micro/nano-fibrillated Cellulose
AM 1.5G	Air Mass 1.5 Global
LPD	Liquid Phase Deposition
TCO	Transparent Conductive Oxide
FTO	Fluorine-doped Tin Oxide
ITO	Indium-doped Tin Oxide
Jsc	Photocurrent density measured at short circuit
Voc	Photovoltage at open circuit
Is	Incident light intensity
FF	Fill factor
Ru(II)	Ruthium
N3	Tris(2,2'-bipyridyl-4,4'-carboxylate) ruthium (II)
IPCE	Incident photo-to-current efficiency
OSE	Organic solvent electrolyte
ILE	Ionic liquid electrolyte
TBP	4-tert-butylpyridine
NMBI	N-methylbenzimidazole
I^-/I_3^-	Iodine/triiodide
CuI	Copper Iodide
CuSCN	Copper Thiocyanate

CoS	Cobalt Sulfide
Eg	Band gap energy
Nb2O5	Niobium Pentoxide
SnO2	Tin Oxide
TEOA	Triethanolamine
TTIP	Tetraisopropoxide
ED	Ethylenediamine
AHFT	Ammonium Hexafluorotitanate
BA	Boric Acid
TBOT	Tetrabutoxytitanium
SAED	Selected-area electron diffraction
FFT	Fast Frourier Transfer
VA	Valeric acid
MO	Methyl Orange
EDTA	Ethylenediaminetetraacetic acid
AGU	Anhydroglucose unit
CNC	Cellulose nanocrystal
A	Frequency Factor
Ea	Activation Energy
R	Universal Constant
K(T)	T-dependent reaction rate constant
A	Degree of conversion
IPA	Isopropanol

PEG	Polyethylene glycol
PVDF	Polyvinylidene fluoride

1 Introduction

1.1 Overview

The research objective presented within this dissertation is to fabricate nano titanium dioxide with unique morphologies, porosities, and other properties through various templating methods, and apply them as photocatalysis and photovoltaics.

In this introductory chapter, the motivation of this research will focus on the solar energy, a renewable source for industry and daily life. Two promising applications as photocatalysts to remove pollutants and dye-sensitized solar cells (DSSCs) for electricity generation and the advantages of titanium dioxide nanomaterials for above applications will be introduced. Then various synthetic routes for synthesizing titanium dioxide will be presented such as sol-gel chemistry, hydrothermal method, liquid phase deposition, templating methods and so on.

The second chapter will discuss the controlled hydrolysis of a sol-gel process utilizing valeric acid and titanium tetraisopropoxide as the base precursor. It will describe the use of a simple but effective hard-template calcium carbonate as a sacrificial structure to create macro/micro/nano porous titania particles, and their applications as powder photocatalysts to degrade the organic dye methyl orange.

The third chapter will focus on the introduction of the cost-effective, biodegradable cellulose, started with brief background knowledge about this natural-existing polymer, followed by experiments proving the successful templating effects for titania micro hollow fiber fabrication. Then micro/nano-fibrillated cellulose (MFCs) fibers will be discussed regarding the scale effect and procedures to prepare homogenized MFCs in our lab.

Chapter 4 will describe a novel combination between MFCs and non-hydrolytic precursor for a controlled hydrolysis of a sol-gel process. The function of MFCs is evaluated through various characterizations on unannealed and annealed samples. The addition of binders such as polyethylene glycol and polyvinylidene fluoride is compared. Films adjusted with different Ti(IV) and cellulose ratios show different photocatalytic capacities when applied as photocatalytic films to degrade organic dye methyl orange.

Chapter 5 will provide more trials using MFCs as the templates but in hydrolytic systems. Liquid phase deposition (LPD) methods will be discussed in detail with two modified reaction systems: (1) titanium tetrafluoride method, in which the manipulation of solvent polarity brings out controllable morphology and thus different photocatalytic capacities; (2) ammonium hexafluorotitanate and boric acid method, where both bulk materials and thin films will be discussed through characterization approaches.

The sixth chapter will turn to dye-sensitized solar cells, starting with an introduction of previous work review on cellulose templated TiO_2 as photoanodes in DSSCs. The detailed preparation of electrodes, electrolyte, dye sensitizer and assembly will be described next. Photovoltaic performances of the cells made with different TiO_2 films will be compared.

1.2 Solar Energy, Photocatalysts and Dye-Sensitized Solar Cells

1.2.1 Solar energy, a clean and safe bet

The report of Intergovernmental Panel on Climate Change has pointed out that global warming brought on by increasing greenhouse gases has had a detrimental impact on oceans and the atmosphere.[1] The huge demand for fossil fuels and the risks of environmental crisis have spurred an interest in renewable energies. The world energy

consumption is estimated to grow by 56% between 2010 and 2040.[2] As Figure 1-1 shows, total primary energy consumption grows by 8.9% from 97.1 quadrillion Btu in 2013 to 105.7 quadrillion Btu in 2040.[3] The consumption of marketed renewable energy increases from 9.0 quadrillion Btu in 2013 to 12.5 quadrillion Btu in 2040, with most of the growth in electric power sector.[3]

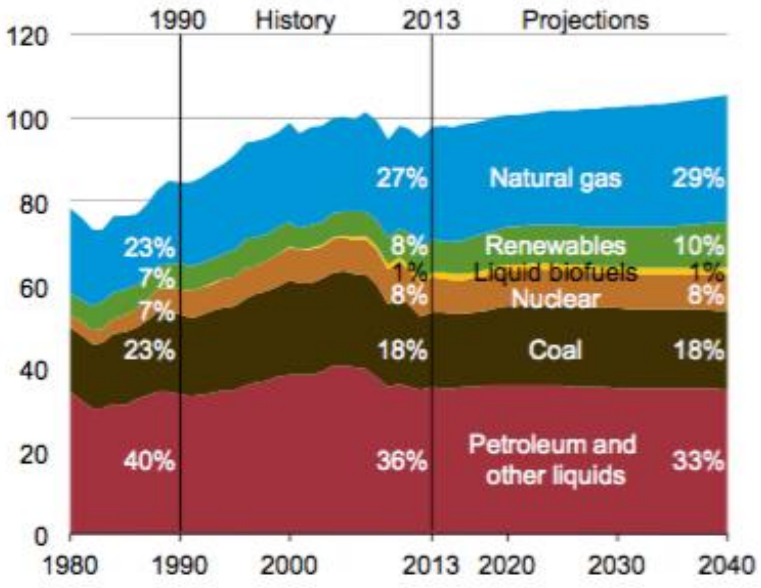

Figure 1-1 Primary energy consumption by fuel (unit of vertical axis: quadrillion Btu)[3] For interpretation of the references to color in this and all other figures, the reader is referred to the electronic version of this dissertation.

Figure 1-2 illustrates the electricity generation amount from 2000 to 2040, where petroleum, coal, and nuclear show a decrease while renewable energies and natural gas increase. In the long term, natural gas fuels more than 60% of the new generation, and growth from renewable energy supplies most of the remainder. Among major types of renewable energy systems, such as solar energy, wind energy, geothermal, biomass, hydroelectric, nuclear and ocean,[4] solar is capable of converting the abundant, free, clean and cost-effective solar energy directly into electricity - the energy is quantitatively large enough to meet the growing demand.

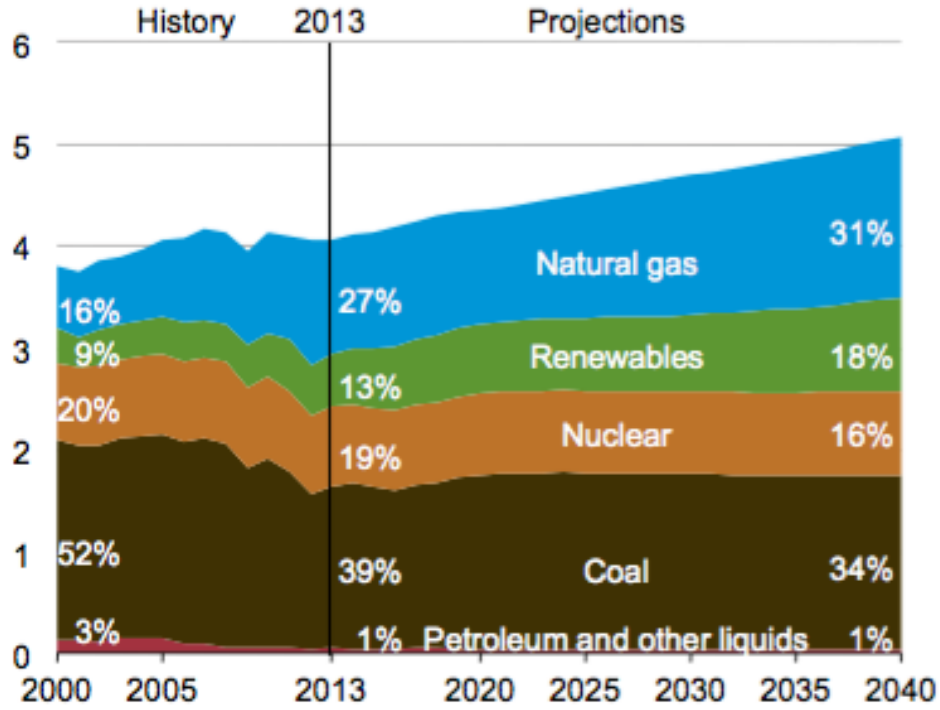

Figure 1-2 Electricity generation by fuel (trillion kilowatt hours)[3]

Although PV only accounts for 0.04% of the overall energy production, there has been a rapid increase of 33%/year since 1997 and an anticipated annual increase of 30% in the next decades.[5] Based on the newest data,[3] wind and solar generation account for almost 67% of the increase in total renewable generation, and solar photovoltaic is the fastest-growing energy source for renewable generation. Solar stands out with a 6.8%/year average annual growing rate when compared to other renewable energy resources for electric generation such as wind (2.4%/year), biomass (3.1%/year), and geothermal (5.5%/year).

1.2.2 Background of solar cells and the dye-sensitized solar cells

Solar cell is an electric device converting phonons directly into electricity through the photovoltaic effect. The first solar cell was developed by Bell Labs in 1950s[6] by Daryl Chapin *et al.* with an efficiency of 6%, utilizing silicon as the light absorber. During the next few decades, solar cells have been tremendously researched and silicon-based solar cells

become the dominant products in the market with high efficiency 27.6% according to National Renewal Energy Laboratory report[7] (shown in Figure 1-3). As a large and growing family, solar cells also have a variety of members, including mono/polycrystalline silicon solar cells, thin-film solar cells such as amorphous Si cells, polycrystalline CdTe cells, chalcopyrite cells, III-V semiconductor cells, and highly efficient multijunction concentrators.[8] Similar with silicon purifying requirements, the high processing cost and raw material scarcity hinder the development of these solar cells.[9] This dissertation will focus on one of the third-generation solar cells, dye-sensitized solar cells (DSSCs) as a potential competitor to traditional silicon solar cells.

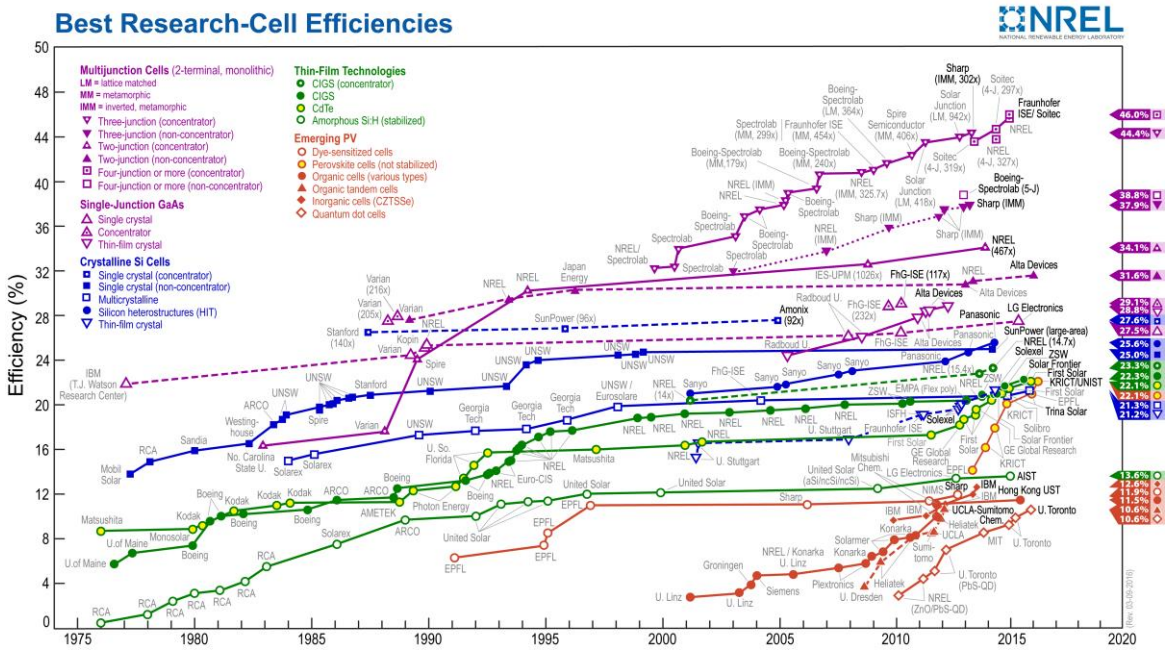

Figure 1-3 Latest solar cell efficiencies research in labs, updated on Mar 7th 2016.[7]

The first DSSC was created in 1991, with an efficiency of 7% by O'Regan and Grätzel.[10] The breakthrough relied on the application of wide band gap nanocrystalline semiconductor network with large surface area for dye sensitizer adsorption and light harvest. Unlike p-n junction solar cells, DSSC separates the photon harvesting and charge

transport processes.[10] DSSCs stand out for the following reasons: (i) no significant requirement on the grade of the semiconductor as silicon cell does, resulting in lower cost; (ii) the materials used are environmentally friendly and present in adequate quantities; (iii) has stable performance under varying thermal conditions.

A dye-sensitized solar cell is composed of four main parts: a nanostructured semiconductor photoanode, dye sensitizers, electrolytes with redox couples, and a catalyst-coated counter electrode, forming a sandwich-like cell assembly. Both of the electrodes use transparent conductive oxides (TCO) as substrates, usually fluorine-doped tin oxide (FTO), or indium doped tin oxide (ITO) films. Nanoporous titania nanocrystalline (TiO_2), ruthenium-based metal-ligand compounds (N3 or N791), iodine/triiodide (I^-/I_3^-) in organic solvents, and platinum-coated FTO represent one typical set of components for DSSCs.

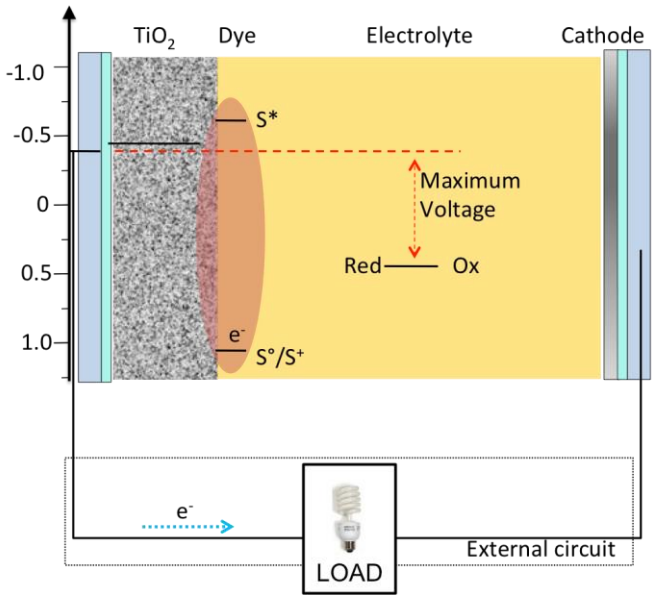

Figure 1-4 Scheme of a typical dye-sensitized solar cell.

The DSSCs operate as follows (Figure 1-4): The dye sensitizer, which is adsorbed as a molecular monolayer, will be excited from state S^0 to S* by illumination, ejecting one electron very quickly into the conduction band of TiO_2. The electron will then diffuse within the domain of the porous TiO_2 layer and reach the FTO film. Simultaneously, the oxidized dye S^+ will be recovered to the original state S^0 by the redox couple I^-/I^{3-} in the electrolyte. Once an external load is applied, the electron will travel through the circuit and arrive at the counter electrode surface, where it will react with the oxidized electrolyte and refresh the redox couple. Thus, the whole cycle of operation is fulfilled.

From photon to electron, diffusion to redox, the working mechanism of DSSCs is kinetic-based with competitions between steps. Possible back reactions are: (a) injected electrons recombine with the oxidized dye, (b) injected electrons react with the oxidized electrolyte, and (c) relaxation to the ground state.[9] The structural optimization of the photoanode is to offer opportunities for improvement in not only the quantity of dye, transport of electrons, and diffusion of electrolytes but also the suppression of recombinations.

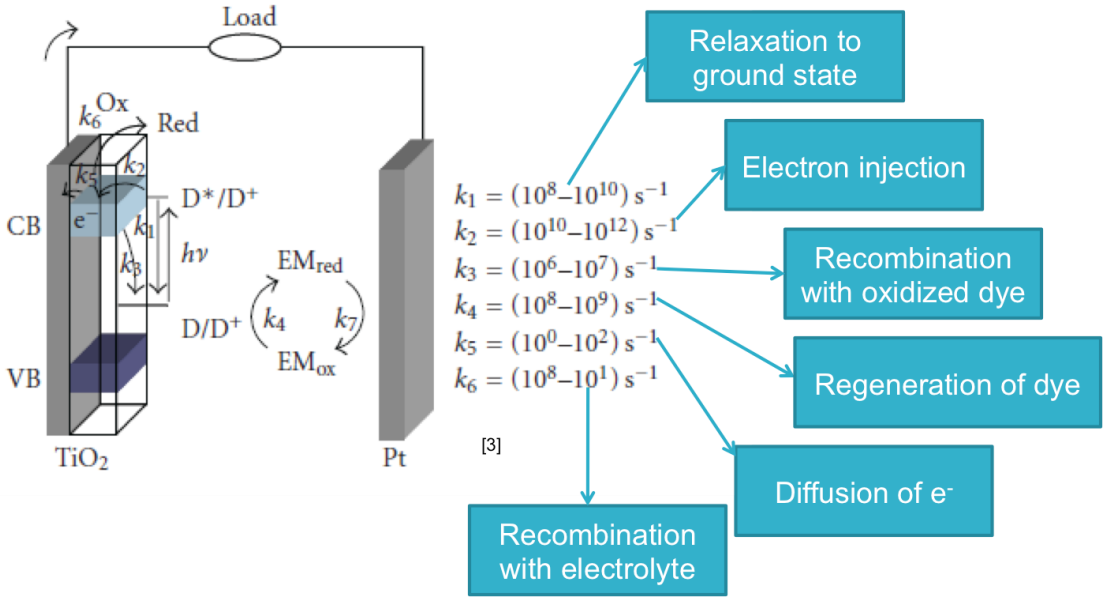

Figure 1-5 Kinetic competitions among multiple reactions in DSSCs under operation.[11]

The processes mentioned above are kinetic-based, indicating that the competition between different steps and reactions will determine the performance of the whole cell. As shown in Figure 1-5, k_1~k_6 stand for the rate constants for separate reaction steps in a full cycle of operation. It is clearly demonstrated that the injection of the photoexcited electron is ultrafast, proceeding on a femtosecond time scale[10] (k_2 =10^{10}-$10^{12}s^{-1}$), while the relaxation to ground state processes on a nanosecond time scale (k_1=10^8-$10^{10}s^{-1}$). Three possible back reactions are undergoing here: injected electron recombines with oxidized dye (k_3), injected electron reacts with oxidized electrolyte (k_6), and the relaxation to the ground state (k_1). Focusing on the electron generated by the very first step photoexcitation, we may notice that either relaxation to the ground state or injection to the semiconductor will occur. The fact is that k_2 is almost 100 times larger than k_1, thus typically the electron prefers to undergo injection. Similar is the situation when the competition between injection and combination with the electrolyte is considered. In addition, since the diffusion rate (k_5) is much smaller than the back reaction rate (k_3 and k_6), even the recovery of dye

by the mediator in electrolytes (k_4) is faster than the recombination between electron and dye (k_3). Although minimal, the back reactions still occur and minimizing them remains an important problem to be solved.[11]

The overall efficiency of a solar cell, η, is represented by

$$\eta = \frac{J_{sc} \cdot V_{oc} \cdot FF}{I_s}$$

J_{sc}, V_{oc} and I_s are the photocurrent density measured at short circuit current, photovoltage at open circuit and incident light intensity respectively, while *FF* is the "fill factor" which is defined as $FF = \frac{P_{max}}{J_{sc}V_{oc}}$. As Figure 1-6 shows, the area underneath the black dashed line is the product of J_{sc} and V_{oc}, and the area beneath the red dashed line is the maximum power P_{max}. *FF* ranges from 0 to 1, and the maximum electrical power is $P_{max} = (J_{sc}V_{oc})_{max}$.

The key parameters to enhancing the photo-to-electricity conversion efficiency are J_{sc}, V_{oc}, and *FF*. Theoretically, the photocurrent is controlled by the sensitizer's light absorption and electron injection processes, while photovoltage is determined from the difference between the semiconductor Fermi level and the Nernst potential of the redox couple. However, recombination reactions could neutralize both J_{sc} and V_{oc}. As for the *FF*, its influence occurs in a more complex way.

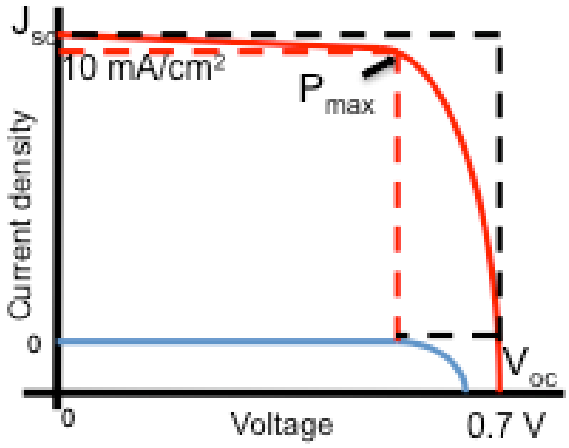

Figure 1-6 Plot of the J-V curve of an operating DSSC. The blue curve is dark current, and the red curve is light current.

Along with the discoveries of more powerful dye sensitizers,[12] [13] redox shuttles,[14] semiconductor compositions[15], and electrolyte carriers,[16] the efficiency of DSSCs has increased from 7 %[10] to 11.5 %[17]. Recent latest DSSCs have reached an efficiency of 15% by using an inorganic-organic composite structure of glass/FTO/TiO_2 /$CH_3NH_3PbI_3$/HTM/Au for improved reproducibility and enhanced photo-to-electricity conversion.[18] Apparently, the optimization of the whole DSSCs could be divided into four major categories based on the component to be modified. Detailed discussions about the modifications will be covered in Chapter 6.

(A) Dye sensitizers

The primary considerations for optimum dyes are a wide absorption spectrum range and the capacity of attaching firmly to the surface of electrode nanomaterials and high electron injection quantum yields.[19] Also, having good thermal and chemical stability is significant for cell performance and long-term running especially for commercial applications. Last but not least, a high enough redox potential can ensure that the dye would be recovered at a fast speed by the electrolyte. [20]

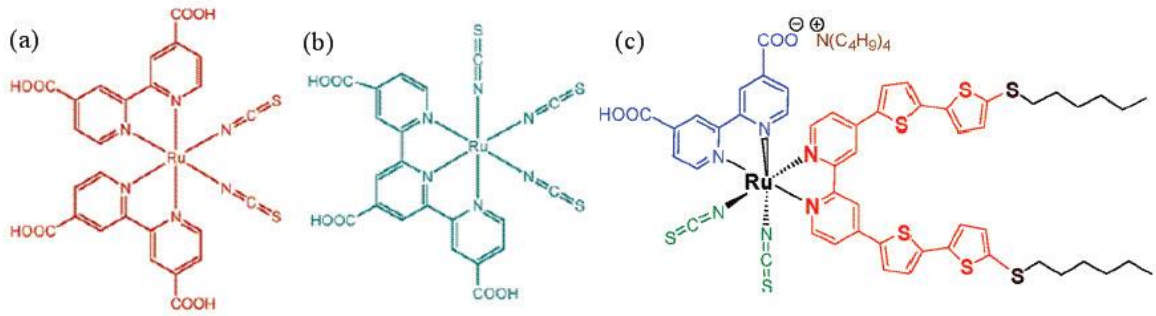

Figure 1-7 Structures of polypyridine Ru(II) dyes. (a) N3, (b) Black dye, (c) CYC-B11[5, 7]

Metal complexes and ruthenium (Ru(II)) have been intensively researched because of the high stability, excellent redox properties, proper absorption spectra. Typically, a Ru-based dye is composed of a central metal ion with ancillary ligands having certain anchoring groups,[21] such as carboxylate or phosphonate group, enabling the electron injection. Other parts of the dye such as ancillary ligands could also be tuned to improve the overall photovoltaic capacity. One of the best-performing ruthenium polypryidyl complex compounds is tris(2,2'-bipyridyl-4,4'-carboxylate) ruthium (II) (N3 dye). It is shown that the electron injection occurs in femtosecond time scale, with an incident photo-to-current efficiency (IPCE) of 80-85%.[20] N_3 dye's tetrabutylammonium salt, tri(cyanato-2,2',2''-terpyridyl-4,4',4''-tricarboxylate) Ru (II) (black dye), was developed to extend 100 nm further into IR region regarding to spectral response.[20] Recently, an even more efficient sensitizer CYC-B11 with a high molar extinction coefficient heteroleptic ruthenium complex is synthesized by incorporating electron-rich hexylthio-bithiophene antennas.[17] The molecular structures of the most successful Ru-based dye sensitizers are shown in Figure 1-7. There haven been tremendous work focusing on exploitation of panchromatic sensitizers to cover the whole visible spectrum to enhance the spectral response up to 920 nm,[11] searching for economical and diverse alternatives such as organic dyes, and co-sensitization instead of one single dye to improve the photo-absorption.[22] In addition, no

matter which kind of modification is done to the dye, an essential purpose is to promote hole charge transfer to the redox couple.

(B) Electrolytes

Redox species are dissolved in the electrolyte, serving as the mediator for regeneration of oxidized dye and reduction at the counter electrode. The electrolyte needs to have long-term chemical and thermal stability. The absorption of sunlight by the dye will reduce if the electrolyte has significant absorption of visible light.

Organic solvent electrolyte (OSE) and ionic liquid electrolyte (ILE) are two general types of liquid electrolytes. OSEs are widely used because of their low viscosity, fast ion diffusion, and high efficiency.[23] OSE usually includes organic solvent like acetonitrile, redox couple I^-/I_3^-, and additives such as 4-tert-butylpyridine (TBP) and N-methylbenzimidazole (NMBI), which contribute to the suppression of dark current.[23] Redox couple iodine/triiodide (I^-/I_3^-) has been demonstrated to have the best performance for dye regeneration, even though other kinds of redox couples have also been tried by different groups.[16] However, a major disadvantage of I^-/I_3^- is the corrosion of sealing materials for cell assembling. ILE has a negligible vapor pressure, non-flammability, and high ionic conductivity, so it has attracted a lot of attention recently. However, since the pure ionic liquid has higher viscosity, the transport speed of redox couple is very slow.[16] So the ionic liquid with both low-viscosity and high-conductivity would be a promising alternative to OSE.

The emerging trend of solid-state electrolytes avoids the leakage and volatilization problem of liquid ones by using a p-type hole transport material to replace the liquid

electrolyte. Besides of the general requirements for electrolytes, qualified hole transport material should have energy levels aligned with the dye molecules, high hole mobility, and good penetration into porous photoanode structure.[9,21] A variety of materials including inorganic compounds (CuI, CuSCN), molecular hole conductors, and conducting polymeric materials have been explored as the solid-state "electrolyte". Major problems remain in the inefficient pore filling for dye molecules to be in contact with both anode and the hole conductor, as well as the losses caused by recombination reactions.[21]

(C) Catalytic counter electrodes

The TCO-coated glass is used as a substrate of DSSC electrode, but itself alone has too high charge transfer resistance to be a qualified counter electrode.[21] Platinum is thus widely used as a catalyst for redox reaction on the cathode, prepared simply by deposition of a thin layer of Pt onto the TCO selected. Depositing nanoclusters of an organo-platinum compound through thermal treatment has been proved to be stable and effective.[24]

The high cost of Pt triggered more research on alternatives including carbon family such as CNTs,[9] graphene nanoplatelets[25], conducting polymers and cobalt sulfide, etc.[21] Carbon materials have been applied to improve the electronic conductivity and catalyze the reduction of triiodide. Researchers started with just graphite and carbon black, then reduced the carbon black size to 30 nm with largely reduced charge transfer resistance, and utilized single wall carbon nanotubes and graphene as well in recent years.[21] As for conducting polymers, poly(3,4-ethylenedioxythiophene) (PEDOT) has been a strong candidate charge transfer resistance less than 1 Ω cm^2 for 1 um thick film on TCO

substrates. Electrodeposited CoS on a flexible substrate was proved to catalyze iodide/triiodide redox couple as well.[21]

(D) Nanostructured metal oxide photoanodes

Photoanode, composed of semiconductor nanomaterials, acts as the support for dye sensitizer, the media for electron transport and electrolyte diffusion in the solar cell. The semiconductor nanomaterial film is required specifically to have a large surface area, highly porous structure, and fast electron transport capacity.

Among various wide band gap metal oxide semiconductors, TiO_2 is the most studied and effective material because of its surface area, porosity, crystallinity, and electron transport capacity. Additionally, titania, is available in large quantities, cost-effective, environmentally friendly, stable chemically and thermally.

Titania exists in three crystal phases, which are rutile, anatase, and brookite. Rutile has compact aggregates resulting in low surface area, while anatase and brookite phases contain porous aggregates and more open structure, which are more suitable for photocatalysis and DSSC applications.[26] The commonly investigated phases are anatase (bandgap 3.2 eV) and rutile (bandgap 3.0 eV), of which the wide bandgaps ensure the photoelectric excitation of TiO_2, followed by scavenging of electrons and holes by surface adsorbed species. [27] Besides TiO_2, other wide band gap semiconductors such as ZnO (Eg=3.2 eV) [28,29], Nb_2O_5 [30] and SnO_2[31] have also been tried, and a very recent investigation of ZnO flower-shaped scattering layer improved the efficiency to 3.2%. However, these efficiencies are still very limited compared to titania-based electrodes.

The design of nanocrystalline semiconductor electrode is significantly important not only because there is relatively a larger range for modifying and optimizing, but also the semiconductor serves as a central part of the cell and could possibly have the bigger contribution to enhancing the overall efficiency of the solar cell. From the big picture of research into the different components of DSSCs provided above, more focus on the structural optimization of the photoanode will be discussed. Structural considerations offer many opportunities for improvements in loading of dyes, transport of electrons, and diffusion of electrolytes and suppression of recombination.

All these years, researchers have made innovations to improve the morphology, shape, and composition, etc. of electrode materials. From different points of views, the advancements could be classified in various groups.[32] In this dissertation, TiO_2 advancements could be separated into categories below: (1) nanoparticle with high surface area; (2) 1D nanotubes or nanowires; (3) 3D hierarchically ordered structure with a combination of large pores, large particles and smaller particles; (4) 3D template-induced macroporous scaffolds; (5) hybrid of TiO_2 with highly conductive carbon materials.[32] More details about the state-of-art advancement about titania electrode will be covered in Chapter 6.

1.2.3 Historical overview of the development of photocatalysis

Efficient approaches to remove contaminants in water have been extensively researched in the past decades due to the environmental pressure aroused from industrial, agricultural, and daily life pollutions into the aqueous systems. Organic contaminants, especially colored waste from textile industry, if not pre-treated, cause tremendous harm to aquatic life.[33] Compared to traditional methods including direct precipitation, or

adsorption on activated carbon, heterogeneous photocatalysis requires no further treatment on the separated or adsorbed secondary pollutes. Additionally, photocatalysis is superior to conventional biological treatments which usually involve a longer period of time and more cost. [34]

The earliest photocatalysis work started back to 1921 when Renz reported a series of partial reduction of metal oxides such as TiO_2, CeO_2, Nb_2O_5 by illumination with sunlight, in the presence of organic compounds.[35] Noble metal salts reduction was found on the surface of TiO_2 and ZnO, as well as hydrogen peroxide formation on ZnO.[34] The first decomposition of a dye on TiO_2 was realized in 1938,[36] where initial absorption spectra and quantum yields were measured. During the several decades afterwards, researchers focused on the theories and mechanisms. Fujishima group found that photocatalysis capacities varied among different TiO_2 crystal phases, and anatase was more active than rutile.[34]

The term "photocatalyst" first appeared in work done by Kato and Mashio in 1956.[37] The landmark year for photocatalysis research might be 1972, when Fujishima and Honda discovered water splitting on TiO_2.[38] The idea of purifying water with illuminated titania was proposed in 1977 by Frank and Bard,[39] where they proved the effectiveness by decomposing cyanide ions under illumination of a xenon lamp. In the 1990s, more attention was paid to solid surfaces specialized in self-cleaning, self-sterilizing, and organic decomposing functions, that relied on less powerful UV photons.[40] Since the 21st century, tremendous research has been done concerning photocatalytic water splitting,[41] photo-induced super-hydrophilicity, and artificial photosynthesis.[37]

In short, photocatalysis is a cost-effective, environmentally friendly, versatile solution to convert solar energy into other forms of chemical energy. It can degrade organic and biological pollutants, aqueous or gaseous, leading to a broad range of potential applications in pollutant cleaning, drinking water treatment, clinical usages, and industrial installations.

It is generally known that for a heterogeneous photocatalytic process, five steps could be summarized as below: (1) diffusion of the reactants to the surface of the catalyst, (2) adsorption of reactants onto the surface of the catalyst, (3) reaction on the surface of the catalyst, (4) desorption of products from the surface of the catalyst, (5) diffusion of the products from the surface of the catalyst.

Heterogeneous photocatalytic reactions begin when a semiconductor catalyst is irradiated by UV light source (wavelength below 400 nm) that has higher energy than the semiconductor band gap energy.[42] When a photon hits the photocatalyst, electrons are excited from the valence band to the conduction band, forming electron-hole pairs. On the surface of a metal oxide (MO) semiconductor, the oxidative reactions initiate, followed by reaction with moisture in air resulting in hydroxyl radicals; the reductive reactions involve oxygen in the atmosphere and form hydroxyl radicals as well. Thus generated hydroxyls are very oxidative and non-selective with a redox potential of E_0=3.06 eV.[37]

Three main steps represent the photocatalytic reactions on titania:

a) photoexcitation of MO generates electrons (e^-) and holes (h^+)

b) electrons (e^-) and holes (h^+) transfer to the TiO_2 surface

c) electrons (e^-) and holes (h^+) react with adsorbed electron acceptors and donors.[43]

Equations and a related scheme are shown below:

$$UV + MO \rightarrow MO\ (h^+ + e^-)$$

$$h^+ + H_2O \rightarrow H^+ + \bullet OH$$

$$2\ h^+ + 2\ H_2O \rightarrow 2\ H^+ + H_2O_2$$

$$H_2O_2 \rightarrow HO\bullet + \bullet OH$$

$$e^- + O_2 \rightarrow \bullet O_2^-$$ superoxide anions

$$\bullet O_2 - + HO\bullet 2 + h^+ \rightarrow H_2O_2 + O_2$$

$$HOOH \rightarrow HO\bullet + \bullet OH$$

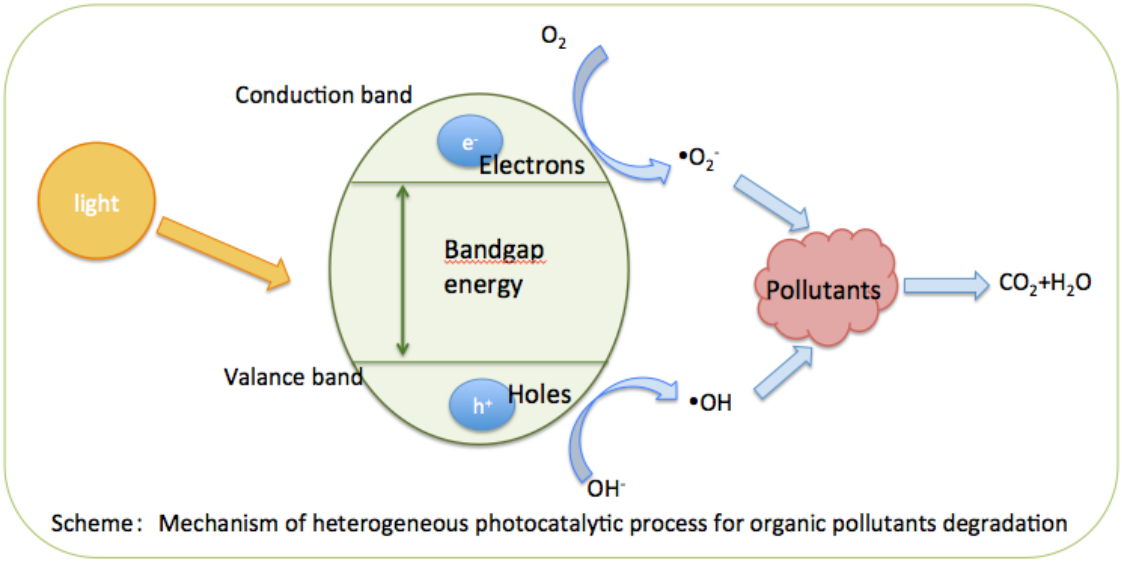

Figure 1-8 Schematic view of the mechanism of photocatalytic process with metal oxide semiconductor catalysts

Parameters influencing the effectiveness of the photocatalytic reaction include: catalyst loading, catalyst surface area, and catalyst charges; solution pH, temperature and target concentration; light wavelength and intensity; chemical additives and even the reacting vessel system design. This is why Ryu and Choi[44] conducted substrate-specific tests, which confirmed that one photocatalyst could not meet all photocatalytic requirements and a standardization of photocatalytic activity is needed but also realistic to be made.

A variety of materials such as TiO_2, ZnO, V_2O_5, SnO_2, Fe_2O_3, ZrO_2, CdS, WO_3[37] have been investigated. However, TiO_2 remains the most popular material for photocatalysis. For example, photo-corrosion problems will happen during the excitation of ZnO in solution, and hematite suffers from rapid charge recombination and short charge carrier diffusion length.[27] The success of TiO_2 could be attributed to its excellent UV absorption capacity, high photoreactivity, chemical and thermal stability, low cost, suitable band gap position to oxidize organic molecules, and long-term photostability.[45] The commonly investigated phases are anatase (bandgap 3.2 eV) and rutile (bandgap 3.0 eV), of which the wide bandgaps ensure the photoelectric excitation of TiO_2, followed by scavenging of electrons and holes by surface adsorbed species.[27] Titanium dioxide photocatalysts could be used as powders that suspend in solutions or immobilized on thin films. Large scale reactor design includes slurry-type or immobilized-type reactors. Drawbacks of titania have been discussed for years due to the facts that it only absorbs wavelength lower than 387 nm in the solar light spectrum, and the charge recombination, hole trapping, electron trapping from defected nanoparticles limit the electron transport properties.

Briefly, current modifying trends on titania photocatalysts include: (1) expanding the response range of TiO_2 to visible light; (2) increasing the adsorption of pollutants for more active reaction sites, (3) improving the charge separation to retard charge recombination for a higher overall efficiency; (4) changing the selectivity or yield of a particular reactant. Surface modifications have been applied to optimize the performance of titania photocatalysts.

1.3 Nano Titania Materials and Synthesis Methods

To improve the solar energy conversion efficiency and meet the current modifying trends, TiO_2 nanomaterials have been researched in various directions, such as spatial structuring and doping,[37] size reduction and shape control,[46] graphene supporting[47] surface engineering[48], etc. To start, general methods to fabricate appropriate titania nanomaterials for photovoltaic and photocatalytic applications should be discussed. Thus, a few representative synthesis methods will be introduced as follows.

1.3.1 Sol-gel method

The sol-gel method has been used to prepare a variety of ceramic materials. [49-52] Based on hydrolysis and condensation reactions, sol-gel chemistry is an attractive wet chemistry approach to synthesize metal oxides.[53] Starting with inorganic metal salts, or metal organic compounds,[45] sol-gel synthesis involves a simple preparation of precursor/solvent system, lower temperature processing, easy coating of large surfaces with variable thickness and high optical/electrical qualities.[54]

Precursors, such as metal alkoxides, metal acetylacetonates, and inorganic metal compounds, go through a hydrolysis and condensation polymerization to form a sol, while further cross-linking combined with solvent loss results in a metal oxide gel. Variations in extent of polymerization and loss of solvent will result in liquid sol, wet gel, or solid gel, while powders, thin films, aerogel, ceramic fibers can further be obtained depending on how the gel phase transfers next.[45]

A typical sol-gel reaction of metal alkoxide initiates with hydrolysis,

$$M - OR + H_2O \rightarrow M - OH + ROH$$

Condensation begins as soon as hydroxyl groups are generated. There might be two competing mechanisms:[53]

(i) Olation: removal of a water or alcohol molecule and formation of hydroxyl bridges.

$$M - OH + M - OHX \rightarrow M - OH - M + XOH$$

$$(X = H\ or\ alkyl\ group)$$

(ii) Oxolation: removal of a water or alcohol molecule and formation of oxygen bridges.

$$M - OH + M - OX \rightarrow M - O - M + XOH$$

$$(X = H\ or\ alkyl\ group)$$

The relationship between these three reactions will determine the final structure and morphology of the resulting network. The rate constants for hydrolysis and condensation depend on water-to-metal ratio, temperature, solvent and precursor composition, etc.[55]

Livage defined the hydrolysis ratio as h=H_2O/M. As h controls the mechanism of condensation and affects the size, structure, and physical properties of macromolecular species, three circumstances were discussed. When h<1, condensation is dominated by oxolation with alkoxy bridging, leading to molecular oxo-alkoxides. When 1 < h < n (n is the coordination number of M), a polymeric gel may be formed. When h>n, cross-linked polymers will be formed, and precipitates can be obtained once excessive water is added.[53]

Titanium, being a transition metal, differs with the extensively studied silicon precursors since it has a lower electronegativity and a higher electrophilicity, which makes titanium alkoxides much more reactive. The molecular complexity of the sol depends on the alkoxy group in the precursor $Ti(OR)_4$. The bulkier the OR group is the smaller the

complexity.[53] The hydrolysis rate will increase with temperature and the value of *h*. Primary alkoxides hydrolyze easier than more complex alkoxides. With an acetic catalyst, the hydrolysis rate increases while condensation decreases, this facilitates the separation between hydrolysis and condensation steps.

Titania nanomaterials have been synthesized from hydrolysis of a Ti precursor with a sol-gel method in numerous ways due to its versatile synthetic procedures and fine control over purity, homogeneity, and crystallization.[56-59] According to the aforementioned theory, limiting the amount of water will suppress the hydrolysis rate and develop Ti-O-Ti chains with the excess titanium alkoxide into a closely packed polymeric skeletons. As *h* increases, $Ti(OH)_4$ forms loosely packed primary particles without formation of polymeric skeletons. While *h* reaches a large excess, tightly packed primary particles are created through a gel skeleton and with extended times or higher temperatures, the average radius of nanoparticles grow linearly with time, and more secondary particles will be formed.[45]

Water content is not the only parameter that guided the sol-gel chemistry for TiO_2 fabrication. Additives and surfactants such as alkylamines, carboxylic acids, and alkylphosphonic acids are effective as shape controllers and act by changing the surface energies of the crystallographic planes.[58] Amines, such as triethanolamine (TEOA), ethylenediamine and diethylenetriamine have been applied to prepare TiO_2 nanoparticles with different aspect ratios. Sodium oleate and sodium stearate could alter TiO_2 cubes from round-corner to sharp-edge.[60] A standard sol-gel procedure[61] to fabricate TiO_2 utilized titanium alkoxide like titanium tetraisopropoxide (TTIP) and tetramethylammonium hydroxide. TTIP was added to 2 °C alcoholic solvents in a three-neck flask and heated at around 50 °C for 13 days. Lee *et al.*[62] developed a two-step sol-gel method where they

applied triethanolamine (TEOA) with a molar ratio of TTIP: TEOA = 1:2 and ethylenediamine (ED) further as the shape controllers because amine groups strongly bond to TiO_2 surfaces when pH > 10.5, yielding anisotropic growth with high aspect ratios. Longer low-temperature heating of the gel could prevent the agglomeration of TiO_2 particles during the high-temperature annealing crystallization process,[45] and templates have also been widely applied with sol-gel method to create TiO_2 with ordered structures like pores, or hollow tubes.

1.3.2 Hydrothermal method

Usually prepared with different types of precursors in steel pressure vessels (autoclaves) under controlled temperature and pressure, the hydrothermal method has been extensively studied to fabricate nanoscale ceramics.[45] The temperature is usually above the boiling point of water, or as high as the self-generated saturated vapor pressure. The pressure in the autoclaves is controlled by the reactants and operating temperature.[63]

The hydrothermal method has been widely utilized to synthesize spherical particles or 1D titania because it requires less cost, mild reaction conditions, and simple equipment compared to chemical vapor deposition, anodic oxidation, seeded growth and other approaches.[63] The broad manipulation opportunities on each parameter (pH, concentration, temperature, reaction time) control the morphology and shape.

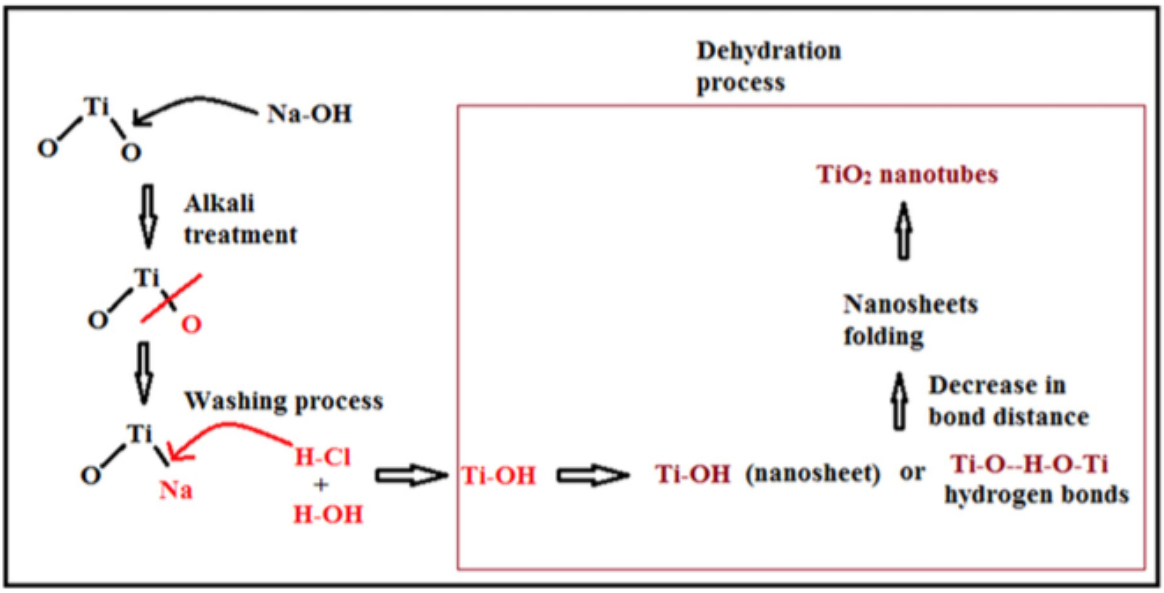

Figure 1-9 Formation mechanism of TiO_2 nanotubes using hydrothermal method.[63]

TiO_2 nanoparticles can be synthesized at 240 °C for 2 hours with the peptized precipitates in water.[64] With added acidity, pure anatase spherical particles with adjustable diameter were made by changing the Ti(IV) concentration and solvent composition.[65] 1D titania nanorods, nanowires have also been prepared through acidic or basic aqueous precursors with hydrothermal methods.[45] When the medium is turned to alkaline (usually concentrated NaOH), titania nanotubes could be easily prepared from TiO_2 powders. The acid washing step introduced by Kasuga *et al.*[66] was to remove the sodium ions, replace with h^+ ions, and form new Ti-OH bonds for further dehydration into Ti-O-Ti. (as Figure 1-9 illustrates)

However, more studies reveal that even without washing step, the hydrothermal step is enough to create nanotube structure.[63] Factors influencing the TiO_2 nanotubes formation were discussed based on the recent literatures in Wong's review[63] in the following manners: (1) Starting materials could vary among titania pure phase powders, commercial Degussa P25 TiO_2 powders (a mixture of anatase and rutile phases), Ti metal, Ti (IV)

alkoxide, layered titanate Na2Ti3O7, and titania sol, leading to various sizes and shapes. (2) The temperature and duration of the hydrothermal step will also determine the morphology and dimensions of the nanotubes. (3) Whether or not applying a sonication pretreatment has influence on the dispersion of the particles, and the crystal growth. (4) Washing step will determine the elemental composition and surface area of the nanotubes.

1.3.3 Liquid phase deposition method

Liquid phase deposition (LPD) method is a simple route to synthesis nano-sized metal dioxides via a ligand exchange equilibrium reaction on a substrate. Early research on LPD dated back to 1980s, when Nagayama innovated a new coating method for silica as shown in Figure 1-10.[67]

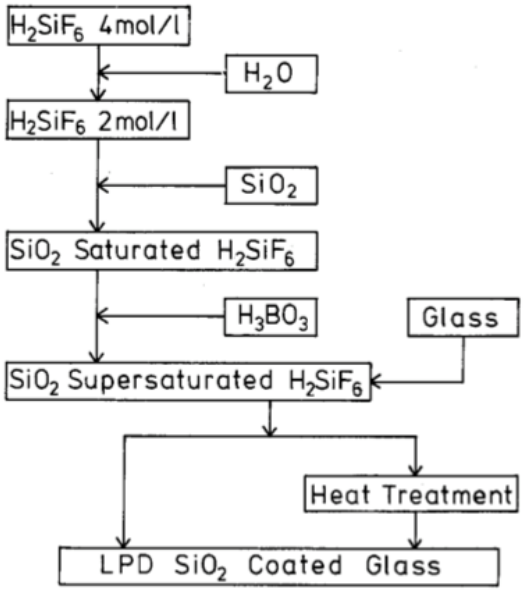

Figure 1-10 Scheme of the synthesis procedures of silica from H_2SiF_6.[67] (Reproduced with permission from J. Electrochem. Soc., 150, H205 (2003). Copyright 2003, The Electrochemical Society)

Hydrofluosilicic acid was diluted with water, followed by the addition of silica gel at 35 °C and kept stirring for 16 hours at the same temperature. The addition of silica led the equilibrium (a) from right to left. However, boric acid was added as a reactant to fluoric

acid, since BF4- is more stable than the noncoordinated F^- ions, changing (a) and leaving the solution supersaturated with silica. Cleaned glass substrates were immersed in the solution for a varied period of time. The deposition of silica on the surface of glass would start and proceed steadily with time. Further washing and annealing were conducted to crystallize the deposited nanoparticles.

$$H_2SiF_6 + 2H_2O \leftrightarrow 6HF + SiO_2 \text{ (a)}$$

$$H_3BO_3 + 4HF \leftrightarrow BF_4^- + H_3O^+ + 2H_2O \text{ (b)}$$

Briefly, this paper pointed out several rules applied in silica LPD process. (1) The deposition rate is influenced by temperature and boric acid amount, in other words, the degree of supersaturation. (2) Lower temperature solution coated film is more dense and stable, and further calcination fortifies this effect.

As for titania synthesis, a very representative system utilizing ammonium hexafluorotitanate (AHFT) and boric acid (BA) has been applied to prepare titania depositions by the ligand exchange of metal fluorocomplex ions $[TiF_6]^{2-}$ and the consumption of F^- with boric acid as a scavenger. In this process, the hydrolysis of the titanium fluoro complex yields titanium hydroxide and free F^- ions, while the addition of boric acid drives the reaction towards right. The properties of the titania product and film thickness could be determined by several factors such as the substrate,[68] concentration of AHFT and BA, [69] reaction temperature, immersion time, [70,71] and calcination temperature and length. [72,73]

Another type of precursor came from a simple titanium salt TiF_4, which has been deposited on different substrates such as glass slides, polymers, cotton fibers, filter paper, porous alumina membranes, by a similar mechanism in acidic aqueous environment. [74,75]

$$TiF_4 + nH_2O \leftrightarrow TiF_{4-n}(OH)_n + nHF$$

$$TiF_{4-n}(OH)_n \quad + (4-n)H_2O \rightarrow Ti(OH)_4 \quad + (4-n)HF$$

$$Ti(OH)_4 \quad \rightarrow TiO_2 + 2H_2O \quad \text{(f)}$$

The hydrolysis and condensation go through stepwise reactions as above equations illustrate. Different from using a F^- scavenger to adjust the supersaturation level, for this method, pH is usually adjusted by adding acidic or basic reagents. When pH is below 1, inefficient hydrolysis prevents the deposition. When pH is above 3, precipitation is preferred so the solution is highly supersaturated with titania rather than forming a uniform coating on substrates. When pH is between 1 and 3, due to the stability of Ti-F bonds, rapid hydrolysis and polymerization of the precursor do not occur; instead, the moderate reaction leads to a stable deposition through heterogeneous nucleation.[75]

There are various ways to develop a thin TiO_2 film, such as vacuum evaporation, sputtering, chemical vapor deposition and sol-gel based spin coating, doctor blade, or dip coating. These methods can not win regarding large scale industrial use. Compared to the above-mentioned methods, LPD is straight-forward, lower-temperature assisted, low-cost, environmentally friendly and does not require any special equipment, besides, works with various types of substrates such as glass, quartz,[72] mica,[76] parylene composites,[69] silica fibers or spheres,[77], polyimide surface on spacecraft,[78] polycarbonate membranes, and

even inorganic salts like $MnCO_3$,[79] cotton fibers[80] and even pre-made TiO_2 nanorods,[81] vanadium oxide nanobelts,[82] graphene,[83] layer-by-layer made PAH/PAA (polyallylamine hydrochloride/polyacrylic acid) films.[84] Most room temperature methods require high-temperature annealing to remove the organic precursor and enhance the crystallinity. Last but not least, this aqueous one-step reaction yields particles with anatase crystallinity directly. [74,81]

The chemical bonding between the deposited nanomaterials and the substrates ensured the strong adhesion of the coating, besides, the chemical and physical properties of the film can be finely tuned by adjusting the parameters (concentration of the reactants, the duration, and temperature of the reaction, pH, solution composition) of the reacting system easily, which will be discussed in the following chapters.

BIBLIOGRAPHY

BIBLIOGRAPHY

(1) Team, C. W.; P, R. K.; Reisinger, A. *Assessment Report (AF4) of the United Nations Intergovernmental Panel on Climate Change (IPCC)*; Geneva, Switzerland; Vol. 2007.

(2) U. S. E. I. A. International Energy Outlook 2013. **2013**, 1–312.

(3) U. S. E. I. A. Annual Energy Outlook 2015 with Projections to 2040. **2015**, 1–154.

(4) Turner, J. A. *A Realizable Renewable Energy Future (Vol 285, Pg 687, 1999)*; Science, 1999.

(5) Doney, S. C.; Schimel, D. S. *Annual Review of Environment and Resources*; 2007; Vol. 32, pp. 31–66.

(6) Goetzberger, A.; Hebling, C. Photovoltaic Materials, Past, Present, Future. *Solar Energy Materials and Solar Cells* **2000**, *62*, 1–19.

(7) National Renewable Energy laboratory. *Best Research-Cell Efficiencies*; 2016.

(8) Green, M. A.; Emery, K.; Hishikawa, Y.; Warta, W.; Dunlop, E. D. Solar Cell Efficiency Tables (Version 43). *Progress in Photovoltaics* **2014**, *22*, 1–9.

(9) Dye-Sensitized Solar Cells: a Safe Bet for the Future. **2008**, *1*, 655–667.

(10) Measuring the Thermal Conductivity of Thin Films: 3 Omega and Related Electrothermal Methods

(11) Caramori, S.; Cristino, V.; Boaretto, R.; Argazzi, R.; Bignozzi, C. A.; Di Carlo, A. New Components for Dye-Sensitized Solar Cells. *International Journal of Photoenergy* **2010**, *2010*, 1–16.

(12) Nazeeruddin, M. K.; Kay, A.; Rodicio, I.; Humphry-Baker, R.; Mueller, E.; Liska, P.; Vlachopoulos, N.; Graetzel, M. Conversion of Light to Electricity by Cis-X2bis(2,2“-Bipyridyl-4,4-”Dicarboxylate)Ruthenium(II) Charge-Transfer Sensitizers (X = Cl-, Br-, I-, CN-, and SCN-) on Nanocrystalline Titanium Dioxide Electrodes. *J. Am. Chem. Soc.* **1993**, *115*, 6382–6390.

(13) Han, L.; Islam, A.; Chen, H.; Malapaka, C.; Chiranjeevi, B.; Zhang, S.; Yang, X.; Yanagida, M. High-Efficiency Dye-Sensitized Solar Cell with a Novel Co-Adsorbent. *Energy Environ. Sci.* **2012**, *5*, 6057–6060.

(14) Nazeeruddin, M. K.; Péchy, P.; Renouard, T.; Zakeeruddin, S. M.; Humphry-Baker, R.; Comte, P.; Liska, P.; Cevey, L.; Costa, E.; Shklover, V.; *et al.* Engineering of Efficient Panchromatic Sensitizers for Nanocrystalline TiO 2-Based Solar Cells. *J.*

Am. Chem. Soc. **2001**, *123*, 1613–1624.

(15) Palomares, E.; Clifford, J. N.; Haque, S. A.; Lutz, T.; Durrant, J. R. Control of Charge Recombination Dynamics in Dye Sensitized Solar Cells by the Use of Conformally Deposited Metal Oxide Blocking Layers. *J. Am. Chem. Soc.* **2003**, *125*, 475–482.

(16) Wu, J.; Lan, Z.; Hao, S.; Li, P.; Lin, J.; Huang, M.; Fang, L.; Huang, Y. Progress on the Electrolytes for Dye-Sensitized Solar Cells. *Pure and Applied Chemistry* **2008**, *80*, 2241–2258.

(17) Chen, C.-Y.; Wang, M.; Li, J.-Y.; Pootrakulchote, N.; Alibabaei, L.; Ngoc-le, C.-H.; Decoppet, J.-D.; Tsai, J.-H.; Grätzel, C.; Wu, C.-G.; *et al.* Highly Efficient Light-Harvesting Ruthenium Sensitizer for Thin-Film Dye-Sensitized Solar Cells. *ACS Nano* **2009**, *3*, 3103–3109.

(18) Burschka, J.; Pellet, N.; Moon, S.-J.; Humphry-Baker, R.; Gao, P.; Nazeeruddin, M. K.; Graetzel, M. Sequential Deposition as a Route to High-Performance Perovskite-Sensitized Solar Cells. *Nature* **2013**, *499*, 316–.

(19) Morandeira, A.; López-Duarte, I.; Martínez-Díaz, M. V.; O'Regan, B.; Shuttle, C.; Haji-Zainulabidin, N. A.; Torres, T.; Palomares, E.; Durrant, J. R. Slow Electron Injection on Ru−Phthalocyanine Sensitized TiO 2. *J. Am. Chem. Soc.* **2007**, *129*, 9250–9251.

(20) Péchy, P.; Renouard, T.; Zakeeruddin, S. M.; Humphry-Baker, R.; Comte, P.; Liska, P.; Cevey, L.; Costa, E.; Shklover, V.; Spiccia, L.; *et al.* Engineering of Efficient Panchromatic Sensitizers for Nanocrystalline TiO 2-Based Solar Cells. *J. Am. Chem. Soc.* **2001**, *123*, 1613–1624.

(21) Hagfeldt, A.; Boschloo, G.; Sun, L.; Kloo, L.; Pettersson, H. Dye-Sensitized Solar Cells. *Chem. Rev.* **2010**, *110*, 6595–6663.

(22) Clifford, J. N.; Palomares, E.; Nazeeruddin, M. K.; Thampi, R.; Grätzel, M.; Durrant, J. R. Multistep Electron Transfer Processes on Dye Co-Sensitized Nanocrystalline TiO 2Films. *J. Am. Chem. Soc.* **2004**, *126*, 5670–5671.

(23) Kong, F.-T.; Dai, S.-Y.; Wang, K.-J. Review of Recent Progress in Dye-Sensitized Solar Cells. *Advances in OptoElectronics* **2007**, *2007*, 1–13.

(24) Papageorgiou, N. An Iodine/Triiodide Reduction Electrocatalyst for Aqueous and Organic Media. *J. Electrochem. Soc.* **1997**, *144*, 876.

(25) Kavan, L.; Yum, J. H.; Grätzel, M. Optically Transparent Cathode for Dye-Sensitized Solar Cells Based on Graphene Nanoplatelets. *ACS Nano* **2010**, *5*, 165–172.

(26) Phase-Pure TiO2 Nanoparticles: Anatase, Brookite and Rutile. **2008**, *19*, 145605.

(27) Ibhadon, A.; Fitzpatrick, P. Heterogeneous Photocatalysis: Recent Advances and Applications. *Catalysts 2013, Vol. 3, Pages 455-485* **2013**, *3*, 189–218.

(28) ZnO Nanotube-Based Dye-Sensitized Solar Cell and Its Application in Self-Powered Devices. **2010**, *21*.

(29) Xu, J.; Fan, K.; Shi, W.; Li, K.; Peng, T. Application of ZnO Micro-Flowers as Scattering Layer for ZnO-Based Dye-Sensitized Solar Cells with Enhanced Conversion Efficiency. *Solar Energy* **2014**, *101*, 150–159.

(30) Le Viet, A.; Jose, R.; Reddy, M. V.; Chowdari, B. V. R.; Ramakrishna, S. Nb2O5 Photoelectrodes for Dye-Sensitized Solar Cells: Choice of the Polymorph. *The Journal of …* **2010**, *114*, 21795–21800.

(31) Snaith, H. J.; Ducati, C. SnO2-Based Dye-Sensitized Hybrid Solar Cells Exhibiting Near Unity Absorbed Photon-to-Electron Conversion Efficiency. *Nano Lett.* **2010**, *10*, 1259–1265.

(32) Maçaira, J.; Andrade, L.; Mendes, A. Review on Nanostructured Photoelectrodes for Next Generation Dye-Sensitized Solar Cells. *Renewable and Sustainable Energy Reviews* **2013**, *27*, 334–349.

(33) Bizani, E.; Fytianos, K.; Poulios, I.; Tsiridis, V. Photocatalytic Decolorization and Degradation of Dye Solutions and Wastewaters in the Presence of Titanium Dioxide. *Journal of Hazardous Materials* **2006**, *136*, 85–94.

(34) A Fujishima, X. Z. D. A. T. TiO2 Photocatalysis and Related Surface Phenomena. **2008**, *63*, 515–582.

(35) Renz, C. Lichtreaktionen Der Oxyde Des Titans, Cers Und Der Erdsäuren. *Helvetica Chimica Acta* **1921**, *4*, 961–968.

(36) Goodeve, C. F.; Kitchener, J. A. Photosensitisation by Titanium Dioxide. *Trans. Faraday Soc.* **1938**, *34*, 570–579.

(37) Xu, H.; Ouyang, S.; Liu, L.; Reunchan, P.; Umezawa, N.; Ye, J. Recent Advances in TiO2-Based Photocatalysis. *J. Mater. Chem. A* **2014**, *2*, 12642–12661.

(38) Fujishima, A.; HONDA, K. Electrochemical Photolysis of Water at a Semiconductor Electrode. *Nature* **1972**, *238*, 37–38.

(39) Frank, S. N.; Bard, A. J. Heterogeneous Photocatalytic Oxidation of Cyanide Ion in Aqueous Solutions at Titanium Dioxide Powder. *J. Am. Chem. Soc.* **1977**, *99*, 303–304.

(40) LINSEBIGLER, A. L.; LU, G. Q.; YATES, J. T. Photocatalysis on Tio2 Surfaces - Principles, Mechanisms, and Selected Results. *Chem. Rev.* **1995**, *95*, 735–758.

(41) Hartmann, P.; Lee, D.-K.; Smarsly, B. M.; Janek, J. Mesoporous TiO 2: Comparison of Classical Sol−Gel and Nanoparticle Based Photoelectrodes for the Water Splitting Reaction. *ACS Nano* **2010**, *4*, 3147–3154.

(42) Rodgher, V.; Moreira, J.; de Lasa, H.; Serrano, B. Photocatalytic Degradation of Malic Acid Using a Thin Coated TiO 2-Film: Insights on the Mechanism of Photocatalysis. *AIChE J.* **2014**, *60*, 3286–3299.

(43) Vautier, M.; Guillard, C.; Herrmann, J.-M. Photocatalytic Degradation of Dyes in Water: Case Study of Indigo and of Indigo Carmine. *Journal of Catalysis* **2001**, *201*, 46–59.

(44) Ryu, J.; Choi, W. Substrate-Specific Photocatalytic Activities of TiO 2and Multiactivity Test for Water Treatment Application. *Environ. Sci. Technol.* **2008**, *42*, 294–300.

(45) Chen, X.; Mao, S. S. Titanium Dioxide Nanomaterials: Synthesis, Properties, Modifications, and Applications. *Chem. Rev.* **2007**, *107*, 2891–2959.

(46) Liu, N.; Chen, X.; Zhang, J.; Schwank, J. W. A Review on TiO2-Based Nanotubes Synthesized via Hydrothermal Method: Formation Mechanism, Structure Modification, and Photocatalytic Applications. *Catalysis Today* **2014**, *225*, 34–51.

(47) Lui, G.; Liao, J.-Y.; Duan, A.; Zhang, Z.; Fowler, M.; Yu, A. Graphene-Wrapped Hierarchical TiO2 Nanoflower Composites with Enhanced Photocatalytic Performance. *J. Mater. Chem. A* **2013**, *1*, 12255–12262.

(48) Chen, F.; Cao, F.; Li, H.; Bian, Z. Exploring the Important Role of Nanocrystals Orientation in TiO 2Superstructure on Photocatalytic Performances. *Langmuir* **2015**, *31*, 3494–3499.

(49) HU, L. L.; YOKO, T.; KOZUKA, H.; SAKKA, S. Effects of Solvent on Properties of Sol Gel-Derived Tio2 Coating Films. *Thin Solid Films* **1992**, *219*, 18–23.

(50) Ohya, Y.; Saiki, H.; Tanaka, T.; Takahashi, Y. Microstructure of TiO2 and ZnO Films Fabricated by the Sol-Gel Method. *Journal of the American Ceramic Society* **1996**, *79*, 825–830.

(51) Schattka, J. H.; Wong, E.; Antonietti, M.; Caruso, R. A. Sol-Gel Templating of Membranes to Form Thick, Porous Titania, Titania/Zirconia and Titania/Silica Films. *J. Mater. Chem.* **2006**, *16*, 1414–1420.

(52) Wang, H.; Ding, J.; Xue, Y.; Wang, X.; Lin, T. Superhydrophobic Fabrics From Hybrid Silica Sol-Gel Coatings: Structural Effect of Precursors on Wettability and Washing Durability. *J. Mater. Res.* **2011**, *25*, 1336–1343.

(53) sanchez, C.; livage, J. Sol-Gel Chemistry From Metal Alkoxide Precursors. *New*

journal of Chemistry **1990**, 513–521.

(54) Sakka, S.; Yoko, T. Sol-Gel-Derived Coating Films and Applications. *Structure and Bonding* **1992**, *77*, 89–118.

(55) Askeland, P. A. Preparation and Characterization of Sol-Gel Derived Metal Oxide Thin Films and Powders for Coatings and Catalysts, 1997.

(56) Antonelli, D. M.; Ying, J. Y. Synthesis of Hexagonally Packed Mesoporous TiO2 by a Modified Sol–Gel Method. *Angewandte Chemie International Edition in English* **1995**, *34*, 2014–2017.

(57) Barbé, C. J.; Arendse, F.; Comte, P.; Jirousek, M.; Lenzmann, F.; Shklover, V.; Grätzel, M. Nanocrystalline Titanium Oxide Electrodes for Photovoltaic Applications. *Journal of the American Ceramic Society* **1997**, *80*, 3157–3171.

(58) Kim, J. Y.; Choi, S. B.; Kim, D. W.; Lee, S.; Jung, H. S.; Lee, J.-K.; Hong, K. S. Surfactant-Assisted Shape Evolution of Thermally Synthesized TiO 2Nanocrystals and Their Applications to Efficient Photoelectrodes. *Langmuir* **2008**, *24*, 4316–4319.

(59) Burunkaya, E.; Akarsu, M.; Çamurlu, H. E.; Kesmez, Ö.; Yeşil, Z.; Asiltürk, M.; Arpaç, E. Production of Stable Hydrosols of Crystalline TiO2 Nanoparticles Synthesized at Relatively Low Temperatures in Diverse Media. *Applied Surface Science* **2013**, *265*, 317–323.

(60) Li, W.; Wu, Z.; Wang, J.; Elzatahry, A. A.; Zhao, D. A Perspective on Mesoporous TiO 2Materials. **2014**, *26*, 287–298.

(61) Chemseddine, A.; Moritz, T. Nanostructuring Titania: Control Over Nanocrystal Structure, Size, Shape, and Organization. *European Journal of Inorganic Chemistry* **1999**, *1999*, 235–245.

(62) Lee, S.; Cho, I.-S.; Lee, J. H.; Kim, D. H.; Kim, D. W.; Kim, J. Y.; Shin, H.; Lee, J.-K.; Jung, H. S.; Park, N.-G.; *et al.* Two-Step Sol–Gel Method-Based TiO 2Nanoparticles with Uniform Morphology and Size for Efficient Photo-Energy Conversion Devices. *Chem. Mater.* **2010**, *22*, 1958–1965.

(63) Wong, C. L.; Tan, Y. N.; Mohamed, A. R. A Review on the Formation of Titania Nanotube Photocatalysts by Hydrothermal Treatment. *J. Environ. Manage.* **2011**, *92*, 1669–1680.

(64) Yang, J.; Mei, S.; Ferreira, J. M. F. Hydrothermal Synthesis of TiO2 Nanopowders From Tetraalkylammonium Hydroxide Peptized Sols. *Materials Science and Engineering: C* **2001**, *15*, 183–185.

(65) Seung Yong Chae; Myun Kyu Park; Sang Kyung Lee; Taek Young Kim; Sang Kyu Kim, A.; Lee, W. I. Preparation of Size-Controlled TiO2 Nanoparticles and Derivation of Optically Transparent Photocatalytic Films. *Chem. Mater.* **2003**, *15*,

3326–3331.

(66) Kasuga, T.; Hiramatsu, M.; Hoson, A.; Sekino, T.; Niihara, K. Formation of Titanium Oxide Nanotube. *Langmuir* **1998**, *14*, 3160–3163.

(67) Nagayama, H.; Honda, H.; Kawahara, H. A New Process for Silica Coating. *J. Electrochem. Soc.* **1988**, *135*, 2013–2016.

(68) Yu, J.; Fan, J.; Cheng, B. Dye-Sensitized Solar Cells Based on Anatase TiO2 Hollow Spheres/Carbon Nanotube Composite Films. *Journal of Power Sources* **2011**, *196*, 7891–7898.

(69) Malvadkar, N.; Dressick, W. J.; Demirel, M. C. Liquid Phase Deposition of Titania Onto Nanostructured Poly-P-Xylylene Thin Films. *J. Mater. Chem.* **2009**, *19*, 4796–4799.

(70) Li, S.; Liu, J.; Feng, T. Low Temperature Coating of Anatase Thin Films on Silica Glass Fibers by Liquid Phase Deposition. *J. Wuhan Univ. Technol.* **2007**, *22*, 136–139.

(71) Lee, M.-K.; Fan, C.-H.; Wang, H.-C.; Chang, C.-Y. Fluorine Passivation of Titanium Oxide Films on ITO/Glass Grown by Liquid Phase Deposition for Electrochroism. *J. Electrochem. Soc.* **2011**, *158*, D511.

(72) Yu, J.-G.; Yu, H.-G.; Cheng, B.; Zhao, X.-J.; Yu, J. C.; Ho, W.-K. The Effect of Calcination Temperature on the Surface Microstructure and Photocatalytic Activity of TiO 2Thin Films Prepared by Liquid Phase Deposition. *J. Phys. Chem. B* **2003**, *107*, 13871–13879.

(73) Maeda, M. Preparation of Titania Films with Cohered Nanosized Particles Using Improved Liquid Phase Deposition Process. *international journal of electrochemical science* **2015**, *10*, 2988–2996.

(74) Shimizu, K.; Imai, H.; Hirashima, H.; Tsukuma, K. Low-Temperature Synthesis of Anatase Thin Films on Glass and Organic Substrates by Direct Deposition From Aqueous Solutions. *Thin Solid Films* **1999**, *351*, 220–224.

(75) Imai, H.; Takei, Y.; Shimizu, K.; Matsuda, M.; Hirashima, H. Direct Preparation of Anatase TiO2 Nanotubes in Porous Alumina Membranes. *J. Mater. Chem.* **1999**, *9*, 2971–2972.

(76) Pourmand, M.; Taghavinia, N. TiO2 Nanostructured Films on Mica Using Liquid Phase Deposition. *Materials Chemistry and Physics* **2008**, *107*, 449–455.

(77) Wu, J.-H.; Li, X.-S.; Zhao, Y.; Zhang, W.; Guo, L.; Feng, Y.-Q. Application of Liquid Phase Deposited Titania Nanoparticles on Silica Spheres to Phosphopeptide Enrichment and High Performance Liquid Chromatography Packings. *Journal of Chromatography A* **2011**, *1218*, 2944–2953.

(78) Gouzman, I.; Girshevitz, O.; Grossman, E.; Eliaz, N.; Sukenik, C. N. Thin Film Oxide Barrier Layers: Protection of Kapton From Space Environment by Liquid Phase Deposition of Titanium Oxide. *ACS Appl. Mater. Interfaces* **2010**, *2*, 1835–1843.

(79) Lee, H.-K.; Sakemi, D.; Selyanchyn, R.; Lee, C.-G.; Lee, S.-W. Titania Nanocoating on MnCO3 Microspheres via Liquid-Phase Deposition for Fabrication of Template-Assisted Core-Shell- and Hollow-Structured Composites. *ACS Appl. Mater. Interfaces* **2014**, *6*, 57–64.

(80) Ghadiri, E.; Taghavinia, N.; Zakeeruddin, S. M.; Grätzel, M.; Moser, J.-E. Enhanced Electron Collection Efficiency in Dye-Sensitized Solar Cells Based on Nanostructured TiO 2Hollow Fibers. *Nano Lett.* **2010**, *10*, 1632–1638.

(81) Yu, H.; Yu, J.; Cheng, B.; Lin, J. Synthesis, Characterization and Photocatalytic Activity of Mesoporous Titania Nanorod/Titanate Nanotube Composites. *Journal of Hazardous Materials* **2007**, *147*, 581–587.

(82) Yu, H.; Yu, J.; Cheng, B.; Liu, S. Novel Preparation and Photocatalytic Activity of One-Dimensional TiO 2hollow Structures. *Nanotechnology* **2007**, *18*, 065604.

(83) Zhang, H.; Xu, P.; Du, G.; Chen, Z.; Oh, K.; Pan, D.; Jiao, Z. A Facile One-Step Synthesis of TiO2/Graphene Composites for Photodegradation of Methyl Orange. *Nano Res.* **2010**, *4*, 274–283.

(84) Kim, J.-H.; Lee, M. J.; Kim, S.; Hwang, J.; Lim, T.-Y.; Kim, S.-H. Fabrication of Patterned TiO2 Thin Film by a Wet Process. *Met. Mater. Int.* **2012**, *18*, 833–837.

2 Titania from a Hard Template $CaCO_3$ and its Photocatalytic Performance

2.1 Background

2.1.1 Porous materials and their benefits

Porous material is a continuous and solid network filled with voids.[1] Porous materials may have high surface area, low density, customizable structures and electronic properties which are important for the fields of adsorption, separation, catalysis and renewable energy.[2] According to IUPAC definition, nanoporous materials have pores smaller than 100 nm and can be subdivided into three categories as: microporous materials (0.2-2 nm) such as zeolites and metal organic framework, mesoporous materials (2-50 nm) such as silica and most metal oxides and macroporous materials (50-1000 nm) such as sponge, cotton and some metal oxides.[1] When considered from the material compositions, they can be classified as purely inorganic, organic-inorganic hybrid and purely organic porous materials. Inorganic porous materials are well known as metal oxides, silica, while organic porous materials are represented by porous carbon and porous polymers. Hybrids are usually formed by strong bonds between the inorganic parts such as metallic ions, clusters, layers or three-dimensional scaffolds, and organic parts such as polycarboxylates, phosphonates, and sulfonates.[3]

Chapter 1 already introduced the five steps of heterogeneous photocatalytic reactions. Nanoporous materials will be beneficial for the first two steps - diffusion and adsorption of reactants on the surface of photocatalysts. Using nanoporous titania rather than its bulk form provides increased surface-to-volume ratio, higher surface area, and diffusion path

for reactants. In addition, the increase of the surface energy for each nanoparticle will improve the contaminant removal, compared to bulk materials without porous structures. Last but not least, less amount of catalyst will be needed because of the increase of the active surface sites. These factors will positively influence the third step – reaction on the surface of the catalyst- as well.

2.1.2 Templating methods for porous TiO_2

In Chapter 1, several synthetic approaches were introduced, such as sol-gel, hydrothermal, and liquid phase deposition. As for sol-gel method, the liquid sol could be transformed into thin films, wet gel, dense ceramics, aerogel, fibers, and powders through various techniques.[4] However, it generally produces TiO_2 with irregular and disordered structures when no surfactant additives or templates are used.[5] Nanoparticles prepared by hydrothermal usually require high temperature and pressure. One of the traditional methods to prepare mesoporous/nanoporous structures of titania is through the hydrothermal method where TTIP was added into nitric acid and went through precipitation, hydrolysis, 8-hour peptization, filtration and hydrothermal treatment for 12 hours more in autoclaves. The final product was rotary-evaporated to a TiO_2 slurry.[6] An alternative approach[7] is to prehydrolyze titanium n-butoxide/ethanol mixture in a dilute aqueous nitric solution, aging for 14 days, drying, grinding, washing and annealing. An improved method reported by Yu *et al*. used high-intensity ultrasonication to control the condensation and agglomeration of pre-made titania sol particles. Spherical particles with sizes of 100-200 nm packed with 10-nm small particles and narrow channels were fabricated, but still lacked the porosity order.[8] Liquid phase deposition is a versatile

method to prepare titania coatings, but could hardly control the porosity of the particles grown on the film.

Traditional methods are time-consuming and lacking ordered structures, while template-directed methods generally pick up structural and morphological properties duplicated from numerous templates. Templates offer the possibility of creating 1D, 2D, and 3D[9] materials such as wires, tubes, rods, sheets, and interconnected hierarchical structures. Just for nanotubes alone, it offers controlled scale of diameters via different templates. There are still some controversial issues such as the extra cost of the template material, complicated fabrication process, and the possibility of destroyed tube or rod morphology during the synthesis process. This work will focus on improving templating methods and overcoming current difficulties for a better solution.

Diblock or triblock copolymers templates are a type of extensively-studied organic templates which make ordered mesostructures, directing the growth of metal oxides in non-hydrolytic environment.[4] Common amphiphilic poly(alkylene oxide) block polymers such as Pluronic P-123 and Pluronic F-127 are typically dissolved in ethanol, followed by the addition of a $TiCl_4$ precursor and gelation in air at low temperature for several days. Calcination will remove the organic templates, leaving a mesoporous structure. However, these methods usually require control of the cooperative assembly, longer gelation time, complicated pH manipulations and the collapse of TiO_2 frameworks due to the phase transition.[4]

Hard-templating, or nano casting, has been developed to use preformed mesoporous solids as templates via precursor infiltration, conversion of the precursor to metal oxide,

and removal of the hard template. Preformed solids could be silicates,[10] aluminas,[11] or zinc oxide,[12] with mesoporous structure of replicated nanowires or nanospheres. The precursor must be able to be incorporated into the channels or pores of the template by adsorption, ion exchange, or covalent grafting.[13] Difficulties are existing in filling the micro channel vacancies of the templates and finding a suitable precursor with high solubility and low thermal stability.[5] For example, titanium precursors tend to precipitate and crystallize in aqueous solutions, clogging penetration channels. On the other hand, if the precursor concentration is too high or too low, either bulk material with a low surface area or insufficient template coating will be formed. At the right amount of precursor to template ratio, it's possible to obtain continuous framework of TiO_2 porous structures from a successful duplicate of the hard template removal by dissolving or etching.

2.1.3 A modified sol-gel method with calcium carbonate template

As mentioned above, various techniques have been developed for the synthesis of meso/nano porous titania. However, macro-structured solids remain more limited.[14] The goal of the project is to develop a comprehensive titania structure with macro/meso/micro pores available for photocatalytic applications. In this chapter, a new series of hard templates were proposed for macro/meso/micro porous titania synthesis. Calcium carbonate has been prepared through some other templates,[15-17] and also worked as templates for synthesis of gold,[18] DNA capsules,[19] and protein microspheres,[20] now it is used as an easy-to-remove template itself with acidification dissolving.

The best example of natural calcium carbonate composite is sea urchin skeletal plates, which have a bicontinuous morphology with 10-15 micrometer pores. A great amount of work has been done with sea urchin plates by first filling the porous network with

materials "precursor" to form a composite structure and then dissolving away the $CaCO_3$, leaving a duplicate morphology of the original plate. The sea urchin skeletal plate could be used directly as the template, or used to prepare a duplicate polymer scaffold as a chemically stable polymer template for future use.[14]

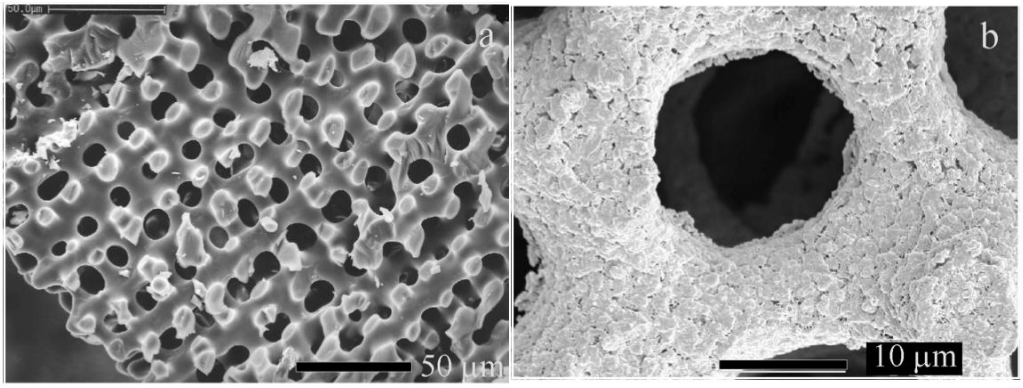

Figure 2-1 SEM images of (a) a cleaned sea urchin skeletal shell (b) sea urchin shell coated with gold and annealed.[18]

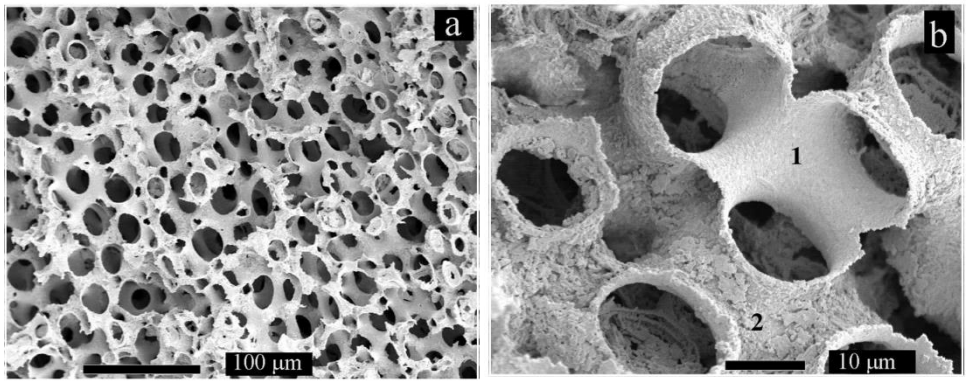

Figure 2-2 SEM images of gold-coated sea urchin skeleton after acid dissolution (a) at lower magnification, (b) at higher magnification. 1 marks the smooth inner surface, while 2 marks the rough outer surface of the gold structure.[18]

An early report[18] used echinoid (sea urchin) skeletal plates as templates for porous gold preparation, with pore diameters in the order of 15 um as Figure 2-1 (a) shows. Gold paint made with organo-stabilized gold particles was coated and annealed with the skeleton, of which the rough surface and structures were duplications from the original

bio-skeleton with similar pore size and the scaffold (Figure 2-1(b)). Removal of $CaCO_3$ was fulfilled by dissolution of the composite in acid. (Figure 2-2)

To prepare a stable polymer duplicate, methyl methacrylate, and ethyl acrylate at a ratio of 13: 7 was mixed with 1% w.t. initiator to immerse the sea urchin plates. After vacuum treatment, curing and template removal, a sponge-like polymer membrane (Figure 2-3) was produced with identical sea urchin structure.[14]

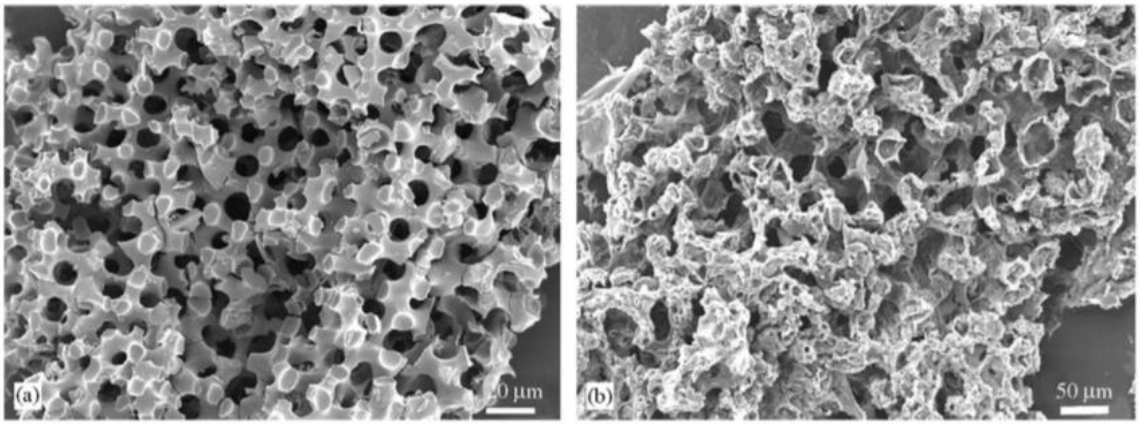

Figure 2-3 SEM images of titania produced by hydrolysis-templating method on polymer replica of sea urchin by (a) titanium tetrachloride, (b) titanium ethoxide.[14]

Through hydrolysis method, silica and titania could also be synthesized from either direct method with sea urchin plate, or indirectly with polymer duplicates (Figure 2-5). As for titania, the plate could not be used if the precursor is acidic. In this case, the polymer scaffold was immersed in titanium ethoxide or titanium tetrachloride, followed by at least 3 days of hydrolysis in a sealed desiccator.[14]

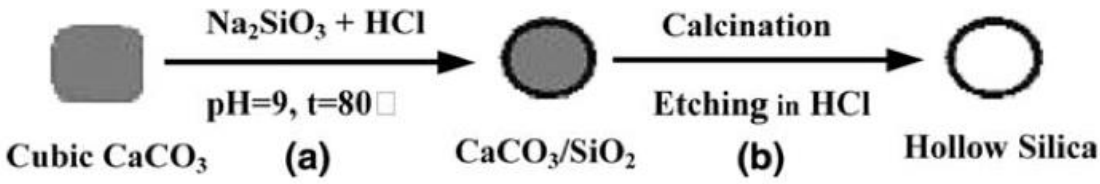

Figure 2-4 Scheme of synthesis procedures of spherical hollow silica .[24]

Commercial $CaCO_3$ at smaller scales have been applied as templates for porous silica[24] and titania synthesis[25,26] as well. Calcium carbonates with cubic and needle-like shapes in nano-size ranges were applied as the sacrificial templates. The hydrolysis of sodium silicate left a continuous coating of SiO_2 on the surface of $CaCO_3$ cores to form a core-shell structure. With further product calcination and dissolving of $CaCO_3$ in HCl dilution solution,[24] hollow silica structures were obtained.(Figure 2-4)

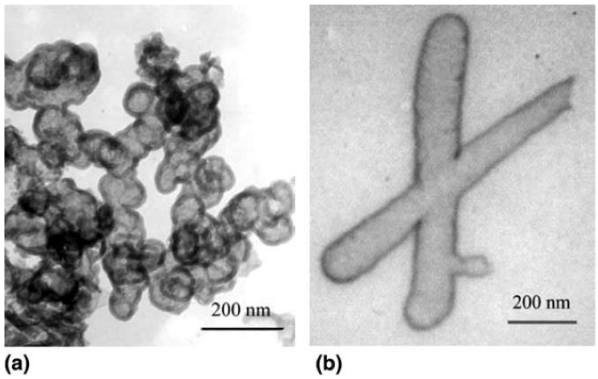

Figure 2-5 TEM images of hollow silica particles using different types of $CaCO_3$: (a) cubic $CaCO_3$, (b) needle-like $CaCO_3$. [24]

Titania hollow spheres were prepared with the same type of nano-sized calcium carbonate, through a sol-gel method with tetrabutoxytitanium (TBOT), annealing, acidification, washing and further high-temperature calcination.[25]

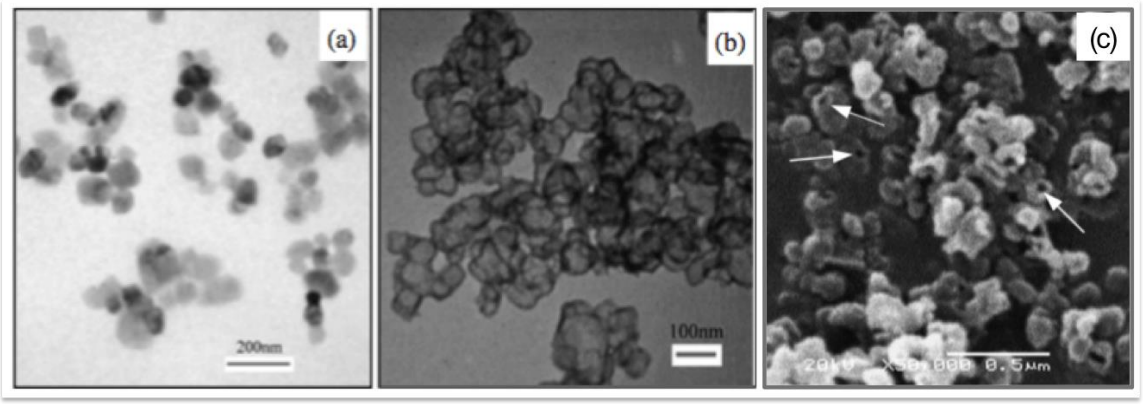

Figure 2-6 TEM images of (a) nano-sized calcium carbonate particles, (b) TiO_2 with hollow structure. (c) SEM images of hollow structure of titania.[25]

Templating with biomineral sea urchin provides a route to produce various inorganic solids with unique and complex morphologies. The drawbacks of these patterned structures are the non-adjustable shape and structure, too large pore size, and the fragility. Applying industrial-level calcium carbonate with smaller sizes will provide more opportunities for scale-down titania and by varying the type of $CaCO_3$ used, the surface area, pore distribution and related applications could be adjusted.

Based on inorganic polymerization reactions, sol-gel chemistry is an attractive wet chemistry approach to synthesize metal oxides with the utilization of hard templates. [5] Metal alkoxides of transition metals such as Ti, V, Zr are highly reactive and typically tend to form oxyhydroxide precipitates when exposed to water. Thus, controlled hydrolysis and condensation rates will be beneficial for a templating method that involves chemical bonding or physical deposition. To control the hydrolysis rates, utilizing chelating ligands such as glycols, organic acids, and beta-diketones is a very promising and simple route. Chelating ligands provide occupations of the coordination sites of the alkoxide, thus reducing the hydrolysis rates.[28] A variety of carboxylic acids were tested to study their chelating capacities on titanium(IV) isopropoxide to produce sol-gel-derived thin films.[28] Valeric acid was proved effective to modify transition metal alkoxides and help produce uniform thin films from the precursor on glass substrates.[29] Thus a titanium valerate became our promising candidate for titanium resource.

In this chapter, a new method (Figure 2-7) with modified sol-gel approach utilizing titanium tetraisopropoxide and valeric acid, was combined with three different types of commercial calcium carbonate as templates, to prepare various titania porous particles with high surface area and diffusion path for photocatalytic degradation of organic

pollutants. Potential practical usage is very promising due to the low cost of calcium carbonate, and the feasible process for large-scale fabrication and industrialization.

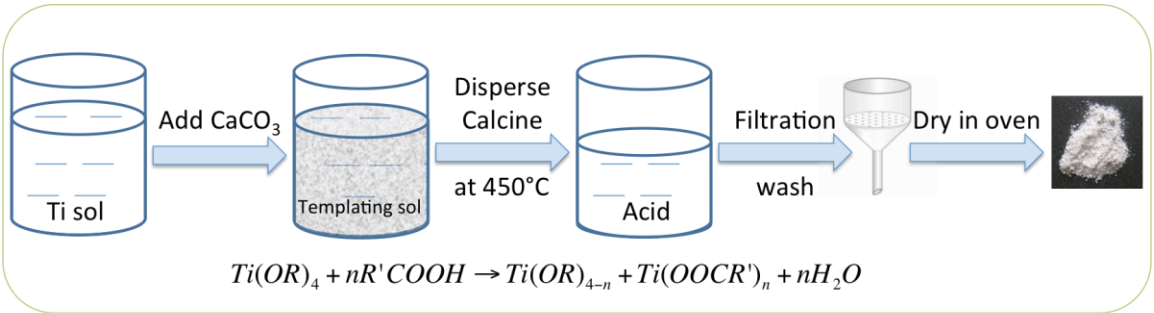

Figure 2-7 Scheme of calcium carbonate templating synthesis method for porous titania particles

2.2 Experimental

2.2.1 Materials and equipment

Materials:

All chemicals were used without pre-treatments unless noted. Three types of calcium carbonates, Hubercarb W4, W3N, and Optfill JSU, were obtained from Huber Engineered Materials. All three Hubercarb products have very few silicas and silicates (≤0.5%) compared to other series, median particle sizes were 5.9 um, 2.8 um, 1 um respectively for W4, W3N, and Optfill JSU (Opt). Titanium(IV) isopropoxide (≥ 97%), valeric acid (≥ 99%), methyl orange (≥ 85% dye content, certified by Biological Stain Commision), titanium(IV) oxide nanopowder (anatase, 99.7%, metals basis, <25 nm), ethanol, (absolute 200 proof, ≥ 99.5%, A.C.S. reagent), 2-propanol (A.C.S. grade, ≥ 99.5%) were purchased from Sigma Aldrich. Hydrochloric acid (analytical reagent grade) was from Mallinckrodt. Plain, pre-cleaned micro glass slides were purchased from VWR International, in a size of 1 inch by 3 inch, with a thickness of 1.2 mm. Free sample of nanosized $CaCO_3$ powder, was from generous Ruicheng Xintai Nanomaterials Technology Co. Ltd, with average size 15-40 nm.

Syringes (1mL and 5mL) and PTFE (polytetrafluorethylene) syringe filters (0.2 um filter size) were purchased from Corning.

Equipment and Characterizations:

(1) The structures of the calcium carbonates templates and titania porous particles were characterized by scanning electron microscopy (Carl Zeiss Auriga CrossBeam SEM-FIB). Samples were prepared by mounting onto a sample holder with carbon paste/tape before being tungsten-coated. EDAX™ EDS Analysis System for SEM–X-ray Microanalysis was applied together with SEM characterization for element analysis on TiO_2 powders as prepared. When a cross-sectional view was necessary, a focused ion beam (FIB) was used to mill surfaces of the materials.

(2) The transmission electron microscopy (TEM) images, high-resolution transmission electron microscopy (HRTEM) images, and selected-area electron diffraction (SAED) patterns were taken on a JEOL 2200FS equipment. TiO_2 samples were dispersed in ethanol by bath sonication for 0.5 h. The ethanol/TiO_2 suspension was dropped and dried on a carbon-coated 400 mesh copper grid overnight prior to TEM analysis. Under HRTEM mode, fast Fourier transfer (FFT) patterns were utilized to optimize image quality with DigitalMicrograph (DM) software.

(3) Flackteck shear mixing machine was used for rapid mixing and grinding of materials such as colloids, fluids, powders, resins, inks and paints. A single wafer spin processor (WS-400A-6NPP/LITE) was purchased from Laurell Technologies Corp and used for film coating. The doctor blade method was completed the MSK-AFA-III compact tape casting coater with vacuum chuck. This doctor blade machine has an adjustable

micrometer film applicator (thickness 0.01-3.5 mm, or fixed thickness at 5 um, 10 um, 15 um and 20 um) with a 100-mm width, as well as a dryer cover that heats up to 100 °C.

(4) UV-Vis spectrophotometer (Perkin Elmer Lambda 900 UV Spectrometer) was applied for methyl orange dye characterization to monitor the absorption of the dye solution, for monitoring the degradation level during photocatalytic experiments.

(5) A LabRAM ARAMIS laser Raman spectrometer (Horiba Scientific) with 532 nm 50 mW DPSS laser was used to inspect sample crystal phases as well. All the samples were tested as is with a 50X objective lens. The resolution in Raman spectrometer could be decided by the spectrometer focal length, diffraction grating, laser wavelength, and the detector. The higher the groove density of the grating is, the higher the spectral resolution. The gratings used in this work is 1800 gr/mm and results in a spectral resolution of about 1.5 m^{-1}. The laser power at the sample ranged in 1-3 mW, and the 1/e laser spot size was about 2 μm at the sample.

(6) Thermogravimetric analysis (TA Instruments Q500) used a high-resolution ramp of 25 °C/min to ~800 °C in air or nitrogen was conducted on TiO_2 samples. Surface area and pore size data were collected with Brunauer–Emmett–Teller (BET) Micromeretics ASAP 2020.

(7) X-ray photoelectron spectroscopy (XPS) was carried out on Perkin Elmer Phi 5400 using Kα line of Mg (1254 eV) X-ray source with a beam voltage of 15 kV and current of 20 mA for the survey spectra scan (pass energy 187.85 eV, and 1 eV step size). For detailed Ti 2p or O 1s high-resolution spectra, a pass energy 29.35 eV and step size 0.1 eV were used. Chamber vacuum was maintained below 1×10^{-7} Torr (1.33 Pa). The sample to be

tested was mounted onto the sample holder with double-sided copper tape, and as for powder form samples, a thin but dense layer of powder was spread on the tape with excess removed. After the measurement, data processing was performed by MultiPak V8.0. If not mentioned, the spectra have been resolved into chemically shifted components by a non-linear least squares procedure.

(8) Photocatalytic reactions were conducted with an RC-500 Xenon UV lamp (Xenon Corp., Wobrun, WA) that has 300 W power, 120 Hz frequency, and a 5-inch linear bulb shape. The lamp was equipped with aluminum reflectors and fused quartz windows to provide optimum transmission of UV radiation. The lamp housing was made of metal, and a forced air convection removed the generated heat. The pulsed xenon arc lamp has a continuous radiation spectrum as shown in [30]. The active time span of each pulse is 100 us, while the interval rest time is 8.3 ms (Figure 2-8 (b)). The range of active UV wavelength lies between 230 and 360 nm. Applying a Pyrex glass cover as a filter will remove ultraviolet wavelength region beneath 290 nm.

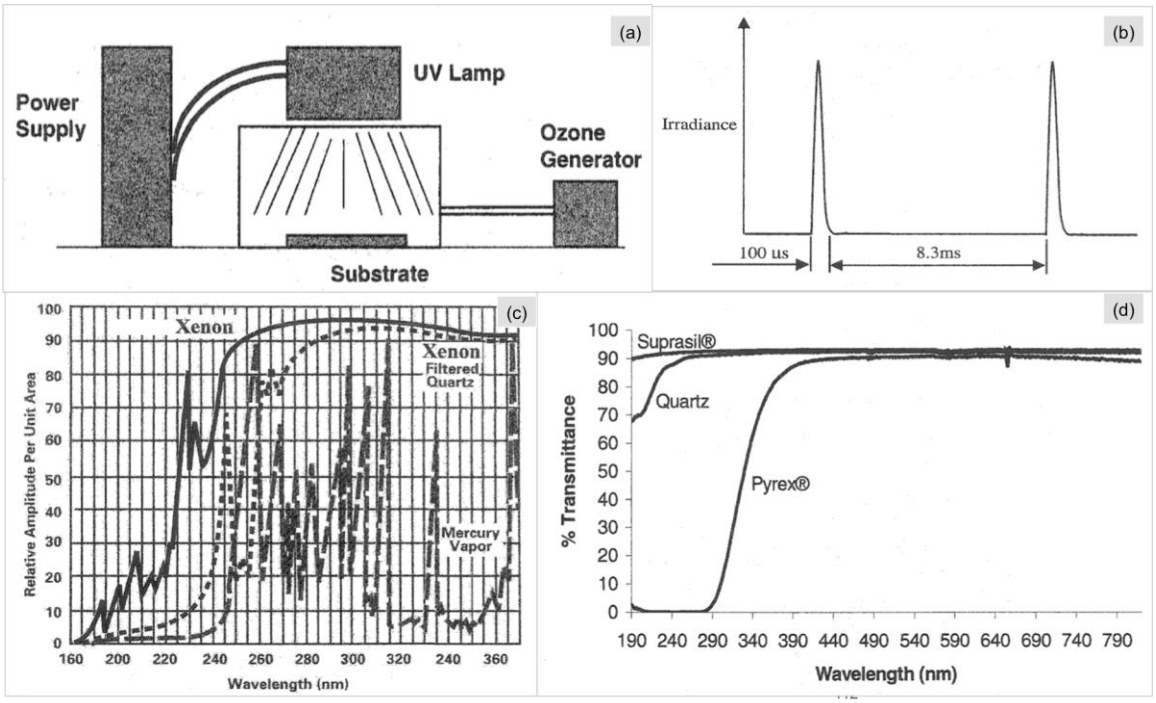

Figure 2-8 (a): the scheme of the UV lamp system (Ozone was not applied in this work). (b): the schedule of the pulsed wave. (c): wavelength range of the outputs from the pulsed xenon UV lamps. (d): UV transmittance of Surasil, quartz, and Pyrex glass filters[source: Xenon Corp.

2.2.2 Synthesis of porous titania particles with $CaCO_3$ templates

A simple and versatile method was developed to fabricate size-controllable titania particles through a sol-gel deposition on calcium carbonate templates. At first, a sol was prepared with titanium(IV) isopropoxide (TTIP), valeric acid (VA) and water, where valeric acid was used as a chelating agent to moderate the hydrolysis and precipitation rates during the sol-gel reactions. Typically, a molar ratio of 1: 9: 2 was used for TTIP: VA: H_2O. As for a 0.004 mol Ti content, while 1.97 mL TTIP was being stirred, slowly add 3.95 mL VA, followed by 0.144 mL water. The mixture was kept stirring at room temperature for more than 1 hour. Then 5% w.t. calcium carbonates were added into the mixture and stirring continued until homogeneity formed. To further improve mixing comprehensively, the mixture was treated with Flackteck shear mixing machine by consequently 1 minute at 1000 RPM, 1 minute at 2000 RPM, 1 minute at 3000 RPM, and 2000 RPM for another 2

minutes. Then the mixture was moved forward to bath sonication for 10 minutes. After a final 2-minute Flackteck mixing at 2000 RPM, the Ti(IV)-$CaCO_3$ mixture was annealed in crucibles at 450 °C for 5 hours. The calcined mixture was added into 1 M hydrochloric acid solution and kept stirring overnight. By filtering the dissolved Ca^{2+} away with 0.22 um filtering membrane, and washing, rinsing for several times, clean TiO_2 was dried in a vacuum oven at 80 °C overnight.

Film casting trials were made by both dip coating and spin coating with the precursor-template mixture. For dip coating, a 1-inch square glass slide was immersed in the mixture, and withdrawn for layer formation. Spin-coated films were finished on the spin coater with different time and spin speed settings.

2.2.3 Photocatalytic performance experiment

A calibration curve for the concentration-absorption relationship of methyl orange (MO) solution was obtained by conducting a series of UV-Vis measurements on diluted MO solutions. Methyl orange standards were prepared from a 5×10^{-4} M aqueous solution. The analysis used water as a reference and monitored the dynamic range between 200 and 800 nm. Absorption data for calibration was taken at peak 465 nm and a calibration curve was generated

The photocatalytic performance measurements were conducted in a Pyrex glass crystallizing dish (70 mm in diameter, 50 mm in height, 180 mL in capacity), equipped with a magnet, and stirring plate. The whole process was conducted in open air at room temperature in a light blocking box. An Approximate 1×10^{-5} M MO solution was prepared and used as the initial solution. For 50 mL as-prepared MO/water solution, 0.2 mg catalyst

was added to the solution, followed by a one-hour stirring in darkness to reach the adsorption-desorption equilibrium before any UV irradiation. The initial starting point was taken as t_0, at the end of the equilibrium period, and before the UV lamp was turned on. The change of the concentration of MO/water solution was monitored by taking 3mL solutions out every 5-minute UV treatment. Solids of catalyst were removed by utilizing a set of syringe/filter (Figure 2-9) so that clear solution could be ready for UV-Vis spectrum collecting. Most experiments were run for 3 times to achieve statistically stable data for error calculations.

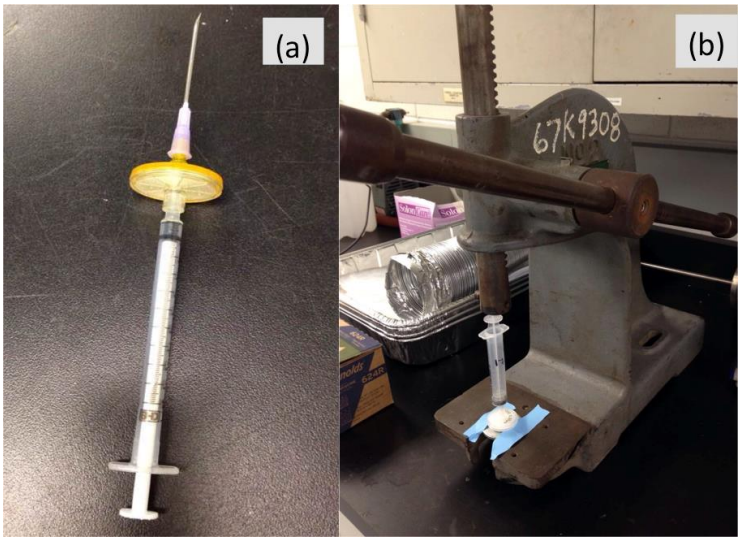

Figure 2-9 (a) 1 mL syringe with syringe filter connection. (b) A simple presser for separation of liquid and solid in MO solution/ TiO_2 catalyst mixture. The clear solution was collected at the bottom of the syringe in a 5 mL vial.

The blank dye test was performed in order to prove that UV light would not damage methyl orange. As-prepared new MO solution was tested at t_0, and measured again after 5-minute UV treatment with a Pyrex petri dish lid covered (t_1), and then 5-minute UV treatment without any coverage (t_2), and 5 minutes more as t_3. This experiment was to prove the low-wavelength UV damage to the dye, and the filtering effect from Pyrex glass for an proper photocatalytic experiment setup.

2.3 Results and Discussions

2.3.1 Titania particles morphology from different templates

As Figure 2-7 shows, the Ti (IV) sol was prepared with TTIP and chelating agent VA with very limited amount of water. During this process, hydrolysis was controlled at a very slow rate, which facilitated the even coating of calcium carbonate during the mixing steps. Direct calcination was used to crystallize the Ti sol/calcium carbonate hybrid, and porous structures were created after the acid dissolution of the calcined product. Without $CaCO_3$ templates, a simple calcination yielded very dense nanoparticle chunks as seen in Figure 2-10 (a), while the addition and removal of template resulted in highly porous structures as (b-d) indicated. The acidification removed calcium carbonate away, and the titania displayed as large particles (diameter around 20 um) with smaller pores (< 5 um) on the surface and in the inner connected structure based on the (d) cross-sectional image. H^+ was able to penetrate into the inner part of the calcined hybrid along previously formed pores or channels to remove all of the templates, leaving quite pure titania with high crystallinity. Pores came not only from the original W4 particles but also broken W4 particles due to mixing and sonication before calcination. The controlled hydrolysis rate was the key to the successful coating of calcium carbonate templates, which allowed enough time for the mixing and depositing.

In order to study the porosity distribution within the particles, the focused ion beam was used to cut into the larger particles. Figure 2-11 further reveals the structure of the internal pores at the milled cross-sectional surface, pore sizes varied between 1 um to 5 um, and the inner surface was very rough, offering an even higher surface area for photocatalytic reactant adsorption.

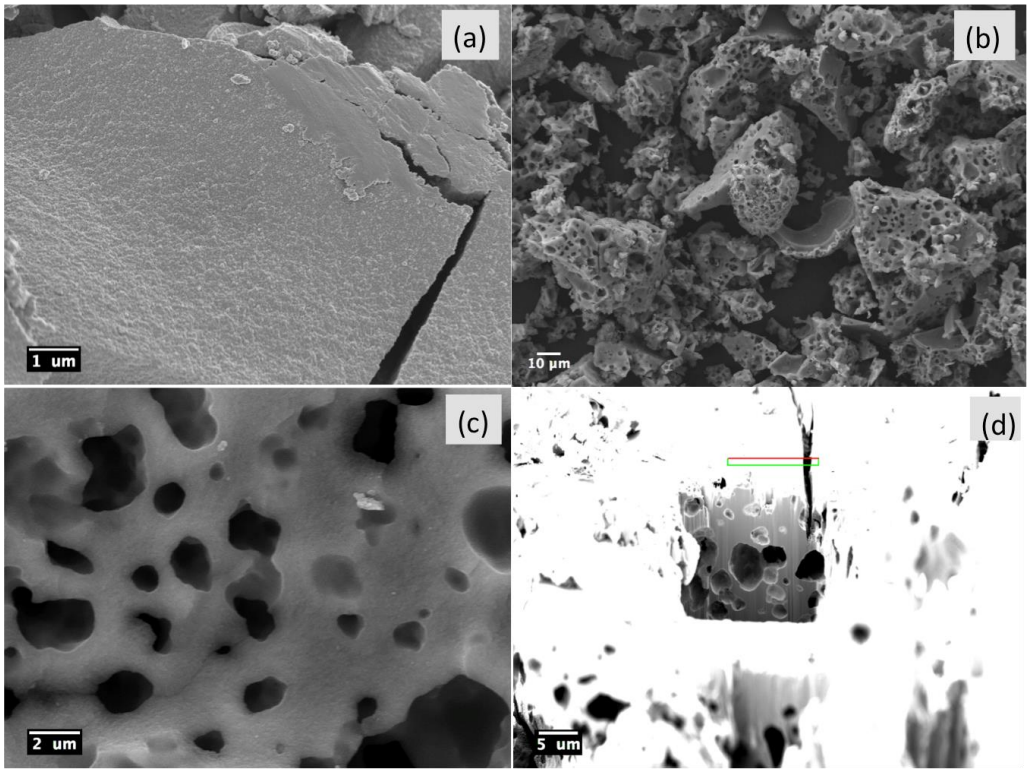

Figure 2-10 SEM images of titania products induced with and without $CaCO_3$ W4 templating (5% w.t.). (a) precursor only, no $CaCO_3$ added; (b) with 5% w.t. W4 templated and (c) at higher magnification, (d) sample (b) at cross-sectional view assisted by FIB.

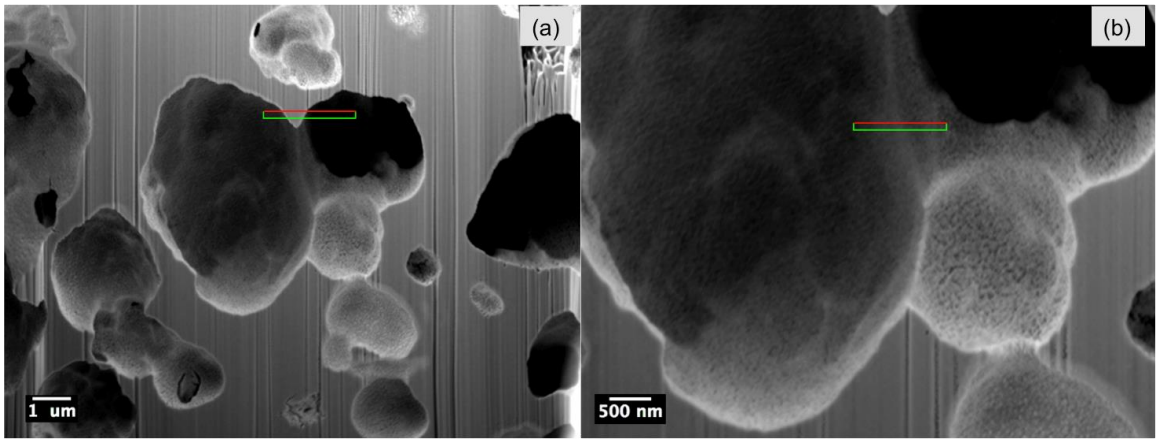

Figure 2-11 A closer view of the cross-sectional inside the porous particles, resulted from 5% w.t. W4.

To compare with the resulted titania and the original templates, the Hubercarb W series calcium carbonates were imaged as well. Figure 2-12 (a) (b) (c) show the size distribution of three types Hubercarb W series $CaCO_3$ with median sizes 5.9 um for W4, 2.8 um for W3N, and 1 um for Opt. All the calcium carbonates used here share low silica

content and are rounded particles with low moisture and chalk-like softness. The material has a magnesium carbonate content of 0.4%, while the rest composition is made of 0.02% crystalline silica and 0.05% silicates. Thus, the majority of the pores created by templates matched the templates' sizes.

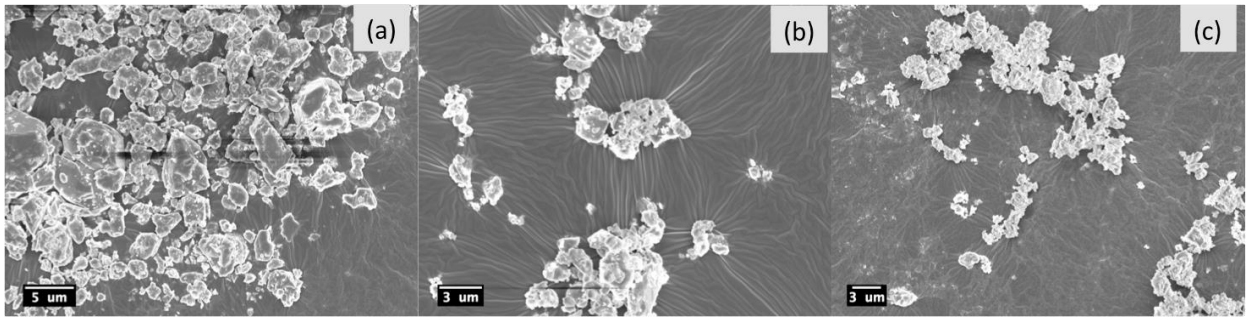

Figure 2-12 SEM images of calcium carbonate templates: (a) W4, (b) W3N, (c) OPT. (all samples were mounted on carbon glue tape on metal stubs)

Increasing the carbonate loading led to smaller particles and pores at the same time. Figure 2-13 shows the structures and morphologies of titania induced with 10% w.t. and 15% w.t. W4 template usage. On the left side, with 10% w.t. $CaCO_3$, the particle size was reduced to 5 um, and the pore size became ~1 um. On the right side, the particle size was 2 um and pore size remained similar to ~1 um. The decrease of particle and pore size were attributed to the fact that a large amount of templates existing in the acid dissolution process would be removed and resulted in more fractures than when 5% w.t. of template was used. Pores smaller than the template sizes were due to the mixing and sonication of the mixture precursor before calcination. Additionally, it is suspected that increased amount of templates tended to be removed together as a whole, leaving more fractured particles with smaller templates which are easier to hold onto the duplicate shapes.

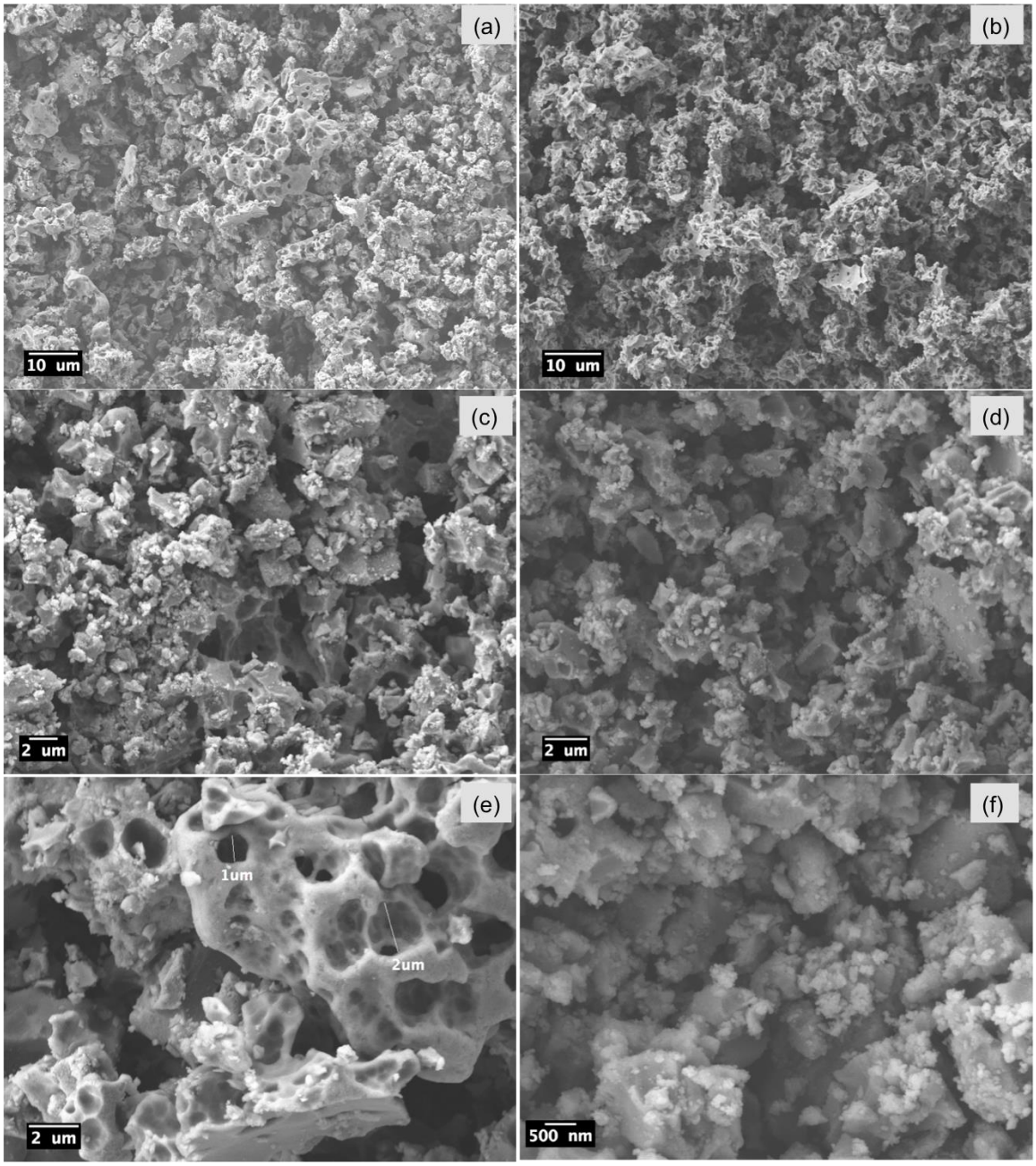

Figure 2-13 Comparison between 10% w.t. and 15% w.t. W4 templates in the titania fabricating process. (a) (c) (e) represents 10% w.t., and (b) (d) (f) are 15% w.t.

As introduced in Chapter 1, immobilized films also act as efficient photocatalysts. To find out whether this mixture is suitable for film formation, two coating methods were applied on clean glass substrates. The Ti (IV) sol mixed with 5% w.t. and 10% w.t. W4 $CaCO_3$ were deposited as films, dried in air for 1 hour and then calcined in the same

procedure as with the bulk materials. Figure 2-14 (a-d) demonstrate the morphologies of the dip-coated films at lower magnification (a), higher magnification (b-c), and tilted cross-sectional surface (d) with an approximate thickness of 1.5 um. Film formed with many large cracks. A porous structure was observed on the surface and from the cross-section. It was hard for the templating precursor mixture to form a uniform homogeneous film due to the size of the templates, weak adhesion between the carbonates and the substrate, and the removal of the template during acid digestion. This effect was intensified when the templates loading was increased to 10% w.t. (Figure 2-14 (e-f)). Films were not able to form due to the removal of calcium carbonate, though the porous vacancy was duplicated from the templates.

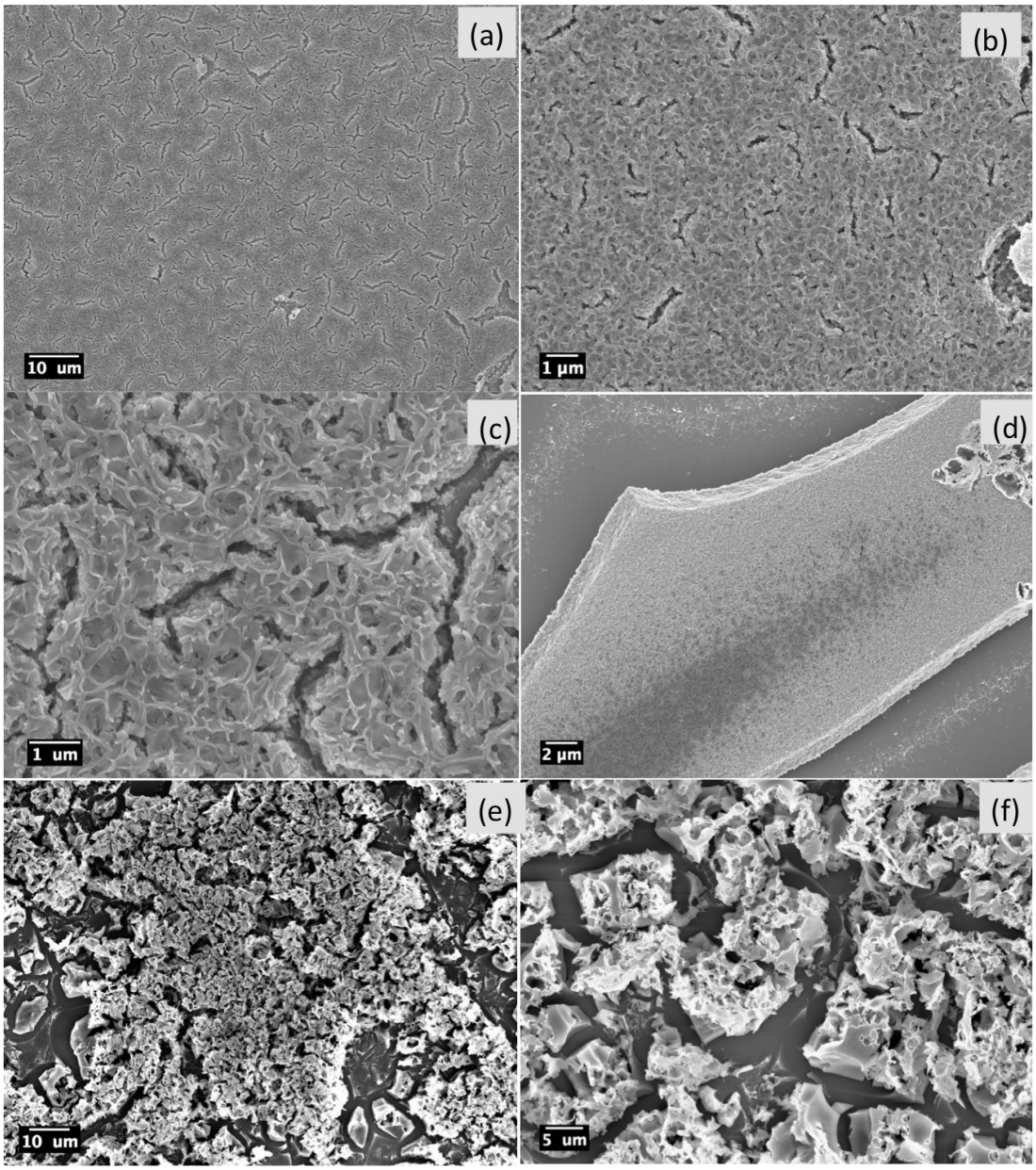

Figure 2-14 SEM images of films made with a mixture of Ti precursor and W4 template by dip coating: (a-d) with 5% w.t. W4 $CaCO_3$, (e-f) with 10% w.t. W4 $CaCO_3$.

Spin coating was also tried with several different speeds for a 45-second period. The thickness of the films seemed to follow the spin coating thickness equation $\propto \frac{1}{\sqrt{w}}$, where w is the angular velocity. Spin coating mechanism could be explained based on Figure 2-15, where the substrate was coated with drops of the suspension (molecules dissolved in a solvent). The high speed applied next will drive most of the solvent off the side, and the

airflow will make the majority of the solvent evaporate. The centripetal force and the surface tension of the solution keeps an even coating layer. The spin speed is a critical parameter to the radial force applied to the liquid, the velocity, and the turbulence of the air above the film surface. The exact thickness of a film is also determined by the material and solvent evaporation.

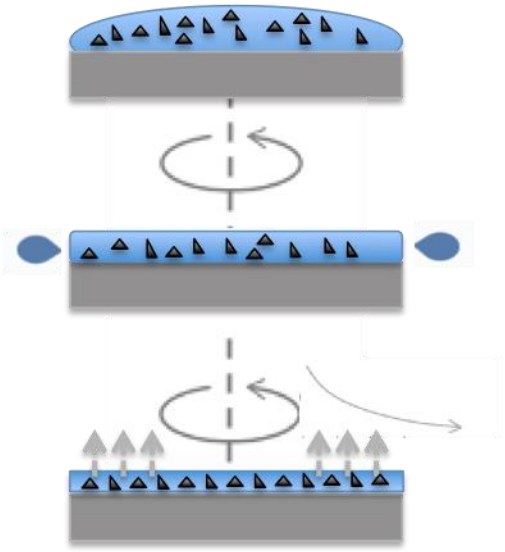

Figure 2-15 Spin coating working mechanism of a small molecule in solution started with a static dispense

The effect of spin coating speed on film quality is seen in Figure 2-16. At 300 RPM, the rotation was too slow to form a complete film. While at 500 and 1000 RPM, both films were coated. When the rate was increased to 3000 rpm, the film became very thin and very few templates were still in the film. However, after calcination, none of the films show a good duplication of template morphology. This indicated that the centrifugal force was too strong for the materials to maintain a good template dispersion.

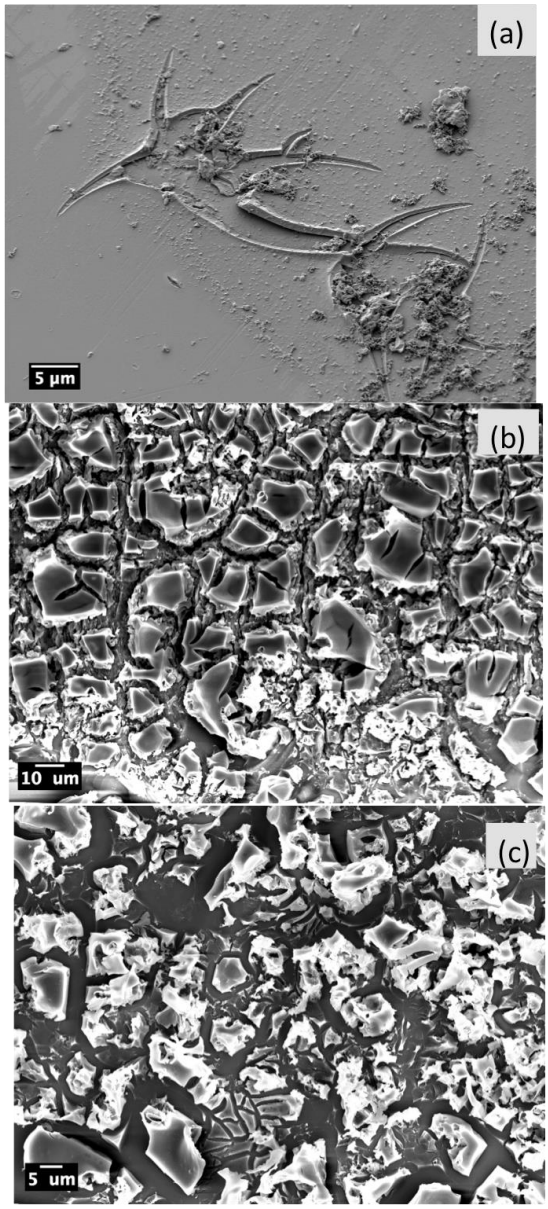

Figure 2-16 SEM images of films made with a mixture of Ti precursor and 5% w.t. W4 template at different spin speeds for 45 seconds: (a) 3000 RPM, (b) 1000 RPM, (c) 500 RPM.

The elemental composition was also studied for spin-coated film structures and surprisingly, there is a quite larger amount of Ca (2.1% atomic) residue compared to the bulk-prepared porous material (0.27% atomic). This might be attributed to the insufficient contact of acid with film due to the adhesion, or the background glass substrate's contribution to Ca element (1.0% atomic from averaged data). The calcium and other

contaminants should be maintained at a minimum amount, due to the need for pure crystalline titania for more active sites on the surface.

Experiments on very fine calcium carbonate were conducted to find out whether nano-size of the template would bring new beneficial features of the porous titania. Thus a new kind of calcium carbonate with only 15-40 nm size was tried in the same protocol described to synthesize porous TiO_2 particles at a 5% w.t. content. Nano-sized $CaCO_3$ particles were very fine, but not providing a stable reproducibility of the materials. Some batches (10% w.t. of nano-sized $CaCO_3$ as templates) of materials had a brown color in some areas with a very high Ca content of 10.0% atomic. Images of the microstructures are shown in [32], where (a-b) and (c-d) came from 5% and 10% w.t. Increasing the nano-sized carbonates loading led to different pore structures and particle distribution. Structures shown in (c-d) had finer particles and porosities, while (a-b) only existed in large chunks and pores in random shapes. When films were deposited by dip coating, larger cracks were observed.

It was found that the highly dispersed nano-sized $CaCO_3$ had been modified with certain unknown surfactants to be hydrophobic. After being calcined at a higher temperature (450 °C) for 12 hours, the calcium carbonate particles turned out to be hydrophilic again, which meant the surfactant was heat-removed. The removal of the surfactant led to the aggregation of the particles as shown in [32]. After the surfactant was removed, a new batch of TiO_2 was synthesized with aggregated TiO_2 and was not ideal for porous materials due to the much larger chunks of TiO_2 and pore limitations.

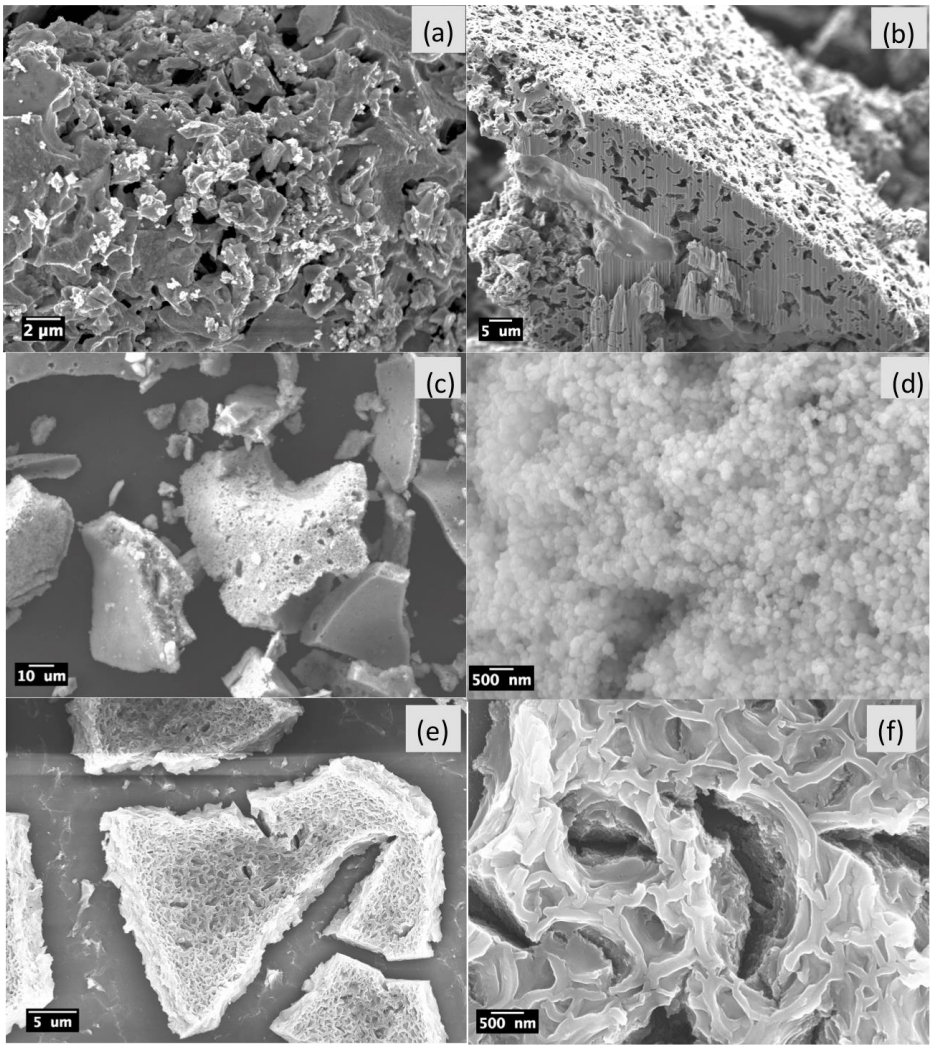

Figure 2-17 SEM images of (a-b) TiO_2 powders and the cross sectional view with 5% w.t. nano-sized $CaCO_3$ templating; (c-d) TiO_2 powders with 10% w.t. nano-sized $CaCO_3$; (e-f) films by dip coating with 5% w.t. nano-sized $CaCO_3$.

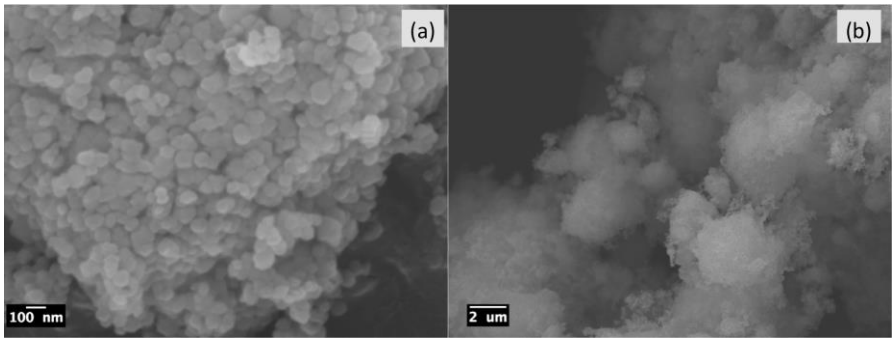

Figure 2-18 SEM images of 15-40 nm $CaCO_3$ particles , (a): as-received, and (b): after calcination 450 °C for 12 hours.

The difference between W4 $CaCO_3$ and nano-sized $CaCO_3$ was compared through Raman and TGA. Figure 2-19 demonstrated the crystallinity of the $CaCO_3$ samples. Nano-

sized calcium carbonate has aragonite phase mostly, while W4 shared a very similar peak distribution but with an elevated curve trend.[34] TGA data from Figure 2-20 showed that at around 380 °C, around 5% w.t. dropped for nano-sized $CaCO_3$ while W4 sample maintained the mass until the temperature reached 655 °C. Nano-sized $CaCO_3$ started to degrade at 600 °C, and the residue was almost 53-55% w.t., while W4 $CaCO_3$ was left a little above, at 56% w.t. This decomposition at ~650 °C transformed calcium carbonate into calcium oxide and carbon dioxide.[35]

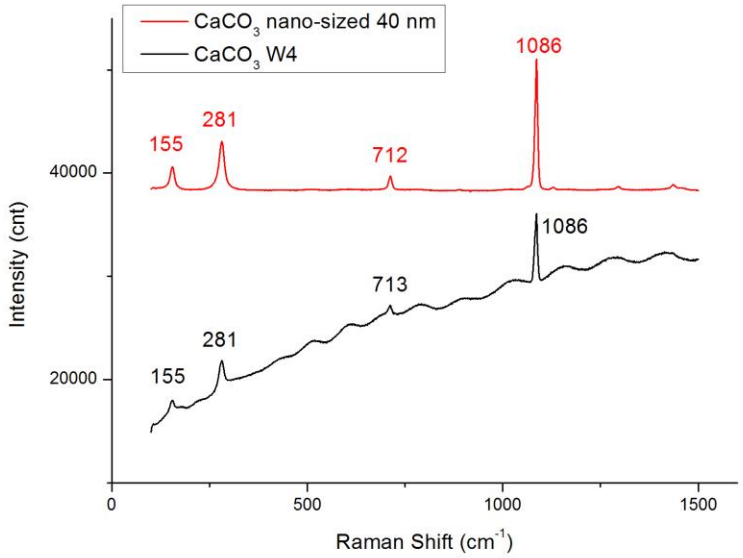

Figure 2-19 Raman spectra of $CaCO_3$ templates of nano-sized type and W4 type. According to Calcite 282, 713, and 1086 cm^{-1}, and Aragonite 155, 207, 704, 1085 cm^{-1}

Thermal analysis(Figure 2-21) was also performed on the titania particles made with W4 and nano-sized $CaCO_3$. It turns out there was a weight loss potentially from nano-sized $CaCO_3$ at around 600 °C. The $CaCO_3$ made with W4 went through dehydration at the beginning, possible loss of minor contaminations without apparent loss observed at either 380 °C or 600 °C, indicating the absence of suspicious organic surfactant in W4 and the complete removal of calcium in titania particle products.

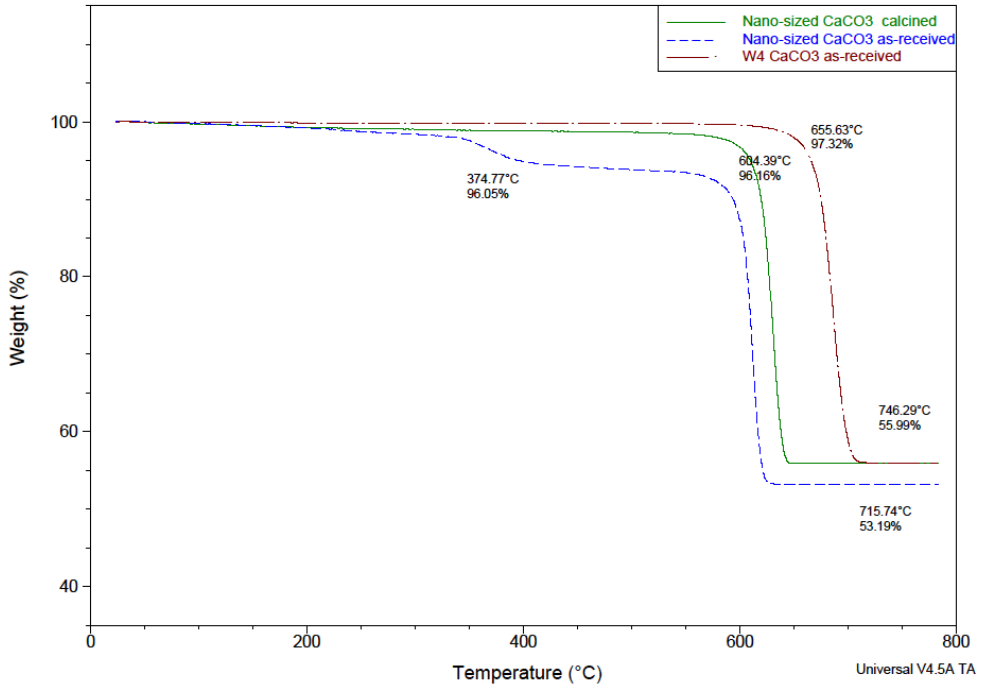

Figure 2-20 TGA of the top red curve: W4 $CaCO_3$ particles, middle green curve: nano-sized $CaCO_3$ after calcination, and bottom blue curve: nano-sized $CaCO_3$ as-received without any treatment.

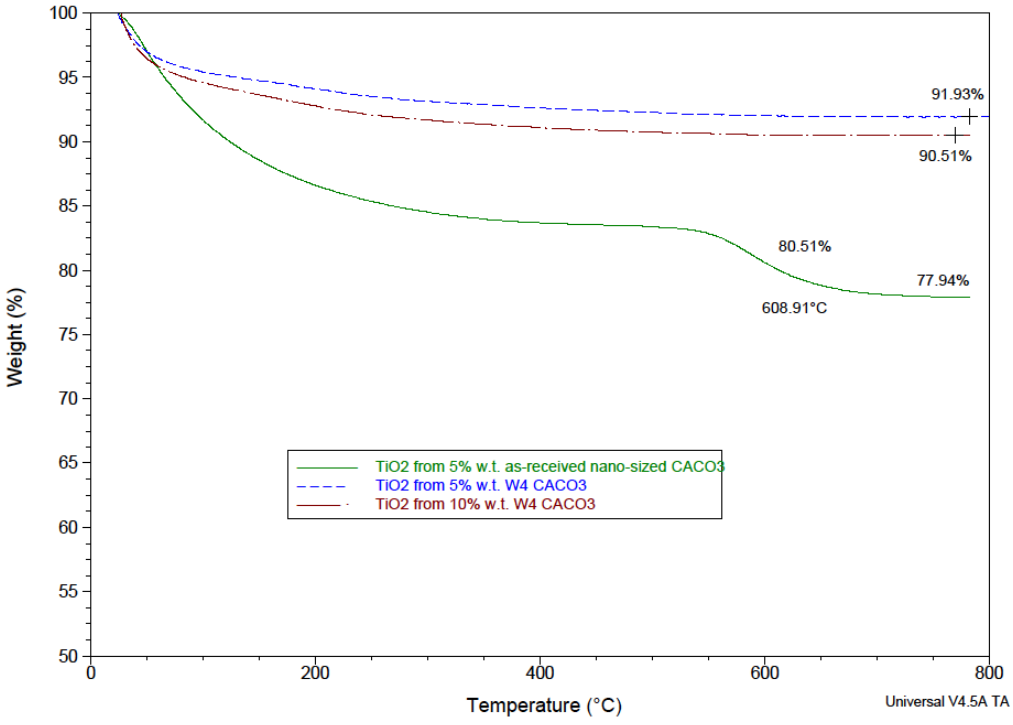

Figure 2-21 TGA of titania particles made with: (top blue)-5% w.t. W4 $CaCO_3$, (middle-red)- 10% w.t. nano-sized $CaCO_3$, and (bottom green)- 5% w.t. nano-sized $CaCO_3$. (Here the nano-sized $CaCO_3$ was not pre-treated.)

The crystallinity of titania particles is an important factor regarding the properties of titania and the activity of photocatalysis. Luttrell *et al*. found that anatase is a better photocatalyst than rutile because the charge carriers excited deeper in bulk and contributed to the surface reactions. Raman spectroscopy was used to characterize titania particles prepared with W4 $CaCO_3$ at three different content ratios. The inelastic scattering on titania happens with energy exchange between phonon and the substance, resulting in a change in the wavelength. The features in Raman spectra were due to the vibrations of molecules (atoms/ions). For crystals, the crystal lattice vibrates as a whole, and if the phase is amorphous, the spectra turned to be more blurred rather than sharp and distinct due to the disordered structure and reduced areas of spatial correlations between the oscillations of the particles. Broadening of the peaks might be due to the defective crystals. Thus Raman spectroscopy could be used to identify and quantify the amorphous and crystalline TiO_2 phases, also the oxygen defects, stress states, and size effects.

Both anatase and rutile titania has a tetragonal structure. For anatase (space group D^{19}_{4h}-$I4_1/amd$), there are six Raman active modes 144 cm^{-1} (Eg), 197 cm^{-1} (Eg), 399 cm^{-1} (B1g), 513 cm^{-1} (A1g), 519 cm^{-1} (B1g), and 639 cm^{-1} (Eg). Rutile (space group D^{14}_{4h}-$P4_2/mnm$) has four active modes 143 cm^{-1} (B1g), 447 cm^{-1} (Eg), 612 cm^{-1} (A1g), and 826 cm^{-1} (B2g).[36] Raman scattering of different morphologies differs as well. The scattering of 1D materials provides information about the subtle changes to the structure and the symmetry of the primitive unit.[37] A new peak at 266 cm^{-1} for titania nanotubes due to the Ti-OH bonds within a tubular structure as reported by Qian et al.[37] This is explained as the intermediate formation of hollow tube structures.

As shown in Figure 2-22, all three samples have peaks representative of the anatase phase. Peaks at the wavenumber of 149, 399, 513, 639 cm^{-1} were detected, while the peaks at 197 and 519 cm^{-1} were weaker to be observed. Anatase is tetragonal with two TiO_2 units per primitive cell. The six Raman modes are related to symmetries A1g+2B1g+3Eg. Sharper peaks were observed for 5% w.t. W4 sample, which could be explained by more pristine TiO_2 corresponding to the EDS result mentioned above.

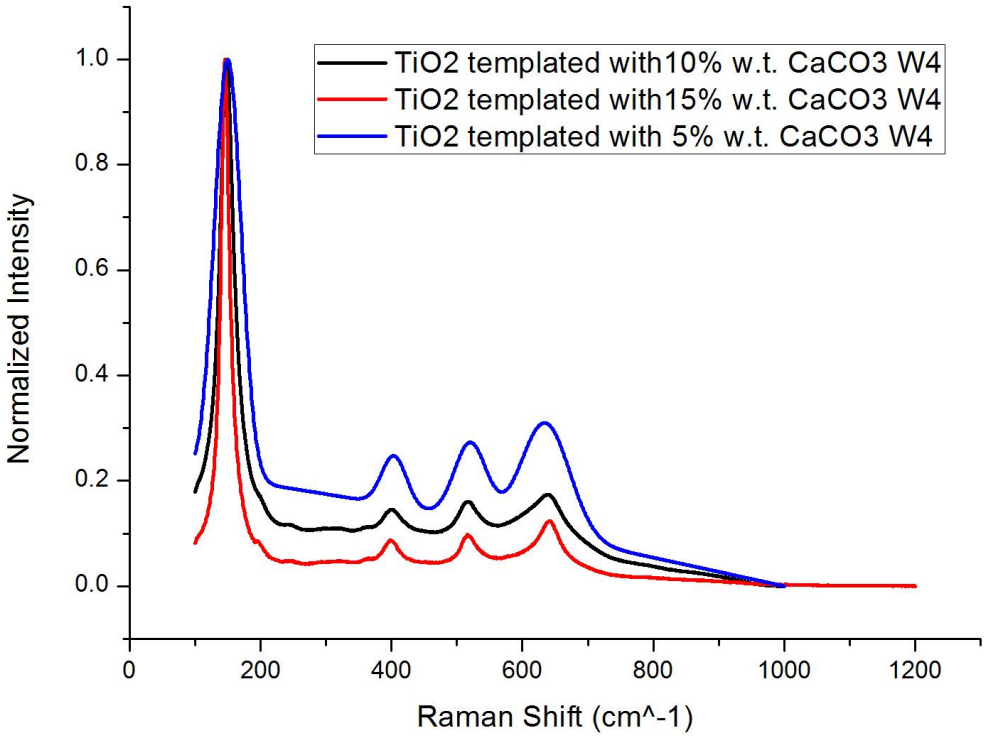

Figure 2-22 Raman spectra of anatase TiO_2 made from the different amount of W4 $CaCO_3$ templates.

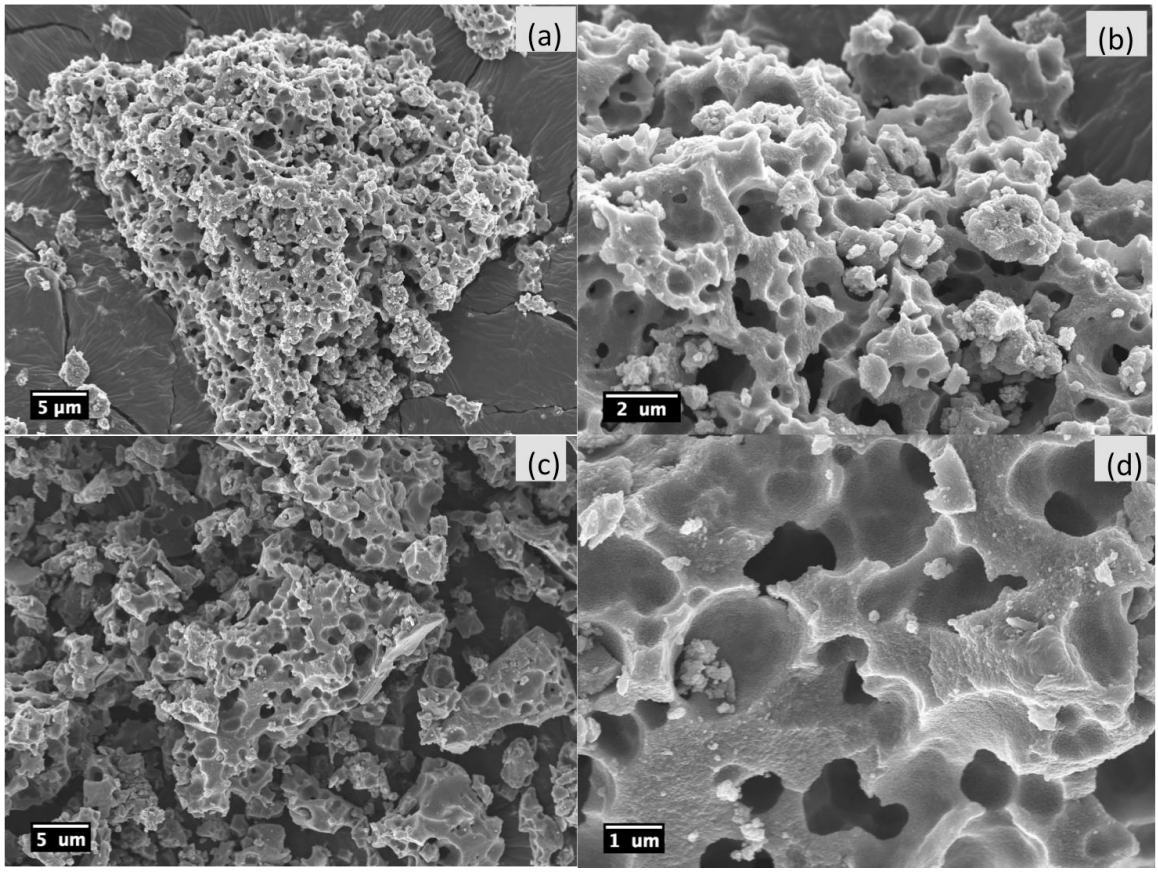

Figure 2-23 SEM images of titania particles templated from: (a-b) 5% w.t. Opt $CaCO_3$ and (c-d) 5% w.t. W3N $CaCO_3$.

After the investigation of the influences induced from W4 and nano-sized $CaCO_3$ on the morphologies and weight percentage directing porosity, two more templates W3N and Opt $CaCO_3$ were applied as well. Following same experimental procedures, porous TiO_2 was created after acid dissolution, washing, filtering and drying. Figure 2-23 shows different morphologies compared to TiO_2 made from W4 templates and nano-sized $CaCO_3$. As for (a-b), particle sizes ranged from 5 um to 20 um, with pore size around 1-2 um; while for (c-d), particle sizes ranged from 5 um to 10 um, with pore size around 2-4 um.

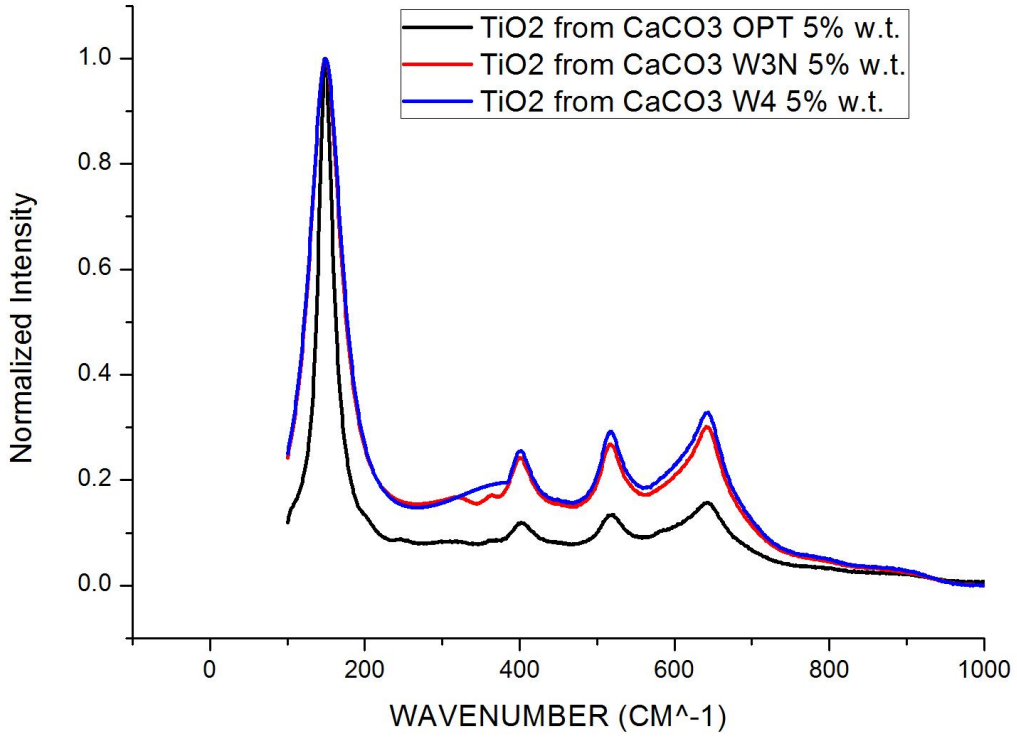

Figure 2-24 Raman spectra of anatase TiO_2 made with three different $CaCO_3$ templates. From top to bottom: W4, W3N, Opt, all in 5% w.t. content

Raman was collected to confirm the anatase phase of the TiO_2 particles from three templates, and the main peaks were summarized in Table 2-1. The peak at 197 cm^{-1} was again too weak to be detected, especially for W4 and W3N templated samples. The peak at around 149 cm^{-1} refers to the lowest frequency Eg phonon mode of anatase and it blue shifted from W3N, to Opt, to W4 templated TiO_2. This blue shift might be due to oxygen deficiency.[37]

Table 2-1 Characteristic peaks of anatase TiO_2 obtained with three different $CaCO_3$ templates

TiO_2 templated with	$E_g(cm^{-1})$	$E_g(cm^{-1})$	B_{1g} (cm^{-1})	$A_{1g}+B_{2g}(cm^{-1})$	$E_g(cm^{-1})$
W4	149.3	-	399.1	517.8	639.8
W3N	148.4	-	400	516.9	640.6
Opt	149.1	199	398.5	516	643

Based on transmitted electrons rather than scattered electrons, TEM could provide not only morphology information at much higher resolution but show the crystallization, diffraction, crystal faces and lattice space. The surface atomic information is relevant to the photocatalytic performance of titania. As described previously, three main types of TiO_2 exist as anatase, rutile, and brookite. Anatase is the most stable phase for nanoparticles smaller than 11 nm, while rutile is the most stable phase for nanoparticles above 35 nm.[38] Anatase in tetragonal bipyramidal shape typically has two main surfaces of ~94% (101) and ~6% (001). Faces (101) and (001) have theoretical surface energy as 0.44 J m^{-2} and 0.90 J m^{-2}. Low surface energy of the face could be maintained during the crystal growth to keep the total surface energy minimum.[39] There are only 50% Ti atoms consisting of five-coordinated Ti_{5c} for face (101), while 100% for (001). Ti_{5c} sites contribute actively to photocatalytic reactions.[40] It was found that the photogenerated h^+ preferred to accumulate on rutile (101) and anatase (001), while the photogenerated e^- tended to rest on rutile (110) and anatase (101)[41] In summary, the difference of energy levels in conduction band or valence band led to various atomic arrangement in facets, and eventually controlled the electron-hole pair and influenced the charge separation.[39]

TEM images were obtained with each type of particle dispersed in ethanol. Figure 2-25 (a-b) show the particle and porosity of the TiO_2 and (c) is the diffraction pattern at selected area obtained at lower magnification. The dimensions of the particles shown in TEM matched the data found in the SEM observations. Clear rings of polycrystallinity were displayed from inner to outer circle as (101), (004), (200), (105), and (204) planes. In the image (d), particles were connected in an ordered pattern with a mean crystal size of

5.8±0.5 nm, while (e) and (f) further reveal the lattice spacing of 0.36 nm, and 0.24 nm, corresponding to facets (101) and (004).

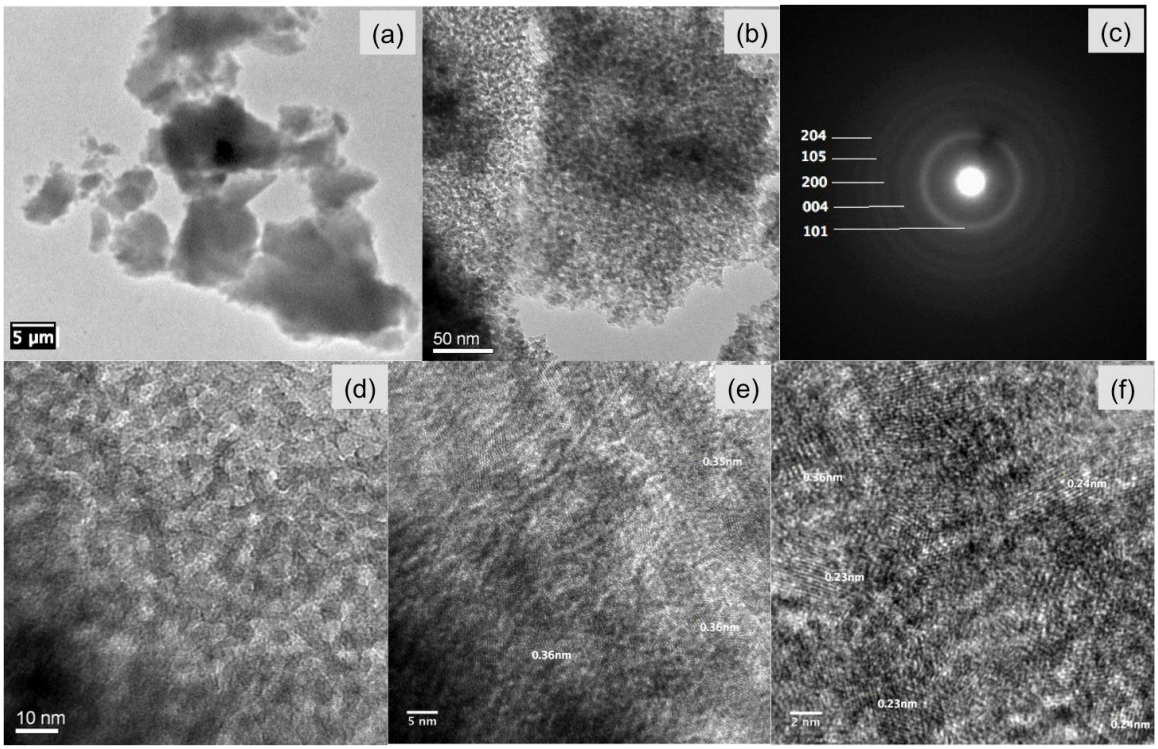

Figure 2-25 TEM images of 5% w.t. W4 $CaCO_3$ templated TiO_2: (a) at low magnification, (b) at increased magnification, (c) selected-area electron diffraction pattern, (d) individual particles in an area with crystal size ~ 5 nm, (e) HRTEM image noted with anatase lattice spacing ~0.35 nm, and 0.36 nm, (f) HRTEM image noted with anatase lattice spacing ~0.24 nm.

As shown in Figure 2-26 (a-b), HRTEM images of detailed pores in TiO_2 nanoparticles were shown. The pore size observed in TEM ranged from 30 nm to 100 nm and mean crystal size is 5.3±0.4 nm. Image (b) again matched the 0.352 nm spacing of lattice (101). Fast Fourier transform (FFT) is used to transform an image from the spatial domain to reciprocal space.[42] For single crystals, the FFT image will show spots, and for polycrystalline, it will show diffuse spots or rings with lattice periodicity. When defects are present, FFT will show random spots together along the crystallographic directions, while when the sample is all amorphous, the FFT will be non-defined diffuse halos. In Figure 2-26

(c), the FFT pattern shows the (101) and (004) diffractions of anatase TiO_2, and the 101 planes have a ring shape due to random orientation.[43]

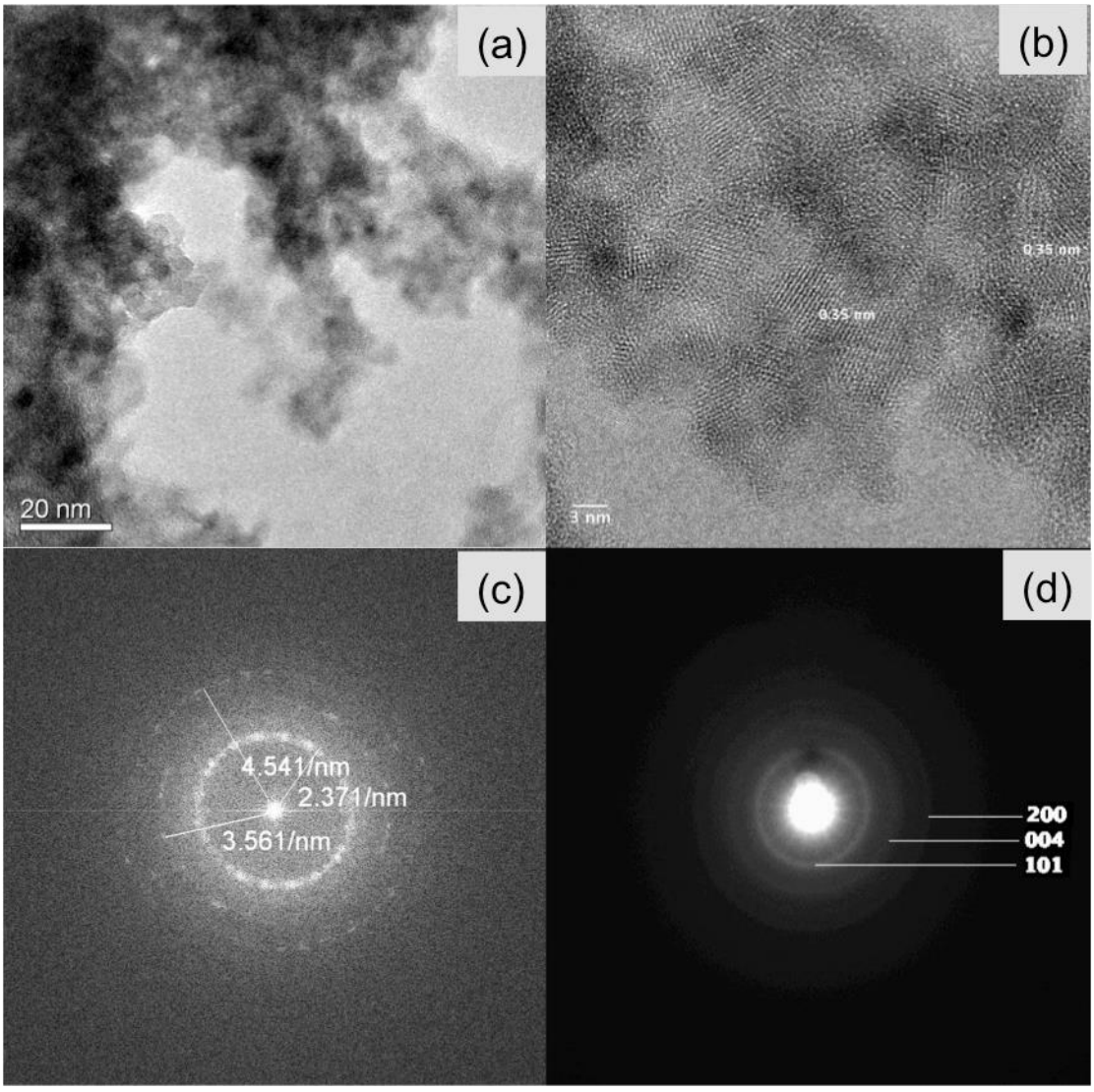

Figure 2-26 HRTEM images of 5% w.t. W3N $CaCO_3$ templated TiO_2: (a) pore formation in a particle (b) at increased magnification, noted with anatase lattice spacing ~0.35nm, (c) corresponding FFT pattern of the single crystal area (d) selected-area electron diffraction pattern

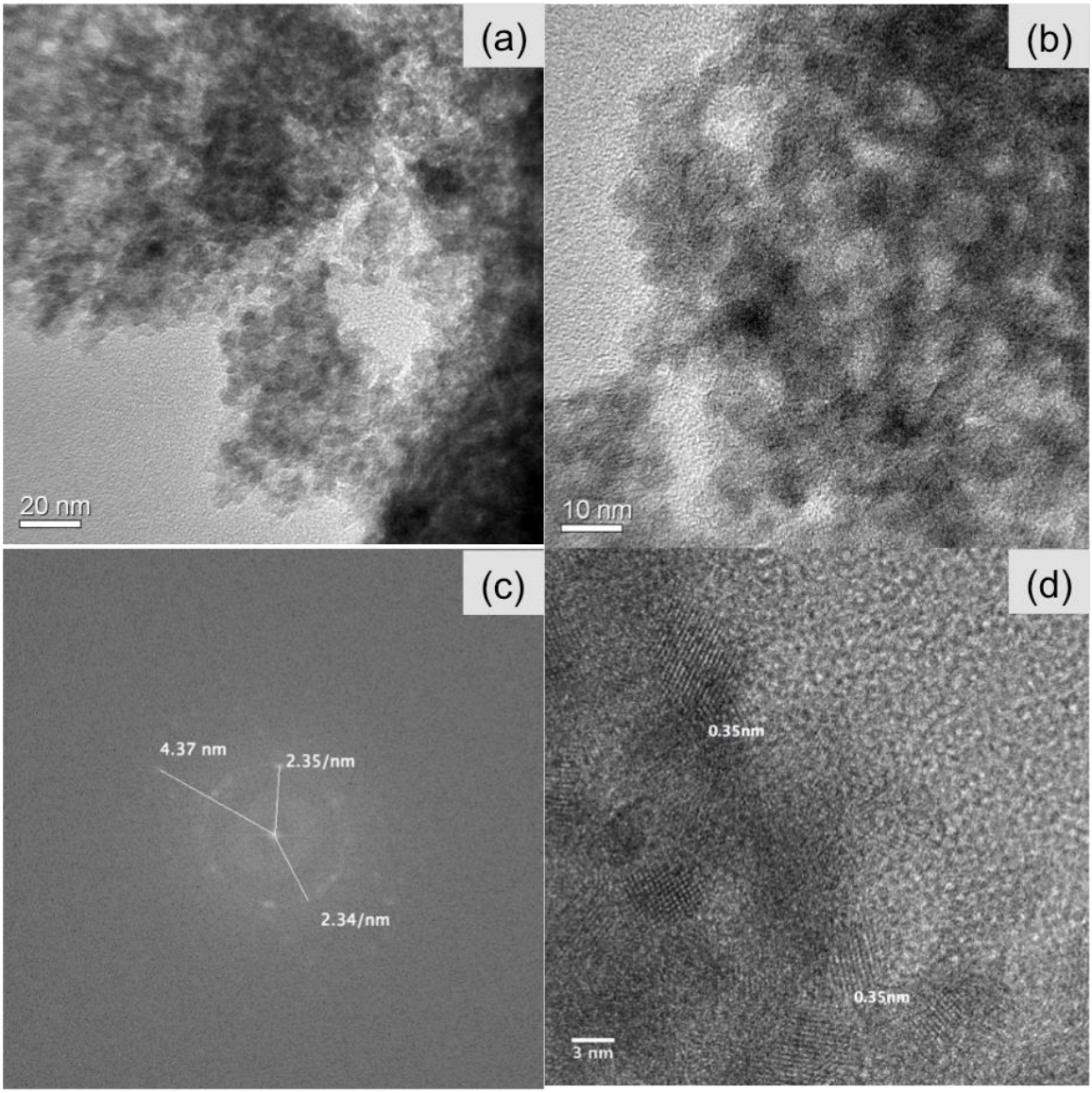

Figure 2-27 HRTEM images of 5% w.t. Opt $CaCO_3$ templated TiO_2: (a) pore formation in a particle (b) at increased magnification, (c) corresponding FFT pattern of the [101] and [004] facets, (d) noted with anatase lattice spacing ~0.35 nm

Last but not least, TiO_2 particles made with Opt $CaCO_3$ was found to have porosities within particles, plus with smaller sizes. The mean crystal size of TiO_2 was 5.0±0.5 nm. Similar with Figure 2-26, the corresponding FFT pattern and the lattice spacing of 0.35 nm further confirmed the crystal phase of anatase.

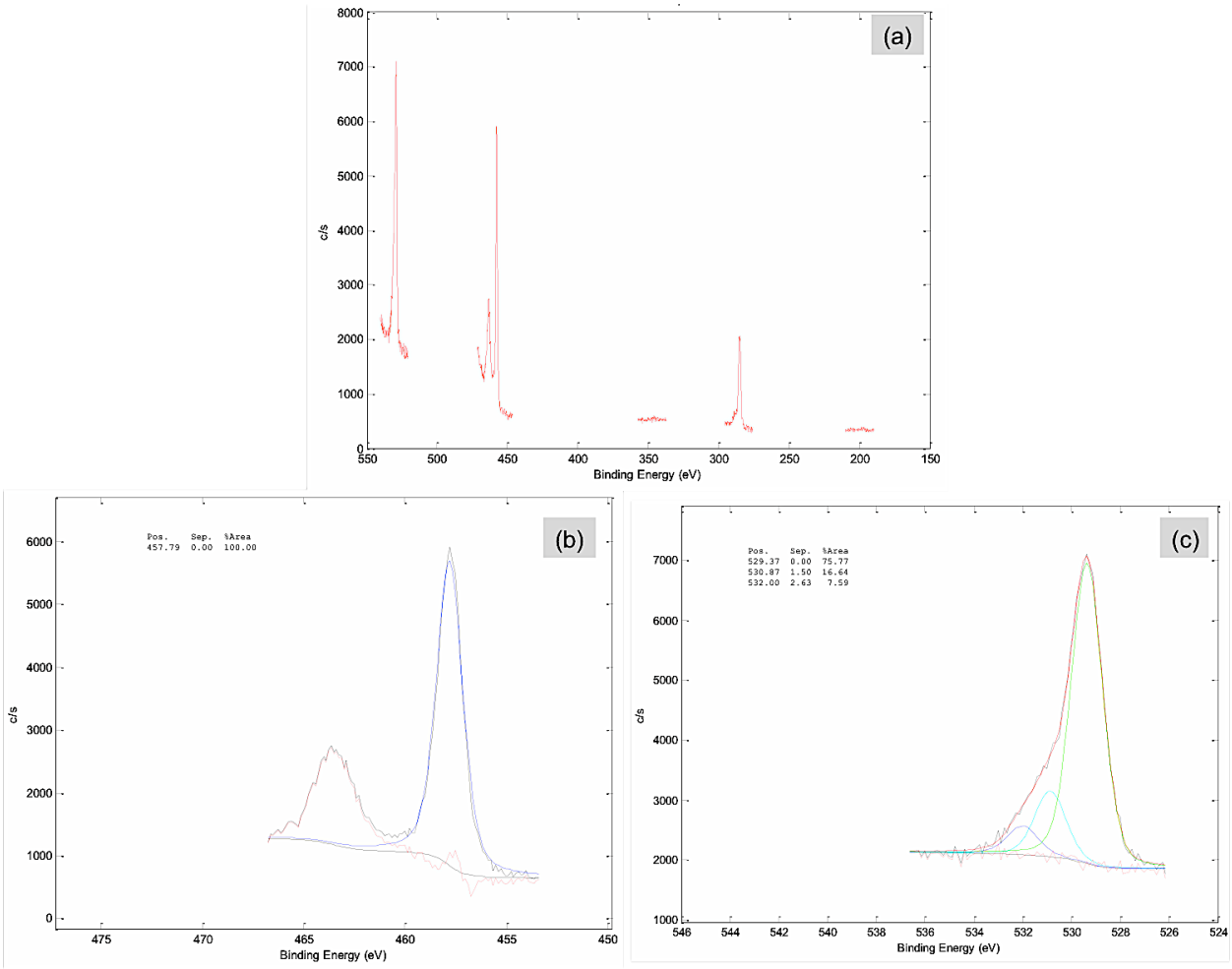

Figure 2-28 XPS data of TiO_2 fabricated with 5% w.t. OPT $CaCO_3$ templates (a) survey spectra, (b-c) high-resolution XPS spectrum for: Ti 2p and O 1s

The surface chemical states of Ti and O atoms in the titania particles were determined by XPS. Ti 2p was presented as peak at 457.8 eV and O 1s at 529.4 eV(75.8%), 530.9 eV(16.6%) and 532.0 eV(7.6%). The largest portion of the O 1s at 529.4 eV stands for metal oxide bond, confirming that the sample is TiO_2. The peaks at 530.9 and 532.0 eV might come from C-O, or C=O bond due to adventitious carbon. Ca $2p_{3/2}$ at around 347 eV was zero from the spectrum obtained, and the further high-resolution analysis shows the atomic concentrations of C 1s, O 1s, and Ti 2p are 38.2%, 44.9%, and 16.9%. The peak at around 295 eV was possibly because of the adventitious carbon. XPS has an analysis depth of 4-5 nm, so the presence of atoms was only detected when they are present at the surface

thickness, while the other atoms will be eliminated. EDS result of W3N samples showed that the amount of calcium left in the sample is 0.2 atomic %. The summary of the XPS and EDS concentrations was concluded in Table 2-2. Calcium existed as a small amount of residue and the difference between XPS and EDS data was due to the surface depth of each equipment.

Table 2-2 Atomic concentrations of C, O, Ca and Ti by spectra of XPS and EDS

TiO_2 prepared with templates	C (%)		O (%)		Ca (%)		Ti (%)	
	XPS	EDS	XPS	EDS	XPS	EDS	XPS	EDS
5% w.t. W4	47.0	45.8	42.5	36.8	0.5	0.4	10.0	13.6
5% w.t. W3N	36.5	42.4	49.7	20.2	0.5	0.3	13.23	14.0
5% w.t. Opt	38.2	48.6	44.9	37.0	0	0.3	16.9	11.7

Table 2-3 Atomic concentrations of high-resolution fitted peaks by XPS of template-induced titania

TiO_2 prepared with templates	O 1s peak and integrated percentage (eV)		Ti 2p (eV)
5% w.t. W4	529.46	74 %	457.85
	531.14	18.8 %	
	532.62	7.2 %	
5% w.t. W3N	529.45	77.5 %	457.85
	530.88	17.1 %	
	532.05	5.5 %	
5% w.t. Opt	529.37	75.8 %	457.79
	530.87	16.6 %	
	532.00	7.6 %	

The N_2 adsorption–desorption experiment demonstrated that the surface area of the TiO_2 ranges 196-238 m^2/g, and the average pore width was 46.5-47.7 Å. TiO_2 synthesized with OPT templating has the highest surface area, finest nanoparticles, small average pore

size, and also small most distributed pore size, as summarized in Table 2-4, Figure 2-30 and Figure 2-29.

Table 2-4 BET surface area and pore size summary

Sample	BET surface area, m^2/g	BJH adsorption average pore diameter (Å)	Highest distributed pore diameter from adsorption(Å)	Average nanoparticle size (Å)
TiO_2, from 5% W4	196.7	47.7	55.9	305.1
TiO_2, from 5% W3N	224.5	47.5	48.5	267.3
TiO_2, from 5% OPT	238.8	46.5	42.6	251.3

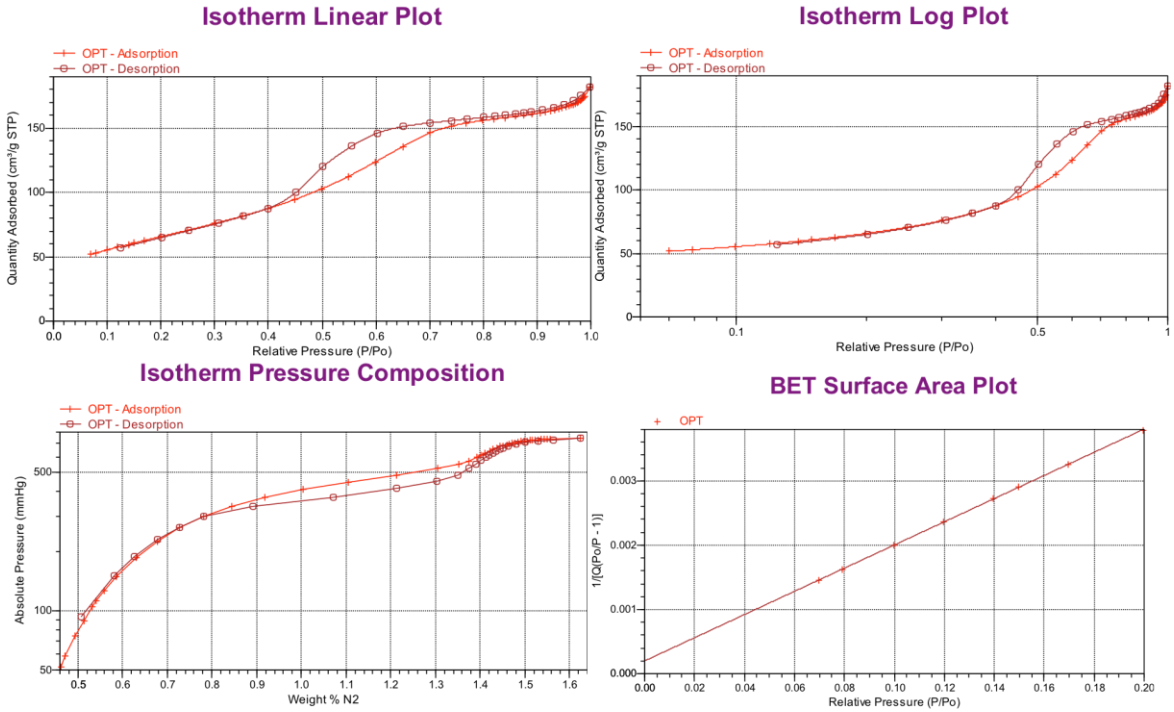

Figure 2-29 Isotherm linear plot, isotherm log plot, isotherm pressure composition and BET surface area plot via BJH adsorption/desorption of titania made with 5% w.t. Opt calcium carbonate templates.

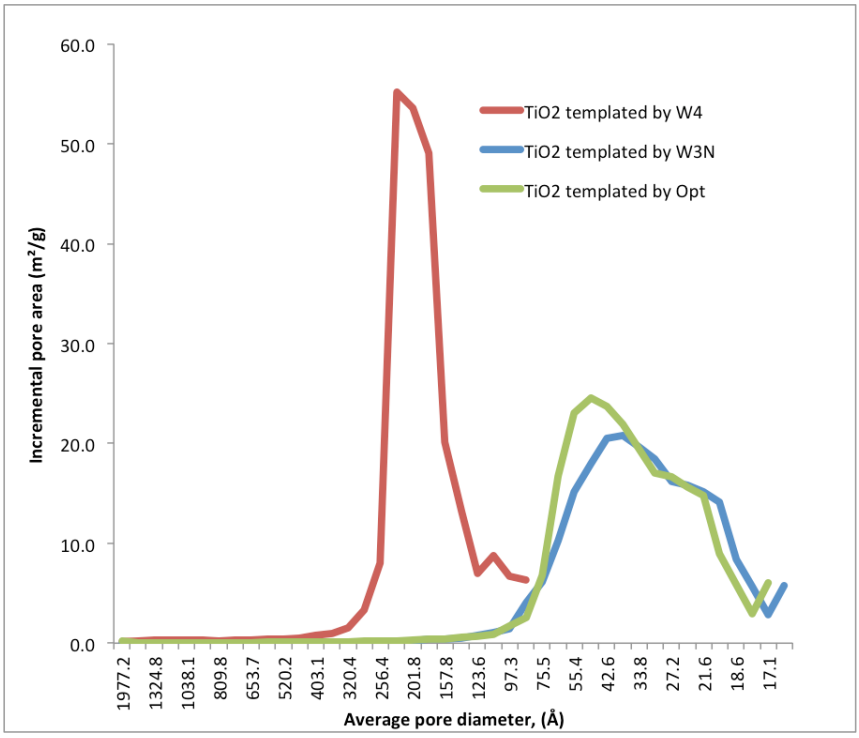

Figure 2-30 Pore size distribution of three titania powders made by calcium carbonate W4, W3N, and Opt.

2.3.2 Photocatalytic performance of porous TiO_2 templated with $CaCO_3$

Methyl Orange (MO) ($C_{14}H_{14}N_3NaO_3S$)(327.34g/mol) is a very standard model compound for accurate evaluation of TiO_2 photocatalytic activity. It is also a general pH indicator because the color will change from red to orange from acidic to basic medium. The UV-Vis spectrum of aqueous MO solution shows two major peaks at around 270 nm and 465 nm, and in this research, the 465 nm peak was utilized as the tracker of concentration change. The theory is based on the Beer-Lambert's law, and different standard concentrations of MO aqueous solutions were tested to make a calibration curve between absorption intensity and MO concentration.

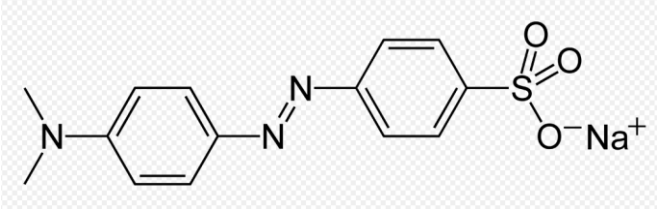

Figure 2-31 Chemical formula of methyl orange

During the process of MO decomposition, the peak at 465 nm will decrease. MO could be adsorbed on the surface of TiO_2 through van der Waals force because it's a polar molecule. Besides, due to the electronegativity of the N, O, S atoms, hydrogen bonds could be formed with the hydroxyls on TiO_2 surface. The concentration of hydroxyl groups will depend on the pH of the semiconductor and dye suspension. When it's acidic, the surface hydroxyl groups mainly exist as Ti-OH and/or $Ti\text{-}H^{2+}$, providing chances for hydrogen bond formation. When it's basic, the surface hydroxyl groups mainly exist as TiO- and TiOH, preventing the hydrogen bonds forming between MO and TiO_2 surface. Thus only when pH is lower, there are both van der Waals force and hydrogen bonds contributing to the adsorption of MO, while when pH is higher, there are no hydrogen bonds helping. In this research, the pH of the MO solution applied was kept as it is without the addition of acid or base, and measured to be between 6 and 7.

Calibration curve was obtained and fitted into a linear line. The blank dye tests showed that when no photocatalyst was added, there is very minimal degradation of the dye under UV light with a Pyrex glass petri dish lid. However, when the lid was removed, UV irradiation will degrade the dye significantly as shown by the blue curve in Figure 2-32, and further degradation continued as the green curve showed. This matched Figure 2-8 (c-d), due to the fact that wavelength < 275 nm was filtered by Pyrex glass lid. Previous work mentioned that it was noted that when no photocatalyst was added, only 4% of the

degradation of methyl orange solution with UV irradiation could be observed,[44] which could be considered as a small enough amount to be neglected compared to the effects of the photocatalysts.

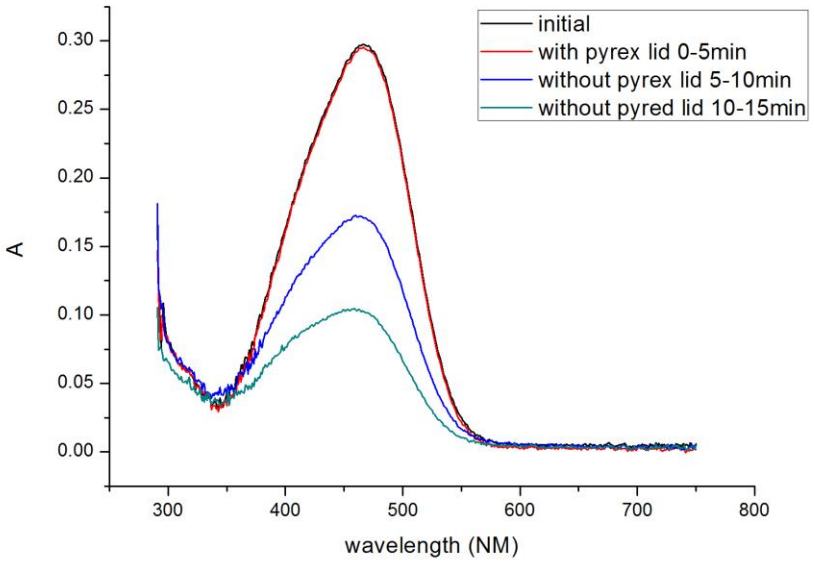

Figure 2-32 Blank dye without catalysts tested with UV light and the comparison of the Pyrex lid effects

By repeating photocatalytic experiments for each sample for at least 3 times, the comprehensive comparison was concluded in Figure 2-33 and Figure 2-34. As shown in [45], almost no concentration change was observed for the blank dye sample, during the 20-minute treatment, and the only minimal change was probably due to the evaporation of some solvent. The degradation levels were compared between the same weight of different titania samples, such as pristine TiO_2 prepared with only TTIP and VA sol, the commercial anatase titania nanoparticles, and the TiO_2 particles made with three types of $CaCO_3$ templates.

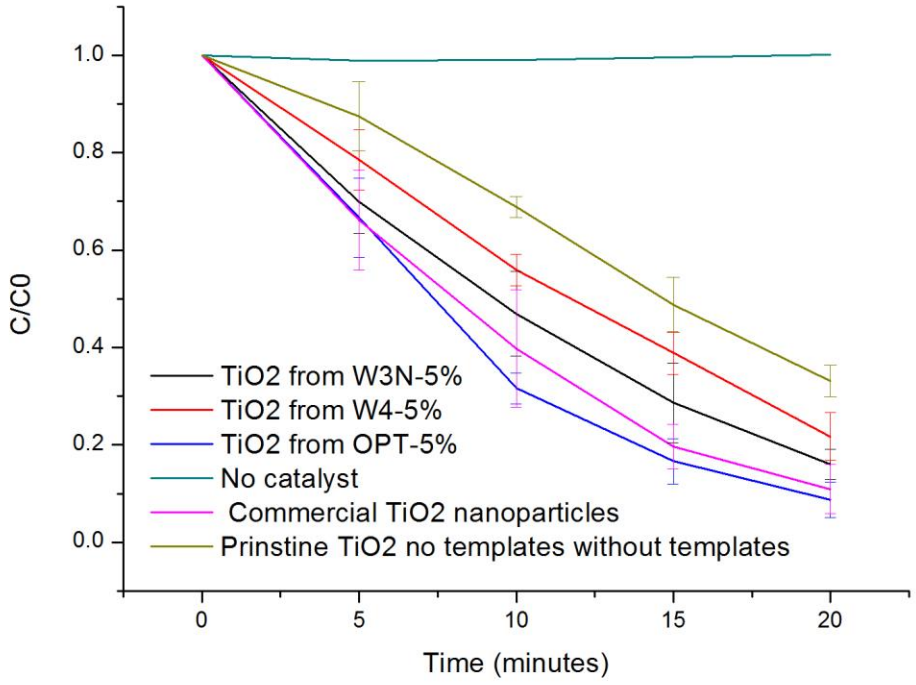

Figure 2-33 Comparison of the photocatalytic capacities through [concentration C/ initial concentration C0] vs. [time], from top to bottom, regarding to: (green) - no catalyst, (olive) - pristine TiO_2 without templates, (red) - TiO_2 from 5% w.t. W4 $CaCO_3$ templating, (black) - TiO_2 from 5% w.t. W3N $CaCO_3$ templating, (pink) - commercial anatase TiO_2 nanoparticles, and (blue) - TiO_2 from 5% w.t. Opt $CaCO_3$ templating.

By utilizing a pseudo-first-order kinetic model, the log[C] vs. time was further plotted in Figure 2-34. Linear fitting results gave the values of the reaction rate constant k as 0.07 min^{-1} for TiO_2 from W4, 0.11 min^{-1} for TiO_2 from W3N, 0.14 min^{-1} for TiO_2 from Opt, 0.05 min^{-1} for TiO_2 made with sol only with templates, and 0.11 min^{-1} for commercial anatase TiO_2.

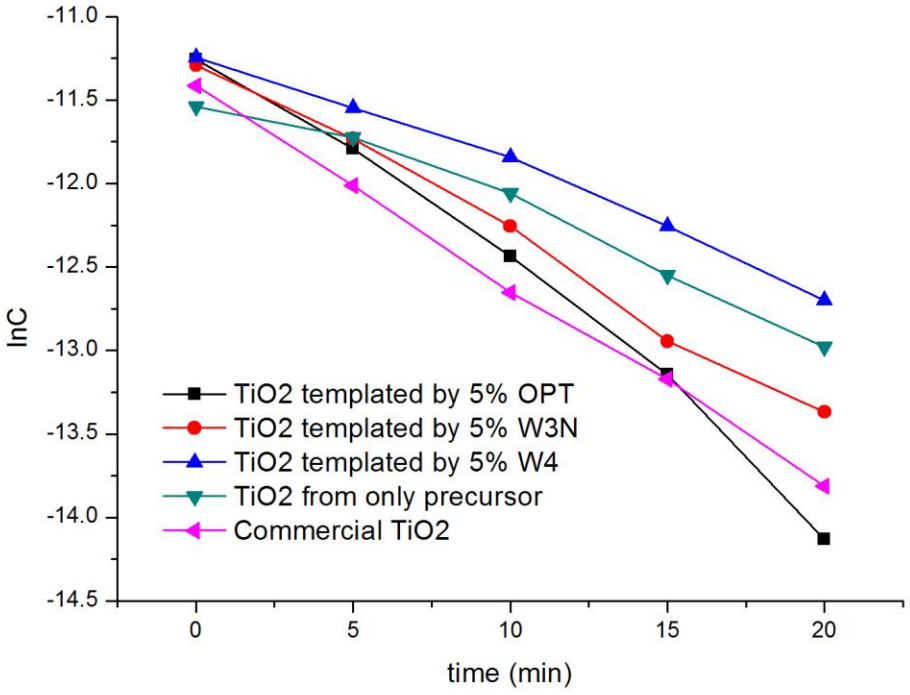

Figure 2-34 Relationship between lnC and time, based on ln(C) = -kt+ln(C0) (k has unit of min-1)

The rate constant of the best-performed TiO_2 templated by 5% w.t. Opt was 27% higher than the commercial anatase TiO_2 particles. The W3N templated product also reached the same level as the commercial one. The highest surface area and largest pore volume explain the reason for the best performance of 5% w.t. Opt templated TiO_2. The macro/micro/meso porosities of the particles were different from traditional particles, and probably provided more reflection, scattering of light harvesting during the photocatalytic process, while at the same time, the improved surface area offered larger dye adsorption and active spots for electron transport.

2.4 Conclusions

A simple and cost-effective modified sol-gel $CaCO_3$ templating method was developed to create macro/micro/nano porous anatase titanium dioxide particles in different sizes,

morphologies, and porosities. A complete removal of $CaCO_3$ removal was confirmed through various of characterizing methods such as SEM, TEM, Raman, XPS, and EDS. Applications in photocatalysts were investigated with UV irradiation and compared among TiO_2 made without templates, with three different templates, and the commercial TiO_2 particles. The results showed a promising 27% improvement compared to commercial particles, and 180% increase compared to no-template induced TiO_2.

2.5 Future Work

2.5.1 Adjusted $CaCO_3$ size and structures to make TiO_2 in different shapes

According to the previous report, $CaCO_3$ could also be lab-made according to a procedure developed for cross-linked DNA capsules.[19] 0.33M aqueous sodium carbonate (Na_2CO_3) solution was rapidly poured into 0.33 M calcium chloride dehydrate ($CaCl_2 \cdot 2H_2O$) solution at same volume under vigorous stirring and mixed for 30 seconds. The product $CaCO_3$ was washed twice by centrifugation, filtration, and drying process. Further removal of $CaCO_3$ was obtained in a mild condition with ethylenediaminetetraacetic acid (EDTA). The resulting porous $CaCO_3$ microparticles have a diameter around 4 um, and worked as an adsorbent for diverse macromolecules such as polyelectrolytes, proteins, and polysaccharides. FE-SEM images confirmed that after the acid etching, a hollow cross-linked DNA capsules were made without collapsing. One thing to notice is that homemade $CaCO_3$ size and morphology may vary due to the solution concentration, reactant addition speed, and the mixing method.

2.5.2 Mixed phase TiO_2

Degussa P25 is a type of titania powder composed of 70% anatase and 30% rutile TiO_2. The surface area of P25 is around 50 m^2g^{-1}. The photocatalytic efficiency of P25 is among the top among commercial products, and this has been attributed to the different charge separation of mixed phase was enhanced compared to anatase only.[46] The energy of anatase trapping site is lower than both anatase and rutile conduction band, so the photogenerated electrons were observed to migrate from rutile to anatase phase. It is the interfacial sites between two phases that lead to a more efficient charge separation and photo-efficiency.

The current results were compared with anatase pure-phase commercial product due to the consistency of the material crystallinity. Further work should be focusing on adjusting the ratio of anatase and rutile phase of the products made from $CaCO_3$ templating and found the optimum parameters such as calcination temperature, time, through the analysis of Raman, XRD, and photocatalytic degradations.

BIBLIOGRAPHY

BIBLIOGRAPHY

(1) Pal, N.; Bhaumik, A. Soft Templating Strategies for the Synthesis of Mesoporous Materials: Inorganic, Organic–Inorganic Hybrid and Purely Organic Solids. *Advances in Colloid and Interface Science* **2013**, *189-190*, 21–41.

(2) Shin, Y.; Exarhos, G. J. Template Synthesis of Porous Titania Using Cellulose Nanocrystals. *Materials Letters* **2007**, *61*, 2594–2597.

(3) Férey, G.; Haouas, M.; Loiseau, T.; Taulelle, F. Nanoporous Solids: How Do They Form? an in Situ Approach. *Chem. Mater.* **2014**, *26*, 299–309.

(4) Chen, X.; Mao, S. S. Titanium Dioxide Nanomaterials: Synthesis, Properties, Modifications, and Applications. *Chem. Rev.* **2007**, *107*, 2891–2959.

(5) Li, W.; Wu, Z.; Wang, J.; Elzatahry, A. A.; Zhao, D. A Perspective on Mesoporous TiO 2Materials. **2014**, *26*, 287–298.

(6) Barbé, C. J.; Arendse, F.; Comte, P.; Jirousek, M.; Lenzmann, F.; Shklover, V.; Grätzel, M. Nanocrystalline Titanium Oxide Electrodes for Photovoltaic Applications. *Journal of the American Ceramic Society* **1997**, *80*, 3157–3171.

(7) Liu, C.; Fu, L.; Economy, J. A Simple, Template-Free Route for the Synthesis of Mesoporous Titanium Dioxide Materials. *J. Mater. Chem.* **2004**, *14*, 1187–1189.

(8) Yu, J. C.; Zhang, L.; Yu, J. Rapid Synthesis of Mesoporous TiO 2 with High Photocatalytic Activity by Ultrasound-Induced Agglomeration. *New journal of Chemistry* **2002**, *26*, 416–420.

(9) Kim, W.; Choi, S. Y.; Jeon, Y. M.; Lee, S.-K.; Kim, S. H. Highly Ordered, Hierarchically Porous TiO 2Films via Combination of Two Self-Assembling Templates. *ACS Appl. Mater. Interfaces* **2014**, *6*, 11484–11492.

(10) Fuertes, AB. Low-Cost Synthetic Route to Mesoporous Carbons with Narrow Pore Size Distributions and Tunable Porosity Through Silica Xerogel Templates. *Chem. Mater.* **2004**, *16*, 449–455.

(11) Lakshmi, B. B.; Dorhout, P. K.; Martin, C. R. Sol-Gel Template Synthesis of

Semiconductor Nanostructures. *Chem. Mater.* **1997**, *9*, 857–862.

(12) Zhuge, F.; Qiu, J.; Li, X.; Gao, X.; Gan, X.; Yu, W. Toward Hierarchical TiO2 Nanotube Arrays for Efficient Dye-Sensitized Solar Cells. *Adv. Mater.* **2011**, *23*, 1330–1334.

(13) Bagheri, S.; Mohd Hir, Z. A.; Yousefi, A. T.; Abdul Hamid, S. B. Progress on Mesoporous Titanium Dioxide: Synthesis, Modification and Applications. *Microporous and Mesoporous Materials* **2015**, *218*, 206–222.

(14) Yue, W.; Park, R. J.; Kulak, A. N.; Meldrum, F. C. Macroporous Inorganic Solids From a Biomineral Template. *Journal of Crystal Growth* **2006**, *294*, 69–77.

(15) Guo, F.; Li, Y.; Xu, H.-X.; Zhao, G.-Q.; He, X.-J. Size-Controllable Synthesis of Calcium Carbonate Nanoparticles Using Aqueous Foam Films as Templates. *Materials Letters* **2007**, *61*, 4937–4939.

(16) Chen, L.; Hu, F.; Zhou, Q.; Sun, J.; Zhang, H. Growth of Hierarchical Calcium Carbonate Crystals Templated by Biomolecules of Lotus Root. *Crystal Research and Technology* **2009**, *44*, 1289–1292.

(17) Jiang, J.; Zhang, Y.; Yang, X.; He, X.; Tang, X.; Liu, J. Assemblage of Nano-Calcium Carbonate Particles on Palmitic Acid Template. *Advanced Powder Technology* **2014**, *25*, 615–620.

(18) Meldrum, F. C.; Seshadri, R. Porous Gold Structures Through Templating by Echinoid Skeletal Plates. *Chem. Commun.* **2000**, 29–30.

(19) Fujii, A.; Maruyama, T.; Ohmukai, Y.; Kamio, E.; Sotani, T.; Matsuyama, H. Cross-Linked DNA Capsules Templated on Porous Calcium Carbonate Microparticles. *Colloids and Surfaces A: Physicochemical and Engineering Aspects* **2010**, *356*, 126–133.

(20) Volodkin, D. V.; Klitzing, von, R.; Moehwald, H. Pure Protein Microspheres by Calcium Carbonate Templating. *Angew. Chem. Int. Ed.* **2010**, *49*, 9258–9261.

(21) Yu, H.; Yu, J.; Cheng, B.; Lin, J. Synthesis, Characterization and Photocatalytic Activity of Mesoporous Titania Nanorod/Titanate Nanotube Composites. *Journal of Hazardous Materials* **2007**, *147*, 581–587.

(22) Yu, H.; Yu, J.; Cheng, B.; Liu, S. Novel Preparation and Photocatalytic

Activity of One-Dimensional TiO 2hollow Structures. *Nanotechnology* **2007**, *18*, 065604.

(23) Pourmand, M.; Taghavinia, N. TiO2 Nanostructured Films on Mica Using Liquid Phase Deposition. *Materials Chemistry and Physics* **2008**, *107*, 449–455.

(24) Chen, J.-F.; Wang, J.-X.; Liu, R.-J.; Shao, L.; Wen, L.-X. Synthesis of Porous Silica Structures with Hollow Interiors by Templating Nanosized Calcium Carbonate. *Inorganic Chemistry Communications* **2004**, *7*, 447–449.

(25) Shao, L.; Chen, J.-F.; Luo, L.-L.; Gao, L.-D. Synthesis of Hollow Titania Using Nanosized Calcium Carbonate as a Template. *Chemistry Letters* **2005**, *34*, 138–139.

(26) Hou, Q.; Tao, X.; Yang, Y.-J.; Ma, Y. Optimal Synthesis of Mesostructured Hollow Titania Nanotubes Templated on CaCO3 Nanoparticles. *Powder Technology* **2010**, *198*, 429–434.

(27) Kumar, P. M.; Badrinarayanan, S.; Sastry, M. Nanocrystalline TiO_2 Studied by Optical, FTIR and X-Ray Photoelectron Spectroscopy: Correlation to Presence of Surface States. *Thin Solid Films 358*, 122–130.

(28) DUNUWILA, D. D.; GAGLIARDI, C. D.; BERGLUND, K. A. Application of Controlled Hydrolysis of Titanium(Iv) Isopropoxide to Produce Sol Gel-Derived Thin-Films. *Chem. Mater.* **1994**, *6*, 1556–1562.

(29) Askeland, P. A. Preparation and Characterization of Sol-Gel Derived Metal Oxide Thin Films and Powders for Coatings and Catalysts, 1997.

(30) Dozzi, M.; Selli, E. Specific Facets-Dominated Anatase TiO2: Fluorine-Mediated Synthesis and Photoactivity. *Catalysts 2013, Vol. 3, Pages 455-485* **2013**, *3*, 455–485.

(31) Imai, H.; Takei, Y.; Shimizu, K.; Matsuda, M.; Hirashima, H. Direct Preparation of Anatase TiO2 Nanotubes in Porous Alumina Membranes. *J. Mater. Chem.* **1999**, *9*, 2971–2972.

(32) Al-Qaradawi, S.; Salman, S. R. Photocatalytic Degradation of Methyl Orange as a Model Compound. *"Journal of Photochemistry & Photobiology, A: Chemistry"* **2002**, *148*, 161–168.

(33) Ulery, A. L.; Drees, R. ***Methods of Soil Analysis: Mineralogical Methods***.

(34) Parker, J. E.; Thompson, S. P.; Lennie, A. R.; Potter, J.; Tang, C. C. A Study of

the Aragonite - Calcite Transformation Using Raman Spectroscopy , Synchrotron Powder Diffraction and Scanning Electron Microscopy. *CrystEngComm* **2010**, *12*, 1590–1599.

(35) L'vov, B. V. Mechanism and Kinetics of Thermal Decomposition of Carbonates. *Thermochimica Acta* **2002**, *386*, 1–16.

(36) Frank, O.; Zukalova, M.; Laskova, B.; Kürti, J.; Koltai, J.; Kavan, L. Raman Spectra of Titanium Dioxide (Anatase, Rutile) with Identified Oxygen Isotopes (16, 17, 18). *Physical Chemistry Chemical Physics* **2012**, *14*, 14567–14572.

(37) Qian, L.; Du, Z.-L.; Yang, S.-Y.; Jin, Z.-S. Raman Study of Titania Nanotube by Soft Chemical Process. *Journal of Molecular Structure* **2005**, *749*, 103–107.

(38) A Fujishima, X. Z. D. A. T. TiO2 Photocatalysis and Related Surface Phenomena. **2008**, *63*, 515–582.

(39) Xu, H.; Ouyang, S.; Liu, L.; Reunchan, P.; Umezawa, N.; Ye, J. Recent Advances in TiO2-Based Photocatalysis. *J. Mater. Chem. A* **2014**, *2*, 12642–12661.

(40) Xu, H.; Reunchan, P.; Ouyang, S.; Tong, H.; Umezawa, N.; Kako, T.; Ye, J. Anatase TiO2 Single Crystals Exposed with High-Reactive {111} Facets Toward Efficient H2 Evolution. *Chem. Mater.* **2013**, *25*, 405–411.

(41) Ohno, T.; Sarukawa, K.; Matsumura, M. Crystal Faces of Rutile and Anatase TiO2 Particles and Their Roles in Photocatalytic Reactions. *New journal of Chemistry* **2002**, *26*, 1167–1170.

(42) Mathew, S. S.; Ma, S.; Kretzschmar, I. Three-Dimensionally Ordered Macroporous TiO2 Electrodes: Fabrication of Inverse TiO2 Opals for Pore-Size-Dependent Characterization. *J. Mater. Res.* **2012**, *28*, 369–377.

(43) Masuda, Y.; Kato, K. Anatase TiO2 Films Crystallized on SnO2:F Substrates in an Aqueous Solution. *Thin Solid Films* **2008**, *516*, 2547–2552.

(44) Li, Y.; Li, X.; Li, J.; Yin, J. Photocatalytic Degradation of Methyl Orange by TiO2-Coated Activated Carbon and Kinetic Study. *Water Research* **2006**, *40*, 1119–1126.

(45) Phase-Pure TiO2 Nanoparticles: Anatase, Brookite and Rutile. **2008**, *19*, 145605.

(46) Li, G.; Chen, L.; Graham, M. E.; Gray, K. A. A Comparison of Mixed Phase Titania Photocatalysts Prepared by Physical and Chemical Methods: the Importance of the Solid–Solid Interface. *Journal of Molecular Catalysis A: Chemical* **2007**, *275*, 30–35.

3 Templating with Natural Cellulose and Micro-Fibrillated Cellulose (MFC)

3.1 Background

3.1.1 Natural templates for inorganic materials

As introduced in Chapter 2, diblock or triblock co-polymers have their limitations, and nano-scale hard templates are facing some crucial challenges as well. Applying calcium carbonate as the hard template yields macro/meso/micro pores within TiO_2 particles and turned out to be excellent photocatalysts. For better defined nanostructures and easier template removal, new interest was transferred to natural biodegradable templates at nano scale.

Using nature as guide to solve scientific challenges in material design is not a new thing. The complex and elaborate structures of biological materials provide tremendous opportunities in the preparation of functional inorganic materials with special morphologies and shapes for novel applications. Utilizing natural templates to build up specific 2D or 3D structures has become an emerging attempt in "bottom-up" synthesis of inorganic micro/nano-materials.

Nanocrystals, nanowires and other hierarchical architectures with sizes ranging from 1-25 nm, match perfectly with the scale of certain types of biological molecules. Natural templates such as cotton fibers[1-3], viruses[4], butterfly wings,[5] eggshell membranes,[6] bacteria,[7] pollen grains,[8] etc. served as templates, and are easily removed by elevated thermal degradation. Hollow inorganic materials made using these templates have low

density, high surface area, and controllable optical and electric properties. Figure 3-1 demonstrates several examples of silica and titania nanomaterials derived from various natural templates.

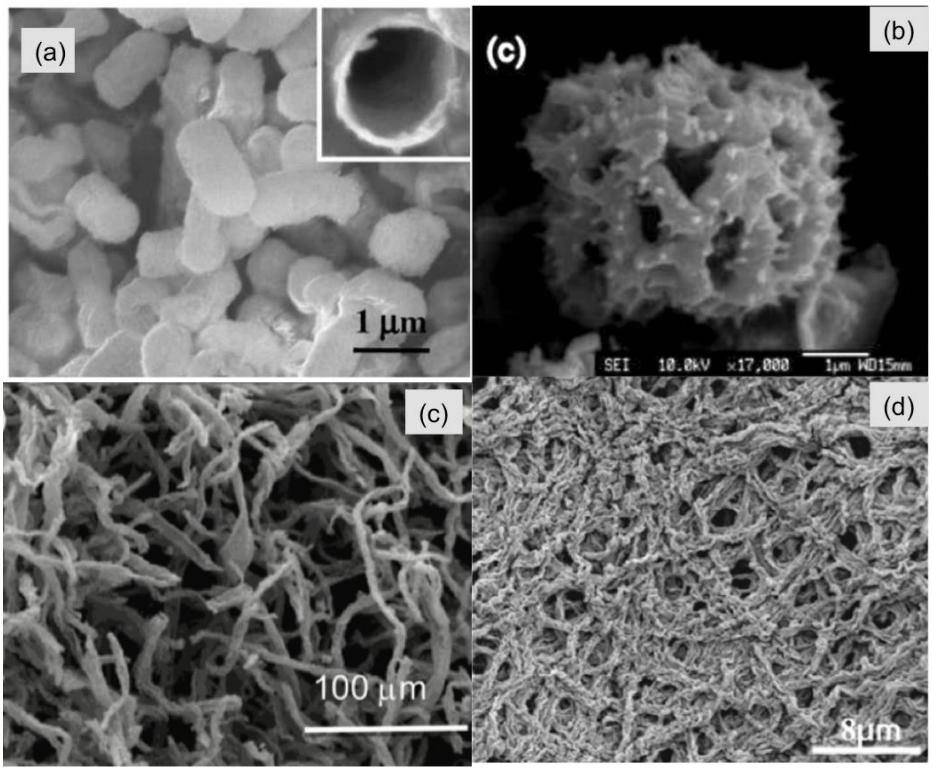

Figure 3-1 SEM images of nanomaterials made with bio-structure templates: (a) hollow silica made with bacteria Escherichia coli (KP7600);[7] (b) porous titania made with dandelion pollen grains;[8] (c) TiO_2 hollow fibers made with cotton wools;[1] (d) hierarchical interwoven titania prepared with eggshell membrane. (reprinted with permission from reference[6])

Among different kinds of natural templates, cellulose fibers have many advantages. They are the most abundant renewable and biodegradable polymer derived from various sources with an annual production of 10^{11}-10^{12} tons.[9] Since its first discovery and isolation in 1838, cellulose have been extensively researched and applied in paper, composite, pharmaceutical, and food industries.[10] As a potential template, it has multiple conveniences including: an abrupt thermal decomposition, being environmentally friendly, a large surface area for material deposition, abundant surface hydroxyl groups for chemical

bonding and very low cost. Being the most abundant organic compound derived from biomass on earth,[11] cellulose is of interest to scientists due to its availability, biocompatibility, renewability, biological degradability, and sustainability.

Cellulose $(C_6H_{10}O_5)_n$ is a long-chain polysaccharide consisting of several hundred to over ten thousand β-1,4-linked D-glucose rings. Each D-glucose ring is corkscrewed 180° with respect to its neighbors, and cellubiose is the repeating segment with non-reducing end and reducing end on each side as Figure 3-2 shows.[10] The monomer anhydroglucose unit (AGU), carries three free hydroxyl groups: one primary hydroxyl on C6, and two secondary hydroxyls on C2 and C3. All these hydroxyl groups along the chain help form the intra- and intermolecular hydrogen bonds,[11]additionally, provide numerous sites for further chemical modification. The polymer chains of cellulose are made of fibrous structures called microfibrils or nanofibrils, which are associated by hydrogen bonds and van der Waals forces.[12] The hydrogen bond network gives cellulose structures rigidity and is used as a structural building block for many plants. Figure 3-3 is a brief synopsis of how cellulose fibers are harvested from plants.

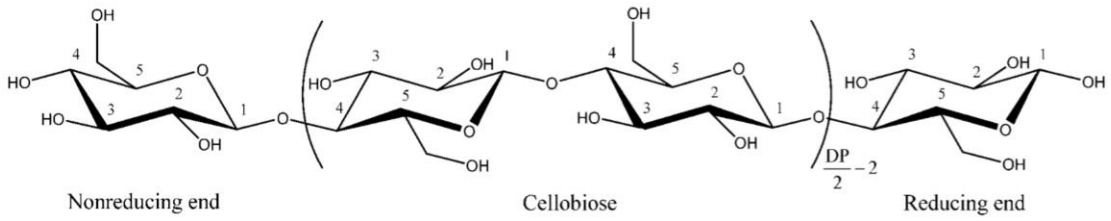

Figure 3-2 Structure of cellulose. (reprinted with permission from reference[10])

Nano-scale cellulose has gained tremendous attention because it retains the original bulk material properties as mentioned above, and also presents high strength, high stiffness comparable to those of inorganic fibers, low weight,[13] and nano-size effects.

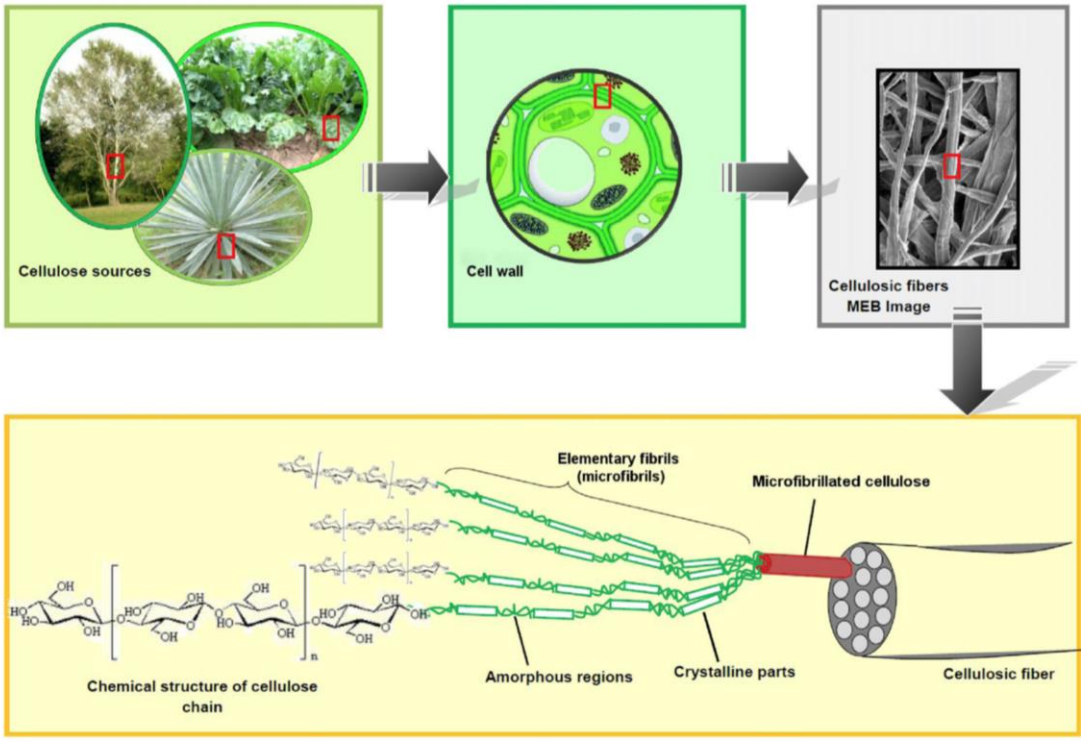

Figure 3-3 Cellulose sources, cell wall, and fibers. The structure level demonstration of cellulosic fiber. (reprinted with permission from reference [11])

Typically, nanofibrils have a size of 2-10 nm in diameter (varies depending on the origin) and several tens of micrometers in length.[12] From various cost-effective sources (wood, cotton, potato, wheat, soy, coconut husk), they are obtained by methods including physical treatments such as cryocrushing, grinding, high-pressure homogenizing, high-speed blundering, ultra-sonicating etc., and chemical treatments such as concentrated acid hydrolysis, biological treatments and oxidations.[12] A combination of the physical and chemical treatments removes wax, extractives, hemicelluloses and lignin chemically prior to grinding or homogenizing afterwards. [14]

Although there are numerous ways to describe nano-scale cellulose, e.g., cellulose nanofibers, microfibers, nanocrystals, nanowhiskers, etc., a recent review of cellulose[11]

described the classification in regards to the processing steps to prepare them. Similarly, a standard terminology will be used for the fibers used in this work.

(1) cellulose nanocrystals, termed as "CNC" in this thesis. These CNCs have a diameter at 2-20 nm, and length ranging from 100 nm to 2 μm, which are prepared from wood, sea plants, or sea animals. From the original cellulose fiber suspensions, it goes through chemical treatment and dialysis, yielding different sizes of nanocrystals. (Figure 3-4)

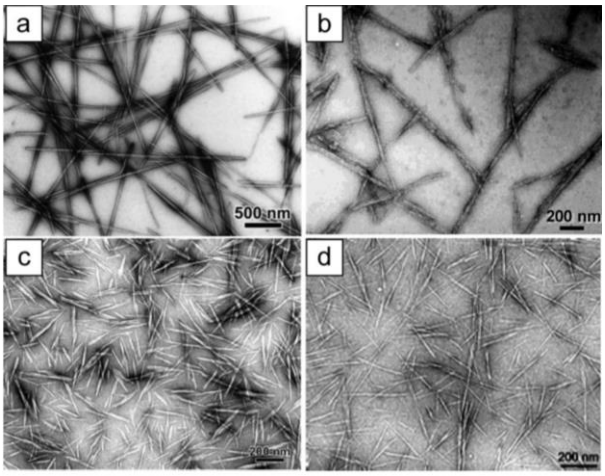

Figure 3-4 TEM images of cellulose nanocrystals derived from (a) tunicate, (b) bacterial, (c) ramie, and (d) sisal. (reprinted with permission from reference[10]

(2) microfibrillated cellulose, termed as "MFC", stands for cellulose fibers with a diameter of 20-60 nm due to a higher extent of aggregation of those 2-10 nm microfibrils. For MFCs that are only processed mechanically, the length is beyond 10 μm, while for MFCs with pre-treatment and mechanical treatment, the length is ~2 μm.(Figure 3-5)[11]

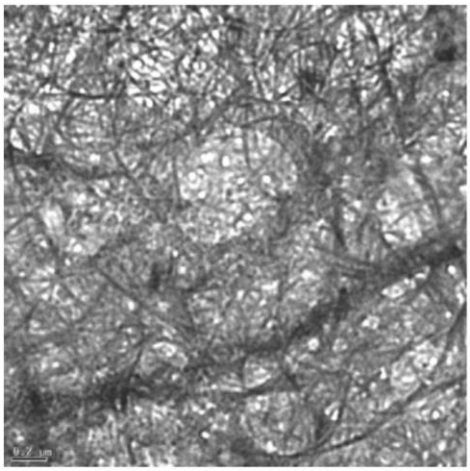

Figure 3-5 TEM image of MFC gel showing cellulose nanofibrils and nanofibrils bundles (reprinted with permission from reference[10,13]

In the coming chapters, terms CNC and MFC are distinguished with "microfibrils" or "nanofibrils", the non-aggregated version.[13] A brief summary of the diameter, length and aspect ratio data for above cellulose structures is seen below.

Table 3-1 Summary of dimensions of cellulose structures

Cellulose structure	Diameter (nm)	Length (nm)	Aspect ratio (L/d)
Microfibril	2-10	>10,000	>1000
Microfibrillated cellulose (MFC) *	20-60	>10,000	>100
Cellulose nanocrystal (CNC)	2-20	100-20,000	10-100

- *The microfibrillated cellulose discussed in this table is processed by mechanical treatments only. partially adapted from.[13]*

Thus, MFC materials may be composed of (1) nanofibrils, (2) fibrillar fines, (3) fiber fragments and (4) fibers. This implies that MFC is not necessarily synonymous with nanofibrils, microfibrils or any other cellulose nano-structure. However, properly produced MFC materials contain nano-structures as a main component, i.e. nanofibrils.[15]

3.1.2 Titania materials fabrication through cellulose templating

Cellulose contains 31.48% w.t. hydroxyl groups, with one primary and two secondary in each AGU. The hydroxyls on the surface of cellulose are the starting point of any chemical functionalization of cellulose. When a cellulose molecule is fully extended, it forms a flat ribbon with –OH groups protruding laterally. The hydrogen bonds are formed inter- and intramolecularly, where the intramolecular bonding between adjacent anhydroglucose rings could improve the linear integrity of the polymer chain and affects the reactivity of the hydroxyl groups especially of the C-3.[9] Due to the existence of hydrogen bonding, cellulose fibrils tend to become aggregated. As Figure 3-3 shows, the amorphous regions are more reactive than the crystalline regions. The degree of crystallinity (ratio between amorphous and crystalline) of cotton cellulose, for instance, is about 40-45%. In addition, the reactivity of the hydroxyls will be influenced by the reaction medium as well. [9]

Cellulose is usually suspended in water or organic solvents such as ethanol or isopropanol for further interaction with the inorganic precursor for titania deposition. Also, it could start as a dry substrate for immersion or soaking in the precursor systems. For pre-suspended cellulose, an ordered layer of water molecules cover the cellulose fibers via hydrogen bonding, and the outside layer was composed of disordered water molecules. If the cellulose was treated with solvent exchange, with up to 99% of the original water removed, the outside layer would be replaced by alcohol, and the inside first layer will retain an ordered network of hydrogen-bonded water molecules.[16] For the second situation, the dry cellulose surface hydroxyls especially the three active ones will interact with the hydroxyls in the precursor and form bonding between the Ti(IV) precursor and the template.

Inorganic material templated with MFCs or CNCs obtain desired porosities via precursor coating and calcination owing to the rigidity and the thermal stability of the cellulose. Different types of titania or titania/cellulose composites have been reported as follows.

3.1.2.1 Tubular and fibril titania

Titania hollow microfibers were prepared by coating TiO_2 onto hydrophilic cellulose fibers through heterogeneous nucleation[1] with ammonium hexafluorotitanate and boric acid through an acid-assisted supersaturated aqueous solution. Pure cotton wool was immersed into this solution, washed, dried, and calcined into hollow titania fibers (Figure 3-6).

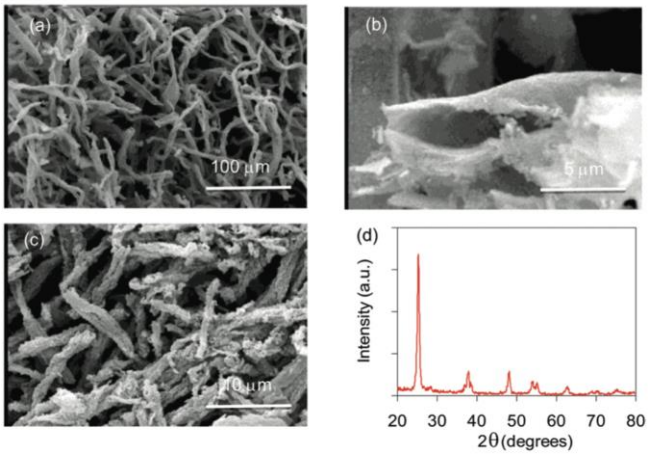

Figure 3-6 SEM images of (a) TiO_2 fibers after template removing (b) cross section of one hollow fiber (c) TiO_2 nanofibers after milling and ultra-sonication to make a paste (d) XRD diagram of the fibers.[1]

An extra step of mixing the above-prepared TiO_2 into an applicable doctor blade paste was required for dye-sensitized solar cell assembly. An efficiency of 7.2% was reached under solar illumination and electron transport properties were enhanced compared to traditional spherical nanoparticles. Another work discussed how titania nanotubes were derived from laboratory filter paper by surface sol-gel coating process. A further

hydrothermal step created a needle-like deposition of rutile TiO_2 along the surface of anatase nanotubes.[17]

Bamboo cellulose fibers were used as a template to make a millimeter-long TiO_2 fibers composed of 30 nm spherical nanoparticles[2] through titanium tetrachloride in an aqueous system. With a molar ratio of $TiCl_4$: $(NH_4)_2SO_4$: HCl at 1: 2: 10, the additives here served as promoter for the anatase phase. A finishing annealing at different temperatures (500, 600, 700, 800, 900 °C) in air removed the cellulose fibers and produced TiO_2 microfibers (Figure 3-7). Superior photocatalytic activity was demonstrated in degradation tests of a phenol solution. Materials that were calcined at 500, 600, and 700 °C achieved higher photodegradation efficiency compared to standard TiO_2 material Degussa, P25 at the same conditions.

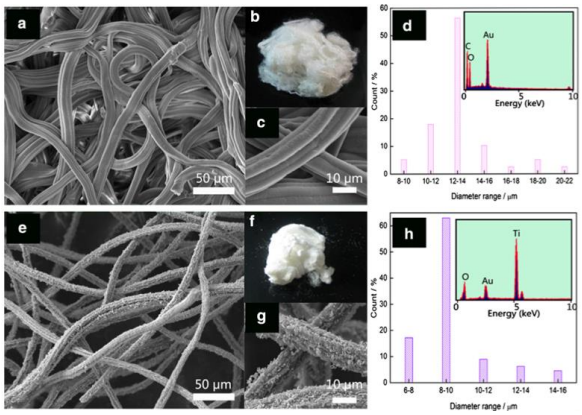

Figure 3-7 (a-d) Low magnification SEM image, photograph, magnified SEM image and diameter distribution with Energy-dispersive X-ray spectrum of pure bamboo cellulose fiber. (e-h) Low magnification SEM image, photograph, and magnified SEM image and diameter distributions of TiO_2 product calcined at 500 °C.[2]

3.1.2.2 Immobilized TiO_2 on cellulose

Coatings of self-cleaning titania can be used as anti-pollutants and anti-bacterial materials especially with its versatile applications on substrates like metal, glass, or even plastic, papers, and cotton fabrics which have very low thermal resistance. Qi and

colleagues developed a simple dip-pad-dry-cure process to obtain anatase titania coated cotton fabric at room temperature in a titanium tetraisopropoxide/acid based sol-gel system.[3] In a typical procedure, cleaned cotton fibers were dipped into a TiO_2 sol (TTIP added drop wise into 0.7% nitric acid containing ethanol and acetic acid, and heated to different temperatures), neutralized in ammonia gas and dried at 80 °C for 5 min and finally cured at 120 °C for 3 min. A uniform layer of coating was formed (Figure 3-8) and XRD results revealed pure anatase phase. The bactericidal activities, colorant decomposition, degradation of red wine and coffee stains under UV irradiation demonstrated the excellent self-cleaning capacities of this organic/inorganic hybrid nanomaterials.

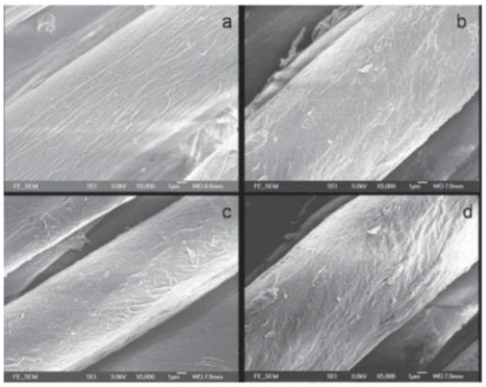

Figure 3-8 SEM images of (a) pristine cotton fiber (b-d) coated cotton fibers, sol prepared at 25, 40 and 60°C [3]

Chauhan *et al*. successfully immobilized 2.5 to 21.0% w.t. titania (diameter 10-20 nm) on cellulose fibers through single-step hydrothermal method instead of multiple steps of synthesis of TiO_2 and then the incorporation onto the cellulose paper. Briefly, the cellulose fibers were dispersed in water/ethanol, followed by a dropwise addition of titanium isopropoxide, stirring, and autoclave treatment. Paper matrices were further prepared with

TiO_2 -coated cellulose and degraded methyl blue and formaldehyde for photocatalytic performance evaluation and antibacterial capacity through E. coli inhibition.

In next section, a simple and brief experimental trial would be conducted on easily accessible lab cellulose materials with the scheme shown in Figure 3-9 to find the working mechanism of the TiO_2 deposition on cellulose surfaces and possible factors that govern the templating and growth. In detail, cellulose (green cylinder) would be coated with a layer of Ti (IV) precursor, and then went through high-temperature cellulose removal, ended up with TiO_2 hollow tubes/fibers. The Ti(IV) precursors used were based on sol gel, and liquid phase deposition discussions from Chapter 1, and will be investigated in further details in future chapters.

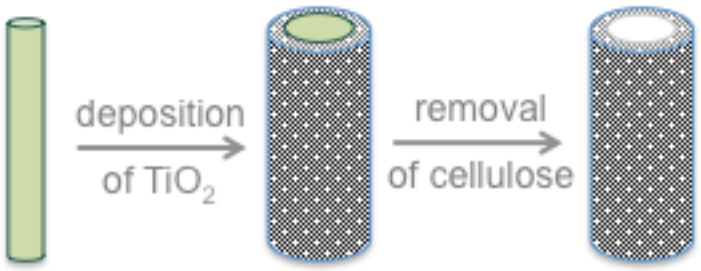

Figure 3-9 Scheme of preliminary TiO_2 deposition on cellulose fiber templates

3.2 Experimental

3.2.1 Materials and equipment

3.2.1.1 Materials:

All chemicals were used without pre-treatments unless noted. Cotton rounds were purchased from Delon Laboratories Inc., with 100% cotton content, bleached, chlorine-free, pure without brighteners. Filter paper (medium porosity with 60 mL/min flow rate and 5-10 μm particle retention) was from Fisher with a diameter of 11 cm. Titanium(IV) fluoride,

titanium(IV) isopropoxide (≥ 97%), valeric acid (≥99%), boric acid (≥99.5%), ammonium hexafluorotitanate (99.99%) were purchased from Sigma Aldrich. Hydrochloric acid (analytical reagent grade) was from Mallinckrodt. anhydrous 2-propanol were obtained from Sigma Aldrich. Ethanol (200 proof, 99.5% ACS grade) and isopropanol (99.5%) were purchased from Michigan State university stores. Cellulose Celish KY100G (90% w.t. in water) was purchased from Daicel, and has been refined only by physical processing without chemical treatment, from highly refined, pure fiber raw materials. Another source of cellulose fibers was purchased from the University of Maine process development center with a water content of 97% w.t. Mineral oil (laboratory grade, heavy) was from Columbus Chemical Industries. Plain, pre-cleaned micro glass slides were purchased from VWR international, in a size of 1 inch by 3 inch, with a thickness of 1.2 mm.

3.2.1.2 Equipment:

(1)Homogenization of cellulose fibers was performed by two sets of instruments. IKA T25 digital ULTRA-TURRAX® package with an input energy of 50W at 50/60Hz. A Mini DeBEE ultrahigh-pressure homogenizer has a single-jet parallel flow pattern (flow rate up to 250 mL/min) with an adjustable operating pressure of 2000 to 45000 psi, and a back pressure of 0 to 5000 psi, which helps process fluids producing uniform particles size reduction to nanoparticles, and high yield cell disruption. Each pass is cooled with a heat exchanger.

(2) The structures of the macro-scale cellulose templates, titania hollow ribbons, MFCs and CNCs were characterized by scanning electron microscopy (Carl Zeiss Auriga CrossBeam SEM-FIB). Samples were prepared by mounting onto a sample holder with

carbon paste/tape prior to being tungsten coated. EDAX™ EDS Analysis System for SEM – X-ray Microanalysis was applied together with SEM characterization for element analysis on TiO_2 powders as prepared.

(3) Thermogravimetric analysis (TA instruments Q500) used a high-resolution ramp of 25 °C/min to ~800 °C in air or nitrogen was conducted on macro-scale cellulose, MFCs, CNCs, and cellulose-TiO_2 sol samples. For instance, MFC samples were dried at 80-100 °C in a vacuum oven overnight, and 0.2 mg sample was tested.

(4) A LabRAM ARAMIS laser Raman spectrometer (Horiba Scientific) with 532 nm 50 mW DPSS laser was used to inspect sample crystal phases as well. All the samples were tested as is with a 50X objective lens.

(5) Fourier transform infrared (FTIR) absorption spectra were collected with Perkin Elmer 2000 Spectrum One FT-IR spectrometer at room temperature. KBr Pellets were prepared by Carver Laboratory press (model 2518) with grounded and pre-dried KBr powder. For MFCs suspension, a drop was cast between two pellets forming a sandwich structure with the excess liquid squeezed out and wiped off. The spectra of the composites were scanned from 4000 to 400 cm^{-1}.

(6)) X-ray photoelectron spectroscopy (XPS) was using a Perkin Elmer Phi 5400. The Kα line of Mg (1254 eV) X-ray source with a beam voltage of 15 kV and current of 20 mA was the excitation source. The survey spectra scan were acquired with a pass energy 187.85 eV, and a 1 eV step size. For detailed C 1s or O 1s high-resolution spectra, a pass energy of 29.35 eV and step size 0.1 eV were used. Chamber vacuum was maintained below 1×10^{-7} Torr (1.33×10^{-5} Pa). The cellulose suspension sample was prepared by drop

casting on a piece of clean glass substrate and then mounted onto the sample holder with double-sided copper tape. After the measurement, data processing was performed by MultiPak V8.0.

3.2.2 Preliminary synthesis of titania hollow ribbons with macro-size cellulose

A 0.04 M TiF_4 aqueous solution was prepared by stirring for one hour at room temperature with the pH adjusted to ~2.5 with diluted hydrochloric acid or ammonium hydroxide aqueous solution. Around 0.07 g cotton rounds that were cut into 1 cm by 2 cm small pieces were added into 50 mL TiF_4 solution. In a separate vial, filter paper was cut into 1 cm by 1 cm sheets and soaked in the solution as well. Then the vial was capped and transferred to a pre-heated mineral oil bath at 65 °C on a stirring hot plate. The reaction lasted 6 hours and the mixture was cooled to room temperature before further use.

Aqueous ammonium hexafluorotitanate (AHFT) (0.30 M) and aqueous boric acid (BA) (0.10 M) were prepared into 20 mL solution each. The pH of the boric acid solution was adjusted to ~2 by adding appropriate amount of HCl solution. Then the AHFT solution was added to BA solution, with vigorous stirring for 1 h at room temperature, resulting in final concentrations of 0.15 M for AHFT and 0.05 M for BA. The prepared stock solution (pH ~2.5) was added to the cut cotton wool and filter paper in different capped vials, and then moved to a 50 °C oil bath to react for 6 hours.

A gentle rinsing was applied to remove excess Ti(IV) left on the surface of the cotton wool or filter paper. Typically, three 100 mL beakers were filled with 80 mL RO water, and the coated filter paper or cotton wool pieces were held by plastic tweezers and rinsed for 5 seconds in each beaker. After the rinsing process, all the coated substrates were dried in a

vacuum oven at 100 °C for 1 hour. Finally, the high-temperature annealing was performed with step-wise temperature program at 200 °C, 300 °C, 350 °C and 500 °C for 0.5 hour each. The multi-step temperature raising was based on the thermal properties of cellulose.

3.2.3 Preparation of homogenized MFCs

To obtain homogenously-dispersed MFCs, as-received cellulose fibers was treated in a high-pressure homogenizer and made into isopropanol and aqueous suspensions (Figure 3-10). The process begins with creating a 5 mg/mL aqueous cellulose suspension by diluting 167 g of cellulose with approximately 833 g water. The mixture was stirred overnight. To improve dispersion, the mixture was pretreated with a kitchen blender and a high circumferential speed disperser (IKA T25 digital ULTRA-TURRAX®) at an input energy of 500 W for 10 min. Then MFCs were obtained using a Mini DeBEE homogenizer, processing the as-prepared suspension with a 0.008-inch zirconium nozzle at 16000 psi (110 MPa) for 30 passes and subsequently a 0.005-inch diamond nozzle at 32000 psi (220 MPa) for 30 passes. The temperature of the process could reach very high due to the energy gaining from the shear forces and it was maintained at around 50-70 °C by the heat exchanger. In order to increase the degree of fibrillation, it might be necessary to repeat the procedure of homogenization several times based on needs.

The non-aqueous MFC suspension was also prepared with an extra solvent exchange step after stirring overnight, by filtering water out of the cellulose/water suspension followed by triple washing/filtering with isopropanol. The subsequent steps remained unchanged.

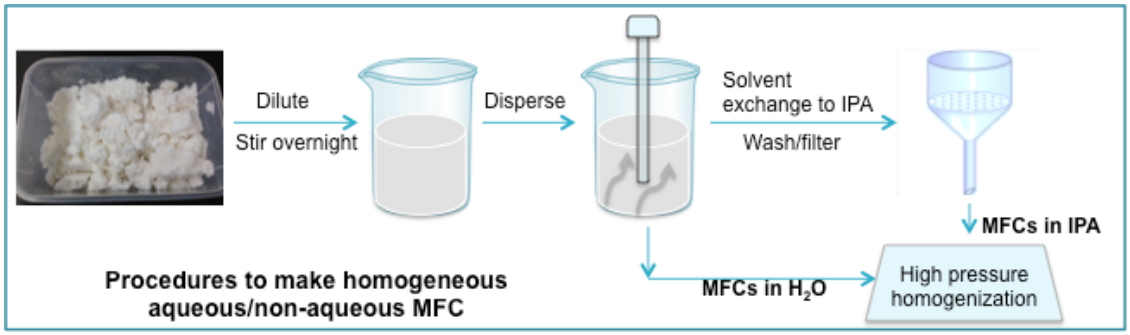

Figure 3-10 Scheme of MFCs suspension preparation

3.3 Results and Discussions

3.3.1 Titania hollow ribbons properties

Before the deposition experiment of Ti(IV) sol, both types of cellulose were observed with SEM.

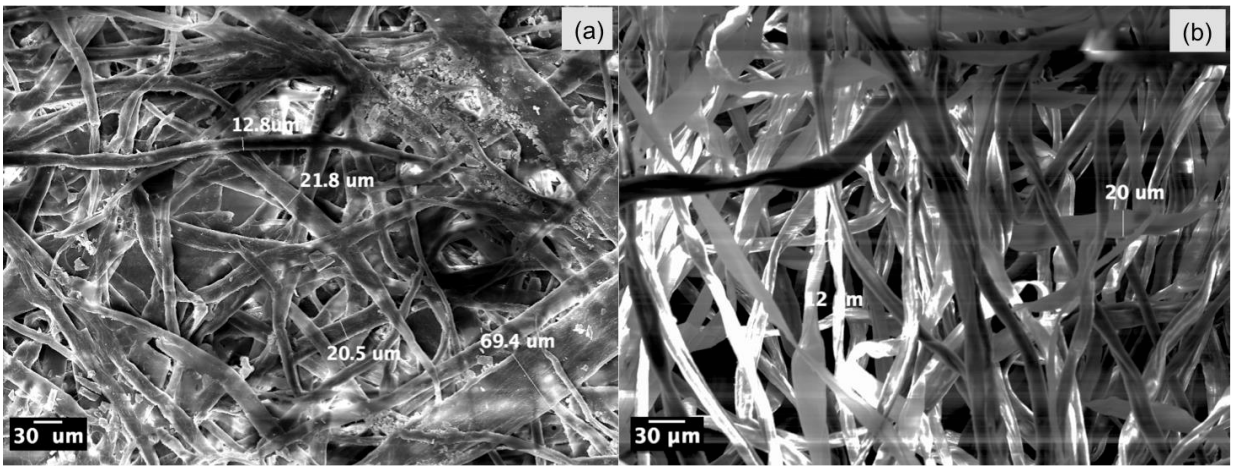

Figure 3-11 SEM images of (a) filter paper pieces, and (b) cotton rounds pieces

In Figure 3-11, the top view (a) of the filter paper was composed of fibers with various diameter, including large aggregated fiber as thick as ~70 um, and smaller fibers with a width of ~12 um. As for cotton rounds (b), the more fluffy structure made focusing more difficult than the 2D filter paper, but it generally showed the diameter of the cotton fiber is between 12 to 20 um. This is the starting point of the TiO_2 deposition and crystal formation.

The first set of experiments were conducted on cotton rounds, including aqueous liquid phase deposition methods TiF_4 deposition and AHFT-BA deposition described in Chapter 1. Results of the titania made with cotton rounds fibers and TiF_4 are shown in Figure 3-12, of which the low-magnification image presented fractured structure while a high-magnification image (b) further exposed the possibly cracked hollow ribbons (width ~ 11.8 um) derived from the deposition of TiF4. The reason for the cracking of large amount of coated hollow fibers are attributed to insufficient coating time, removal of materials through washing, or unstable scaffold built up with this type of cotton fibers. The starting cotton fibers before immersion was 0.12 g, and 0.1270 g after immersion reaction, rinsing, and vacuum oven drying. After calcination, 92.7% w.t. of the weight was removed being the degradable cellulose portion.

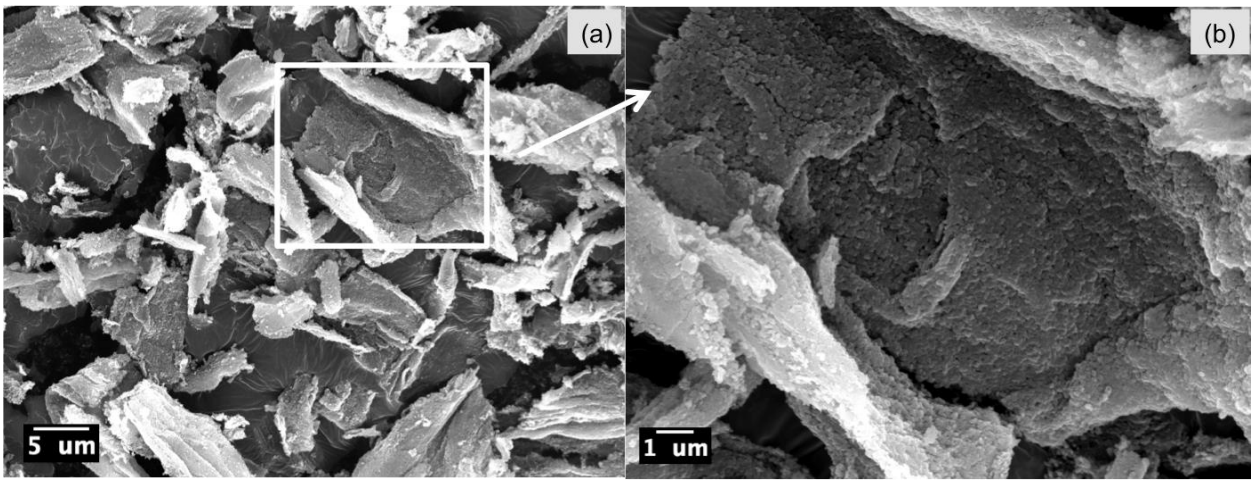

Figure 3-12 SEM images of TiO_2 made from deposition of TiF_4 on cotton rounds pieces: (a) lower magnification, and (b) higher magnification of the framed section in (a).

The AHFT-BA system deposition on cotton rounds fibers was greatly improved. As Figure 3-13 (a) shows, separate long fibers of cotton with width around 18 um were evenly coated with Ti(IV) sol. At higher magnification (b) shows the rough surface of amorphous nanoparticles of titania before high-temperature annealing.

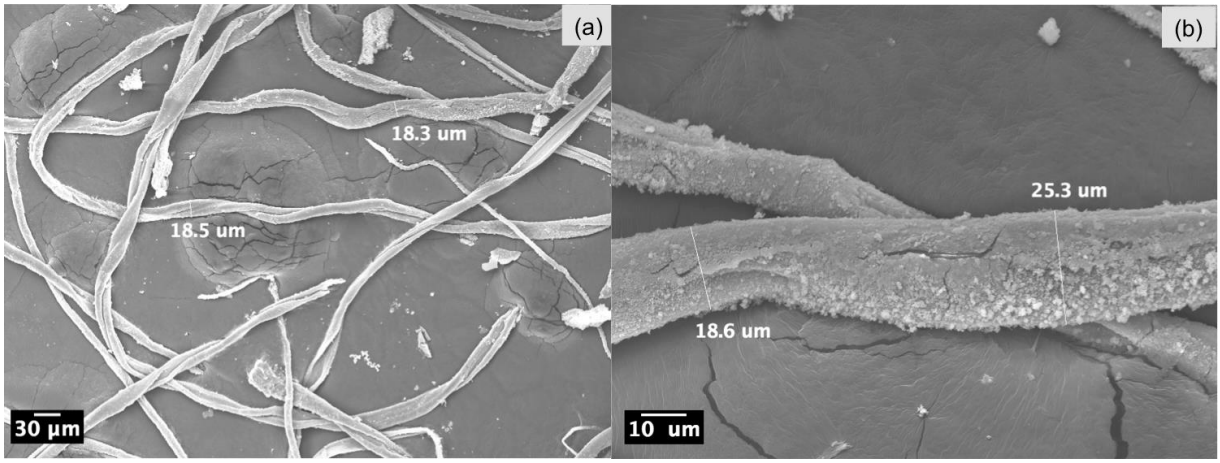

Figure 3-13 SEM images of cotton rounds coated with AHFT and BA without further calcination: (a) at lower magnification with selected dimensions (b) at higher magnification with surface features

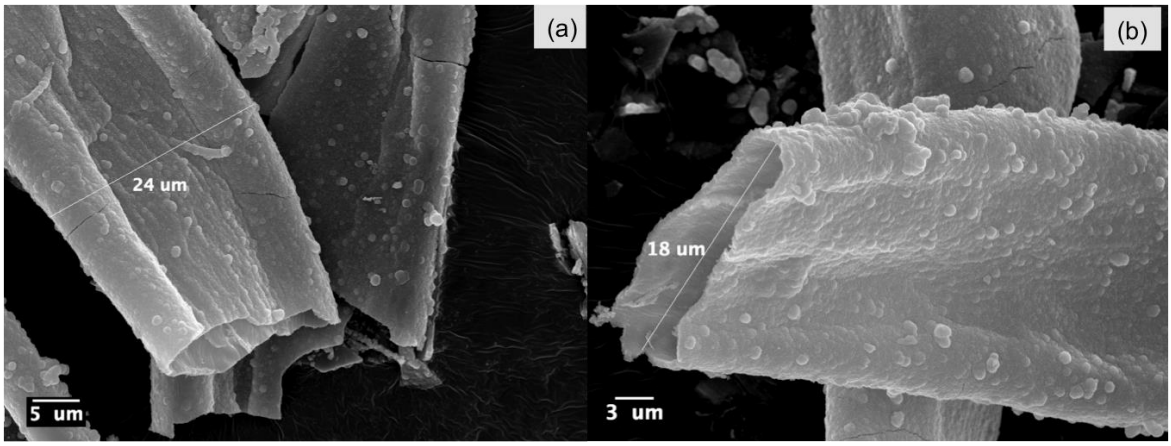

Figure 3-14 SEM images of TiO_2 made from cotton rounds coated with AHFT and BA after calcination: (a) hollow ribbon structure of as-prepared TiO_2 ; (b) at higher magnification with the cross section of hollow ribbon wall, and the rough ribbon surface.

After thermal treatment, the inner cotton fibers were removed as Figure 3-14 shows. Based on the comparison between Figure 3-13 and Figure 3-14, the width of the calcined titania hollow ribbons were similar, further confirming the duplicating effect from the cellulose. The ribbon thickness was estimated to be less than 0.5 um and mostly dependent on the reaction time. Extra particles were formed on the surface of the ribbon due to the excess Ti(IV) sol nucleation.

Similar experiments were also conducted on filter paper pieces for both TiF_4 and AHFT-BA systems. As Figure 3-15 showed below, the TiF_4 coating on filter paper resulted

in fractured TiO_2 again and very few long fiber-like TiO_2 was observed. The deposition of TiF_4 solution needs to be modified for a better TiO_2 formation and this will be discussed in future chapters. A 67.2% w.t. loss was recorded from the immersed, rinsed and dried product, compared to the original clean cotton fibers. After calcination, 91.6% w.t. mass was eliminated.

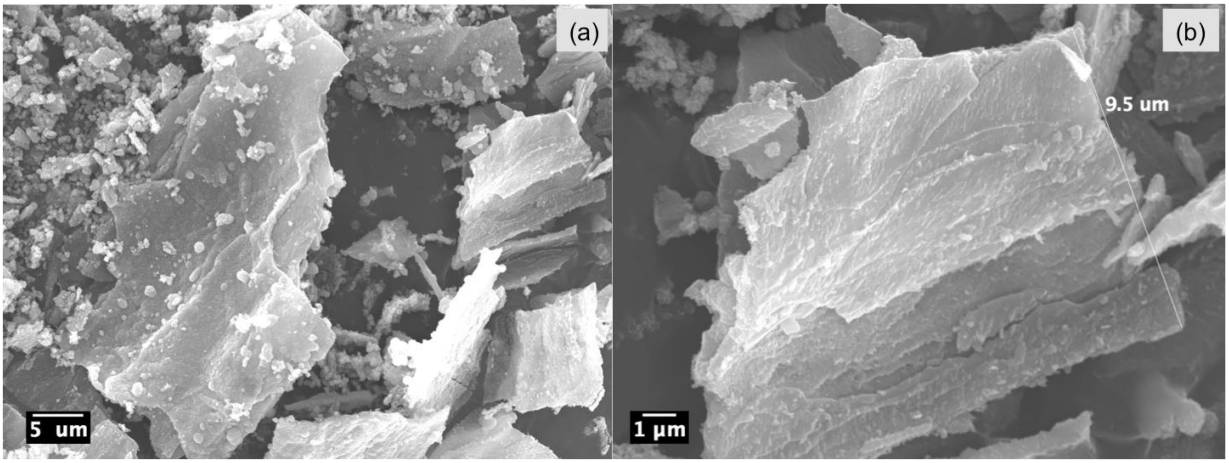

Figure 3-15 SEM images of TiO_2 made from filter paper coated with TiF_4 after calcination: (a) fractures of titania (b) surface of the as-prepared TiO_2 at higher magnification.

A more successful coating was realized on filter paper with AHFT-BA solution, as Figure 3-16 (a-d) shows. Figure 3-16 (a) and (b) show the deposition before calcination, with excess formation of amorphous particles (diameter = 1-3 um) on the fiber surface. The particles were formed randomly, due to the nucleation site activity of the fiber surface and the coating reactivity. After calcination (c), there are bunches of hollow TiO_2 tubes, and two well-formed hollow titania ribbons with diameters of around 5 um and 15 um. The surface was composed of ~200 nm nanoparticles. The original filter paper gained 83.1% w.t. after the immersion reaction (rinsed and dried in vacuum oven). After calcination, 90.1% w.t. was removed as C, O and H.

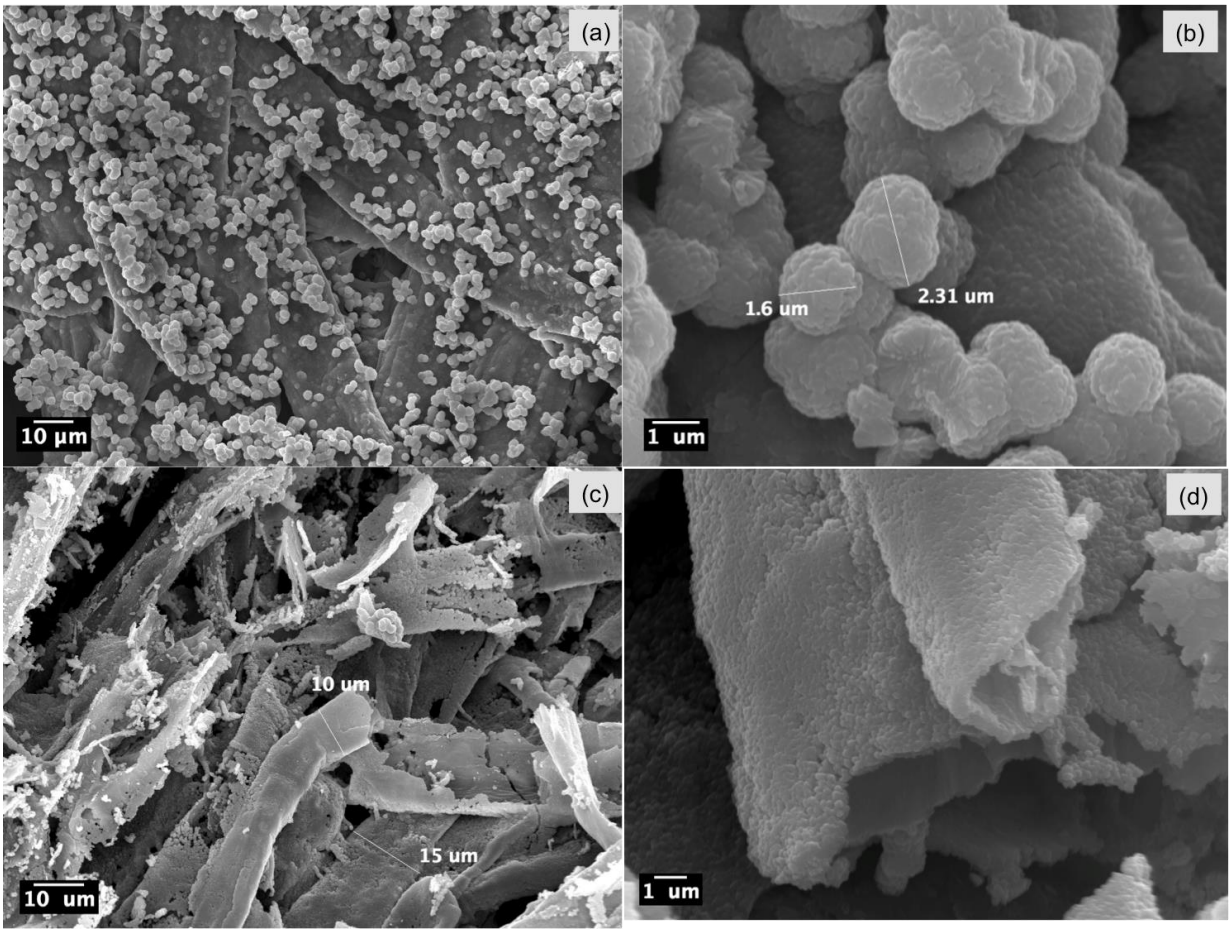

Figure 3-16 SEM images of filter paper coated with AHFT and BA: (a-b), before calcination, at low and high magnifications highlighting the fiber layout and the nucleation of amorphous TiO_2 on the surface of the preliminary coating. (c-d), after calcination, at low and high magnification demonstrating long hollow fibers and the cross section of two TiO_2 tubes.

Thermogravimetric analysis (TGA) measures the decrease in sample mass caused by the release of volatiles or devolatilization during heating, and becomes the most widely used thermoanalytical technique in solid-phase thermal decomposition filed. Different types of signals are presented from the obtained raw data:

(a) mass vs. temperature, sample mass change over the applied thermal conditions, named as TGA.

(b) –dm/dt vs. temperature, the first derivative of thermogravimetric curves over time, known as derivative thermogravimetry (DTG), which provides the maximum reaction rate.

In the 1970s, thermal decomposition of cellulose was extensively studied with DSC and the mainstream mechanism consisting of 3 steps: (1) Dehydration of the cellulose which produces anhydrocellulose, in the temperature range of 200-280 °C. The anhydrocellulose is very active, and will result in CO_2, CO, H_2O and most of the residual char. (2) Non-reacted cellulose goes through depolymerization during which levoglucosan appears as an intermediate at 280 °C. (3) The levoglucosan might volatilize into gaseous products and residual char in an endothermic way, or be trapped by the overlay of cellulose and decompose exothermally, or a combination. [18]

Others have discussed studies based on TGA analysis[19] revealing that three stages of mass loss were involved in the thermal decomposition. (1) Water evaporation: from room temperature to around 120 °C, the loss of physically adsorbed water. (2) Oxidation of cellulose: in the temperature range of 250-360 °C, the main rapid loss is due to dehydration and decarboxylation. This will yield combustible gases like aldehydes, ketones, ethers and so on. The maximum decomposition rate of cellulose shows up in this region. (3) Oxidation of carbonaceous residues: From 360 to 450 °C, the loss of carbonaceous residue.

Lots of kinetic models have been studied for the cellulose pyrolysis since the early 20th century, by performing a series of experiments under isothermal conditions at different temperatures. But no consensus has been reached in terms of issues such as the actual reaction temperature, the physical and chemical nature of the primary products, the considerations of the intermediate products, and the order of the reactions etc.[20-22]

In theory, very kinetic model's rate law obeys the classic fundamental Arrhenius rate equation:

$$k(T) = A \exp(\frac{-E_a}{RT})$$

where T is the absolute temperature, A is the frequency factor, E_a is the activation energy of the reaction, R is the universal gas constant, and k(T) is the T-dependent reaction rate constant. When the kinetics of cellulose decomposition is routinely predicated as a single reaction, the rate of the isothermal process is expressed as,

$$\frac{d\alpha}{dt} = k(T)f(\alpha) = A \exp(\frac{-E_a}{RT})f(\alpha)$$

where α is the degree of conversion;

since,

$$\frac{d\alpha}{dT} = \frac{d\alpha}{dt}\frac{dt}{dT} = \frac{k(T)}{\beta}f(\alpha) = \frac{A}{\beta}\exp(\frac{-E_a}{RT})f(\alpha)$$

where $\frac{dt}{dT} = \frac{1}{\beta}$, describes the inverse of the heating rate;

Thus, for a reaction with $(1-\alpha)$ remaining fraction of volatile material in the sample and reaction order n,

$$\frac{d\alpha}{dT} = k(T)(1-\alpha)^n$$

The cellulose pyrolysis process is still under debate with controversies till now. However, three categories could be concluded out of the various pyrolysis kinetic models, which are, single-step global reaction models, multiple-step models, and semi-global models.[21] Experimental conditions might influence the biomass reaction kinetics, such as

heating rate, particle size effects, surrounding atmosphere.[21] A higher heating rate results in lower char yields compared with lower heating rate probably because the increased heating rate allows enough time for the completion of the decomposition. As for the ambient gas atmosphere during the reaction, an oxidative environment brings out a more active degradation reactions than in the inert atmosphere, lowers the active pyrolysis temperature and boosts the combustion of chars at higher temperatures.[21] It is also found that the addition of inorganic salts has an influence on the decomposition of cellulose.[19] It will lower the temperature range for the second stage and the total heat of combustion for phosphoramidate treated cellulose [23].

For this research, although not devoted to analyzing the pyrolysis kinetics, it is important to have an adequate understanding of the basic decomposition theories so that the templating role of the cellulose will be legible and definite in further discussions.

The thermal properties of cotton round fibers and filter paper were analyzed by TGA (Figure 3-17). After losing the absorbed water content, cotton rounds began to degrade rapidly at ~350 °C, and at ~375 °C 80% w.t. of the original weight was removed. A second decomposition peak appeared at 500 °C and the material was completely removed at 525 °C. The filter paper started to degrade at ~325 °C and at ~375 °C, there was still 30% w.t. left. The second decomposition peak appeared at 475 °C, then a total degradation was reached at 500 °C.

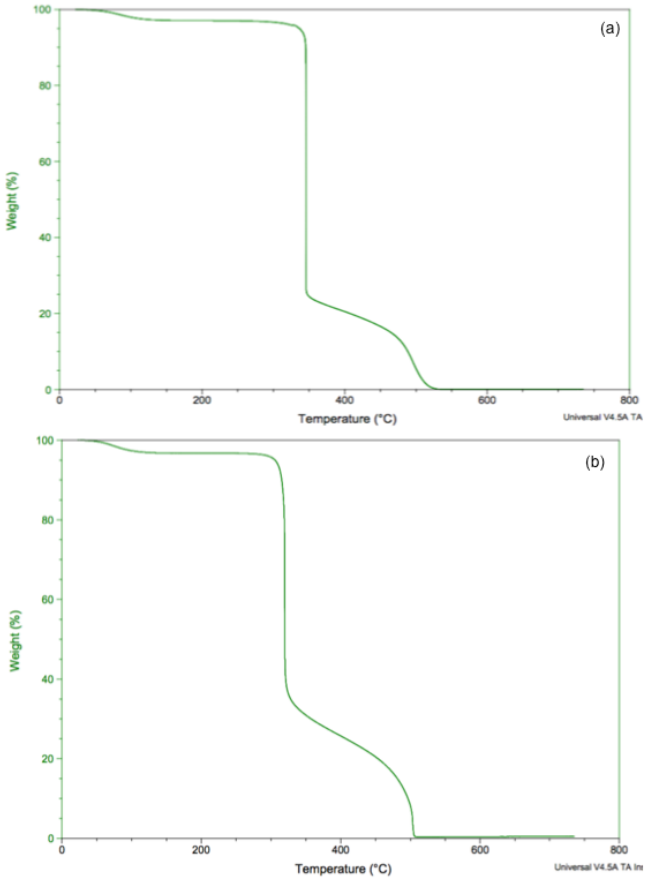

Figure 3-17 TGA of (a) cotton rounds, (b) filter paper

From the TGA of the TiO_2 coated fibers (Figure 3-18), the AHFT-BA coated cotton fibers had a rapid weight drop at 295 °C from 91.0% w.t., reached 35.3% w.t. at 500 °C, and remained 33.4% w.t. after temperature reached 600 °C. AHFT-BA coated filter paper began losing weight at 89% w.t., reached 37.6% w.t. at 500 °C, and resulted in 34.8% w.t. in the end. In addition, the TiF_4 coated filter paper had a much lower percentage of mass as 10.5% w.t. at 500 °C and 9.8% w.t. in the end. This explains the net TiO_2 amount in the dried coated cellulose, and further confirms a better deposition method as AHFT-BA compared to TiF_4.

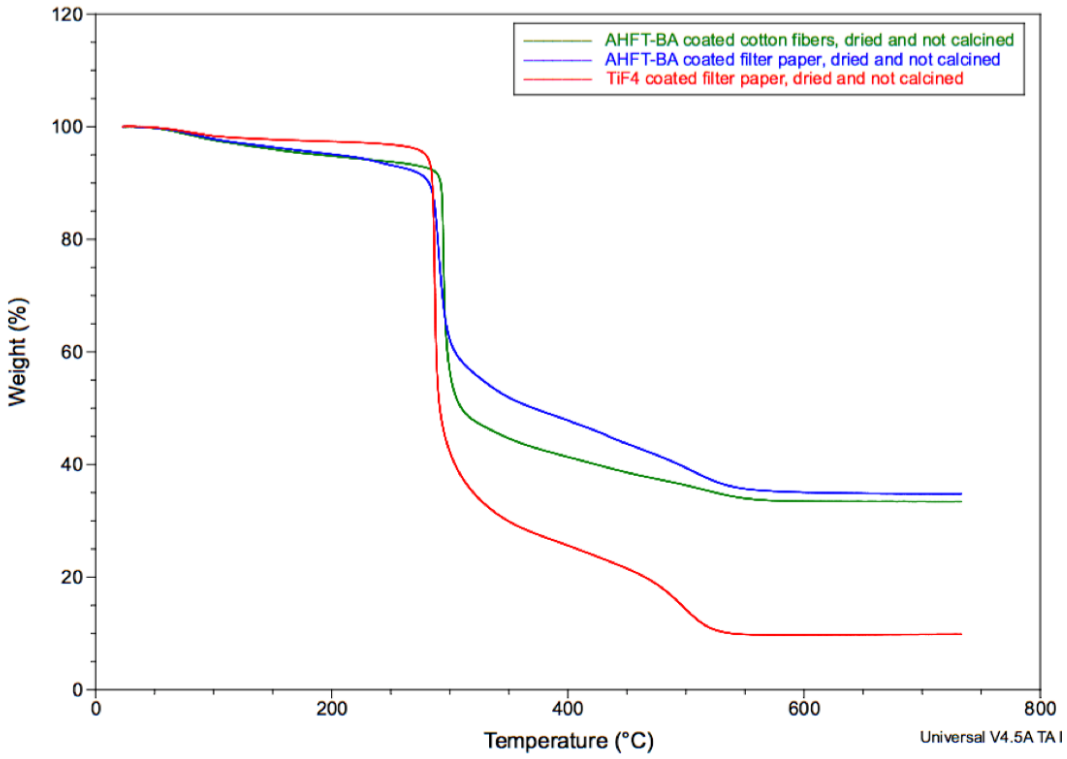

Figure 3-18 Thermal analysis through TGA on non-calcined soaked cellulose substrates including cotton round fibers and filter paper.

To understand the elemental composition of the samples before and after calcination, EDS was conducted on sets of samples. Table 3-2 listed the summarized data for cotton fibers, cotton fibers after deposition without calcination & with calcination, filter paper after deposition without calcination, and with calcination. By measuring the X-ray spectrum emitted by the solid sample resulted from the bombardment with a focused beam of electrons, EDS could obtain qualitative and quantitative analysis of the element present in the sample. Depending on the sample density and accelerating voltage of the incident beam, the analysis depth is usually 0.5-3 um, where the secondary electrons are generally formed. Cotton rounds were composed carbon and oxygen, and coated ones with AHFT-BA were still detected with carbon, possibly due to uneven thickness (< 0.5um) of the coating spot. After calcination, cellulose was removed, resulting in Ti and O, as Figure 3-19 shows.

Sharp and intense peak at 4.508 keV referred to Ti Kα, smaller peak at 4.930 keV corresponded to Ti Kβ, and peak at 0.452 keV referred to Ti Lα. The energy for O was located at 0.522 keV. Similarly, when filter paper was used as the substrate for TiO_2 deposition, C, O, Ti and N were observed, and this N Kα (0.395 keV) was likely to come from AHFT that was not rinsed off. Once the cellulose template was removed by annealing, the composition became O and Ti as well.

Table 3-2 EDS atomic percentage of C, O, Ti and other elements in TiO_2 materials

EDS data	C(% atomic)	O(% atomic)	Ti(% atomic)	N(% atomic)
Cotton rounds	73.6	26.4		
Cotton rounds coated with AHFT & BA, uncalcined	17.6	46.7	35.7	
Cotton rounds coated with AHFT & BA, calcined		58.6	41.4	
Filter paper, coated with BA & AHFT, uncalcined	16.2	57.5	20.1	6.2
Filter paper, coated with BA & AHFT, calcined		60.8	39.2	

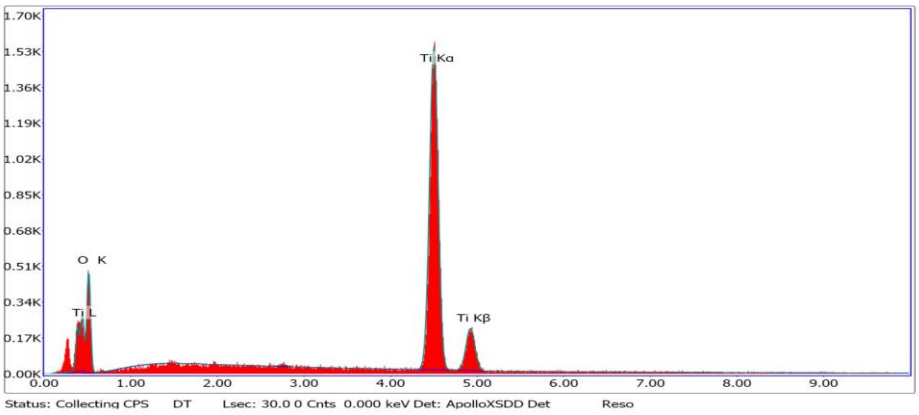

Figure 3-19 EDS spectrum of AHFT-BA coated cotton round fibers, after calcination

The Raman spectra for the calcined titania samples (Figure 3-20) reveal the major characteristic peaks of anatase TiO_2 for all samples. The 145 cm^{-1}, 199 cm^{-1}, 395 cm^{-1}, 515

cm^{-1} and 636 cm^{-1} corresponded to Eg, Eg, B1g, A1g or B1g, and Eg respectively.[24] This further confirmed the existence of TiO_2 and the successful crystallization of anatase phase with the removal of cellulose since no cellulose peaks were shown in the Raman spectra. Anatase is the most effective crystal phase for potential applications in photocatalysis and photovoltaics.

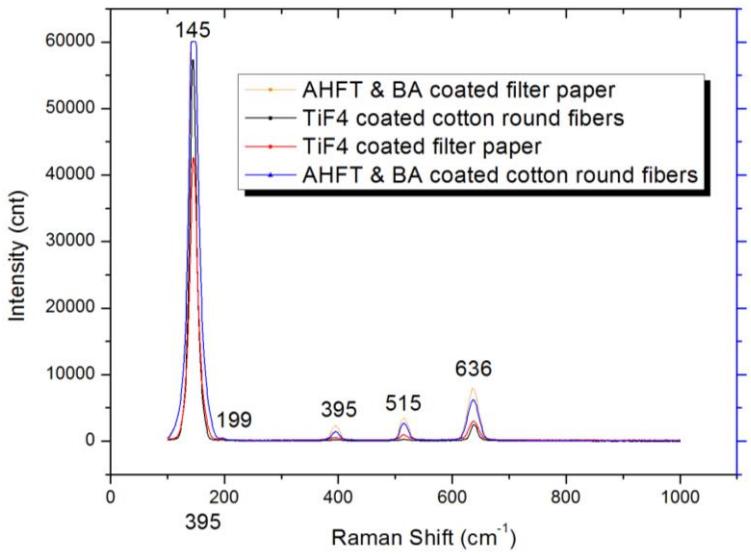

Figure 3-20 Raman spectra of TiO_2 templated from AHFT and TiF_4 systems on both cotton round fibers and filter paper

3.3.2 Homogenized MFCs characterizations and benefits

Compared to non-processed cellulose fibers, microfibrillated cellulose (MFCs) has a much higher surface area and aspect ratio, which make it a good candidate to form rigid networks.[11] A powerful physical method was developed to disintegrate cellulose materials into a viscous and shear thinning gel-like suspension.

Since the first cellulose homogenizing process in 1985,[25] the homogenizer has become a well-developed instrument applying high shear to obtain viscous MFC suspensions at low concentrations.[26] In one cycle, a cellulose slurry is pumped at high pressure and goes through a spring-loaded valve assembly, where the high pressure drop facilitates the

microfibrillation. By repeating the procedures, the resulting MFC consists of microfibrils with different levels of entanglement and disorder, increased surface area, and extensive hydrogen-bonding ability.

As mentioned above, the degree of crystallinity is an important factor of reactivity. It was shown that ratio of crystalline region to amorphous region decreased as the number of grinding passes increased from 1 to 30,[11] which could be due to the homogenization of the cellulose nanofibers under a high shear rate.

After homogenization, the original aggregated cellulose fibers were transformed into 20-60 nm wide, several micrometers long, but web-like network. This splitting process greatly increased the surface area of the fibers. SEM observation of a drop of 5 mg/mL cellulose water suspension coated and dried on a metal stub shows the web-like structure in Figure 3-21. The high-pressure homogenizer treatment of the as-received cellulose fibers help homogenize the large and aggregated fibers into reduced sizes and suspend extensively in the solvent (water or IPA). Size reduction is observed in Figure 3-21, where (a) to (c) demonstrate the effects of the homogenization process. Figure 3-21 (a) is at the stage after the kitchen blender and a high circumferential speed disperser treatments, where large aggregated bundles were visible. After 30 passes on the homogenizer, bundles of fibers were gradually removed and growing amounts of fibers were distributed evenly. At the end of homogenization (c), the cellulose fiber size was reduced to approximately 30 nm, and presented a well-dispersed MFC suspension. Homogenized MFCs are generally 30-50 nm in diameter, with length in micrometers or longer. The degree of fibrillation was increased simply by repeating the procedure of homogenization for more times. With more

energy input, the disintegration of cellulose was improved by increasing the number of the passes from 2, 6, 14, 22 to 30 times.[27]

It is important to note that the homogenized product, mainly composed of microfibrils bundles, cannot be redispersed simply by dissolving if it is dried to form microfibril agglomerates.

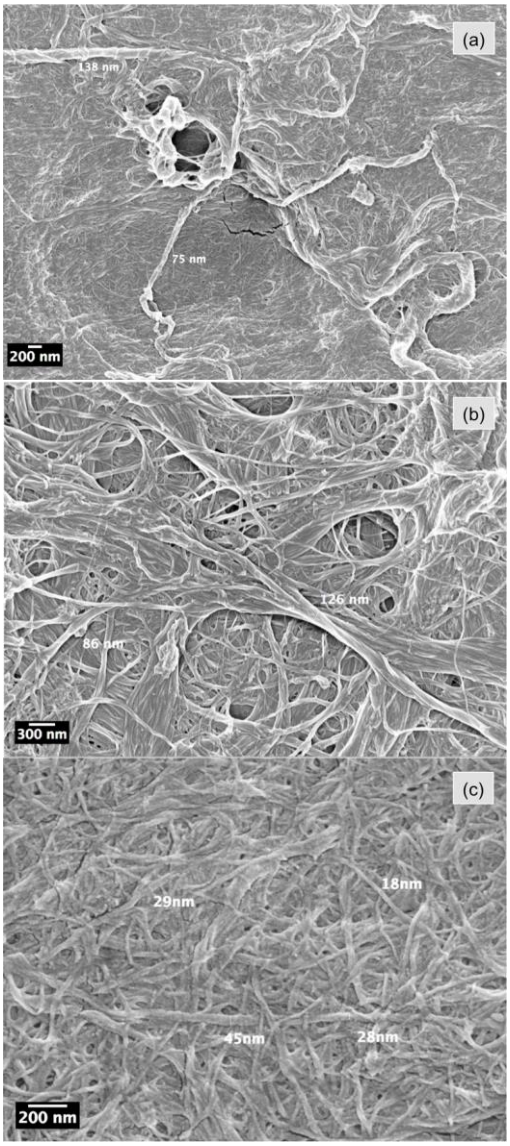

Figure 3-21 Cellulose fibers treatment effects: (a) after the kitchen blender and a high circumferential speed disperser treatments, (b) after 30 passes on the homogenizer, (c) after 60 passes on the homogenizer.

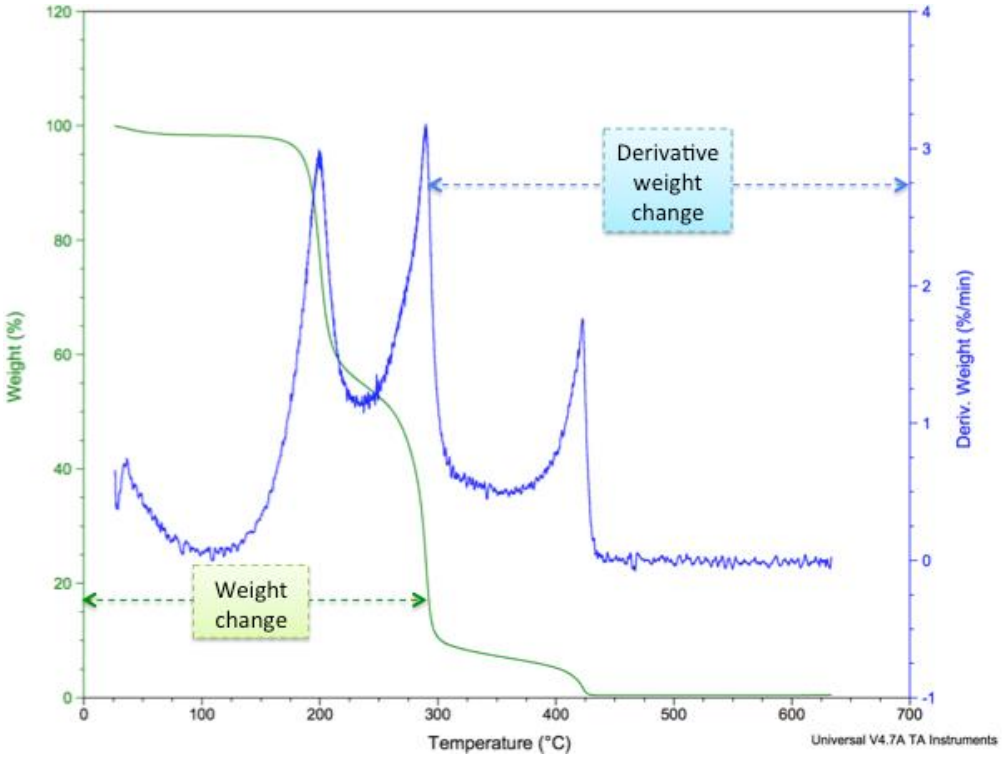

Figure 3-22 TGA of MFCs made by Celish KY100G (90 wt% in water) purchased from Daicel, with water evaporated by 12-hour vacuum oven heating. TGA was conducted in air through a high-resolution ramp program at a heating rate of 25 °C/min.

Figure 3-22 shows several stages of the heating of MFCs derived from Celish cellulose, with mass vs. temperature in green color, and DTG, in blue color. There were rapid weight losses at 200 °C, 300 °C, and 425 °C. A slight weight loss before 100 °C was due to the removal of absorbed water molecules, and then between 200 and 300 °C, the dehydration of the cellulose produced anhydrocellulose, rapidly converted to CO_2, CO, and H_2O. The remaining carbonaceous residues went through further oxidation, which matched with the last peak at 425 °C. At 430 °C, the remaining cellulose mass reached as little as 0.3% w.t.

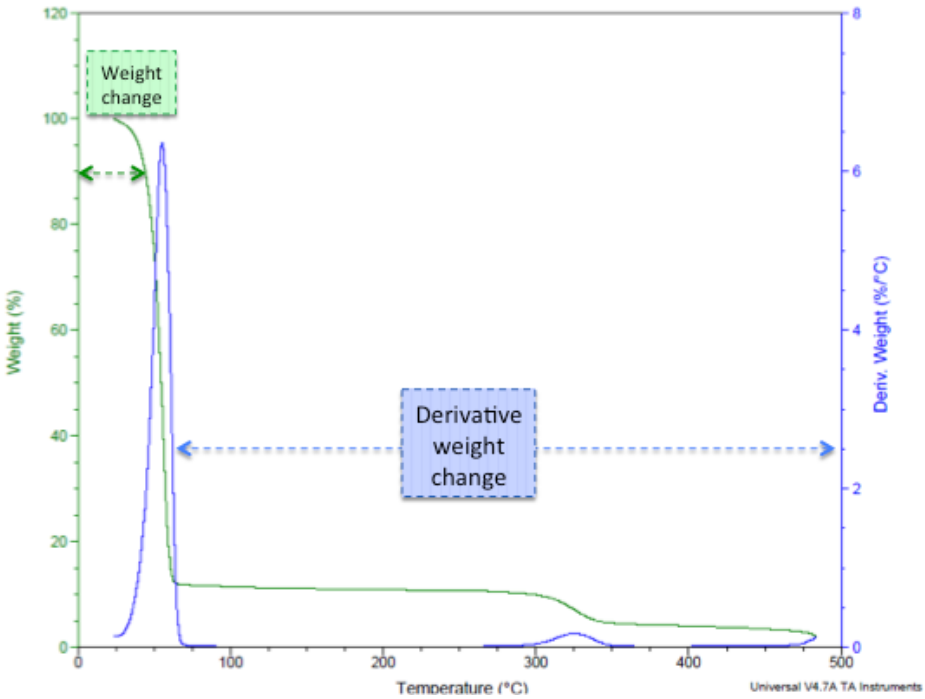

Figure 3-23 TGA of non-homogenized Celish KY100G (90% w.t. in water) purchased from Daicel, without further treatment. TGA was conducted in air through a high-resolution ramp program at a heating rate of 25 °C/min.

The first DTG peak referred to the loss of the approximately 90% w.t. water when temperature reached 62 °C as shown in Figure 3-23. Then no rapid loss was observed until it was 325 °C. In comparison with homogenized and dried MFCs in Figure 3-22, DTG peaks varied a lot. Since most of the cellulose researched with were in original forms or decreased into micro-to-millimeter dimensions, it's interesting to learn how the MFCs or CNCs react in pyrolysis process. As a matter of fact, the thermal stability of the dried MFCs decreased after homogenization and subsequent drying, besides, the char level at the end of the pyrolysis was higher than for cellulose fibers. [26] It's concluded that the formation of a higher number of contacts between the homogenized microfibrils, microfibrils bundles, and agglomerates, as a network, induces an earlier degradation.

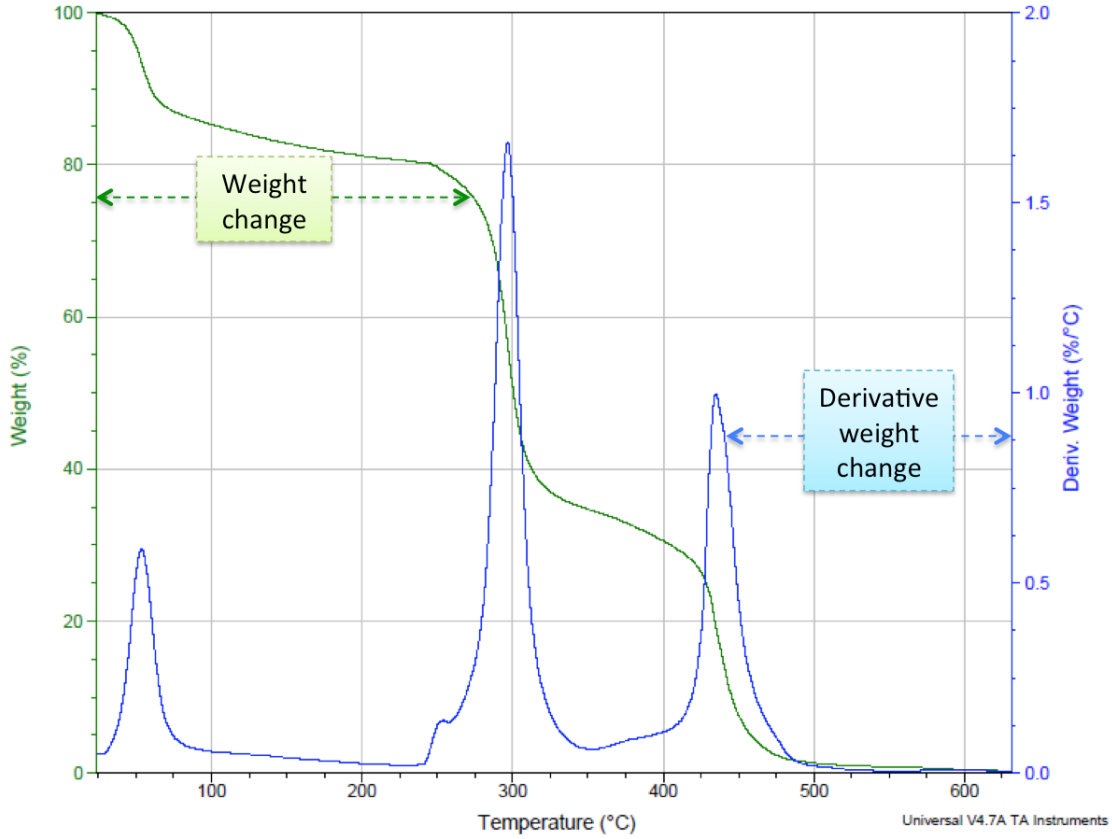

Figure 3-24 TGA of dried MFCs purchased from the University of Maine process development center with a water content of 97% w.t. To eliminate the water evaporation step during thermal analysis, sample was dried in vacuum oven overnight at 80C before the test. TGA was conducted in air through a high-resolution ramp program at a heating rate of 25 °C/min

Different types of homogenized cellulose carry different thermal stabilities. Figure 3-24 shows several stages of the calcination of MFCs, with mass vs. temperature in green color, and DTG, in blue color. Between room temperature and 100 °C, the residue free water content not removed from drying process was evaporated, giving a major peak in the derivative weight change curve. The following weight loss before the temperature reached around 200 °C was attributed to the detachment of the absorbed water on the surface of porous cellulose structure. At 300 °C, a large derivative weight change peak appears, resulting from the rapid loss of weight due to oxidation of cellulose. During this stage, dehydration and decarboxylation will produce anhydrocellulose and combustible gases like

aldehydes, ketones, ethers, and so on. From 360 °C to 450 °C, the carbonaceous residues were oxidized and resulted in CO_2, CO and H_2O. Around 0.2% w.t. char was left after heating process till 500 °C.

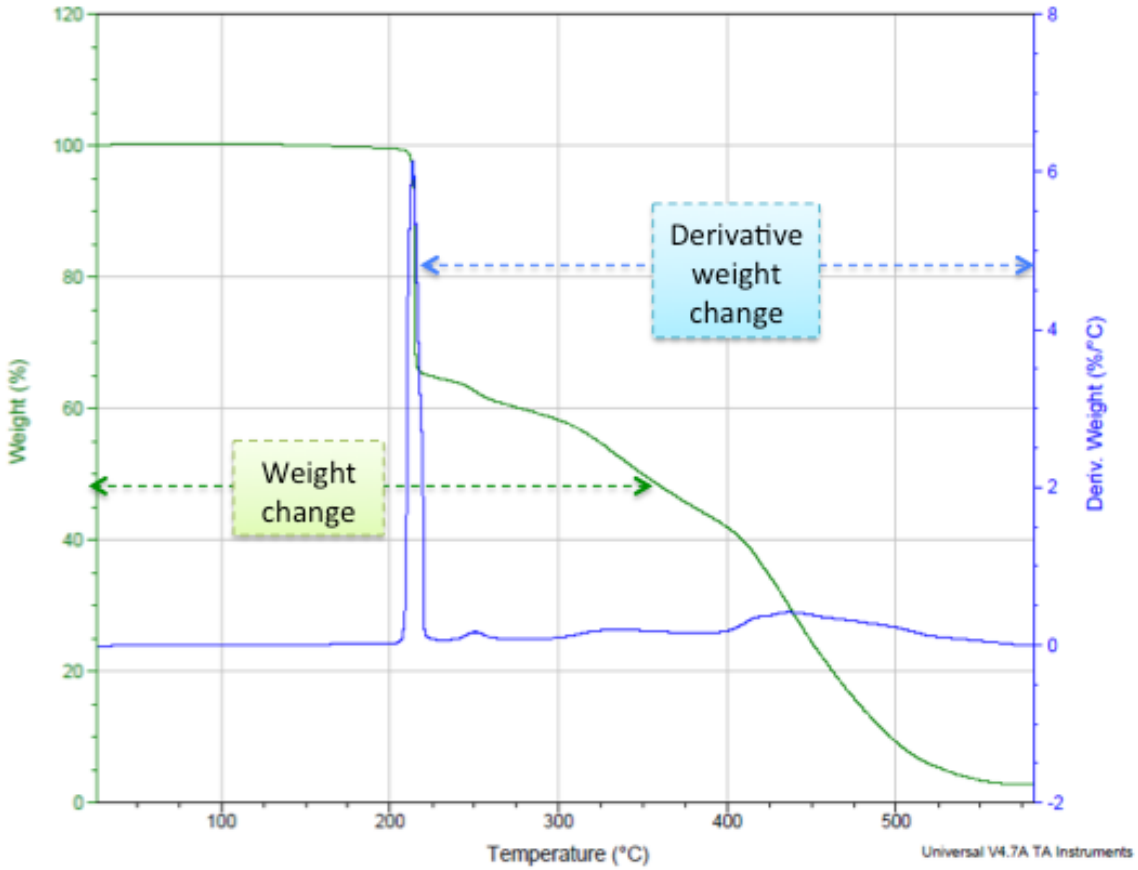

Figure 3-25 TGA of dried CNCs purchased from the University of Maine process development center with a water content of 93.8% w.t. To eliminate the water evaporation step during thermal analysis, sample was dried in vacuum oven overnight at 80C before the test. TGA was conducted in air through a high-resolution ramp program at a heating rate of 25 °C/min.

The thermal stability of CNCs is quite different compared to MFCs, the major peak of DTG appeared at ~210 °C, and then at 600 °C there was still 4% w.t. left as the residue material. Nearly 40% w.t. mass was lost in the 200-210 °C region, followed by another 55% w.t. mass loss between 210 and 600 °C. This suggest a different mechanism compared to MFCs. Due to the smaller size of CNCs compared to MFCs and original cellulose materials, the larger surface area of CNCs opens up more exposure to heat. It has also been reported

that the existence of sulfur in most CNCs due to sulfuric acid hydrolysis might influence the thermo-stability of CNCs.[28]

The real mass of cellulose in the homogenized suspension was measured by drying 20mL as-prepared suspension in vacuum oven at 100 °C for 24 hours and weighing the resulting product. The real concentration of the final cellulose suspension product was 4% w.t.

The surface area was not tested for MFCs for the following reasons: (a) A dried sample is required for BET testing conditions (b) By drying the MFCs either by vacuum oven heating, or freeze drying, aggregation would happen (c) The data collected by BET measurement couldn't represent the real surface properties of MFCs.

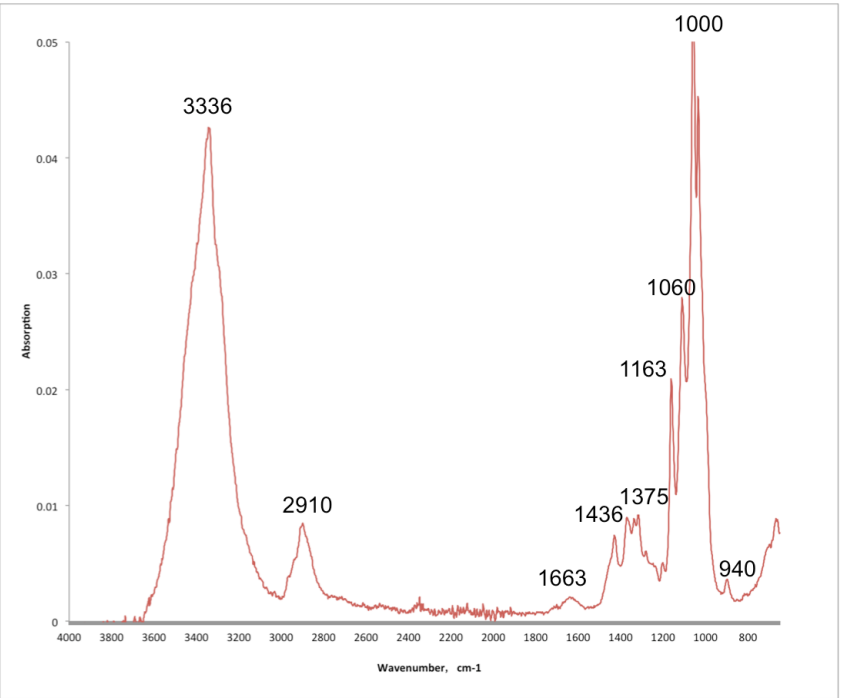

Figure 3-26 FTIR spectra of MFCs

Infra-red spectroscopy was applied to detect the vibrations of typical chemical bonds in the cellulose materials based on the absorption of infrared radiation. The spectra were

collected with 4 acquisitions in the range of 4000-400 cm^{-1} as shown in Figure 3-26. The broad peak in the 3000-3650 cm^{-1} region corresponded to O-H stretching vibrations, and smaller peak at 2910 cm^{-1} was due to C-H stretching vibrations. Peak at 1643 cm^{-1} could be explained as the adsorbed water in the cellulose. According to Lu *et al*[28], the peak at around 1436 cm^{-1} was because of the bending of the CH_2-, and all the features between 600 and 1600 cm^{-1} were from the deformation and twisting modes of the anhydroglucopyranose unit. Peaks representing C-OH stretching (1060 cm^{-1}), C-O-C bending vibrations (1163 cm^{-1}), and C-O or C-C stretching or C-OH bending (1030 cm^{-1}) were also featured in the spectra.

XPS was also applied for the surface composition study on MFCs in a 0.5% w.t. water suspension (Figure 3-27). The O 1s and C 1s ratio in atomic concentration was 40.6 %: 59.4% = 0.68, which is lower than theoretical value of 0.83 based on the formula of cellulose. This further confirmed that the homogenization didn't induce any new chemical composition onto the surface of the cellulose. The deconvolution of the C peak showed the presence of three types of carbon bonds: C-C (C_1 284.6 eV), C-O (C_2, 286.2 eV), and O-C-O (C_3, 287.8 eV).

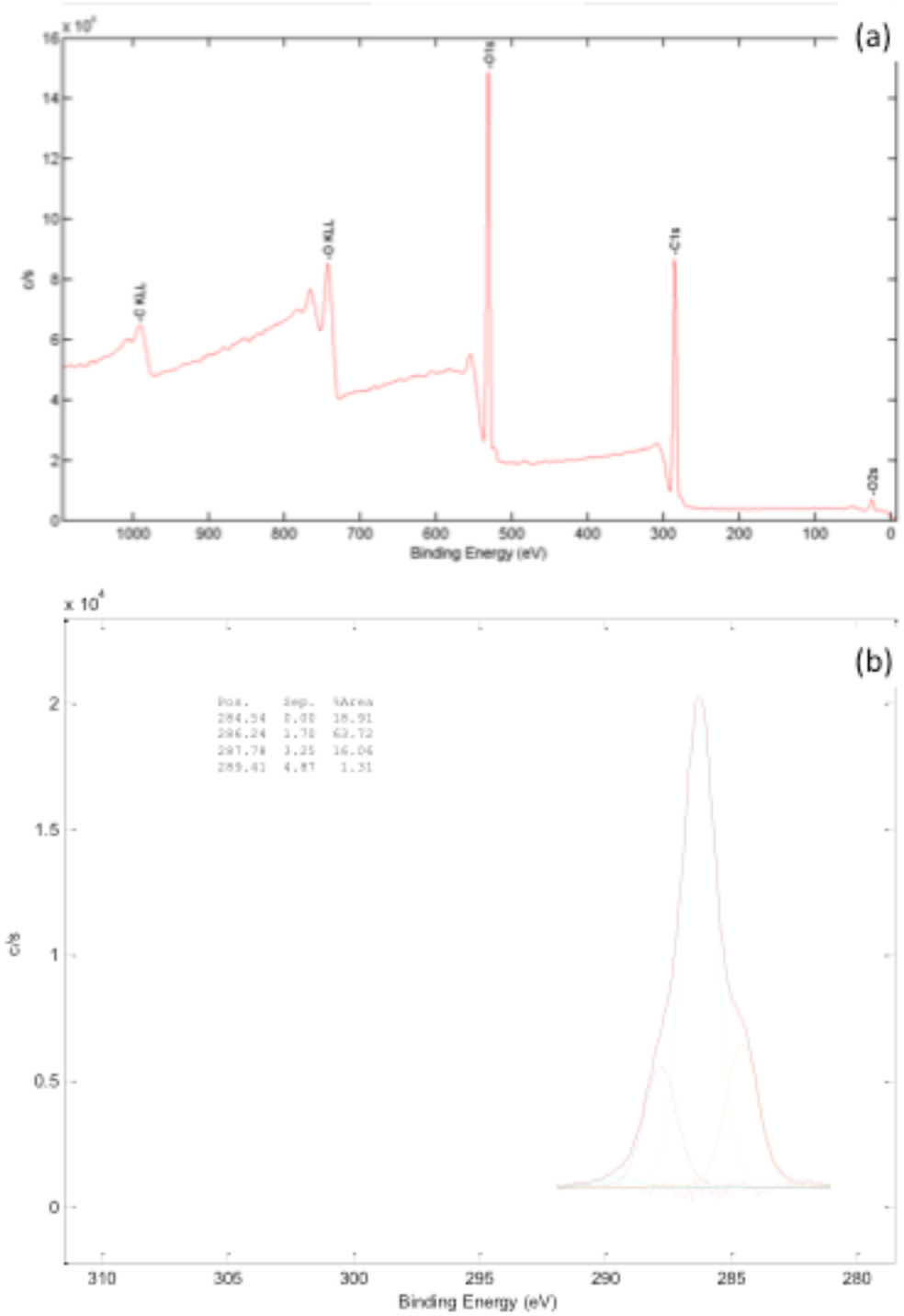

Figure 3-27 (a) XPS spectrum of MFCs ; (b) and deconvolution of its C1s peak.

3.4 Conclusions

In this chapter, a brief literature review on the benefits of using natural bio-template materials to fabricate inorganic metal oxide nanomaterials especially various titania

materials was discussed. To confirm the feasible functions of cellulose as a template for TiO_2 fabrication, cotton rounds and filter paper were utilized, in combination with two aqueous precursor systems. Tubular or hollow ribbon shaped titania in anatase phase were produced from above systems. The shape of the cellulose was successfully duplicated in the ammonium hexafluorotitanate system, while the titanium tetrafluoride system resulted in more fractured hollow structures. The hydroxyl groups of the cellulose fibers interacted with the Ti-O through H-bonding, which led to the nuclei growth on the surface and finally generated TiO_2 nanoparticles.

The high surface area, high aspect ratio, crystallinity, flexibility and a large amount of hydroxyl groups on the surface made micro/nano-fibrillated cellulose (MFCs) an even better candidate. Homogenization of cellulose was conducted and suspension of cellulose in both water and isopropanol were prepared for future precursor templating. Thermo stability analysis indicated the effects MFCs will make in the crystallization of titania. FTIR and XPS confirmed the chemical structure and surface composition of the homogenized MFCs as well.

Current tubular titania materials have been made with micro/macro size cellulose templates, which usually result in fracture of the product, further slurry making for certain applications such as dye-sensitized solar cell photoanode. The other popular titania/cellulose composite has been developed as titania supported by paper or sheets. This extra addition of cellulose might retard the pristine properties of titania in terms of electron transport, phonon harvest, and so on. In a word, a facile simple with least step deposition of titania film will be promising no matter for photoanode preparation, or the

immobilized –type photocatalytic films. In the coming chapters, the focus will be put on developing Ti (IV) precursor with MFCs templates for multiple applications.

BIBLIOGRAPHY

BIBLIOGRAPHY

(1) Ghadiri, E.; Taghavinia, N.; Zakeeruddin, S. M.; Grätzel, M.; Moser, J.-E. Enhanced Electron Collection Efficiency in Dye-Sensitized Solar Cells Based on Nanostructured TiO_2 Hollow Fibers. *Nano Lett.* **2010**, *10*, 1632–1638.

(2) Lu, Y.; Sun, Q.; Liu, T.; Yang, D.; Liu, Y.; Li, J. Fabrication, Characterization and Photocatalytic Properties of Millimeter-Long TiO_2 Fiber with Nanostructures Using Cellulose Fiber as a Template. *Journal of Alloys and Compounds* **2013**, *577*, 569–574.

(3) Qi, K.; Daoud, W. A.; Xin, J. H.; Mak, C. L.; Tang, W.; Cheung, W. P. Self-Cleaning Cotton. *J. Mater. Chem.* **2006**, *16*, 4567.

(4) Lee, Y. M.; Kim, Y. H.; Lee, J. H.; Park, J. H.; Park, N.-G.; Choe, W.-S.; Ko, M. J.; Yoo, P. J. Highly Interconnected Porous Electrodes for Dye-Sensitized Solar Cells Using Viruses as a Sacrificial Template. *Adv. Funct. Mater.* **2011**, *21*, 1160–1167.

(5) Lou, S.; Guo, X.; Fan, T.; Zhang, D. Butterflies: Inspiration for Solar Cells and Sunlight Water-Splitting Catalysts. *Energy Environ. Sci.* **2012**, *5*, 9195.

(6) Dong, Q.; Su, H.; Cao, W.; Zhang, D.; Guo, Q.; Lai, Y. Synthesis and Characterizations of Hierarchical Biomorphic Titania Oxide by a Bio-Inspired Bottom-Up Assembly Solution Technique. *Journal of Solid State Chemistry* **2007**, *180*, 949–955.

(7) Nomura, T.; Morimoto, Y.; Ishikawa, M.; Tokumoto, H.; Konishi, Y. Synthesis of Hollow Silica Microparticles From Bacterial Templates. *Advanced Powder Technology* **2010**, *21*, 218–222.

(8) Hall, S. R.; Swinerd, V. M.; Newby, F. N.; Collins, A. M.; Mann, S. Fabrication of Porous Titania (Brookite) Microparticles with Complex Morphology by Sol-Gel Replication of Pollen Grains. *Chem. Mater.* **2006**, *18*, 598–600.

(9) Varshney, V. K.; Naithani, S. Chemical Functionalization of Cellulose Derived From Nonconventional Sources. In *Cellulose Fibers: Bio- and Nano-Polymer Composites*; Springer Berlin Heidelberg: Berlin, Heidelberg, 2011; pp. 43–60.

(10) Habibi, Y.; Lucia, L. A.; Rojas, O. J. Cellulose Nanocrystals: Chemistry, Self-Assembly, and Applications. *Chem. Rev.* **2010**, *110*, 3479–3500.

(11) Lavoine, N.; Desloges, I.; Dufresne, A.; Bras, J. Microfibrillated Cellulose - Its Barrier Properties and Applications in Cellulosic Materials: a Review. *Carbohydrate Polymers* **2012**, *{90}*, {735–764}.

(12) Chen, W.; Yu, H.; Liu, Y. Preparation of Millimeter-Long Cellulose I Nanofibers

with Diameters of 30–80 Nm From Bamboo Fibers. *Carbohydrate Polymers* **2011**, *86*, 453–461.

(13) Siró, I.; Plackett, D. Microfibrillated Cellulose and New Nanocomposite Materials: a Review. *Cellulose* **2010**, *17*, 459–494.

(14) Xu, C.; Zhu, S.; Xing, C.; Li, D.; Zhu, N.; Zhou, H. Isolation and Properties of Cellulose Nanofibrils From Coconut Palm Petioles by Different Mechanical Process. *PLOS ONE* **2015**, *{10}*.

(15) Chinga-Carrasco, G. Cellulose Fibres, Nanofibrils and Microfibrils: the Morphological Sequence of MFC Components From a Plant Physiology and Fibre Technology Point of View. *Nanoscale Res Lett* **2011**, *6*, 417.

(16) Sun, D.; Yang, J.; Wang, X. Bacterial Cellulose/TiO_2 Hybrid Nanofibers Prepared by the Surface Hydrolysis Method with Molecular Precision. *Nanoscale* **2010**, *2*, 287–292.

(17) Heterogeneous Nanotubular Anatase/Rutile Titania Composite Derived From Natural Cellulose Substance and Its Photocatalytic Property. **2013**, *15*, 5586–5590.

(18) Arseneau, D. F. Competitive Reactions in the Thermal Decomposition of Cellulose. *Canadian Journal of Chemistry* **2011**, *49*, 632–638.

(19) Rantuch, P.; Chrebet, T. Thermal Decomposition of Cellulose Insulation. *Cellulose Chemistry and Technology* **2014**, *48*, 461–467.

(20) Burnham, A. K.; Zhou, X.; Broadbelt, L. J. Critical Review of the Global Chemical Kinetics of Cellulose Thermal Decomposition. *Energy Fuels* **2015**, *29*, 2906–2918.

(21) White, J. E.; Catallo, W. J.; Legendre, B. L. Biomass Pyrolysis Kinetics: a Comparative Critical Review with Relevant Agricultural Residue Case Studies. *Journal of Analytical and Applied Pyrolysis* **2011**, *91*, 1–33.

(22) Lédé, J. Cellulose Pyrolysis Kinetics: an Historical Review on the Existence and Role of Intermediate Active Cellulose. *Journal of Analytical and Applied Pyrolysis* **2012**, *94*, 17–32.

(23) Gaan, S.; Rupper, P.; Salimova, V.; Heuberger, M.; Rabe, S.; Vogel, F. Thermal Decomposition and Burning Behavior of Cellulose Treated with Ethyl Ester Phosphoramidates: Effect of Alkyl Substituent on Nitrogen Atom. *Polymer Degradation and Stability* **2009**, *94*, 1125–1134.

(24) Frank, O.; Zukalova, M.; Laskova, B.; Kürti, J.; Koltai, J.; Kavan, L. Raman Spectra of Titanium Dioxide (Anatase, Rutile) with Identified Oxygen Isotopes (16, 17,

18). *Physical Chemistry Chemical Physics* **2012**, *14*, 14567–14572.

(25) Turbak, A. F.; Snyder, F. W.; Sandberg, K. R. Micro-Fibrillated Cellulose and Process for Producing It.

(26) QuiEvy, N.; Jacquet, N.; Sclavons, M.; Deroanne, C.; Paquot, M.; Devaux, J. Influence of Homogenization and Drying on the Thermal Stability of Microfibrillated Cellulose. *Polymer Degradation and Stability* **2010**, *95*, 306–314.

(27) Siqueira, G.; Bras, J.; Dufresne, A. Cellulosic Bionanocomposites: a Review of Preparation, Properties and Applications. *POLYMERS* **2010**, *{2}*, {728–765}.

(28) Lu, P.; Hsieh, Y.-L. Preparation and Properties of Cellulose Nanocrystals: Rods, Spheres, and Network. *Carbohydrate Polymers* **2010**, *82*, 329–336.

4 Synthesis of Porous Web-structured Titania with Micro/nano-fibrillated Cellulose as Templates by Sol-Gel Method

4.1 Background

4.1.1 Utilizing nano-scale cellulose for inorganic materials design

As introduced in Chapter 3, micro and nano-scale cellulose are superior among the large cellulose family, due to their much higher surface area and aspect ratio, cost-effective price and environmentally friendly properties, adequate surface hydroxyl groups for chemical bonding and abrupt decomposition behavior with heat treatment. Traditionally, cellulose fibers in the range of 2-10 um in diameter are usually used as a template at the reaction stage, then either through thermal removal and separation, or pre-separation and annealing, the inorganic products are left as random distributed structures, which requires further paste forming for thin film coating. Emerging research has focused on utilizing micro/nano-scale cellulose for nano-sized metal particles,[1] porous metal oxide materials,[2] nanocubic TiO_2,[3] and porous titania scaffolds.[4]

Previously, different nano/micro-cellulose types and Ti precursors were combined, and the resulting morphologies and porosity were different as well. For instance, Shin *et al* [2] used lab-made cellulose crystals with width of 5-10 nm and length of 150-200 nm to form a dried free-standing film, coated with Tyzoer-LA 50% solution, followed by 500 °C calcination. The TiO_2 materials went through severe shrinkage of the cellulose film, but still, with adequate surface area (170-200 m^2) promising in catalysis applications. Zhou *et al* [3] took advantage of the morphology-inducing effect of nano-scale cellulose, to create new

nanocube structures. It was indicated that the cellulose nanocrystals influenced the nucleation and growth of TiO_2, as well as served as a hydrophilic polymer chain coordinate agent. They might promoted favoring of some certain facets of TiO_2 particles and induced the nanocube shape, besides, stabilizing the whole system and preventing aggregation. Ivanova *et al*.,[4] chose a complicated procedure to assemble pre-synthesized crystal anatase particles into the nanocrystal cellulose templated titania scaffold. By varying the weight percentage of the preformed TiO_2 particles, the crystallinity of the films could be tuned without changing annealing temperature or losing surface area and porosity.

The porous photocatalysts discussed in Chapter 2 are in powder form templated from calcium carbonate. Although efficient, in practice, the reclamation of used powder-form photocatalysts is difficult due to their small sizes. A further separation by centrifugation or micropore-sized filtering will be energy-consuming and disobey the initial idea of economical usage of phonon energy. Thus photocatalysts on film is an optimized concept since there is no need for separation. Eliminating the separation steps of the previous methods will simplify processing. A thin film catalyst eliminates the separation procedure in pollutant treatment when using powder catalysts. When well-dispersed nano cellulose fiber suspension is applied as templates in a controlled sol-gel approach, the precursor will become thick, homogeneous, and beneficial to thin film coating.

Thus we propose a novel method to make immobilized titania thin films with transparency, porosity, and photocatalytic activity by templating with nano-sized cellulose fibers.

4.1.2 Controlled hydrolysis in a sol-gel process for MFCs templating

Chapter 1 has discussed the theory of sol-gel method to synthesize metal oxide materials, and the specialty of Titanium precursors as transition metal source. Sol-gel derived materials can be prepared by tailoring parameters with high surface area, controlled porosity, and desired electric and optical properties. A controlled hydrolysis is crucial for manipulation of materials size, morphology, and chemical properties. Chapter 2 described a successful method to prepare porous TiO_2 with $CaCO_3$ templating in a titanium tetraisopropoxide-valeric acid based sol gel environment, which utilized strong chelating ligands of valeric acid for occupation of the coordination sites of the alkoxide to lower hydrolysis rates. Chapter 3 illustrated how cellulose fibers worked as soft templates for inorganic materials fabrication in hydrolytic media. To further the exploration of cellulose templating, the combination of much smaller cellulose MFCs and a hydrolysis-controlled sol-gel process will be discussed in this chapter.

Micro-fibrillated Cellulose (MFC) is made by a homogenization process, at high shear, yielding microfibrils with a diameter range of 10-40 nm, a length of several tens of micrometers, and a web-like structure.[5] Different from the other cellulose fibers discussed earlier, MFCs applied in this investigation have smaller diameters and higher aspect ratios. The work here will not only give insights on how the type of cellulose influences the metal oxide deposition, but offers wide applications in photocatalysis, photoelectric, and inorganic/organic hybrid from *in-situ* film deposition.

MFCs combined with the titanium precursor in modified sol-gel systems will result in encapsulation of the MFCs in the growing direction of the TiO_2 crystalline nanoparticles.

After calcination, the MFC will cleanly decompose resulting in the formation of micro/nano channels in the TiO_2 nanoporous film as Figure 4-1 shows. The benefits are expected to be a more ordered interconnection and less aggregation with nano/micro channels.

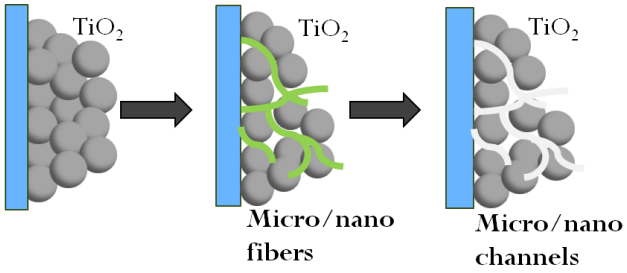

Figure 4-1 Scheme of applying MFCs as a template for porous TiO_2 network synthesis

4.2 Experimental

4.2.1 Materials and equipment

Materials:

All chemicals were used without pre-treatments unless noted. MFCs in isopropanol (IPA) were processed by Mini DeBEE ultrahigh-pressure homogenizer as Chapter 3 described. Titanium(IV) isopropoxide (≥ 97%), valeric acid (≥ 99%), polyethylene glycol (PEG, Mw=20000), polyvinylidene fluoride (PVDF, Mw=534,000), methyl orange (≥ 85% dye content, certified by Biological Stain Commision), ethanol (≥ 99.5%, A.C.S. reagent), 2-propanol (A.C.S. grade, ≥ 99.5%) were purchased from Sigma Aldrich. Plain, pre-cleaned micro glass slides were purchased from VWR International, in a size of 1 inch by 3 inches, with a thickness of 1.2 mm.

Equipment and Characterizations:

(1) The structures of the cellulose (MFCs) templates and titania porous thin films were characterized by scanning electron microscopy (Carl Zeiss Auriga CrossBeam SEM-FIB).

Samples were prepared by drying and gold or tungsten coating before being loaded into the SEM chamber. EDAX™ EDS Analysis System for SEM – X-ray Microanalysis was applied together with SEM characterization for element analysis on films before and after calcination. When cross-sectional views were necessary, a focused ion beam (FIB) was used to mill surfaces of the materials.

(2) The transmission electron microscopy (TEM) images, high-resolution transmission electron microscopy (HRTEM) images, and selected-area electron diffraction (SAED) patterns were taken on a JEOL 2200FS equipment. TiO_2 films were scratched off from glass substrates and then dispersed in ethanol by bath sonication for 0.5 h. The ethanol/TiO_2 suspension was dropped and dried on a carbon-coated 400 mesh copper grid overnight prior to TEM analysis. Under HRTEM mode, fast Fourier transfer (FFT) patterns were utilized to optimize image quality with DigitalMicrograph (DM) software.

(3) A single wafer spin processor (WS-400A-6NPP/LITE) was purchased from Laurell Technologies Corp and used for film coating. Part of the doctor blade method was completed by a manual Scotch tape method with a clean sharp razor blade, while part of the doctor blade used the MSK-AFA-III compact tape casting coater with vacuum chuck. This doctor blade machine has an adjustable micrometer film applicator (thickness 0.01-3.5 mm, or fixed thickness at 5 um, 10 um, 15 um and 20 um) with an 100-mm width, as well as a dryer cover that heats up to 100 °C.

(4) A UV-Vis spectrophotometer (Perkin Elmer Lambda 900 UV Spectrometer) was applied for TiO_2 films absorption and transmission characterizations. The UV-Vis absorption spectra of the TiO_2 films were recorded in the range of wavelength 300-800 nm.

A diffuse reflectance spectroscopy (DRS) was utilized to analyze the degradation of methyl orange on the surface of the titania films.

Reflectance is the base quantity characterizing the process of reflection, and it's defined as the ratio of the reflected radiant flux to the incident radiant flux. One of the important factors that affects the diffuse reflectance spectra of a sample is the particle size for powered samples and surface properties.[6] When the diameter of the particles is between the size of the beam cross-section and the light wavelength, diffraction will occur. Part of the incident light goes at all angles back, so all the reflection, refraction, diffraction, and absorption by particles are called diffuse reflection. Theoretically, an ideal diffuse reflection follows Lambert Cosine Law, which states that the remitted radiation per unit surface and unit solid angle is proportional to the cosine of the angle I of the incident light and the cosine of the angle of observation e. If the particle size is smaller than the wavelength, the contributions of reflection, refraction, and diffraction of the remitted radiation flux are comparable and impossible to separate. Thus this is called scattering. There are a few theories to interpret single particle scattering, however, when the distance between particles is too small, multiple scattering becomes dominant. This is primarily a qualitative technique with limited quantitative applications.

An integrating sphere attachment was used for the diffuse reflectance measurements to establish the optical band gap and the reflection/transition before and after photocatalytic dye degradation. The TiO_2 films were placed at the entrance port of the integrating sphere and measured in the 250-800 nm wavelength range.

(5) Fourier transform infrared (FTIR) absorption spectra were collected with Perkin Elmer 2000 Spectrum One FT-IR spectrometer at room temperature. KBr Pellets were prepared by Carver Laboratory press (model 2518) with ground and pre-dried KBr powder. For liquid samples, a drop of solution was cast between two pellets forming a sandwich structure with the excess liquid squeezed and wiped off. For solid samples, KBr powder was mixed with samples with a sample weight ratio of ~ 0.2% w.t. The spectra of the composites were scanned from 4000 to 400 cm^{-1}.

(6) A LabRAM ARAMIS laser Raman spectrometer (Horiba Scientific) with 532 nm 50 mW DPSS laser was used to inspect sample crystal phases as well. All the samples were tested as is with a 50X objective lens. The gratings used in this work is 1800 gr/mm and results in a spectral resolution of about 1.5 m^{-1}. The laser power at the sample ranged in 1-3 mW, and the 1/e laser spot size was about 2 μm at the sample. The crystallographic structures of the solid samples were also determined with XRD, Bruker Davinci Diffractometer. Dry powders could be deposited into the hollow space of a flat plate sample holder. Thin films were tested with minimal preparations.

(7) Thermogravimetric analysis (TA instruments Q500) used a high-resolution ramp of 25 °C/min to ~800 °C in air or nitrogen was conducted on TiO_2 samples. Surface area and pore size data was collected with Brunauer–Emmett–Teller (BET) Micromeretics ASAP 2020. As for thin film samples, films were scratched off and collected for analysis. To further remove moisture and impurities, samples were degassed at 150 °C for > 4 hours under vacuum.

(8) X-ray photoelectron spectroscopy (XPS) was using a Perkin Elmer Phi 5400. The Kα line of Mg (1254 eV) X-ray source with a beam voltage of 15 kV and current of 20 mA was the excitation source. The survey spectra scan were acquired with a pass energy 187.85 eV, and a 1 eV step size. For detailed C 1s or O 1s high resolution spectra, a pass energy of 29.35 eV and step size 0.1 eV were used. Chamber vacuum was maintained below 1×10^{-7} Torr (1.33×10^{-5} Pa). The sample to be tested was mounted onto the sample holder with double-sided copper tape, and as for powder form samples, a thin but dense layer of powder was spread on the tape with excess removed. After the measurement, data processing was performed by MultiPak V8.0. If not mentioned, the spectra have been resolved into chemically shifted components by a non-linear least squares procedure.

(9) Photocatalytic reactions were conducted with a RC-500 Xenon UV lamp (Xenon Corp., Wobrun, WA) that has 300W power, 120Hz frequency and a 5-inch linear bulb shape. The lamp was equipped with aluminum reflectors and fused quartz windows to provide optimum transmission of UV radiation. The lamp housing was made of metal, and a forced air convection removed the generated heat. The pulsed xenon arc lamp has a continuous radiation spectrum as shown in Figure 2-8. Top right image also illustrates that the active time span of each pulse is 100 us, while the interval rest time is 8.3 ms. The range of active UV wavelength lies between 230 and 360 nm. Applying a Pyrex glass cover as a filter will remove ultraviolet wavelength region beneath 290 nm.

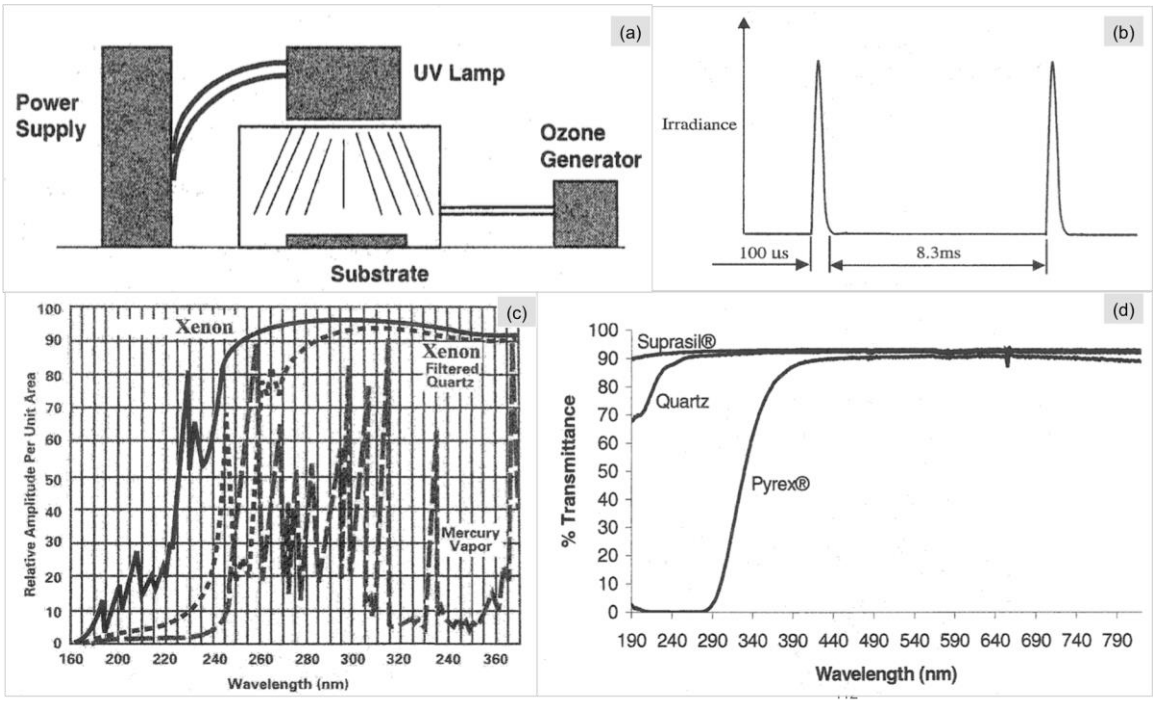

Figure 4-2 (a): the scheme of the UV lamp system (Ozone was not applied in this work). (b): the time schedule of the pulsed wave. (c): wavelength range of the outputs from the pulsed xenon UV lamps. (d): UV transmittance of Surasil, quartz, and Pyrex glass filters[source: Xenon Corp.

(10) A HIMONT Plasma Science PS 0500 Plasma Surface Treatment System was used to clean the glass substrates for ~0.5 h. The oxygen pressure was 0.270 Torr and the power was 300 W.

4.2.2 Synthesis of a porous TiO_2 network as thin film

In order to moderate the hydrolysis and precipitation rates during the sol-gel reactions, valeric acid was used as a chelating agent for the non-aqueous environment. Valeric acid (v-acid) was added to titanium isopropoxide (TTIP) followed by water as shown in Figure 4-3, The atomic ratio of v-acid: water: TTIP is 9: 1.5: 1 respectively.[7] The mixture was vigorously stirred in capped vials at room temperature for 1 h. Then the as-prepared titanium valerate was combined with MFC/isopropanol suspension at a ratio of 1: 1 and kept in a 50 °C oil bath for 14 h. The mixture turned from a colorless, transparent solution to cloudy.

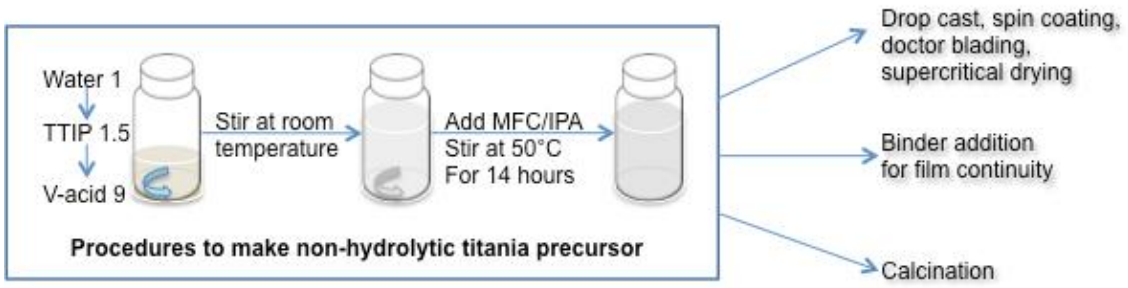

Figure 4-3 Scheme of MFCs-templating slow sol-gel method

Titania films were fabricated by drop-casting onto a glass substrate. Spin-coating was attempted with different amounts of precursor solution, rotating rates and times, however, the existence of cellulose fibers made it difficult for a uniform film formation, even with multi-layer spinning. Binders, PEG (10% w.t.) or PVDF (10% w.t.), were added into the Ti/cellulose precursor to reach a smooth slurry texture for spin or doctor blade coating as well.

For photocatalytic films, the precursors were made with a modified ratio between Ti(IV) and cellulose, to improve the TiO_2 content and activity of the films. Three different ratios were tested as titanium valerate: MFCs (in isopropanol)= 2: 1, 4: 1, and 8: 1, then the mixtures were kept in a 50 °C oil bath for more than 12 h as well. Specifically, a 67 mL MFC/IPA suspension was used as a base volume, and 0.605, 1.21, 2.42 mL TTIP were used with 1.98, 3.95, 7.90 mL valeric acid respectively for the increasing ratios.

Films were made with 0.13 mL precursor drop cast for same thickness, dried in dry room hood for 1 hour to avoid moisture, followed by step-wise annealing at 200 °C, 300 °C, 350 °C, 450 °C.

4.2.3 Measurements of photocatalytic performance of porous titania thin films

The photocatalytic performance was evaluated by monitoring the degradation of methyl orange (MO) aqueous dye solution with the illumination of Xenon RC500 lamp. MO solution with a concentration of 5×10^{-4} M was prepared and kept in a capped glass container. Diffuse Reflectance Spectroscopy (DRS) was chosen to keep track of the reflectance change during the whole process. Typically, for a series of tests, the first data point was taken on a pristine as-prepared TiO_2 film (treated with plasma). The second was taken on the same film with a coating of 10 uL 5×10^{-4} M solution, left in darkness to reach equilibrium and solvent evaporation for 0.5 hour. Then UV treatment was started in a manner of 1 min, 2 min, 2 min, and 2 min, where films were located 2.5 inches underneath the UV lamp, with a Pyrex petri dish lid to remove the extremely strong short waves below 290 nm (Figure 4-4). After each treatment, a data point was recorded as well.

Plasma treatment of TiO_2 films provide opportunities for improving the photochemical capacities as for solar cells or photocatalysts. The glow-discharge plasma contains reactive ions, radicals, and electrons to break down the covalent chemical bonds and remove organic contaminants on the surface.[8] Thus a higher contact surface area is created as active spots for electrode/dye/electrolyte interfacial and also electron transport path with fewer obstacles.

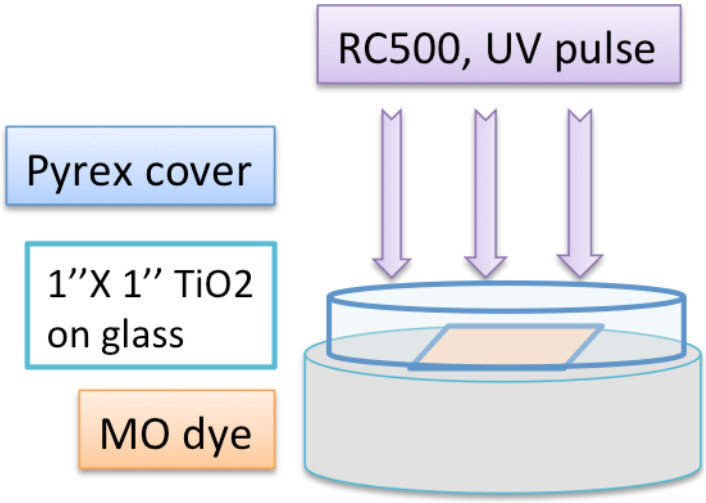

Figure 4-4 Scheme of photocatalytic degradation experiment

4.3 Results and Discussions

4.3.1 Fabrication of titanium dioxide precursor with MFCs templates

Following homogenization, the cellulose was reduced to microfibers with typical fiber diameters around 30 nm and lengths extending from several to tens of micrometers uniformly suspended in isopropanol. Figure 4-5 (a) shows the morphology and dimensions of the homogenized fibers. There are occasional thick fibers with diameters exceeding 100 nm, however, most of the fibers have uniform dimensions. Figure 4-5 (b) and (d) clearly illustrate the influence of cellulose on the titania morphology after calcination. The image in Figure 4-5 (b) shows films that were condensed with low porosity, while (d) shows that the titania has adopted the morphology of tangled cellulose and retained its porous structure. For comparison, coated MFCs without calcination are shown in Figure 4-5 (c). The removal of cellulose fibers and shrinkage of the precursor left large holes on the surface of films.

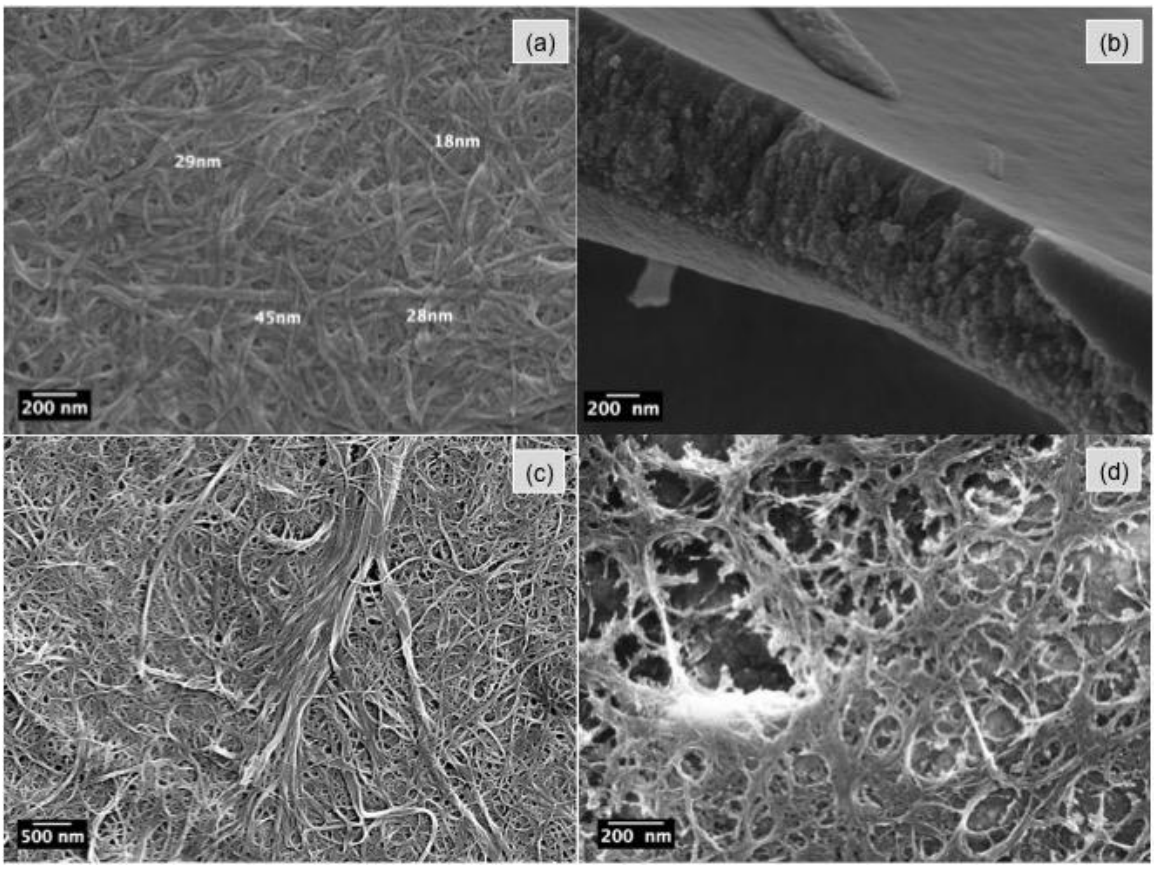

Figure 4-5 (a) Homogenized MFCs. (b) titanium precursor without cellulose, calcined at 450 °C for 2 h. (c) titanium precursor coated cellulose fibers, before calcination. (d) titanium precursor with cellulose (ratio is 1: 1), calcined at 450 °C for 2 h.

To prevent large amounts of cracks, a two-stage calcination was utilized for the crystallization of as-prepared titania precursor. Starting from room temperature, the film was heated to 250°C for 1h, followed by an increase to 450°C for another 1h. A new morphology was formed as shown in Figure 4-6 (a-c). Through the modification of precursor, hydrolysis, gelation, precipitation, drying, and heat treatment, the nanoporous TiO_2 network thin film was formed. The fine titania particles were grown along the fiber's direction and channel-like pores were produced when the cellulose was decomposed with heat treatment. The inorganic network was determined by the competition between hydrolysis and precipitation steps, and the removal of cellulose fibers. When hydrolysis is fast and condensation is slow, small pores are formed in gels; otherwise, a gel consisting of

an interconnected network is formed, leaving enough time and space for template interactions.

Thermogravimetric analysis (TGA) was performed on the cellulose fibers and titanium precursor-cellulose composite. As a reference, 30mL of TTIP, valeric acid, and the cellulose mixture were taken and evaporated in an oil bath at 80°C, and then analyzed with TGA. This indicates that cellulose fibers alone started to decompose from around 250°C and were eliminated at ~430°C (Figure 4-7). In the composite sample, at 250°C cellulose started decomposing and there was approximately 20% w.t. titania left in the tested specimen. The two-stage calcination was then utilized to balance the temperature difference between cellulose degradation and crystal transformation.

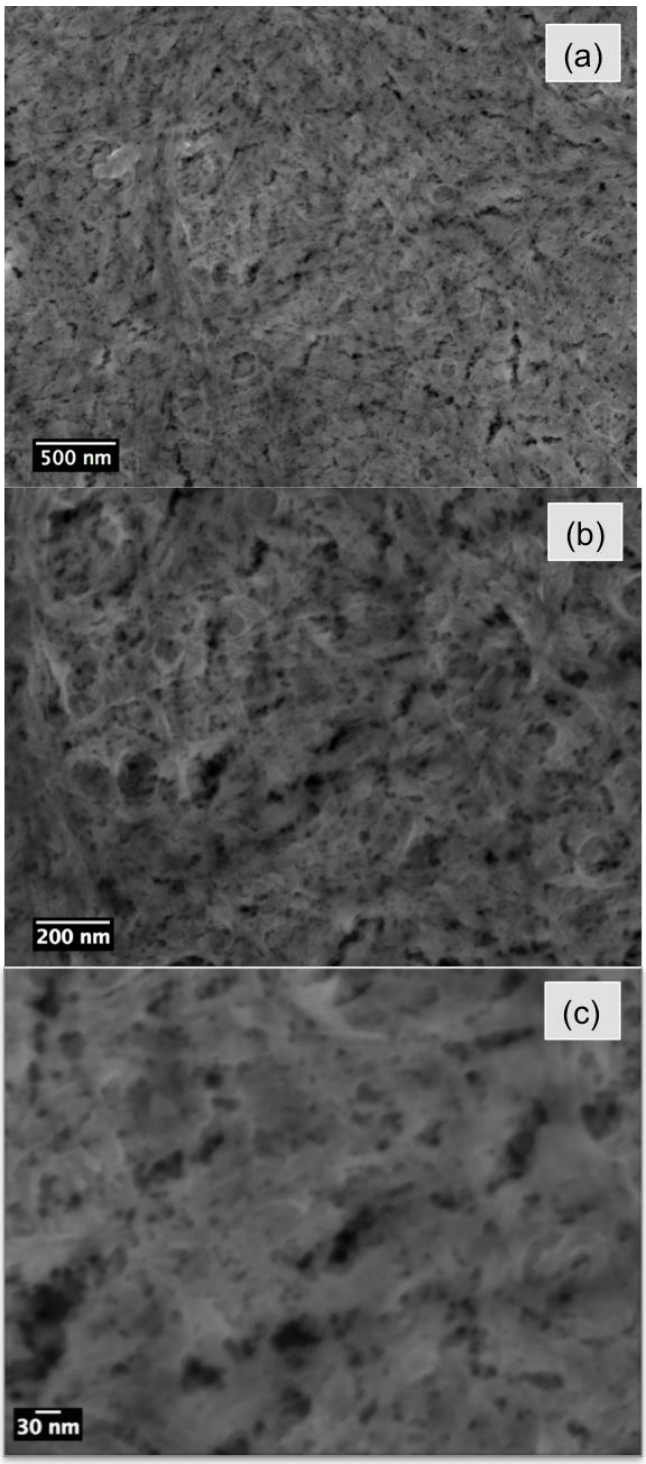

Figure 4-6 (a-c) titanium precursor with cellulose, calcined with a two-stage method at 250 °C for 1h and 450 °C for 1.5 h at increasing magnifications.

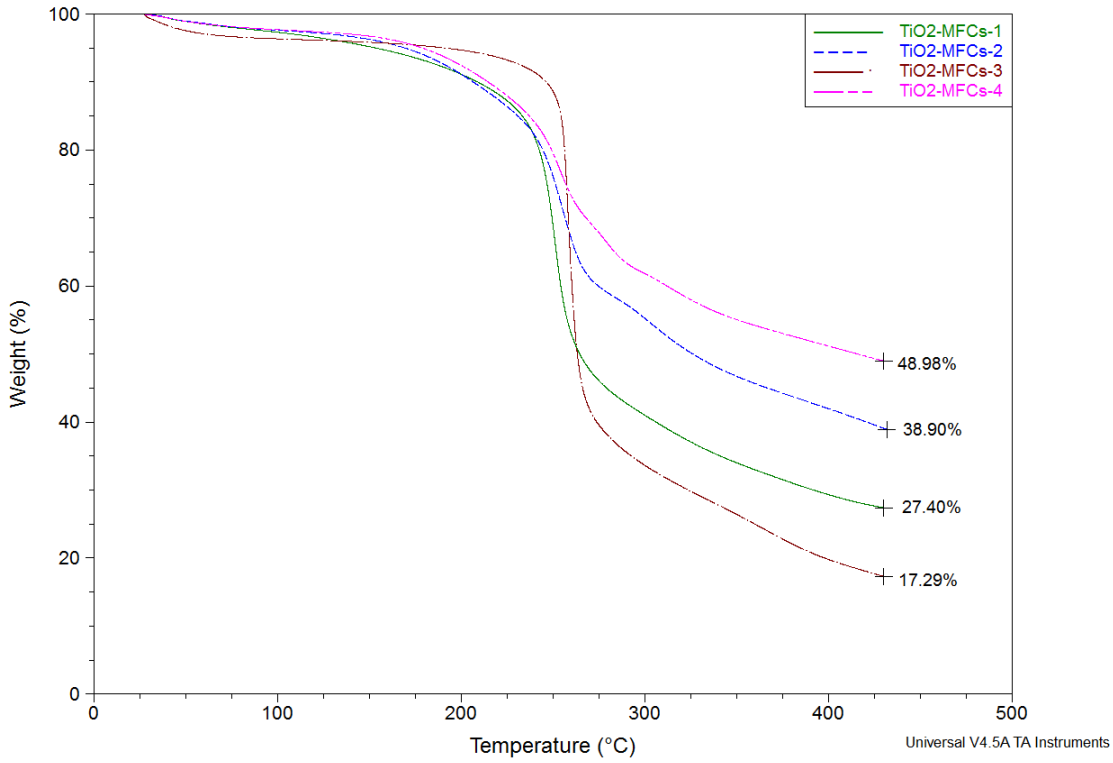

Figure 4-7 TGA results of different Ti: cellulose ratios: 1 (green) Ti: cellulose = 1: 1, reacted at room temperature. 2 (blue) Ti: cellulose = 1: 1, reacted at 50 °C. 3 (brown) Ti: cellulose = 0.5: 1, reacted at room temperature. 4 (pink) Ti: cellulose = 2: 1, reacted at room temperature. All reactions lasted 14 hours with same volume of MFC suspensions at 0.5mg/mL concentration.

Figure 4-7 also indicated that the different ratios of Ti(IV) to MFCs yielded different amounts of titania. Curve 3, 1, 4 had an increased amount of titania residue since their Ti: cellulose ratios grew from 0.5: 1, 1: 1, and 2: 1. Curve 2 had higher TiO_2 products than curve 1 because an elevated reaction temperature was used, which promoted the hydrolysis and condensation. Other chemical molar ratios were tried such as Ti: cellulose = 10:1 or 20:1, however, films after calcination showed a much denser morphology.

Thick films were prepared via repeating the coating-drying process for stronger Raman spectrum signals. All films were confirmed anatase by Raman. Figure 4-8 shows the comparison between uncalcined precursor-cellulose, calcined precursor-cellulose, and the

blank glass substrate. The Raman spectrum of the calcined film clearly shows that titania is anatase as evidenced by the characteristic peaks at 144, 197, 399, 513, 519, 639 cm^{-1}.[9]

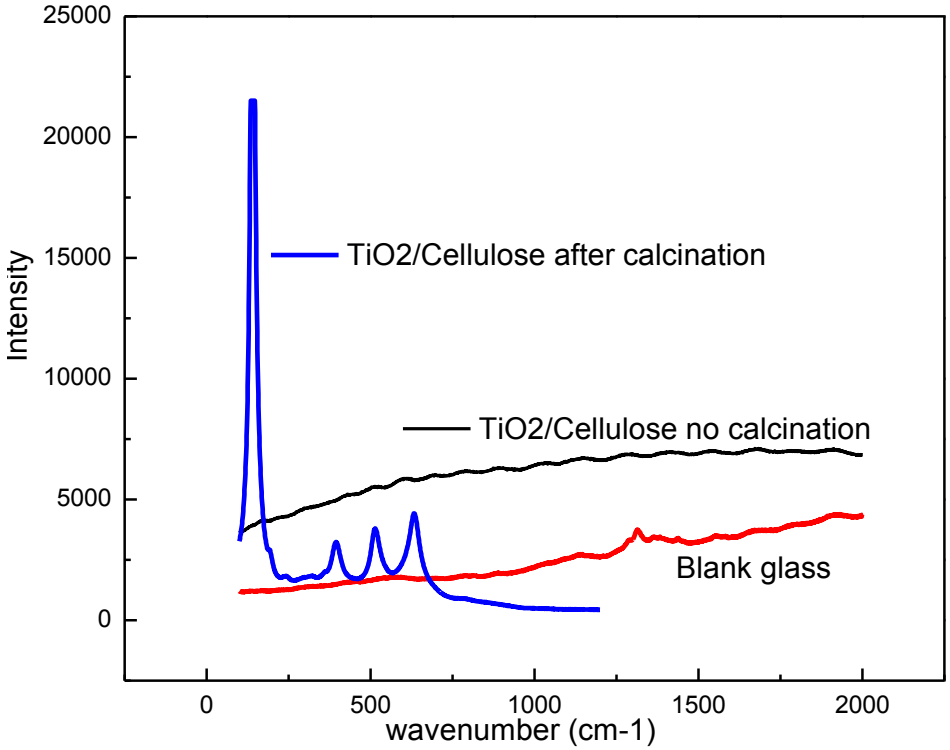

Figure 4-8 Raman spectra of blue: calcined precursor-cellulose; Red: the blank glass substrate; Black: uncalcined precursor-cellulose.

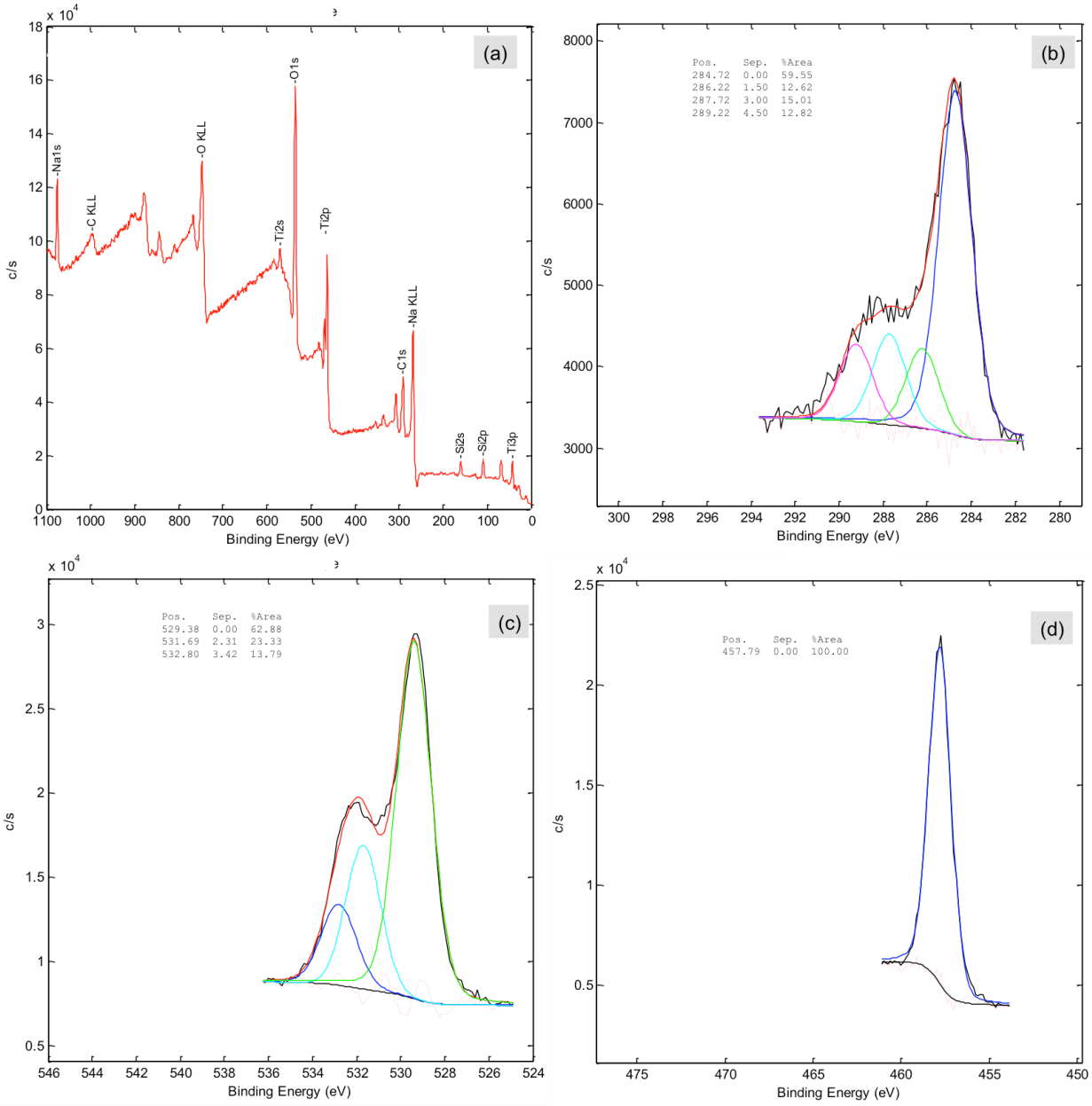

Figure 4-9 X-ray photoelectron spectra of TiO_2 thin film after calcination.

Quantitative XPS analysis was conducted on the annealed thin films. Figure 4-9(a) shows signals of all peaks, and (b-d) gave the high-resolution evolution of elements C, O, Ti. The atomic concentration of Ti 2p was 10.5% based on calculations from detailed evolution. Figure 4-9 (b) illustrates C 1s peaks at 284.7 eV (C-C, or C-H), 286.2 eV (C-O-C, or C-OH), 287.7 eV (C=O), and 289.2 eV (O-C=O). Some of these peaks exist even after high-

temperature annealing, which has been reported by others for TiO_2 films and powders after sintering.[10] It is adventitious carbon that possibly came from ex-situ preparation process. Most samples that have been exposed to atmosphere will get a layer of 1-2 nm carbon contamination. Also, carbon could be due to small amounts of organic residuals from titanium isopropoxide and cellulose. From the O 1s peak spectra in Figure 4-9 (c), binding energy about 529.4 eV presented O^{2-} for TiO_2, and 531.7 eV was from hydroxyl species, considered as defect states. Higher ratios of $[OH]/[O^{2-}]$ would indicate more trapping states, while in this case, the pristine $[O^{2-}]$ was almost three times of the [OH] species based on the integrated area. In addition, another source of hydroxyl species might be from adsorbed alcohols on titania both molecularly and dissociatively at room temperature.[11] Figure 4-9 (d) explained the Ti 2p core level spectrum, at binding energies 457.8 eV referred to TiO_2 .

Coating methods matter regarding the results of the adhesion and film morphology. For the templated precursors, spin coating was not ideal due to the existence of fibrous cellulose agglomeration. The binders (PEG and PVDF) were incorporated into the samples to improve the continuity of the films and make thicker films through doctor blade method or spin coating. TGA analysis of the binders found that PEG began to degrade at ~235 °C, while PVDF degradation wouldn't begin until the temperature reached 420 °C.

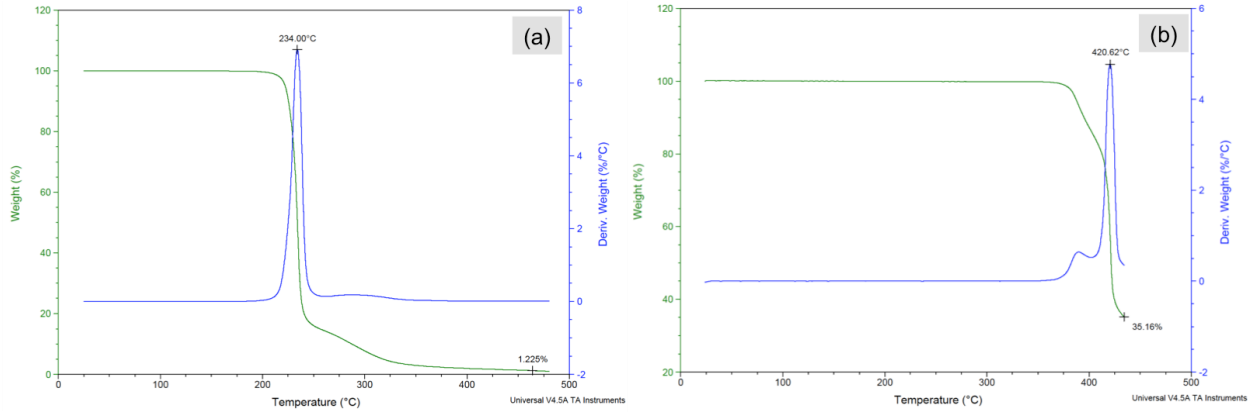

Figure 4-10 TGA results of (a) PEG and (b) PVDF through thermal degradation in air

When using PEG as a binder, larger aggregates and wider cracks tended to appear, due to the fact that PEG melted, decomposed and interfered with the distribution of the metal oxide. However, with a much higher decomposition temperature, PVDF helped stabilize the film structure. Figure 4-11 (a-e) shows the calcined films with different binders and coating methods. Figure 4-11 (a-b) shows that with increased coating thickness by spin-coating, dense structures started to form, while (c) shows more porosity on the surface when doctor blade was applied. Generally, spin coated PEG-added films still presented minimum cracks, while with PVDF, films were filled with large cracks, and left with large pores as shown in Figure 4-11(d-e). The residual of PEG binder was around 1.2% w.t. after 450 °C, while PVDF had a much higher residual content at around 30% w.t. Although the coating and morphology could be improved to some extent, no organic residue was expected in the network of titania films for future applications.

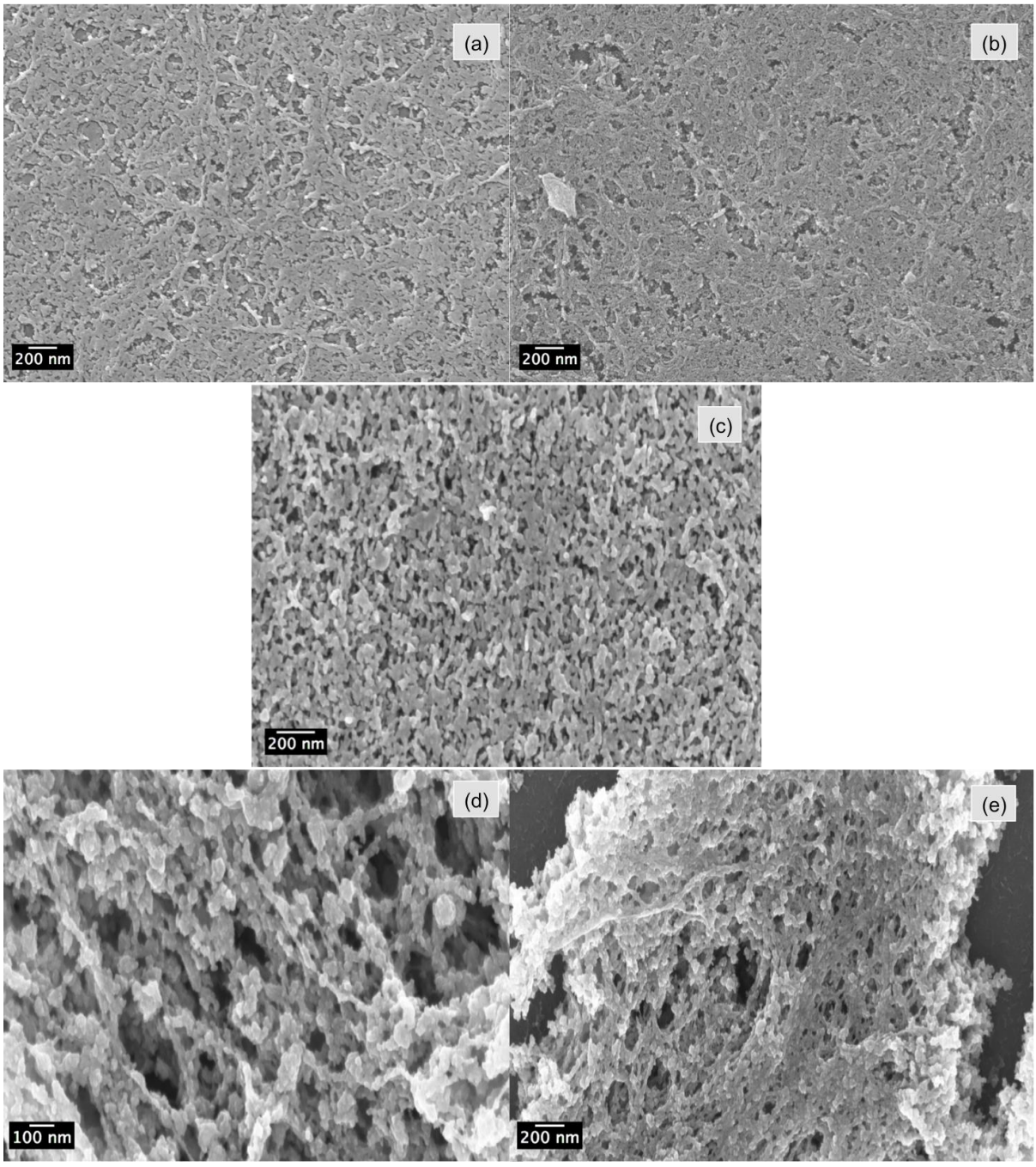

Figure 4-11 Calcined Ti-MFCs thin films with different binders. With 10% w.t. PVDF, spin coated: (a)1 layer, (b)4 layers; doctor blade coated (c) 1 layer. With 10% w.t. PEG: (c)spin coated, 1 layer (d)doctor bade coated, 1 layer.

Preliminary dye adsorptions were conducted with an organic dye (Rose Bengal) on binder-free calcined TTIP/cellulose films, PEG-assisted, and PVDF-assisted TTIP-cellulose

films. UV-vis spectroscopy results demonstrated that the binder does not facilitate more dye loading.

An interesting fact of F on the growth of TiO_2 crystal was revealed while experimenting with the parameters of binder addition. When the amount of PVDF was increased to ~30% w.t. to change the low viscosity of the original precursor solution, a new morphology was created as Figure 4-12 shows. It was reported that when {101} planes of TiO_2 nanocrystals were stabilized by chemical bonds, more selective growth of {001} planes will occur, resulting in rod-like TiO_2 .[12] However, fluorine-mediated TiO_2 nanocrystals usually have more stabilized {001} facets in various aqueous TiO_2 synthesis routes[13], indicating that the grains on the surface came from the spatial steric hindrance and less available interfacial contacts as nucleation sites, while the rice-like shape couldn't be explained completely yet in this work.

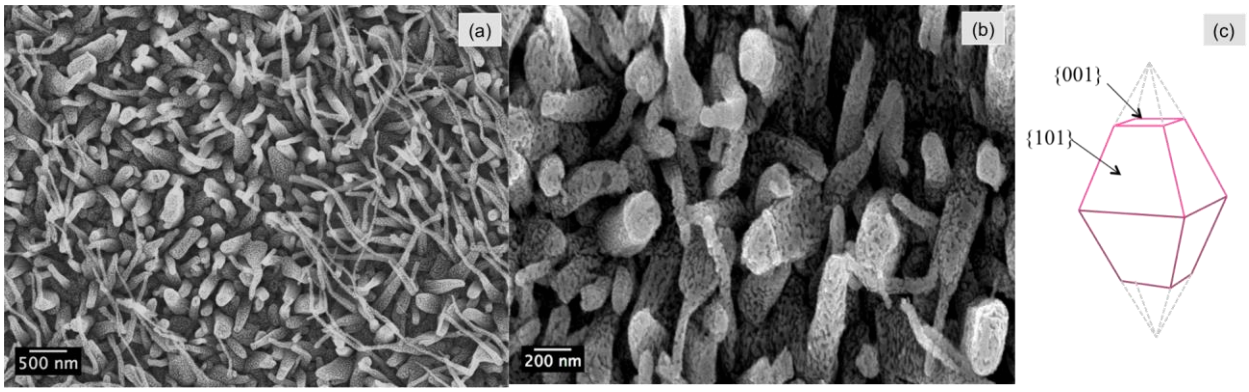

Figure 4-12 (a-b) Calcined Ti-MFCs thin films with ~30% w.t. PVDF, grain-surface rice-shaped TiO_2 . (c) An anatase tetragonal {101} bi-pyramid.

4.3.2 Photocatalysis performance of immobilized titania thin films

The modified sol-gel method with cellulose template created nano/meso porous titania films as discussed before. It was applied as photocatalytic film in our research, to

study the influence of morphology, concentration, and thickness to the performance of immobilized film photocatalysts.

Films made with three ratios between Ti (IV) and cellulose 2: 1, 4: 1, and 8: 1 were tested, in the degradation process of methyl orange (MO) aqueous solutions.

Table 4-1 Atomic concentration comparison between variable films made from TTIP/V-acid/MFCs precursor

	Calcined films: TTIP V-acid+MFCs, with varied Ti: cellulose ratios, and layers	C1s	O1s	Na1s	Si2p	Ti2P
1	1 layer, 2:1 Ti:cellulose film	24.3	46.5	13.7	0	15.5
2	1 layer, 4:1 Ti:cellulose film	24.0	46.4	12.1	2.3	15.2
3	1 layer, 8:1 Ti:cellulose film	22.5	50.3	6.8	8.6	11.8
4	2 layer, 2:1 Ti:cellulose film	23.3	47.1	11.8	1.8	16.0
5	2 layer, 4:1 Ti:cellulose film	25.0	44.9	13.2	1.6	15.3
6	2 layer, 8:1 Ti:cellulose film	26.5	47.9	5.3	6.7	13.6

As shown in Table 4-1, the atomic concentrations of C 1s, O 1s, Ti 2p, Na 1s, and Si 2p were obtained through XPS. The concentration of Ti(IV) increased from one-layer films to two-layer films for the same Ti: cellulose ratios. When Ti: cellulose was 2: 1, it gave the highest Ti concentration, and the 8: 1 ratio films were the lowest among the three types.

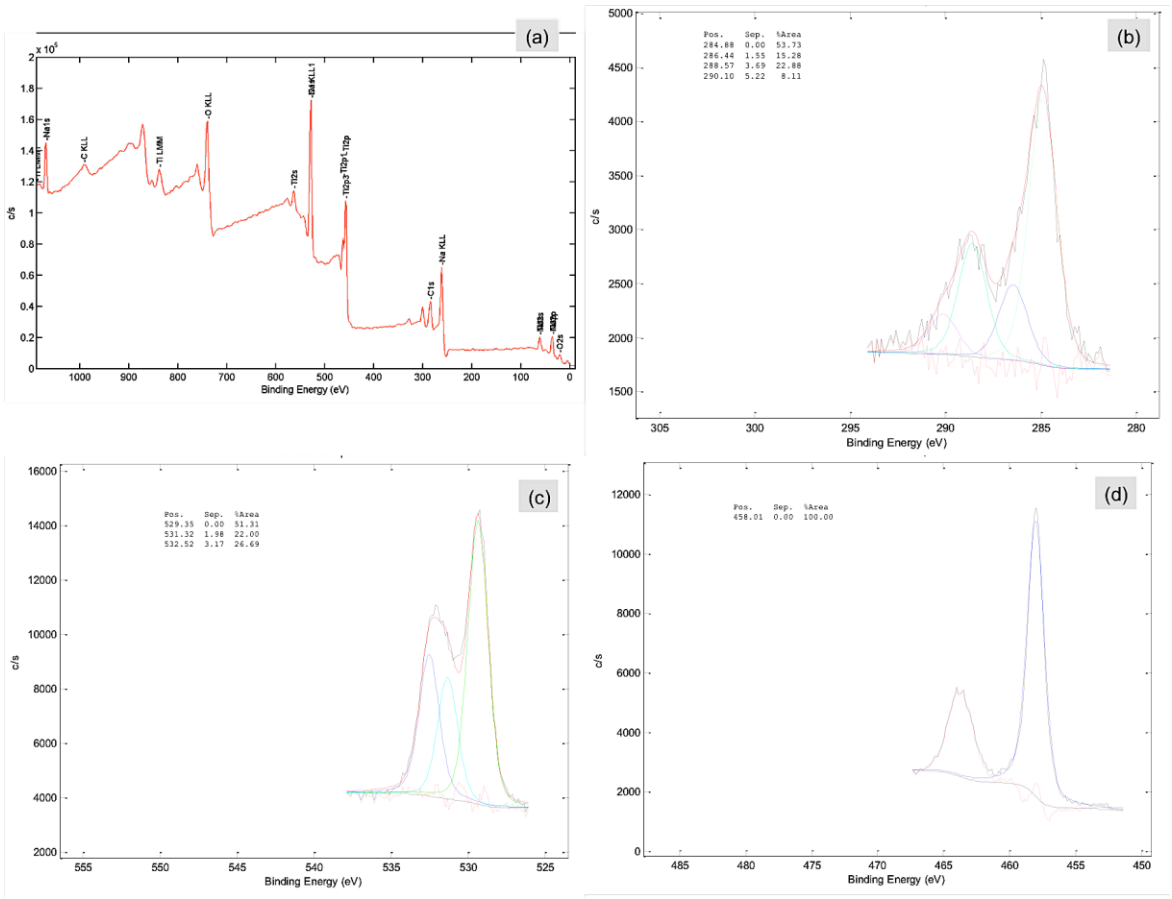

Figure 4-13 XPS spectra of TiO_2 thin film after calcination, made from TTIP/V-acid/MFCs, with Ti: cellulose = 2:1. (a) XPS spectrum with element labeling. (b-d) High-resolution data fitting.

The C 1s, O 1s, and Ti 2p were fitted and analyzed as shown in Figure 4-13 for Ti: cellulose = 2: 1 thin films after calcination. As mentioned before, C 1s peaks at 284.8 eV (C-C, or C-H), 286.4 eV (C-O-C, or C-OH), 288.6 eV (C=O), and 290.1 eV (O-C=O) were from adventitious carbon. From the O 1s peak spectra in Figure 4-13 (c), binding energy about 529.4 eV presented O^{2-} for TiO_2, and 531.2 eV was from hydroxyl species, the pristine [O^{2-}] was twice of the [OH] species based on the integrated area. Figure 4-13 (d) explained the Ti 2p core level spectrum, at binding energies 458.0 eV referred to TiO_2 .

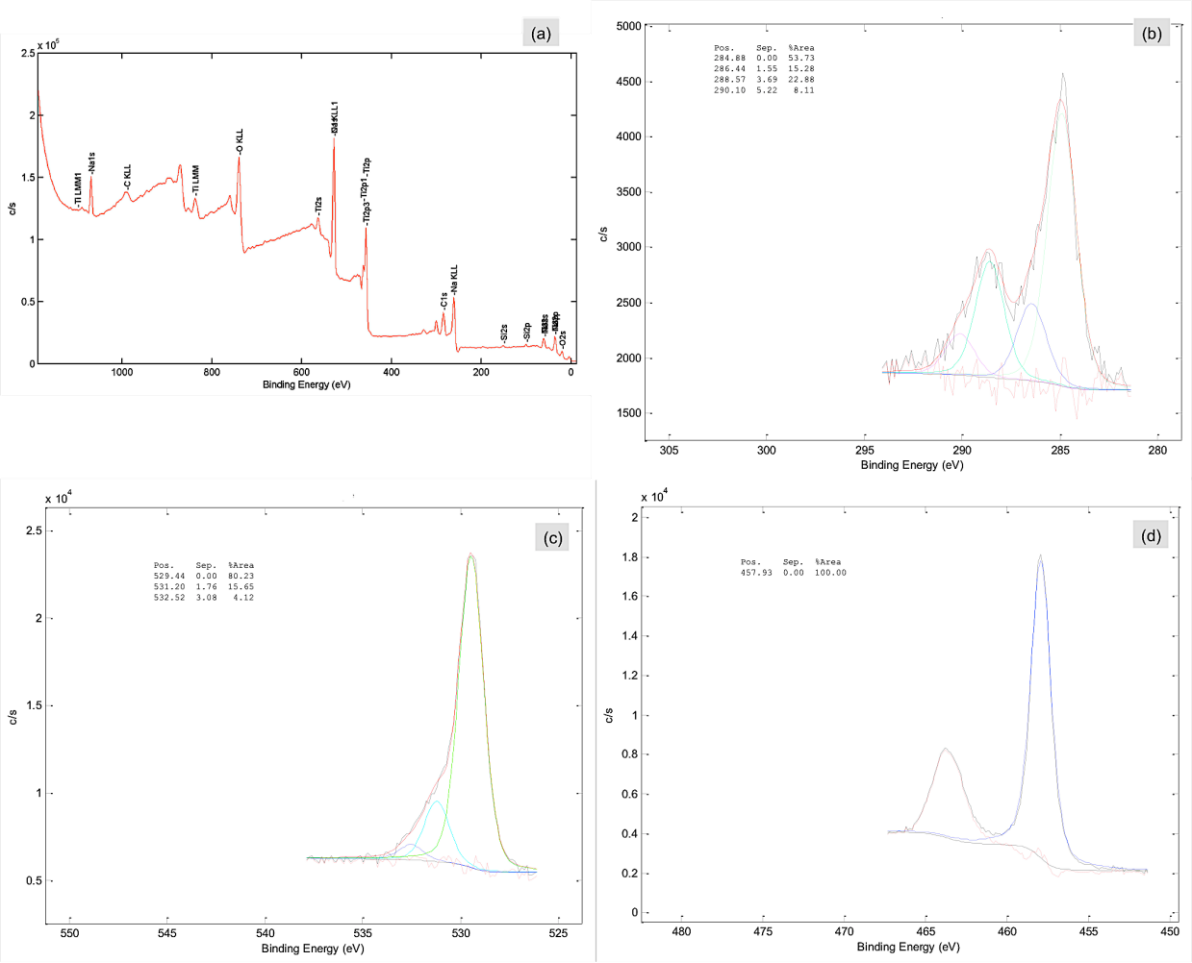

Figure 4-14 XPS spectra of TiO_2 thin film after calcination, made from TTIP/V-acid/MFCs, with Ti: cellulose = 4:1. (a) XPS spectrum with element labeling. (b-d) High-resolution data fitting.

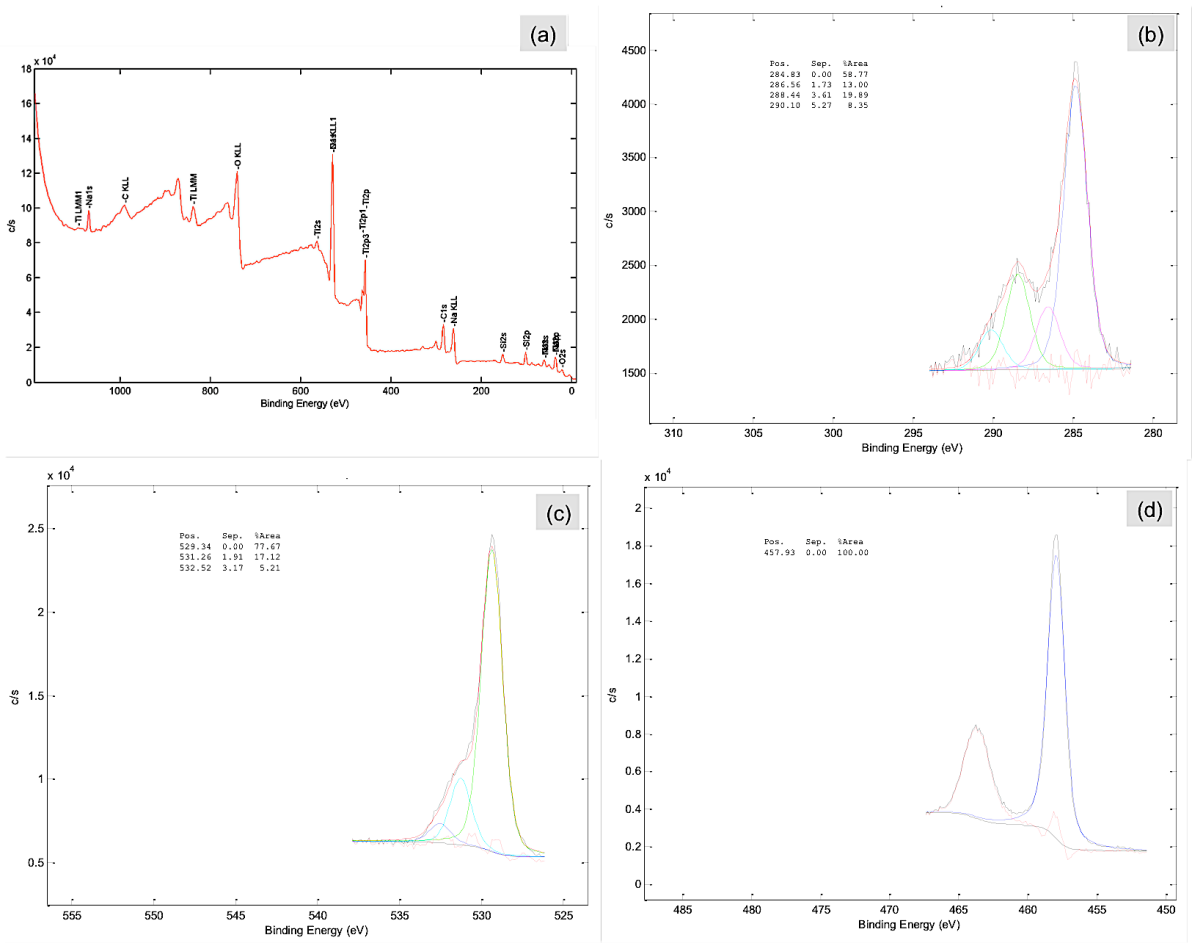

Figure 4-15 XPS spectra of TiO_2 thin film after calcination, made from TTIP/V-acid/MFCs, with Ti: cellulose = 8:1. (a) XPS spectrum with element labeling. (b-d) High-resolution data fitting.

Figure 4-14 and Figure 4-15, similarly, illustrated the XPS spectra of films made with Ti: cellulose = 4:1 and 8:1. After summarizing the ratio of the C 1s, O 1s, and Ti 2p evolutions, some general ideas were concluded as follows:

(1) Adventitious carbon was recorded in four peaks representing different C bonds, and difficult to be distinguished from the film properties. (whether the film contains carbon). The distribution of 4 fitted peaks were very consistent, with 56% - 14% - 22% - 8%.

(2) O 1s fitted peaks have lied in the same binding energy region as 529.4 eV, 531.3 eV, and 532.52 eV. The integrated area of the 529.4 eV peak was 51%,

80%, and 78% for sample 2:1, 4:1, 8:1, which corresponds to the Ti(IV) amount trend summarized in Table 4-1.

(3) Ti 2p was fitted into 457.9 eV representative of titania and was the only Ti species observed for all samples.

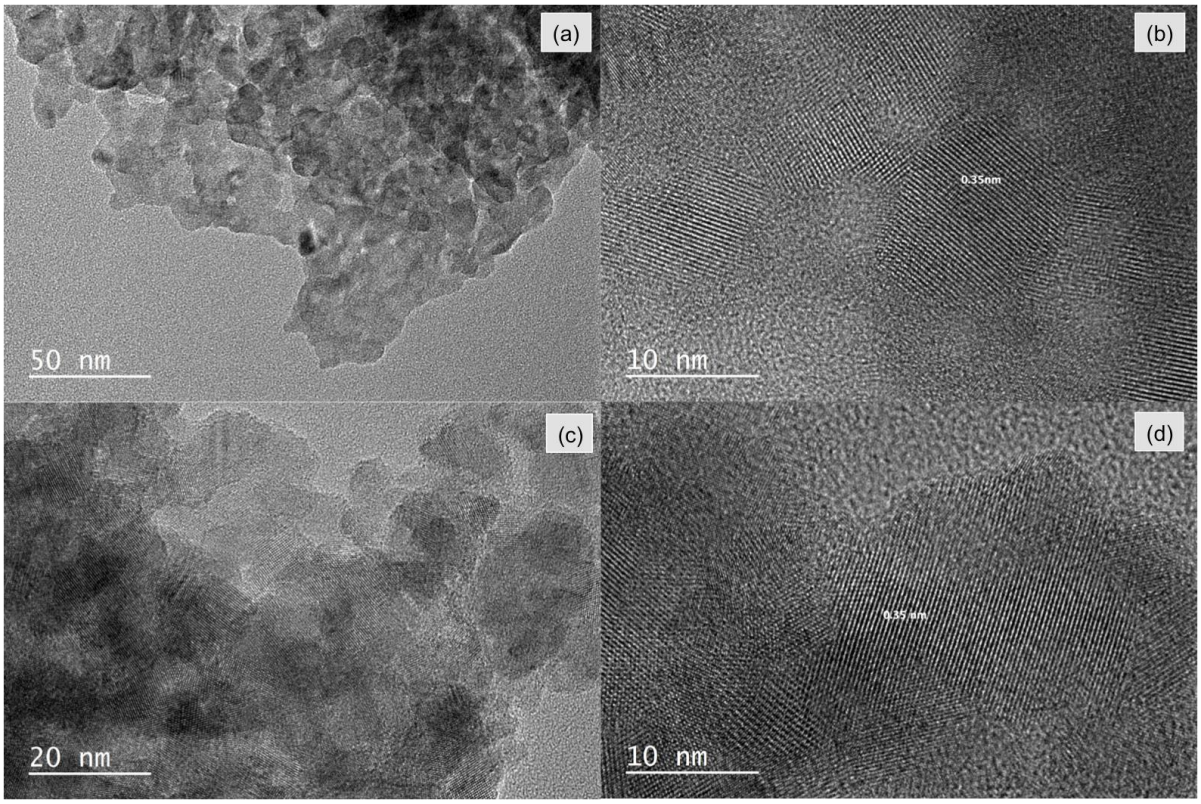

Figure 4-16 TEM images of anatase TiO_2 film generated by modified sol-gel method with TTIP/V-acid/MFCs, with Ti: MFCs = 2:1. (a) and (c) porous structure, at lower magnifications (b) and (d) HRTEM image noted with anatase lattice spacing ~0.352 nm of the plane (101).

TEM images of each type of films were obtained at high resolution and anatase phase was further confirmed with selected area diffraction pattern and the lattice spacing measured at 0.35 nm corresponding to dominate plane (101) (JCPDS No. 21-1272).

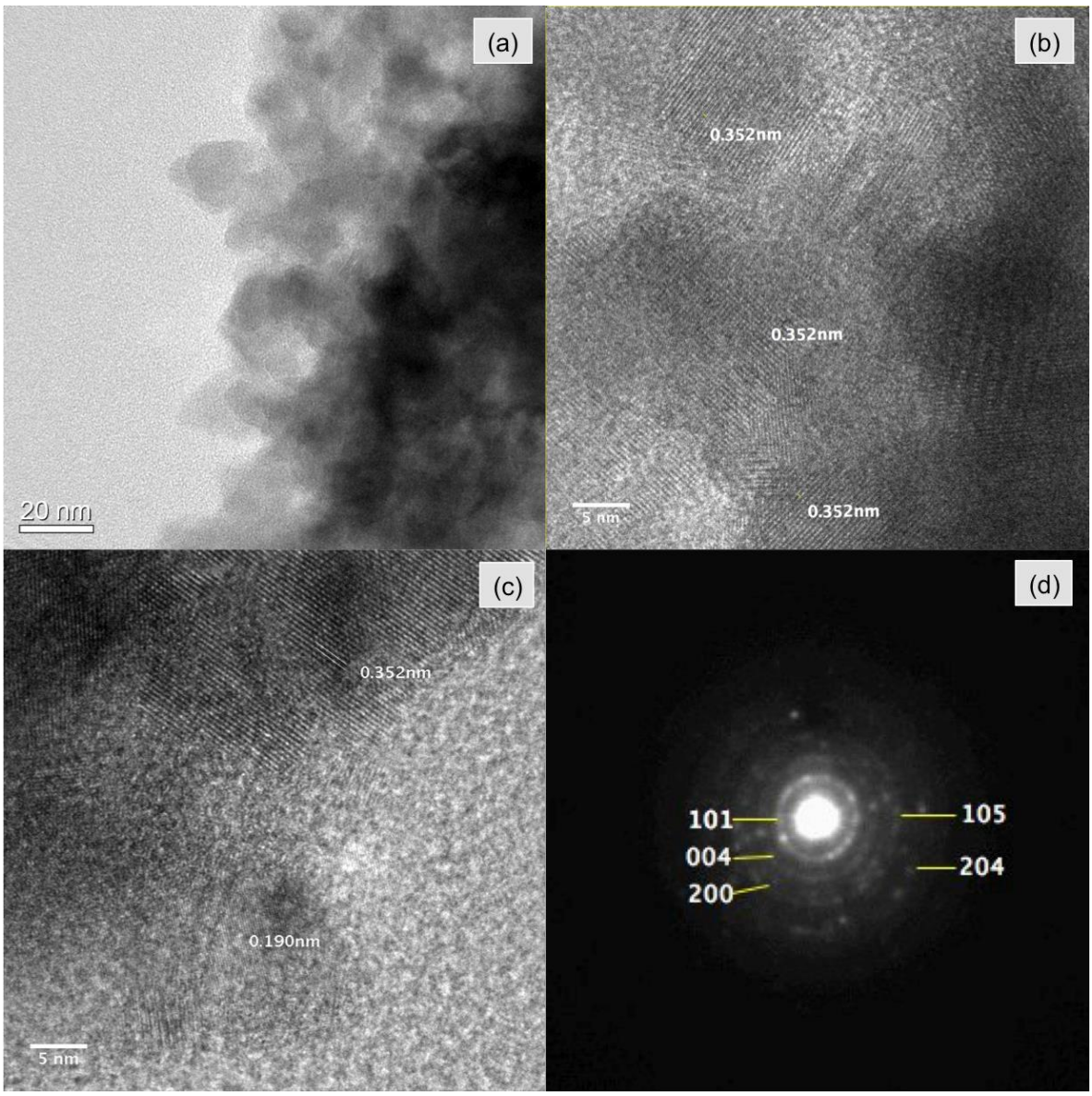

Figure 4-17 TEM images of anatase TiO_2 film generated by modified sol-gel method with TTIP/V-acid/MFCs, with Ti: MFCs = 4:1. (a) showed the porous nanoparticles, (b) and (c) HRTEM image noted with anatase lattice spacing ~0.352 nm of plane (101) and ~0.19 nm of plane (200). (d) SAED diffraction pattern shows the polycrystalline rings.

Figure 4-16, Figure 4-17, and Figure 4-18 showed the crystal sizes of TTIP/V-acid/MFCs induced films with Ti: cellulose (2:1, 4:1 and 8:1) ratios were, respectively: 15 nm, 12 nm and 21 nm. The diffraction pattern indicated that TiO_2 films were composed of polycrystalline anatase TiO_2 with the Debye-Scherrer concentric rings (101), (004), (200), (105) and (204).

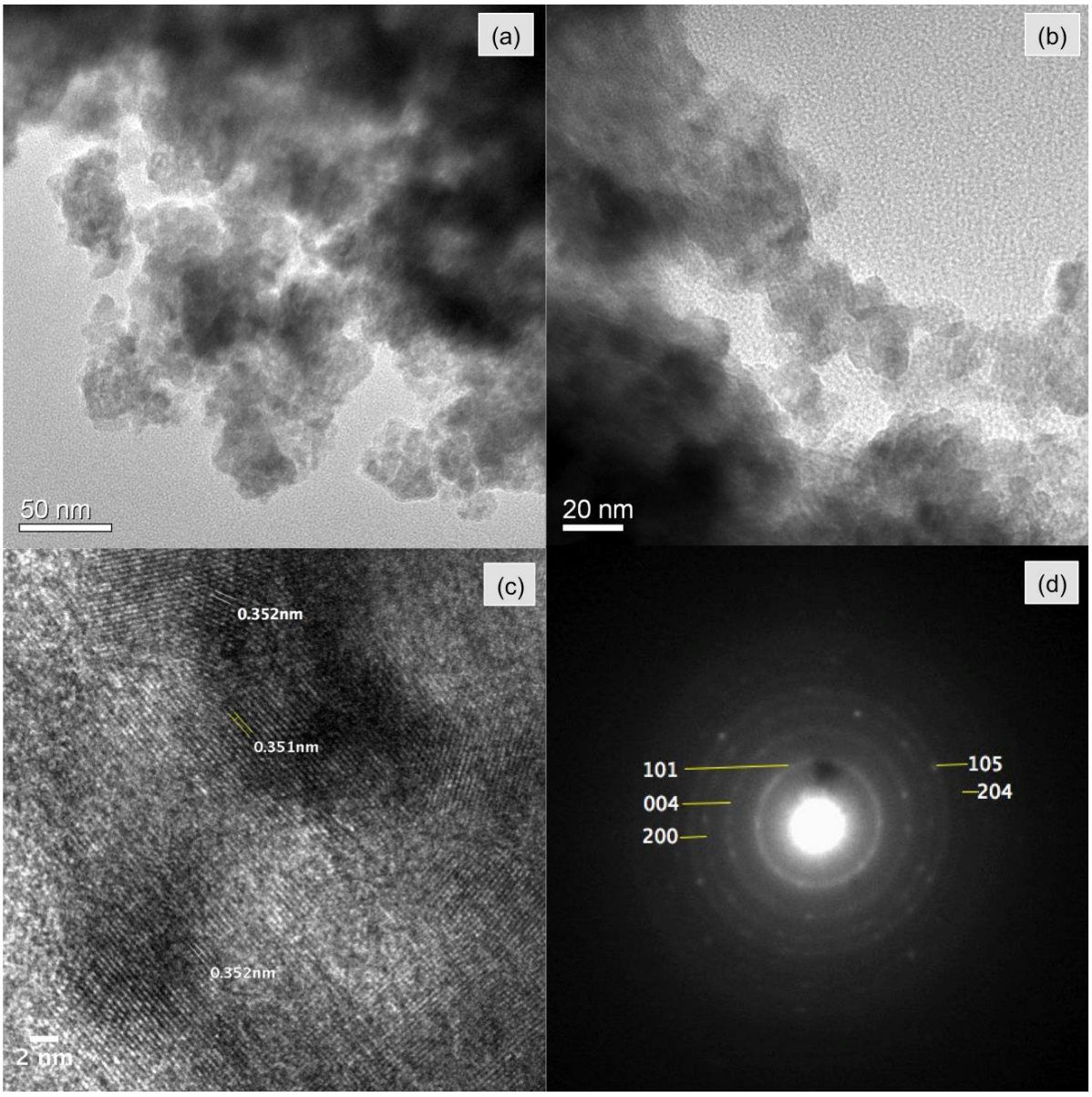

Figure 4-18 TEM images of anatase TiO_2 film generated by modified sol-gel method with TTIP/V-acid/MFCs, with Ti: MFCs = 8:1. (a-b) showed the porous nanoparticles, and (c) HRTEM image noted with anatase lattice spacing ~0.352 nm of plane (101). (d) SAED diffraction pattern shows the polycrystalline rings.

The surface area of these films was by scraping off the materials from the glass substrate and collected for Brunauer-Emmett-Teller (BET) test. The surface area of TTIP/V-acid/MFCs films were 40.9 m^2/g (Ti: MFCs = 2:1), and 41.5 m^2/g (Ti: MFCs = 1:1). This procedure, to some extent, damaged the original shape of the film and the adhesion between the film and substrate. Also, the limited amount of thin film materials that could

be obtained hindered the test. Thus, this data could be seen as a reference data with accuracy worth doubting.

In chapter 2, MO has been briefly introduced as a powerful photocatalytic performance indicator. During the process of MO decomposition, the peak at 465 nm will decrease. Previous work[14] showed that a new peak t 270 nm will show up in the preliminary stage, and its intensity started to increase at first. Gradually, both peaks at 465 nm and 270 nm decreased and disappeared eventually, leaving the only peak at 254 nm increasing with time. This was explained to be related to the chemistry bonding change during the degradation of MO. At first, the polyaromatic ring in MO was degraded, but created mono substituted aromatics, so the 465 nm peak decreased, while the 270 nm peak increased. Then further degradation converted all the MO and byproduct into CO_2, H_2O, and mineral ions, shown as the fading of both peaks.

There is an optimum concentration where the best photodegradation rate constant was reached.[14] Generally, decreasing the concentration ensures an increasing constant k due to the saturation level.

The method applied here was based on the observation of reflectance spectra change from pristine TiO_2 films, to dye-coated TiO_2 films, and the evolution of the photocatalyzed dye-coated TiO_2 films. A simple quantitative method is used on the wavelength of 395 nm to calculate the reflectance difference between the real-time data and the initial data, thus by comparing the trend of the difference, the dye amount that was eliminated could be estimated.

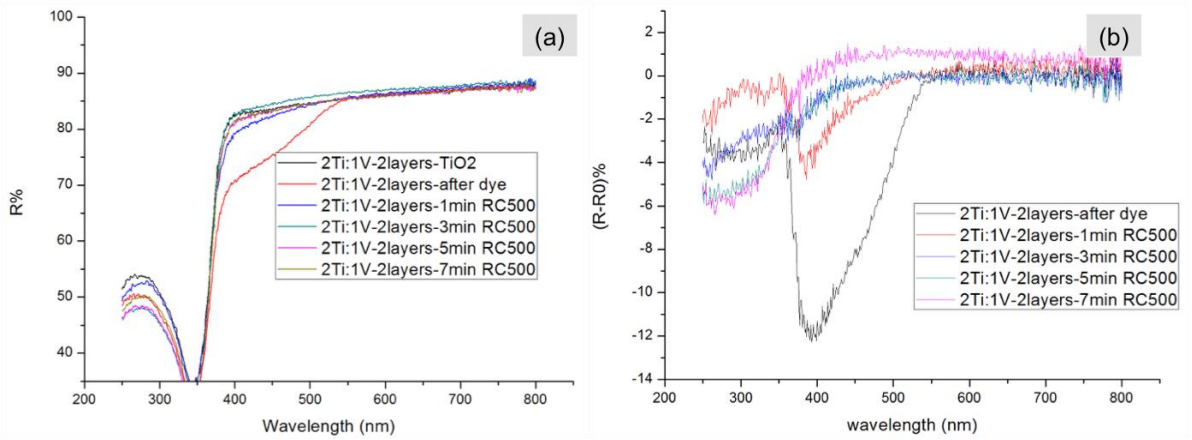

Figure 4-19 Reflectance change over time of UV-illuminated TiO_2 film with 1×10^{-5} M MO solution adsorbed. Titania film was made with TTIP/V-acid/MFCs and Ti: cellulose = 2: 1. (a) Reflectance change from clean TiO_2, MO solution adsorbed (after dye), and treated with UV lamp for a total time of 1 min, 3 min, 5 min, and 7 min. (b) Reflectance difference over time, from dye adsorption, to photocatalytic degradation.

Before MO solution was adsorbed onto titania films, the reflectance was measured as black curve in Figure 4-19 (a), while after dye equilibrium, the red curve was moved away from the initial stage. Once photocatalytic degradation started, the curve moved back to the original stage gradually. The difference between real-time reflectance and the original state was plotted vs. wavelength, and at 395 nm, the characterizing peak was used to represent the dye decomposition amount.

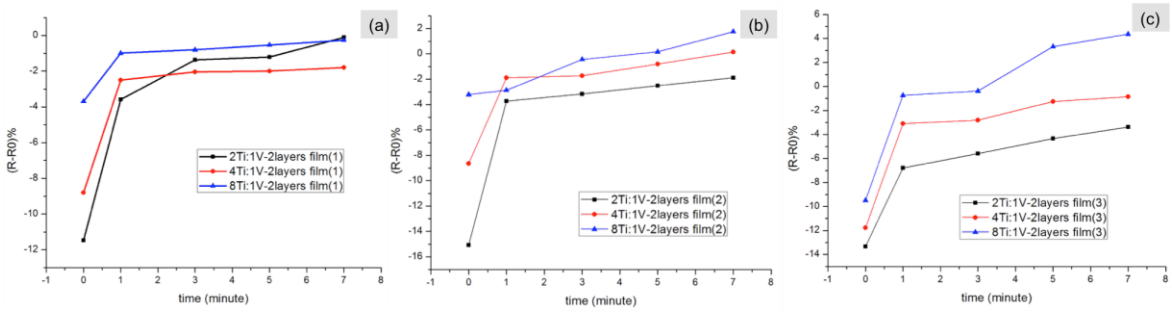

Figure 4-20 For the film made with TTIP/V-acid/MFCs, and two layer coating, reflectance difference change at wavelength 395 nm v. s. time. (a-c): three sets of data, where Ti: cellulose = 2: 1 (black), Ti: cellulose = 4: 1 (red) and Ti: cellulose = 8: 1 (blue)

Three ratios of Ti to cellulose (2:1, 4:1 and 8:1) precursors were prepared into two-layer films, by depositing one layer, drying, depositing again, drying and annealing. Three

sets of films are shown in Figure 4-20. Ratio 4: 1 and 2: 1 had won over 8: 1 films in terms of the degradation percentage. Single-layer films were studied with different volume of precursor for coating, and the photocatalytic performance is shown in Figure 4-21.

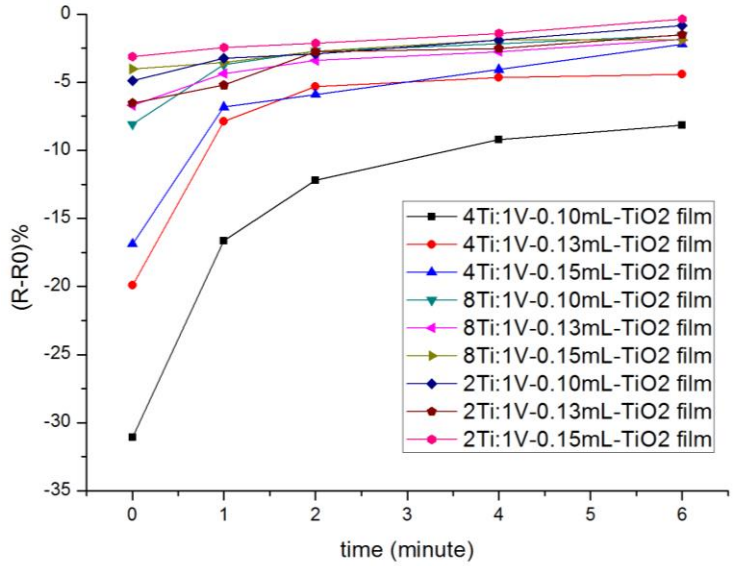

Figure 4-21 For the film made with TTIP/V-acid/MFCs, and one layer coating, reflectance difference change at wavelength 395 nm v. s. time. : three sets of data with different volume of coating precursor.

The kinetics model was not fitted into an established model yet, thus a simple (R-R0)/t calculation was used for parallel comparison between single-layer films, double-layer films, and different Ti over cellulose ratios. The best candidate for TiO_2 photocatalytic film is the 2: 1 and 4: 1 ratio. When the films have composition ratio of 8: 1, although TiO_2 amount was greatly increased, the porosity and film surface area would be lowered down. Table 4-2 summarizes the efficiency and rate scales for reference.

Table 4-2 Degradation and decomposition rate for various films

	degradation efficiency	(R-R0)%/t(min^{-1})		degradation efficiency	(R-R0)%/t(min^{-1})
2Ti-1MFC two-layer	0.87	1.64	2Ti-1MFC 0.10 mL one layer	0.83	0.58

Table 4-2 (cont'd)

4Ti-1MFC two-layer	0.88	1.38	2Ti-1MFC 0.13 mL one layer	0.78	0.72
8Ti-1MFC two-layer	0.92	1.48	2Ti-1MFC 0.15 mL one layer	0.89	0.40
	degradation efficiency	(R-R0)%/t(min^{-1})		degradation efficiency	(R-R0)%/t(min^{-1})
4Ti-1MFC 0.10 mL one layer	0.86	3.17	8Ti-1MFC 0.10 mL one layer	0.90	0.90
4Ti-1MFC 0.13 mL one layer	0.85	2.25	8Ti-1MFC 0.13 mL one layer	0.88	0.89
4Ti-1MFC 0.15 mL one layer	0.86	2.16	8Ti-1MFC 0.15 mL one layer	0.59	0.43

4.4 Conclusions and Future Work

A rate-controlled sol-gel method has been developed with chelating agent valeric acid, and template micro/nano-fibrillated cellulose. Cellulose was removed cleanly by thermal treatment and *in-situ* coating techniques created thin titania films on substrates with porous structures, created by the vacancy left from cellulose. The theory was further explored by SEM, TEM, TGA, XPS, EDS and BET. Two-stage calcination was utilized to improve the interface between organic and inorganic composition, and binders such as PEG and PVDF were studied as well.

Different ratios of Ti to cellulose were examined as photocatalytic films to degrade methyl orange adsorbed on film. Degradation efficiencies of the films were related to

thickness and Ti(IV) concentration and proved to be a promising immobilized photocatalytic tool for pollution removal.

Future work could focus on more versatile binder to improve the film quality, without leaving residual within the film. Surfactants are also affordable and exciting directions to further control crystal growth and size.

BIBLIOGRAPHY

BIBLIOGRAPHY

(1) Shin, Y.; Bae, I.-T.; Arey, B. W.; Exarhos, G. J. Simple Preparation and Stabilization of Nickel Nanocrystals on Cellulose Nanocrystal. *Materials Letters* **2007**, *61*, 3215–3217.

(2) Shin, Y.; Exarhos, G. J. Template Synthesis of Porous Titania Using Cellulose Nanocrystals. *Materials Letters* **2007**, *61*, 2594–2597.

(3) Zhou, Y.; Ding, E.-Y.; Li, W.-D. Synthesis of TiO2 Nanocubes Induced by Cellulose Nanocrystal (CNC) at Low Temperature. *Materials Letters* **2007**, *61*, 5050–5052.

(4) Ivanova, A.; Fravventura, M. C.; Fattakhova-Rohlfing, D.; Rathouský, J.; Movsesyan, L.; Ganter, P.; Savenije, T. J.; Bein, T. Nanocellulose-Templated Porous Titania Scaffolds Incorporating Presynthesized Titania Nanocrystals. *Chem. Mater.* **2015**, 150903090311005–150903090311008.

(5) Siró, I.; Plackett, D. Microfibrillated Cellulose and New Nanocomposite Materials: a Review. *Cellulose* **2010**, *17*, 459–494.

(6) Ulery, A. L.; Drees, R. ***Methods of Soil Analysis: Mineralogical Methods***.

(7) Askeland, P. A. Preparation and Characterization of Sol-Gel Derived Metal Oxide Thin Films and Powders for Coatings and Catalysts, 1997.

(8) biris, A. S. The Structure of Titanium Oxidie Titania (Tio2) Photoactive Water-Splitting Catalysts by Raman Spectroscopy. **2009**, 1–7.

(9) Phase-Pure TiO2 Nanoparticles: Anatase, Brookite and Rutile. **2008**, *19*, 145605.

(10) Oekermann, T.; Zhang, D.; Yoshida, T.; Minoura, H. Electron Transport and Back Reaction in Nanocrystalline TiO 2Films Prepared by Hydrothermal Crystallization. *J. Phys. Chem. B* **2004**, *108*, 2227–2235.

(11) Kumar, P. M.; Badrinarayanan, S.; Sastry, M. Nanocrystalline TiO_2 Studied by Optical, FTIR and X-Ray Photoelectron Spectroscopy: Correlation to Presence of Surface States. *Thin Solid Films 358*, 122–130.

(12) Kim, J. Y.; Choi, S. B.; Kim, D. W.; Lee, S.; Jung, H. S.; Lee, J.-K.; Hong, K. S. Surfactant-Assisted Shape Evolution of Thermally Synthesized TiO 2Nanocrystals and Their Applications to Efficient Photoelectrodes. *Langmuir* **2008**, *24*, 4316–4319.

(13) Dozzi, M.; Selli, E. Specific Facets-Dominated Anatase TiO2: Fluorine-Mediated

Synthesis and Photoactivity. *Catalysts 2013, Vol. 3, Pages 455-485* **2013**, *3*, 455–485.

(14) Al-Qaradawi, S.; Salman, S. R. Photocatalytic Degradation of Methyl Orange as a Model Compound. *"Journal of Photochemistry & Photobiology, A: Chemistry"* **2002**, *148*, 161–168.

5 Synthesis of Porous Titania network with Micro/nano-fibrillated Cellulose as Templates by Liquid Phase Deposition

5.1 Background

5.1.1 Liquid phase deposition

When controlled hydrolysis of metal ions happens in an aqueous solution, and generates metal oxides and related precursor species, this deposition process on a substrate is called liquid phase deposition (LPD). As mentioned in Chapter 1, LPD is a versatile and cost-effective method to prepare titania films that do not require additional equipment and works well with various types of substrates. Also, it supports low-temperature reactions, provides strong adhesion between the film and the substrate and excellent crystallinity. The reaction mechanism, adjustable parameters and relevant applications of two advanced approaches - ammonium hexafluorotitanate (AHFT)/boric acid (BA) LPD, and titanium tetrafluoride (TiF_4) acidic LPD - will be discussed

AHFT and BA method:

Emerging research has been conducted on titanium dioxide synthesis through LPD, typically, by the ligand exchange of metal fluorocomplex ions $[TiF_6]^{2-}$ and the consumption of F^- with boric acid as a scavenger.

$$TiF_6{}^{2-} + nH_2O \leftrightarrow TiF_{6-n}(OH)_n{}^{2-} + nHF \quad (5\text{-}1)$$

$$H_3BO_3 + 4HF \leftrightarrow BF_4^- + H_3O^+ + 2H_2O \quad (5\text{-}2)$$

Further hydrolysis of $TiF_{6-n}(OH)_n^{2-}$ can be represented as follows

$$TiF_{6-n}(OH)_n{}^{2-} \xrightarrow{H_2O} TiF_{5-n}(OH)_{n+1}{}^{2-} + H^+ + F^- \xrightarrow{(5-n)H_2O}$$

$$Ti(OH)_6{}^{2-} + (6-n)H^+ + (6-n)F^- \quad (5\text{-}3)$$

$$Ti(OH)_6{}^{2-} + 2H^+ \rightarrow TiO_2 + 4H_2O \quad (5\text{-}4)$$

Equation (5-1) demonstrates the hydrolysis of the titanium fluoro complex, which yields titanium hydroxide and free F^- ions. It will shift towards right with the addition of F^- scavenger boric acid (equation (5-2)). TiO_2 formation is achieved as shown equations (5-3 &4).

A type of representative work is to immerse cleaned glass/quartz slides into the prepared solution for extended hours.[1] Concentrations and ratios of AHFT and BA typically result in different degrees of supersaturation, thus influencing the formation and growth rate of the TiO_2 films. The calcination of LPD-induced films was also comprehensively studied[2] by varying calcination temperatures from 100-900 °C in air for 1 h respectively.

The thickness of the film deposited on a flat surface is dependent on the reactant concentration, reaction temperature and deposition time. For a 0.1 M AHFT and 0.3 M BA, a soaking at room temperature for 48 hours at pH 3.9 gave films with average thickness of 300 nm after calcination at 500 °C.[2] Another case with a similar concentration ratio reacted at 60 °C and pH~2.5 for 5 h followed by 500 °C calcination post-treatment resulted in 800-1000 nm.[3] This confirms that the growth and deposition of TiO_2 are endothermic, so that increasing the system temperature will speed the deposition.

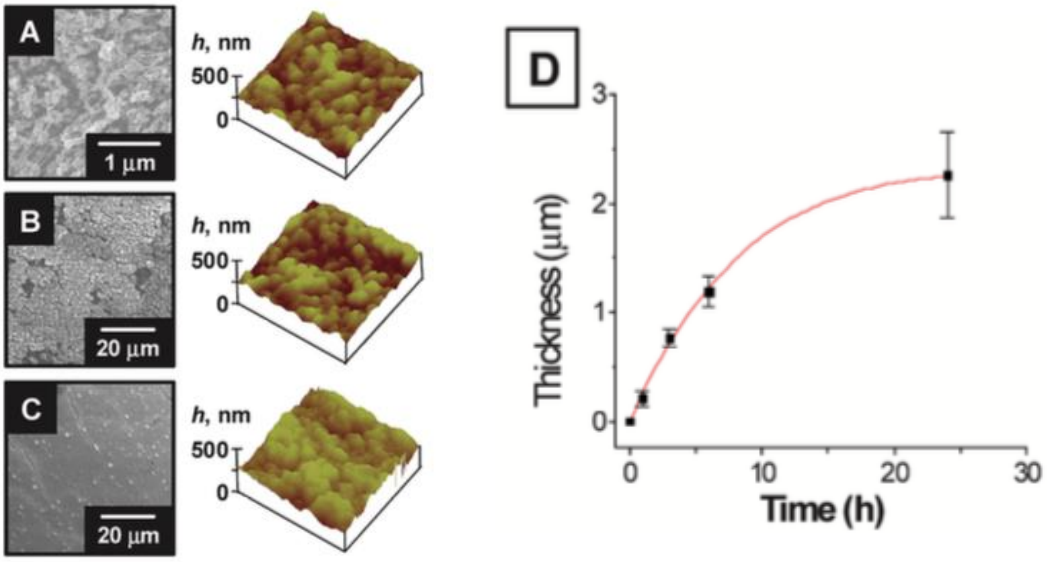

Figure 5-1 (A-C) SEM and AFM images of different LPD bath treatment times. (A) 3 h, (B) 6 h, (C) 24 h. (D) Growth of LPD titania layer thickness. [4]

As shown in Figure 5-1, at conditions such as 0.05 M AHFT/0.15 M BA, pH 2.88, temperature 50 °C with deposition time ranging between 3 h to 24 h, the thickness grew with prolonged reaction time. Similar observations are shown in Figure 5-2, where reactions with 0.05 M AHFT/0.2 M BA at 40 °C for up to 8 h were conducted. Film thickness increased with longer reaction time, while the depositing speed decreased. Once Ti^{4+} was consumed, the reaction would stop. Figure 5-2 (c) shows the ratio influence on the film thickness. A molar ratio of $H_3BO_3/[TiF_6]^{2-}$ =2~4:1 is suitable for the deposition. If the BA concentration is too low, scavenging of non-coordinated F^- will not be sufficient, making the hydrolysis of $[TiF_6]^{2-}$ slow. Thus, an excess amount of BA will lead to more amorphous TiO_2 because of the lack of F^- ions. [5] The growth rate of films was 43 nm/h at 40 °C while only 13 nm/h at 30 °C,[6] indicating that temperature is also an influencing factor.

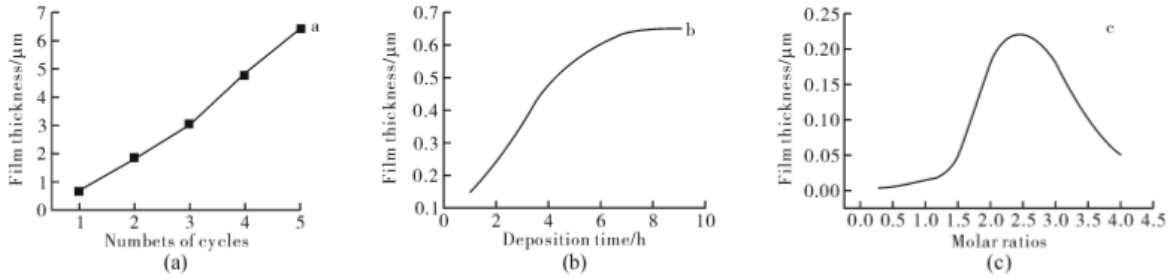

Figure 5-2 Influence of (a) cycles (b) time (c) molar ratios to the thickness of titania films. [5]

At pH lower than 2.5, the deposition amount was very limited because of the suppression of nucleation and crystal growth. However, when pH increases, the degree of supersaturation increases since the hydrolysis equilibrium shifts right. The difference is presented in Figure 5-3. By defining the theoretical and real solubility curves of $Ti(OH)_4$, an optimum range of pH was found for more efficient nuclei formation, and highly dense and transparent films.

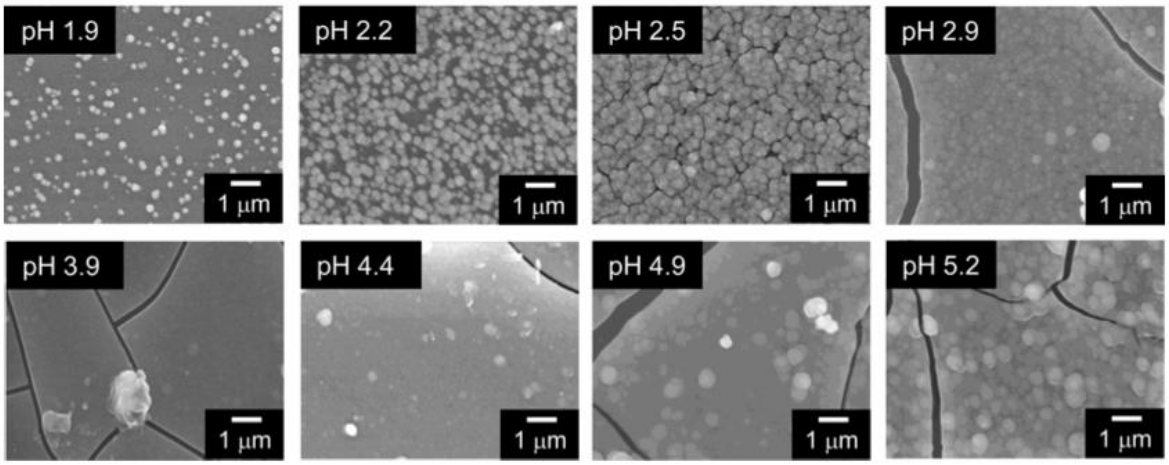

Figure 5-3 SEM images of annealed titania films made by LPD AHFT and BA with various pH values. [7]

TiF_4 in acidic media method:

Another type of precursor comes from a single titanium salt TiF_4, which has been deposited on different substrates such as glass slides, polymers, cotton fibers, filter paper, porous alumina membranes, by a similar mechanism in acidic aqueous environment. [8,9]

Typically, a 0.005-0.1 M TiF_4 aqueous solution is prepared with adjusted pH by hydrochloric acid (HCl) or ammonia (NH_4OH) solutions. Substrates, e.g., clean glass slides, filter paper, or polypropylene are immersed into the reactants, at temperature ranging between 25-70 °C for various lengths of time. The following wash in water and alcohol solvents cleans the excess precursor on the substrates and a gentle drying procedure will get the coated substrates ready for different further treatments.

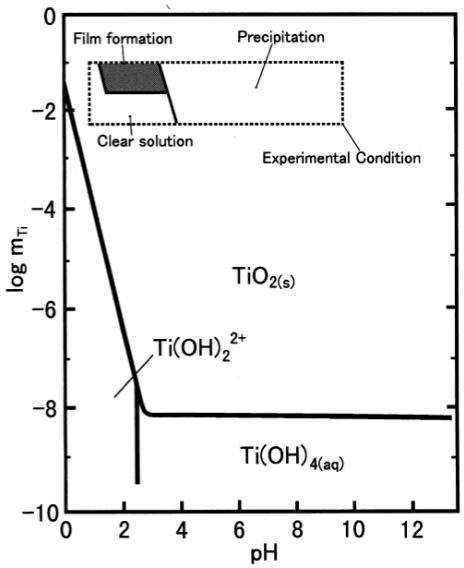

Figure 5-4 The relationship between Ti concentration, and pH level, with the deposition scale on the substrate.[8]

In a glass substrate experiment,[8] the concentration of TiF_4 was maintained at 0.03-0.1 M, pH at 1-3.1 and temperature at 40-70 °C. When pH was below 1.0, or the TiF_4 concentration was below 0.03 M, there was no precipitation nor film formation. When pH was larger than 3.1, the solutions were highly supersaturated, so many precipitates were observed while no film deposition formed on glass. Ideal deposition regions for heterogeneous nucleation on the substrates was between the highly supersaturated and the metastable. Different from using the F^- scavenger to adjust the supersaturation level,

pH is the key parameter for controlled deposition. The F^- ions bonded to Ti were assumed to suppress the ultra-fast hydrolysis conditions.[9]

The type of substrates for deposition would influence the film adhesion. The more hydrophobic the substrates were, the more easily the films peeled off. Firmly adherent titania films are usually formed on hydrophilic surfaces, which provides possibilities for site-selective growth and formation of patterned films.[10] The addition of surfactant n-hexadecyltri- methylammonium bromide ($C_{16}H_{33}N(CH_3)_3Br$, CTAB) into the solution help create smaller anatase particles, fewer cracks, and higher transparency, since CTAB retarded the crystalline growth on the particle surface.

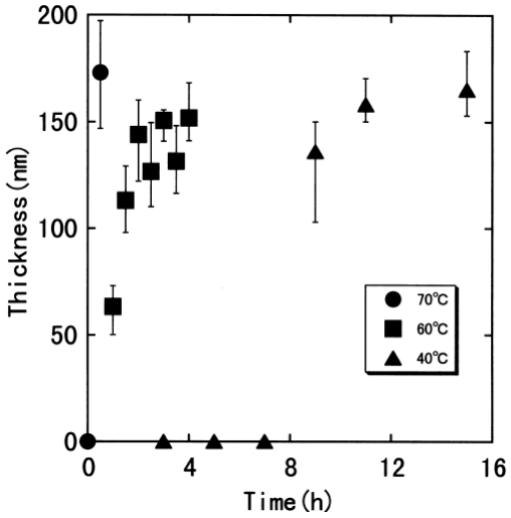

Figure 5-5 Relationship between thickness of the deposited film and reaction time.[8]

The diameter of the deposited particles was proportional to the deposition time, and the transparency of the film decreased at longer reaction time. When the reacting temperature was low (~40 °C), not much deposition was formed during the first 8 h, confirming that higher temperature did promote the film formation from Figure 5-5. Even without calcination, the titania showed anatase crystallinity.[8]

Shapes can be well controlled by choice of substrates, resulting in nanorods,[9] micro-hollow fibers,[11] mesoporous titania nanorod/titanate nanotube composites,[12] and other hollow structures.[13]

Some researchers also applied boric acid into this titanium tetrafluoride method.[12] The reaction was performed at 60 °C for 12 hours. With a comparatively lower TiF_4 concentration at 0.025 M, the addition of 0.075 M boric acid help shift the hydrolysis equilibrium to the right. Hydrothermal-made amorphous titanate nanotubes (d=7-12 nm, l= several hundred nm) acted as the substrates for liquid phase deposition, and ultrafine nanorods (d=5-10 nm, l=15-40 nm) were uniformly coated on the surface of the titanate nanotubes. The resultant composites obtained higher surface area and larger pore volume compared to titanate nanotubes or P25 particles, leading to an enhancement of the photocatalytic performance for the oxidation of acetone.

Some other work, interested in removing templating substrates *in situ*, developed a vanadium oxide nanobelts directed deposition with one-step HF dissolution of the template.[13] At a TiF_4 concentration between 0.005 M and 0.1 M, vanadium oxide nanobelts were added into the 60 mL TiF_4 solution at 60 °C for 12 h. The concentration of the byproduct HF increased during the immersion time, and gradually dissolved the vanadium oxide until completely consumed. The concentration of TiF_4 is the key factor to determine the thickness of the hollow wall, in other words, the amount of the deposition.

More and more work reveal that solution concentration and temperature are tightly related to the crystal growth and deposition rates. Comparatively higher concentration and temperature resulted in more supersaturated system, leading to faster and complete

deposition.[10] The pH of the whole system dropped at the beginning due to the byproduct HF, then changes only very slowly for an extended time. In this same paper, a detailed three-step deposition procedure was brought up as follows[10]:

(1) Initial delay: at this stage, the thickness had a very limited increase, but only for lower temperature and lower concentration conditions. For highly saturated systems, the initial delay could be hardly observed. (2) Fast growth: during this stage, nuclei on the surface are ready to grow into crystals, governed by a first order kinetics (3) Growth saturation: after a deposition thickness of ~500 nm at favorable temperature and concentration; for low-temperature solutions, this stage could not be reached even after 70 hours.

However, films made in this way tend to be dense, especially denser as the temperature of annealing goes up. An alternative approach is desired to improve the surface area and the porosity of the titania nanoparticles on the film. Recently, researchers have accomplished the immobilization of titania nanoparticles via a TiF_4 LPD method on a silicone nanofilaments-coated glass substrate.[14] Silicone nanofilaments were prepared from trichloromethylsilane (TCMS) in a custom-built chamber with precisely controlled water ratio. Plasma treatment was followed to induce hydrophilicity on the surface of the silicone as a prerequisite for further LPD functionalization. TiF_4 was the titanium source in a series of ethanol/water solvents (with adjusted polarity) at different temperatures. Titania nanoparticles with sizes 50-90 nm were synthesized after calcination and the photocatalytic capacities were investigated by methyl blue degradation.

In Chapter 3, preliminary experiments were conducted on large-scale cellulose fibers like cotton wool fibers and filter paper with AHFT/BA, and TiF_4 acidic conditions. We discussed the hollow tubular titania prepared and the unique properties of MFCs. In Chapter 4, sol gel synthesis of porous titania via MFCs proves the benefits of MFCs as templates. In this chapter, MFCs were studied for bulk material fabrication, and thin film coating via LPD. The photocatalytic capacities were tested through methyl orange degradation.

5.2 Experimental

5.2.1 Materials and equipment

Materials:

All chemicals were used without pre-treatments unless noted. MFCs in isopropanol (IPA) were processed by Mini DeBEE ultrahigh-pressure homogenizer as Chapter 3 described. Titanium(IV) fluoride, boric acid (≥99.5%), ammonium hexafluorotitanate (99.99%), methyl orange (≥ 85% dye content, certified by Biological Stain Commision), ethanol (A.C.S. reagent), 2-propanol (A.C.S. grade, ≥ 99.5%) were purchased from Sigma Aldrich. Hydrochloric acid (analytical reagent grade) was from Mallinckrodt. Ethanol (200 proof, 99.5% ACS grade) and isopropanol (99.5%) were purchased from Michigan State university stores. Plain, pre-cleaned micro glass slides were purchased from VWR international, in a size of 1 inch by 3 inches, with a thickness of 1.2 mm. Mineral oil (laboratory grade, heavy) was from Columbus Chemical Industries.

Equipment and Characterizations:

(1) The structures of the organic/inorganic composite films, colloidal crystals and mesoporous annealed films were characterized by scanning electron microscopy (Carl Zeiss Auriga CrossBeam SEM-FIB). Film samples were prepared by necessary drying and gold or tungsten coating before loading into SEM chamber. Free-standing powder samples were prepared by mounting onto a holder with carbon paste/tape after. EDAX™ EDS Analysis System for SEM–X-ray Microanalysis was applied together with SEM characterization for element analysis on films before and after calcination. When a cross-sectional view was necessary, a focused ion beam (FIB) was used to mill surfaces of the materials.

(2) The transmission electron microscopy (TEM) images, high-resolution transmission electron microscopy (HRTEM) images, and selected-area electron diffraction (SAED) patterns were taken on a JEOL 2200FS equipment. TiO_2 films were scraped off from glass substrates and then dispersed in ethanol by bath sonication for 0.5 h. The ethanol/TiO_2 suspension was dropped and dried on a carbon-coated 400 mesh copper grid overnight before TEM analysis. Under HRTEM mode, fast Fourier transfer (FFT) patterns were utilized to optimize image quality with DigitalMicrograph (DM) software.

(3) A single wafer spin processor (WS-400A-6NPP/LITE) was purchased from Laurell Technologies Corp and used for film coating. Part of the doctor blade method was completed by a manual Scotch tape method with a clean, sharp razor blade, while part of the doctor blade used the MSK-AFA-III compact tape casting coater with a vacuum chuck. This doctor blade machine has an adjustable micrometer film applicator (thickness 0.01-3.5 mm, or fixed thickness at 5 um, 10 um, 15 um and 20 um) with a 100-mm width, as well as a dryer cover that heats up to 100 °C.

(4) A UV-Vis spectrophotometer (Perkin Elmer Lambda 900 UV Spectrometer) was applied for TiO_2 films absorption and transmission characterizations. The UV-Vis absorption spectra of the TiO_2 films were recorded in the range of wavelength 300-800 nm. An integrating sphere attachment was used for diffuse reflectance measurements to establish the optical band gap and the transition before and after photocatalytic dye degradation. The TiO_2 films were placed at the entrance port of the integrating sphere and measured in the 250-800 nm wavelength range. Data was arbitrarily normalized before comparison.

(5) Fourier transform infrared (FTIR) absorption spectra were collected with Perkin Elmer 2000 Spectrum One FT-IR spectrometer at room temperature. KBr Pellets were prepared by Carver Laboratory press (model 2518) with ground and pre-dried KBr powder. For liquid samples, a drop of solution was cast between two pellets forming a sandwich structure with the excess liquid squeezed out and wiped off. For solid samples, KBr powder was mixed with samples with a sample weight ratio of ~0.2% w.t. The spectra of the composites were scanned from 4000 to 400 cm^{-1}.

(6) XRD: The crystallographic structures of the solid samples were determined with XRD, Bruker Davinci Diffractometer. A LabRAM ARAMIS laser Raman spectrometer (Horiba Scientific) with 532 nm 50 mW DPSS laser was used to inspect sample crystal phases as well. All the samples were tested as is with a 50X objective lens. The resolution in Raman spectrometer could be decided by the spectrometer focal length, diffraction grating, laser wavelength, and the detector. The higher the groove density of the grating is, the higher the spectral resolution. The gratings used in this work is 1800 gr/mm and results in a spectral

resolution of about 1.5 m^{-1}. The laser power at the sample ranged in 1-3 mW, and the 1/e laser spot size was about 2 μm at the sample.

(7) Thermogravimetric analysis (TA instruments Q500) used a high-resolution ramp of 25 °C/min to ~800 °C in air or nitrogen on TiO_2 samples. Surface area and pore size data were collected with Brunauer–Emmett–Teller (BET) Micromeretics ASAP 2020. As for thin film samples, films were scraped off and collected for analysis. To further remove moisture and impurities, samples were degassed at 150 °C for over 4 hours under vacuum.

(8) X-ray photoelectron spectroscopy (XPS) was using a Perkin Elmer Phi 5400. The Kα line of Mg (1254 eV) X-ray source with a beam voltage of 15 kV and current of 20 mA was the excitation source. The survey spectra scan were acquired with a pass energy 187.85 eV, and a 1 eV step size. For detailed C 1s or O 1s high resolution spectra, a pass energy of 29.35 eV and step size 0.1 eV were used. Chamber vacuum was maintained below 1×10^{-7} Torr (1.33×10^{-5} Pa). The sample to be tested was mounted onto the sample holder with double-sided copper tape, and as for powder form samples, a thin but dense layer of powder was spread on the tape with excess removed. After the measurement, data processing was performed by MultiPak V8.0. If not mentioned, the spectra have been resolved into chemically shifted components by a non-linear least squares procedure.

(9) Photocatalytic reactions were conducted with an RC-500 Xenon UV lamp (Xenon Corp., Wobrun, WA) that has 300 W power, 120 Hz frequency, and a 5-inch linear bulb shape. The lamp was equipped with aluminum reflectors and fused quartz windows to provide optimum transmission of UV radiation. The lamp housing was made of metal, and a forced air convection removed the generated heat. The pulsed xenon arc lamp has a

continuous radiation spectrum as shown in Figure 2-8. The top right image also illustrates that the active time span of each pulse is 100 us, while the interval rest time is 8.3 ms. The range of operating UV wavelength lies between 230 and 360 nm. Applying a Pyrex glass cover as a filter will remove ultraviolet wavelength region beneath 290 nm.

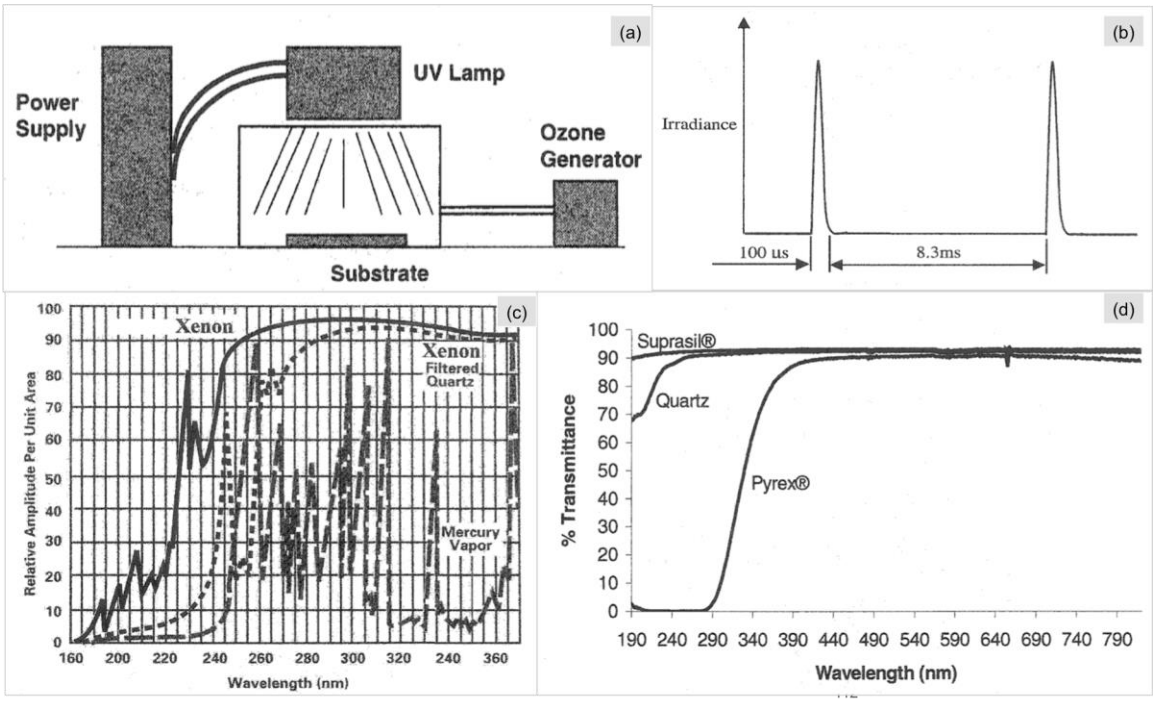

Figure 5-6 (a): the scheme of the UV lamp system (Ozone was not applied in this work). (b): the schedule of the pulsed wave. (c): wavelength range of the outputs from the pulsed xenon UV lamps. (d): UV transmittance of Surasil, quartz, and Pyrex glass filters[source: Xenon Corp.

(10) A HIMONT Plasma Science PS 0500 Plasma Surface Treatment System was used to clean the glass substrates for ~0.5 h. The oxygen pressure was 0.27 Torr, and the power was 300W.

5.2.2 Synthesis of TiO_2 bulk material via TiF_4- MFCs LPD method

At the beginning of research, two methods to combine TiF_4 and cellulose were studied. One method was to make TiF_4 dissolved in water at a concentration of 0.08 M with a pH value around 2.5, and then add the prepared solution into the same volume of MFCs/water,

capped and reacted in an oil bath at 65 °C for 8 h. A turbid and white sol was generated and the sol was dried and calcined at 250 °C and 450 °C for 1 hour each. Another approach was to add the corresponding amount of TiF_4 directly into the MFCs/water to achieve a 0.04 M TiF_4 concentration. After heating at 65°C for 8h, the precursor was also annealed at two-stage temperature for 2 h in a crucible. Water only without template was tried for comparison, with all other conditions kept at the same(the process is summarized in Figure 5-7 below).

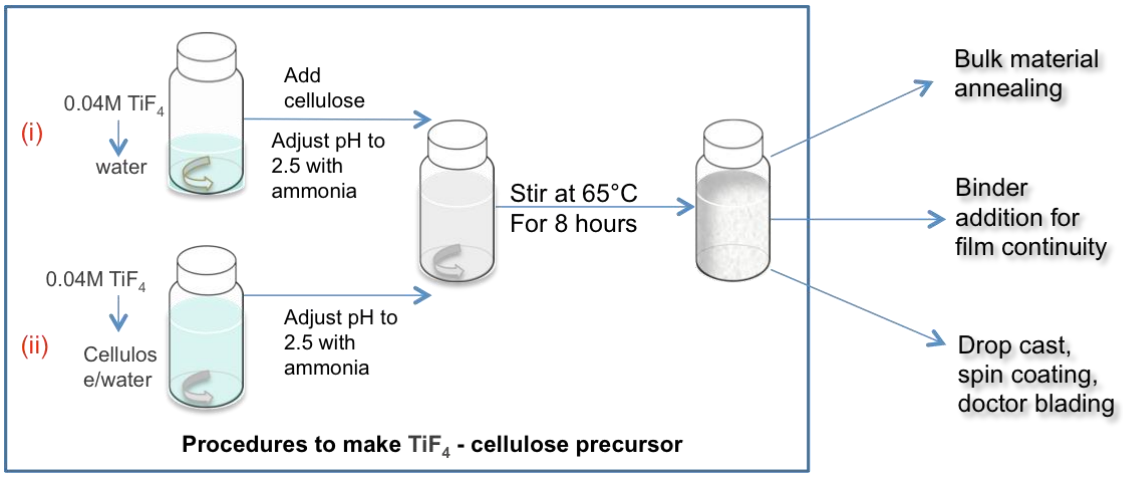

Figure 5-7 Scheme of TiF_4- MFCs precursor preparation

5.2.3 Synthesis of porous TiO_2 thin films via TiF_4- MFCs LPD method

A 0.04 M TiF_4 solution was prepared by adding 0.0991 g TiF_4 into a vial with 20 mL 5 mg/mL MFC-water suspension while stirring. After one-hour mixing at room temperature, the pH was adjusted to ~2.5 by the addition of diluted hydrochloric acid or ammonium hydroxide aqueous solutions. Then the vial was capped and transferred to a pre-heated mineral oil bath at 65 °C on a stirring hot plate. The reaction went for 6 hours and the mixture was cooled down to room temperature before further use.

Solvent polarity was manipulated by changing the ratio of the MFC/isopropanol and MFC/water. A series of ratios of isopropanol to water suspensions (I/W) = 0:1, 1:1, 4:1, and 1:0 was investigated with same procedures as above. A drop cast film was made with 0.1 mL stock solution and dried in vacuum oven for 1 h at room temperature, followed by increasing temperature to 100 °C for 1 hour and a step-wise annealing at 200 °C, 250 °C, 300 °C, 350 °C for 15 minutes each, with a finishing 450 °C session for 1 hour. The whole process could be demonstrated in Figure 4-3. To compare between MFC suspension and solvent only reagents, similar I/W ratios were utilized for a set of TiF_4 deposition reactions as well.

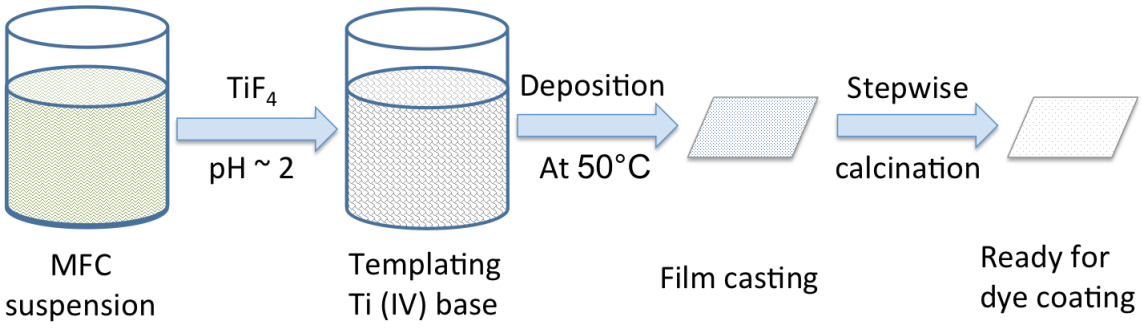

Figure 5-8 Scheme of MFCs-templating TiF_4 LPD thin films on glass.

5.2.4 Measurements of photocatalytic performance of porous titania thin films

The photocatalytic performance was evaluated by monitoring the degradation of methyl orange (MO) aqueous dye solution with the illumination of Xenon RC500 lamp. MO solution with a concentration of 5×10^{-4} M was prepared and kept in a capped glass container. Diffuse Reflectance Spectroscopy (DRS) was chosen to keep track of the reflectance change during the whole process. Typically, for a series of tests, the first data point was taken on a pristine as-prepared TiO_2 film (treated with plasma). The second was taken on the same film with a coating of 10 μL 5×10^{-4} M solution, left in darkness to reach

equilibrium and solvent evaporation for 0.5 hour. Then UV treatment was started in a manner of 1 min, 2 min, 2 min, and 2 min, where films were located 2.5 inches underneath the UV lamp, with a Pyrex petri dish lid to remove the extremely strong short waves below 290 nm (Figure 4-4). After each treatment, a data point was recorded as well.

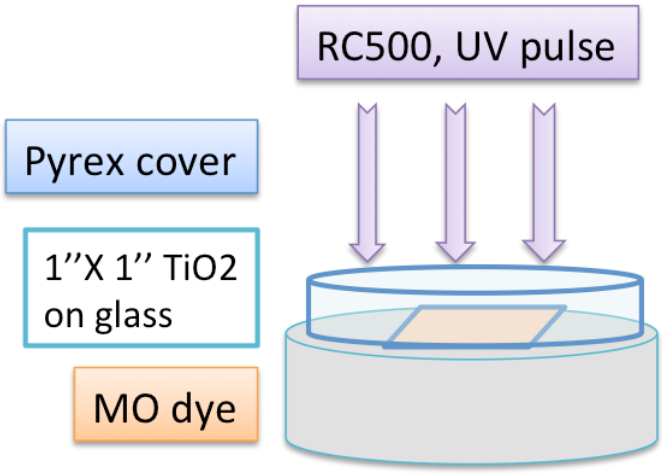

Figure 5-9 Scheme of photocatalytic degradation experiment

5.2.5 Synthesis of porous titania network via ammonium hexafluorotitanate and boric acid LPD method

Additional titania thin films were prepared via liquid phase deposition with MFCs and drop cast coating. A stock solution of Ti^{4+} (0.05 M) was prepared by mixing a homogenized MFCs/water suspension with ammonium hexafluorotitanate (AHFT) (0.05 M) and boric acid (BA) (0.15 M), followed by vigorous stirring for 1h at room temperature. The prepared stock solution (pH adjusted to ~2.5) was then moved to a 50°C oil bath to react for 20h. After the reaction, the solution turned from translucent to white. For comparison, different ratios were prepared between BA and AHFT as 0.15:0.05, 0.15:0.15, 0.15:0.30, and 0.30:0.15 M. Films were prepared using doctor blade on glass substrate, dried in air at room temperature, then a vacuum oven at 80°C, and finally annealed at 250 °C and 450 °C for 1 h each.

PEG as a binder could improve the viscosity and continuity of the precursor. After 6-hour LPD reaction, various amounts of PEG were added and kept stirring for two more hours. Films were prepared via doctor blade then.

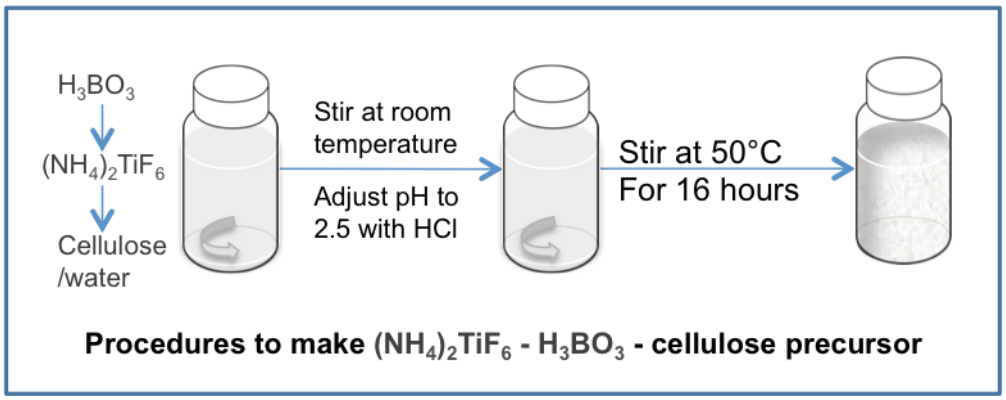

Figure 5-10 Scheme of AHFT-BA/MFCs synthesis

5.3 Results and Discussions

5.3.1 TiF_4- MFCs bulk materials

When the precursor was calcined as bulk materials in crucibles, uniform cubes of titania were formed. Figure 5-11 shows the bulk calcined materials at different magnifications. Cellulose provided a substrate for nucleation and growth, and while the deposition continued, surface crystals kept growing. This is suspected to result from the fluoride-stabilized {001} facets. [15] Nanoparticle grains were characterized in Figure 5-11 (c) where the cubes were connected by particle edges as well. The cube length is around 200 to 300 nm. The mechanism of TiO_2 formation is explained by equations below:

$$TiF_4 + nH_2O \leftrightarrow TiF_{4-n}(OH)_n + nHF$$

$$TiF_{4-n}(OH)_n + (4-n)H_2O \rightarrow Ti(OH)_4 + (4-n)HF$$

$$Ti(OH)_4 \rightarrow TiO_2 + 2H_2O \quad \text{(f)}$$

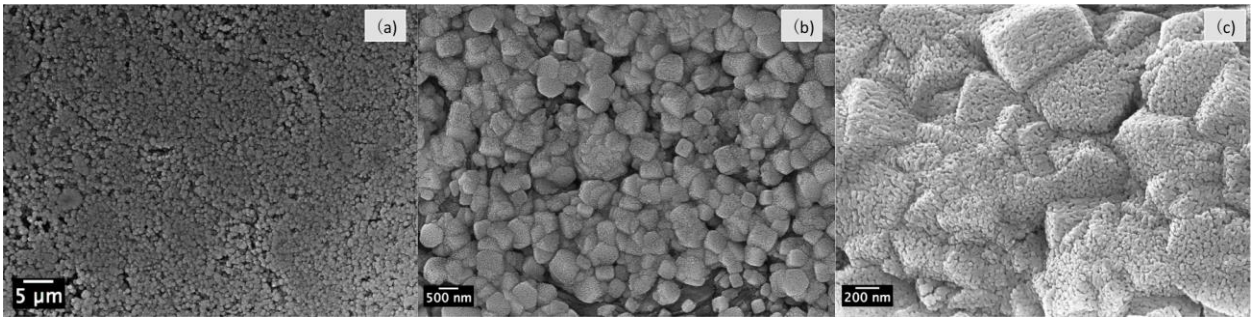

Figure 5-11 0.04 M TiF_4 in 20 mL IPA/water suspension, calcined as bulk material. (a), (b), (c) are the same area with increasing magnifications.

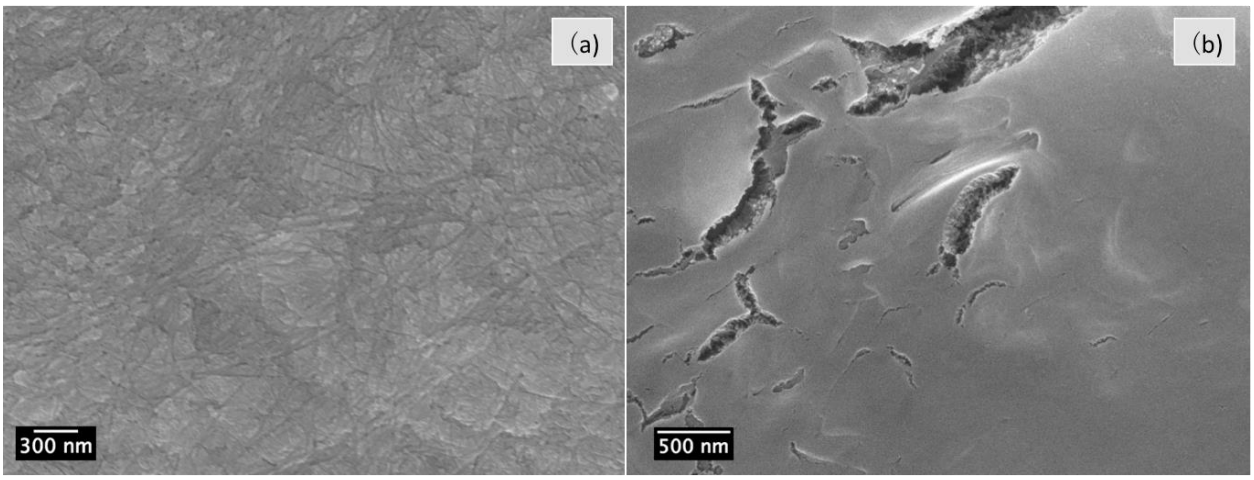

Figure 5-12 0.04 M TiF_4 in 20 mL IPA/water suspension, calcined as bulk material. pH adjusted at 4 during deposition reaction.

TiF_4 went through step-wise hydrolysis and condensation to become TiO_2. It does not use F^- as a scavenger, but by controlling pH level, the supersaturation could be manipulated as well. When pH is below 1, inefficient hydrolysis step prevents the deposition. When pH is above 3, precipitation is preferred so the solution is highly supersaturated with titania rather than forming a uniform coating on substrates. When pH is between 1 and 3, due to the stability of Ti-F bonds, rapid hydrolysis and polymerization of the precursor do not occur here. Instead, a moderate reaction leads to a stable deposition through heterogeneous nucleation.[9] A pH level of 2.5 was selected through experiments for cellulose templating to make bulk materials and thin films. The morphology of TiO_2

induced by precursor with higher pH at 4 is shown in Figure 5-13, where the supersaturation results in dense films with fewer particles and secondary particle grains.

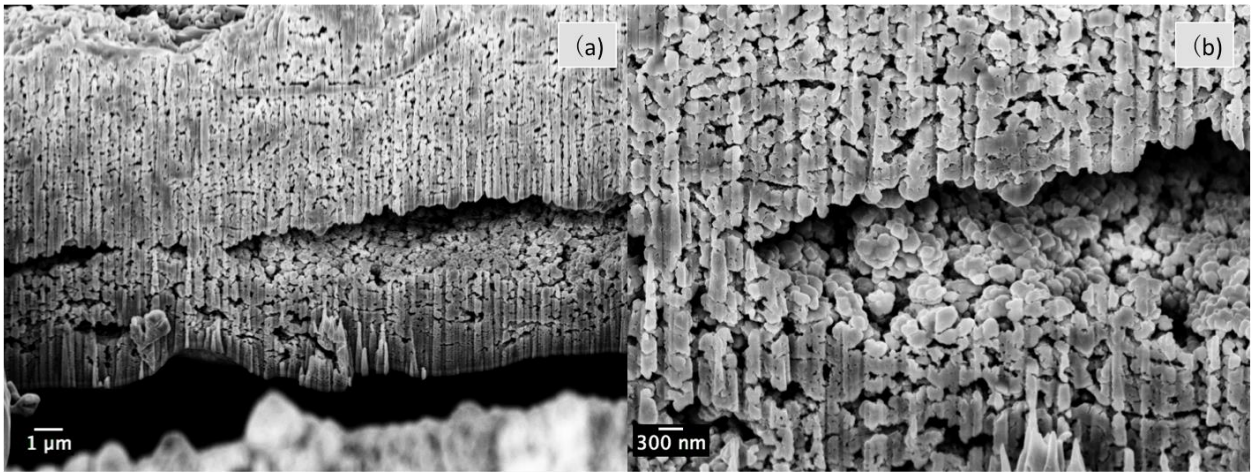

Figure 5-13 0.04 M TiF_4 in 20 mL IPA/water suspension, calcined as bulk material. FIB-cut cross section (a), (b) are taken from the same area with increasing magnifications.

Figure 5-13 reveals a highly porous surface at the ion beam cut cross section. The inner part of the bulk materials had cracks and variable pore sizes. It indicated the removal of cellulose fibers, and the difficulty of preparing a more ordered nanoporous network.

As comparison, samples made with TiF_4 only without cellulose templates were tested as shown in Figure 5-14. When no cellulose was applied, the base precursor was calcined into randomly distributed particles. When the focused-ion beam was used to cut through the particles, large dense aggregates without patterned nanopores or mesopores were revealed.

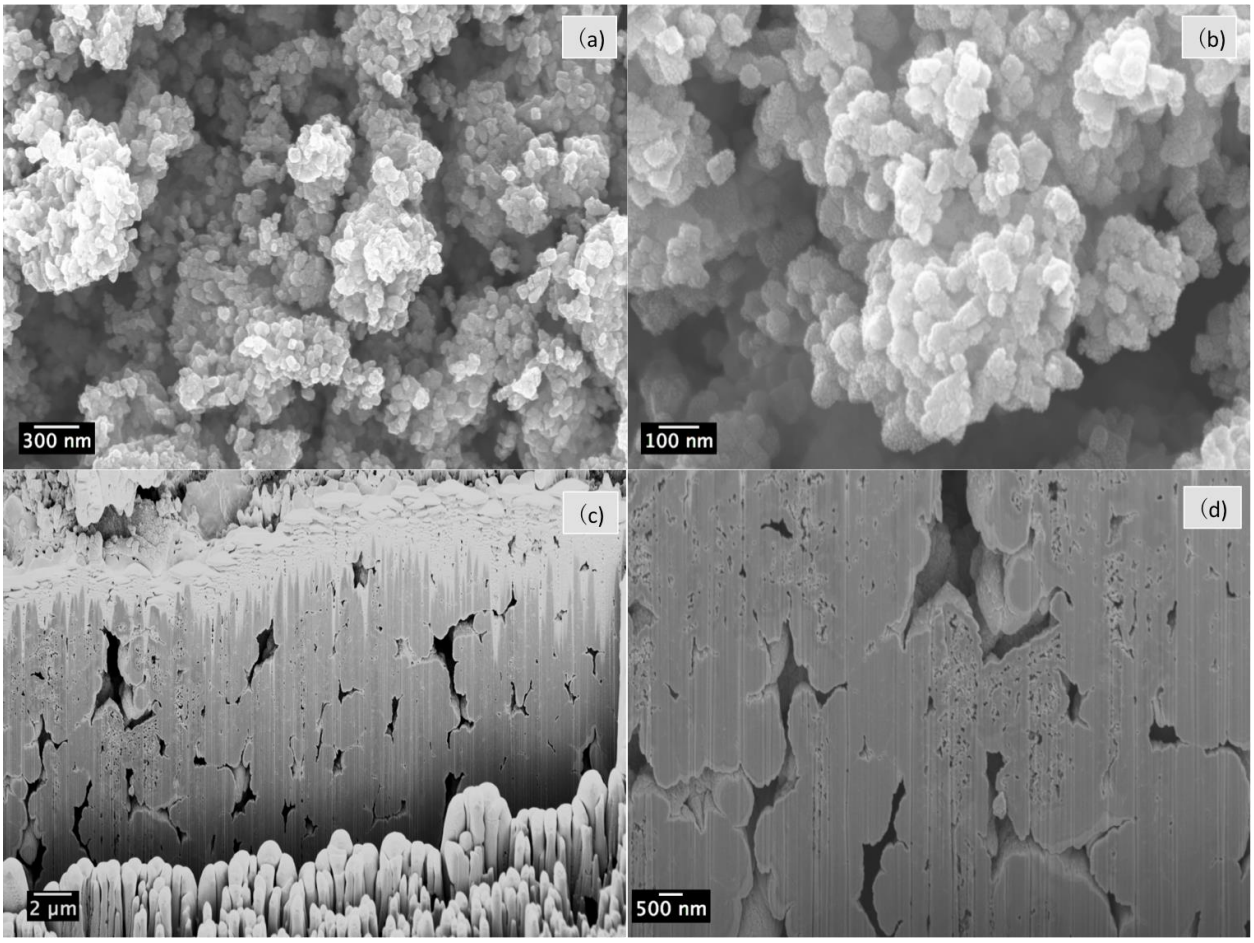

Figure 5-14 0.04 M TiF_4 in 20 mL water, calcined as bulk material. (a) and (b) are surface features at same area with increasing magnifications. (c-d) FIB-cut cross-sectional view at increasing magnifications.

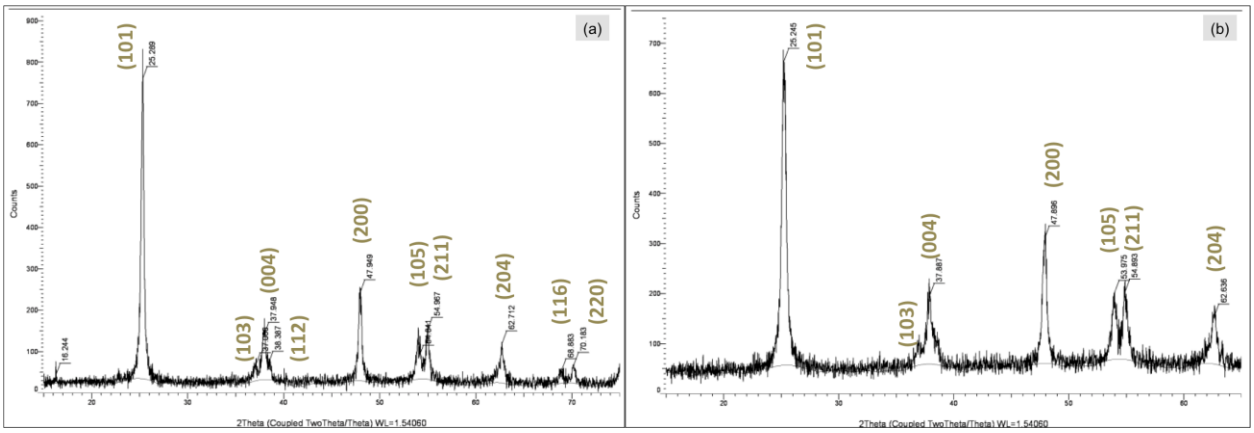

Figure 5-15 XRD patterns of (a) TiF_4 and water precursor, calcined bulk material, (b) TiF_4 and MFCs/Water, calcined bulk material.

The products were in anatase phase from the characteristic peaks labeled in Figure 4-5. Both samples were detected with peaks at around 25.3, 38.2, 48.2, 54.0, 55.2 and 63.0

°, which represented plane (101), (004), (200), (105), (211) and (204) [JCPDS 78-2486]. Crystal sizes were calculated using the Scherer Equation:

$$D = \frac{k \cdot \lambda}{\beta \cdot cos\theta}$$

D: crystal size

k: constant=0.89

λ: X-ray wavelength, 1.5406 Å

β: full width at half maximum of the peak

θ: half the Bragg's diffraction angle of the peak

The results from the XRD spectrum were, 27.9 nm for pure TiF_4 induced TiO_2, and 18.5 nm for TiF_4 with cellulose templating TiO_2. Besides, surface area tested by BET was 112 m^2/g.

5.3.2 TiF_4- MFCs induced TiO_2 with tunable sphere chain morphology

To improve the photocatalytic capacity of titania, we consider several aspects such as: the adsorption of pollutants, the absorption of photons, charge separation, the reactivity of the surface sites, recombination rate of photogenerated electron-hole pairs. When this consideration is applied to materials, it brings up higher surface area, better crystallinity, beneficial morphology and nanostructures.

5.3.2.1 Surface properties of TiO_2 films and related materials

Scanning electronic microscope (SEM):

As-received cellulose was treated with high-pressure homogenization which transferred the large and aggregated fibers into reduced sizes and suspended extensively in the solvent (water and IPA). Homogenized MFCs are generally 30 nm in diameter, with length in micrometers or longer as shown in Chapter 3.

Figure 5-16 illustrates the influence of cellulose templates and the effect of the percentage of isopropanol in the solvent for calcined thin films on glass substrates. Figure 5-16 (a) indicates that without the addition of cellulose, a film with huge cracks and large aggregates of TiO_2 particles larger than 10 um was formed. From Figure 5-16 (b) to (d), TiF_4 solutions were prepared with MFC suspensions, respectively, at isopropanol to water (I: W) ratios 0:1, 1:1, and 4:1. As the isopropanol ratio increased to 4:1, a uniform of spherical nanoparticles were formed along the chain of MFCs with a diameter around 200 nm.

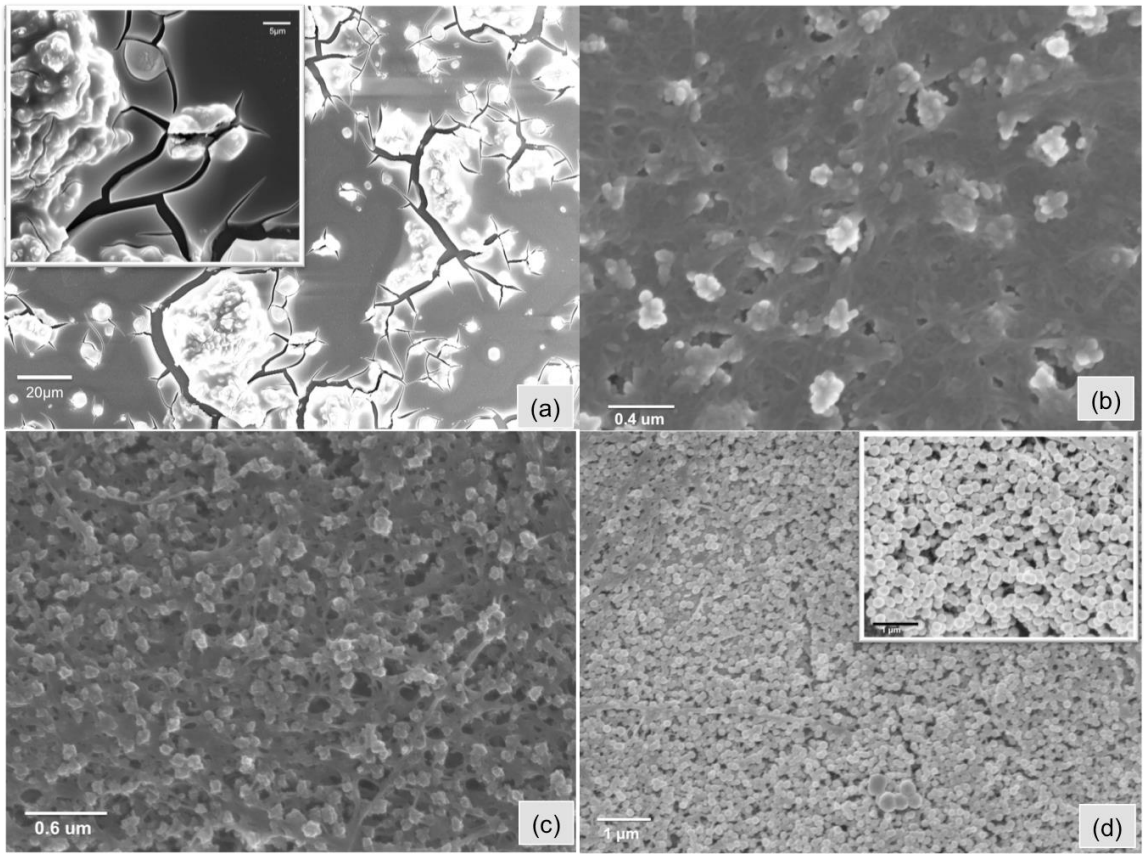

Figure 5-16 SEM images of 4 samples without and with MFCs templates, at different isopropanol to water (I: W) ratios. All reactions last for 6 hours, and films were coated and calcined. (a) Without MFC templates, 0.04 M TiF_4 in water. The inset image scale bar reads 5 um. (b-d) With MFC templates, at I: W ratios 0:1, 1:1, and 4:1 respectively. The scale bar of the inset image of (d) reads 1 um.

Figure 5-17 and Figure 5-18 compare the influence of time and TiF_4 suspension on the film morphologies. When water was the reaction environment, large cracks formed on the surface of the film, and as reaction time accumulated, the film was denser and thicker, while cracks larger. When MFCs/water was the reaction environment, the film was covered with a few aggregations of titania particles, and some porosity was visible. Also, as time went by, more and more aggregations formed on the surface of the film, even the removal of cellulose templates could not contribute much to the porosity formation.

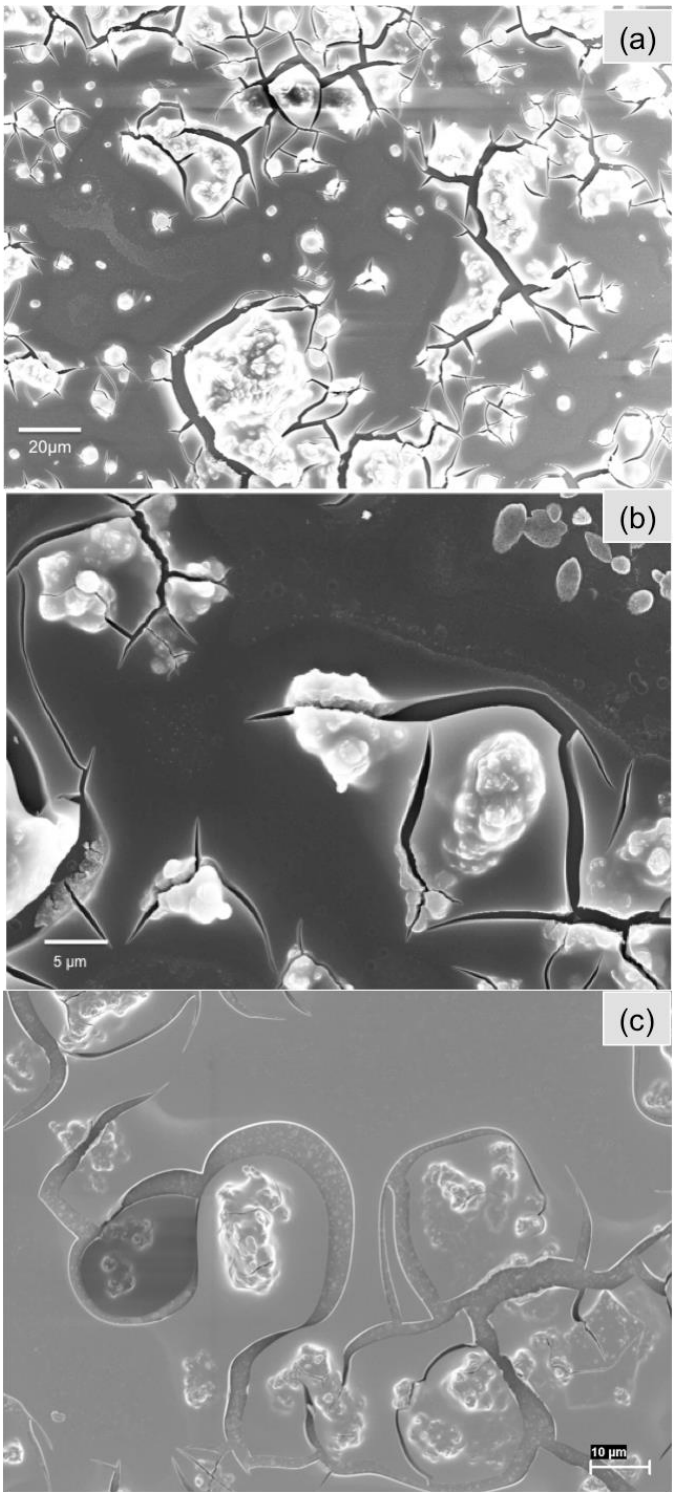

Figure 5-17 0.04 M TiF_4 reacted in H_2O for (a) 6 hours, (b) 15 hours, and (c) 40 hours.

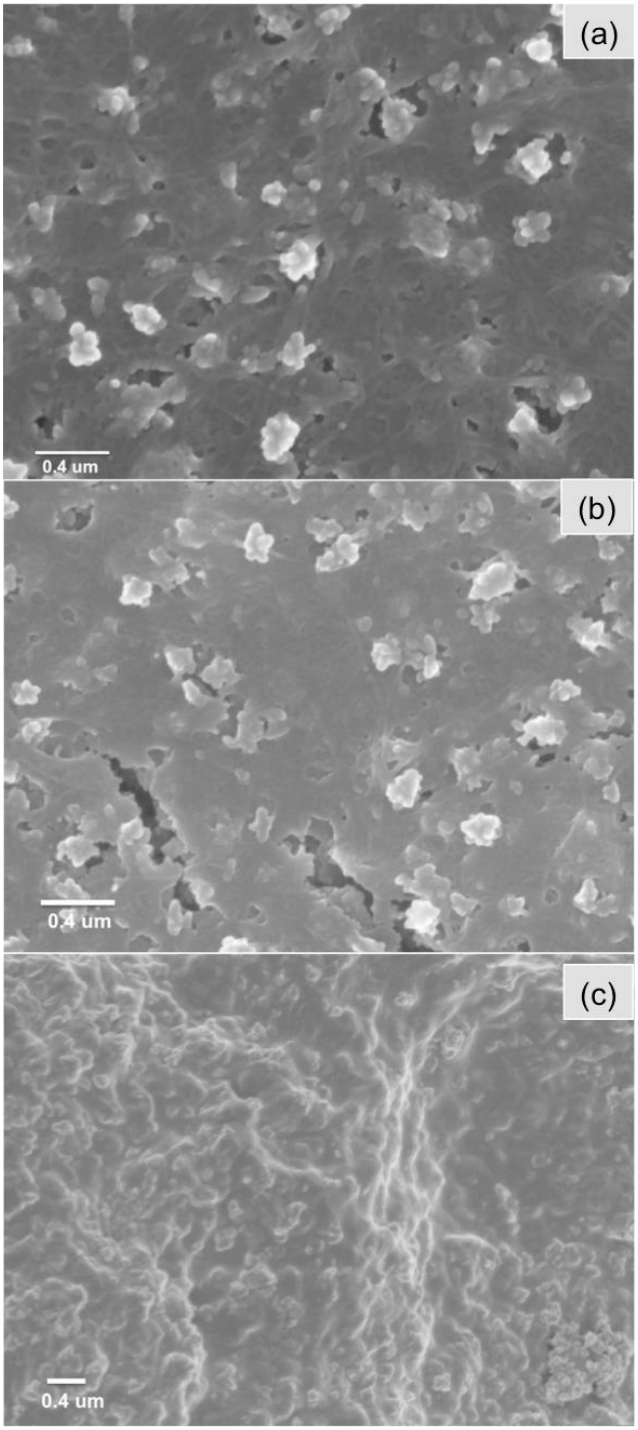

Figure 5-18 0.04 M TiF_4 reacted in 5 mg/mL MFC water suspension for (a) 6 hours, (b) 15 hours, and (c) 40 hours.

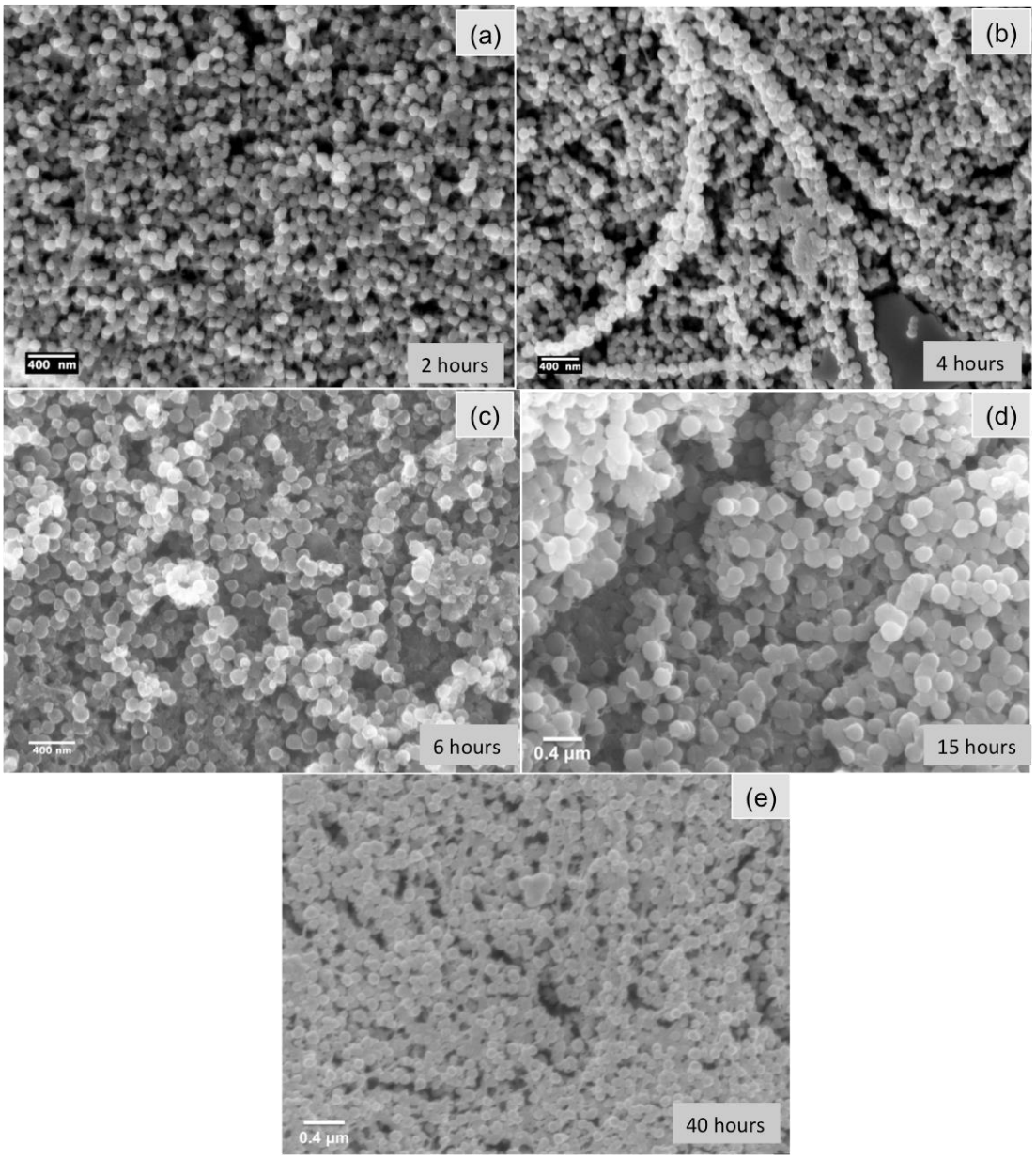

Figure 5-19 0.04 M TiF_4 reacted in 5 mg/mL MFC water and isopropanol suspension mixture at I:W = 4:1 ratio for (a) 2 hours, (b) 4 hours, (c) 6 hours, (d) 15 hours, and (e) 40 hours.

Size variations based on different reaction time lengths are summarized in Figure 5-19 and Table 5-1. Sizes were measured based on around 75-150 data points, collected and calculated by Image-pro Plus 5.0 for each sample. The size of the spherical particles grew larger as the reaction time increased, and reached the top at around 14 hours, while started to decrease at prolonged reaction times. As for samples reacted for the same 6-hour period,

the uncalcined amorphous particle size was 14% larger compared to the annealed samples. TiO_2 formed using bulk calcination (precursor stock solution calcined directly in a crucible with the same manner of temperature control) had smaller spheres as well.

Table 5-1 Summary of particle size formed of the I: W= 4:1 sample, with different reaction time and treatments

TiF_4-Cellulose-4IPA-1H_2O , with various treatment methods	**Spherical particle mean size (nm)**	**Standard deviation (nm)**
2-hour reaction, calcined	101.8	8.4
4-hour reaction, calcined	111.0	8.3
6-hour reaction, calcined	125.4	10.3
14-hour reaction, calcined	187.3	11.8
40-hour reaction, calcined	139.1	13.3
6-hour reaction, dried in vacuum, uncalcined	142.4	14.4
6-hour reaction, bulk calcination	114.2	10.8

The chain-like uniform sphere structures were present not only on the surface of the film, but on the back of the film, and the cross-sectional area. Figure 5-20 (a) shows the back of the film, where the inset is a piece of partially-lifted film. Figure 5-20 (b) shows the cross-sectional linking between the spherical particles which followed the tangled pattern of MFCs. When no water was applied in the reaction media, a similar structure with fewer nanoparticles and porous fibril TiO_2 formed on the surface of the calcined films as shown in Figure 5-21.

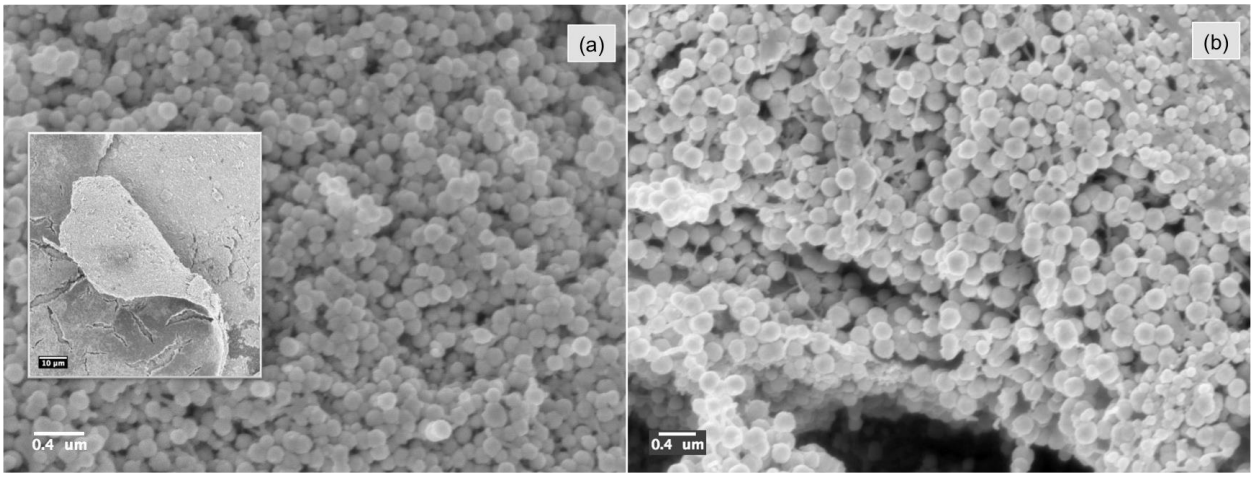

Figure 5-20 The three-dimensional in-depth view of titania film made with the TiF_4- with MFCs in I: W=4:1 suspension. (a) The reverse side of the film, from the inset image of (a). (b) The cross-sectional view of the film.

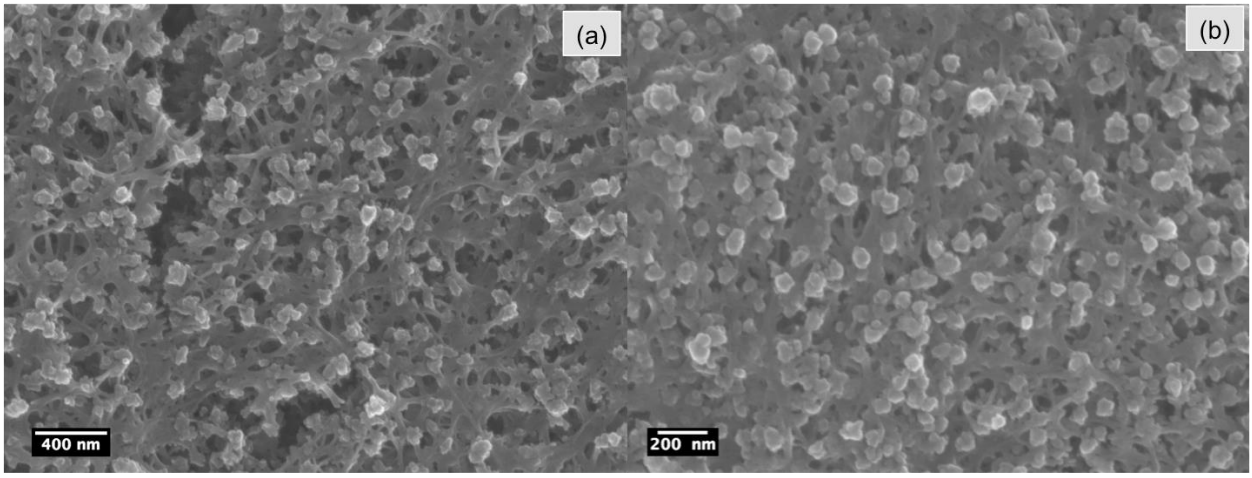

Figure 5-21 0.04 M TiF_4 reacted in 5 mg/mL MFC isopropanol suspension at I: W = 1:0 ratio for 6 hours. Calcined films morphologies.

To understand better how cellulose was guiding the crystal growth of titania, more SEM images were obtained for various sample films before calcination. Figure 5-22, Figure 5-23 and Figure 5-24 provide the information at different magnifications separately. The amount of the patterned spherical particles was increased as the I: W ratio changed from 0:1, to 1:1 and finally to 4:1. Spherical particles before calcination had similar sizes at around 140 nm.

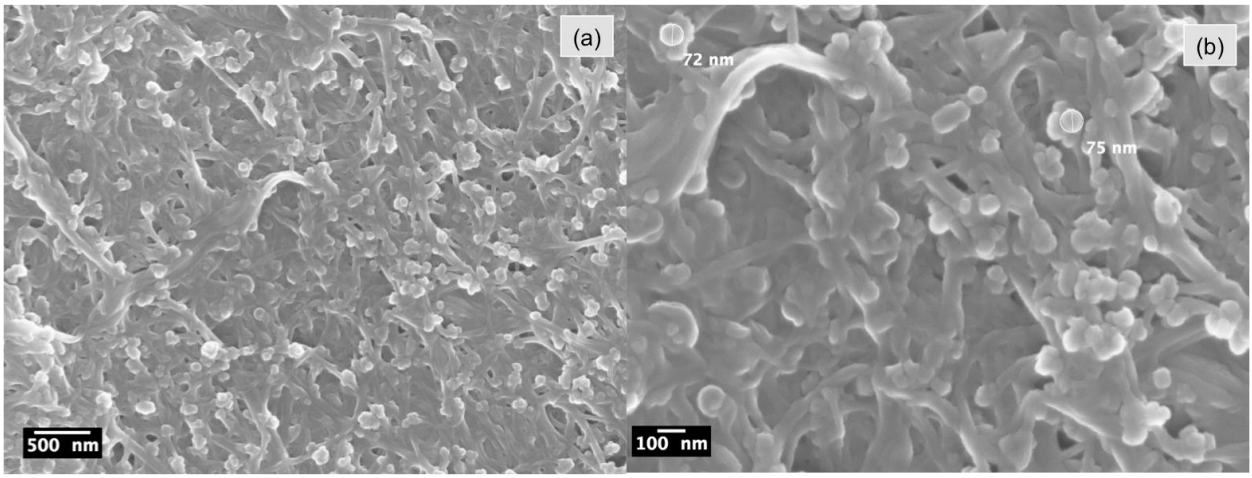

Figure 5-22 0.04 M TiF_4 reacted in 5 mg/mL MFC aqueous suspension at I: W = 0: 1 ratio for 6 hours, coated on glass substrate, and dried in vacuum oven, without calcination applied.

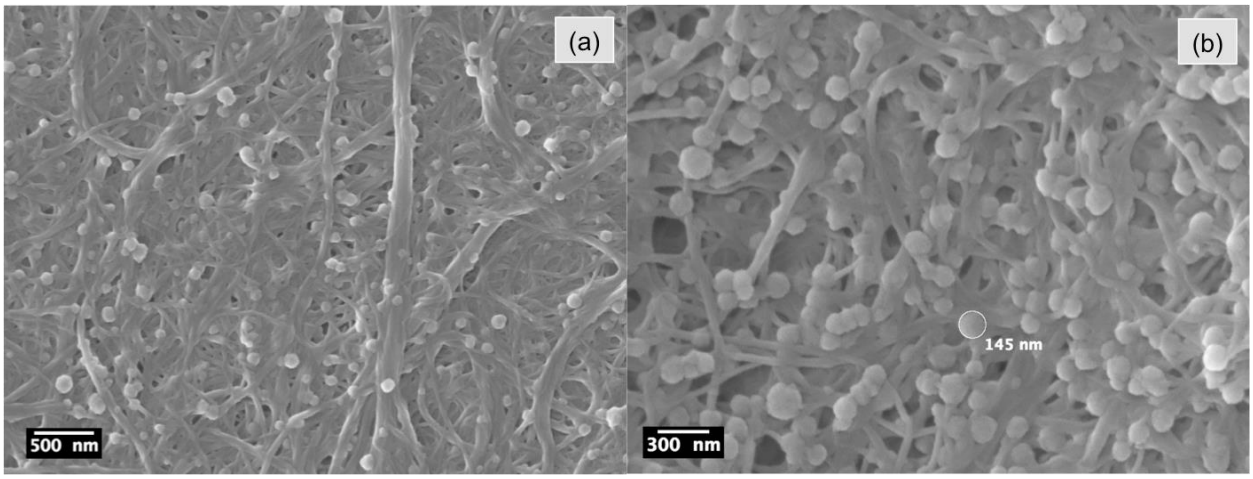

Figure 5-23 0.04 M TiF_4 reacted in 5 mg/mL MFC aqueous suspension at I: W = 1: 1 ratio for 6 hours, coated on glass substrate, and dried in vacuum oven, without calcination applied.

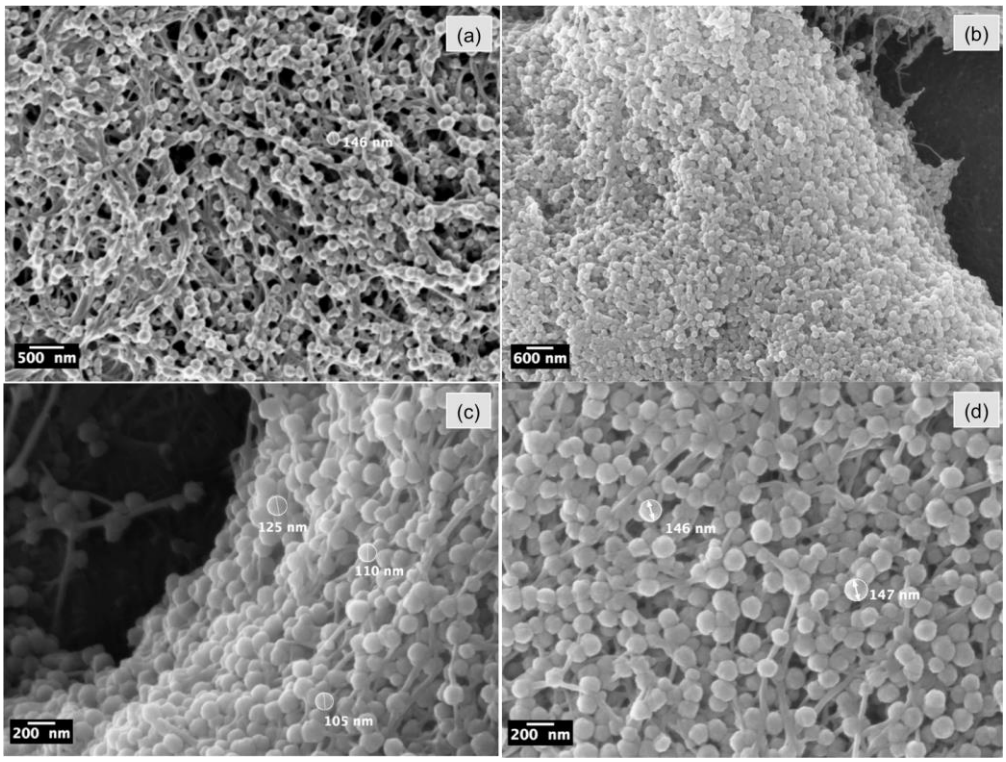

Figure 5-24 0.04 M TiF_4 reacted in 5 mg/mL MFC aqueous suspension at I: W = 4: 1 ratio for 6 hours, coated on glass substrate, and dried in vacuum oven, without calcination applied.

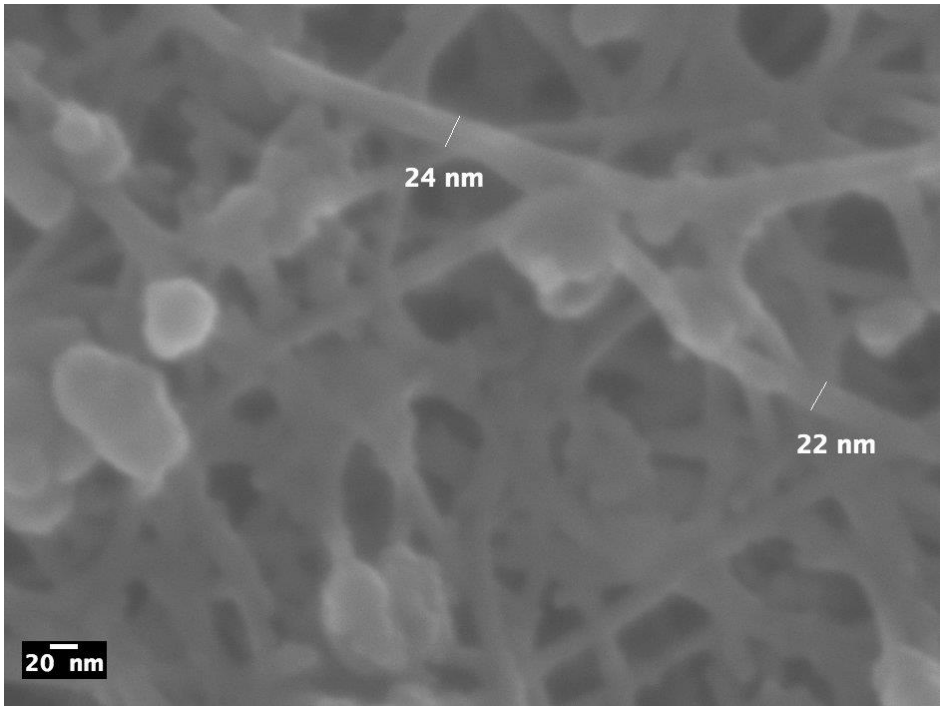

Figure 5-25 SEM image of TiO_2 hollow fibers formed after film calcination from sample TiF_4 with MFCs in aqueous suspension.

In addition to the formation of TiO_2 spheres, the cellulose also acted as a sacrificial template to produce titania hollow fibers or tubes after the heat removal of MFCs. Figure 5-25 represents the fiber-like TiO_2 material from one of the samples at the I: W ratio of 0:1. Other series samples such as I: W= 4:1 had intense spheres coverage along the "chain", resulting in the difficulty observing the TiO_2 hollow fibers. However, after dispersion and a further preparation of TEM samples of I: W = 4:1 samples, the details could be well characterized as shown in Figure 5-29.

To further prove the influence of templating MFCs in the system, control was conducted on TiF_4 dissolved in isopropanol and water mixture at two ratios, 4:1 and 1: 1, without any cellulose. Figure 5-26 shows the morphologies of coatings made on the surface of glass substrates after reaction time 2 hours, 4 hours, and 6 hours. Only TiO_2 clusters were formed randomly and thick films with cracks were observed. Figure 5-27 shows a more aggregated surface with TiO_2 clusters, but still lacked a controlled morphology and porosity.

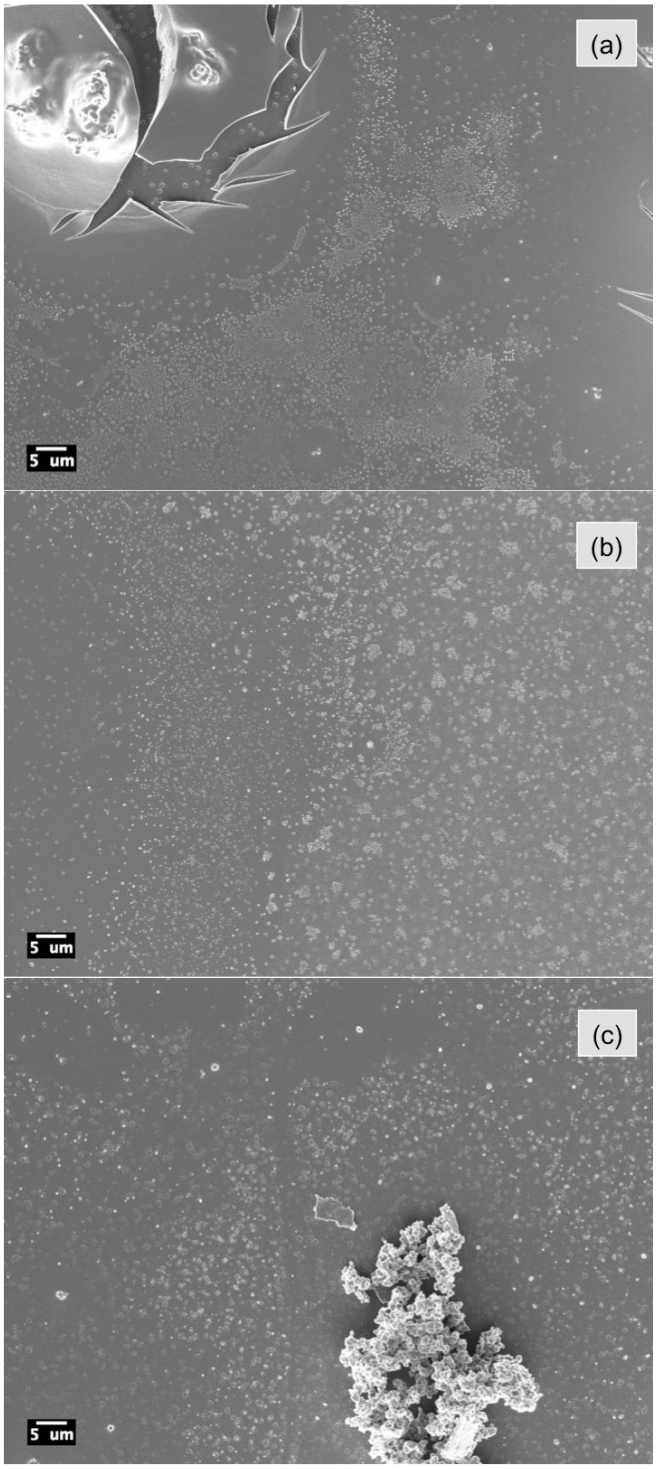

Figure 5-26 TiF_4 reactions in IPA and water mixture at I:W ratio of 4:1 for (a) 2 hours, (b) 4 hours, (c) 6 hours.

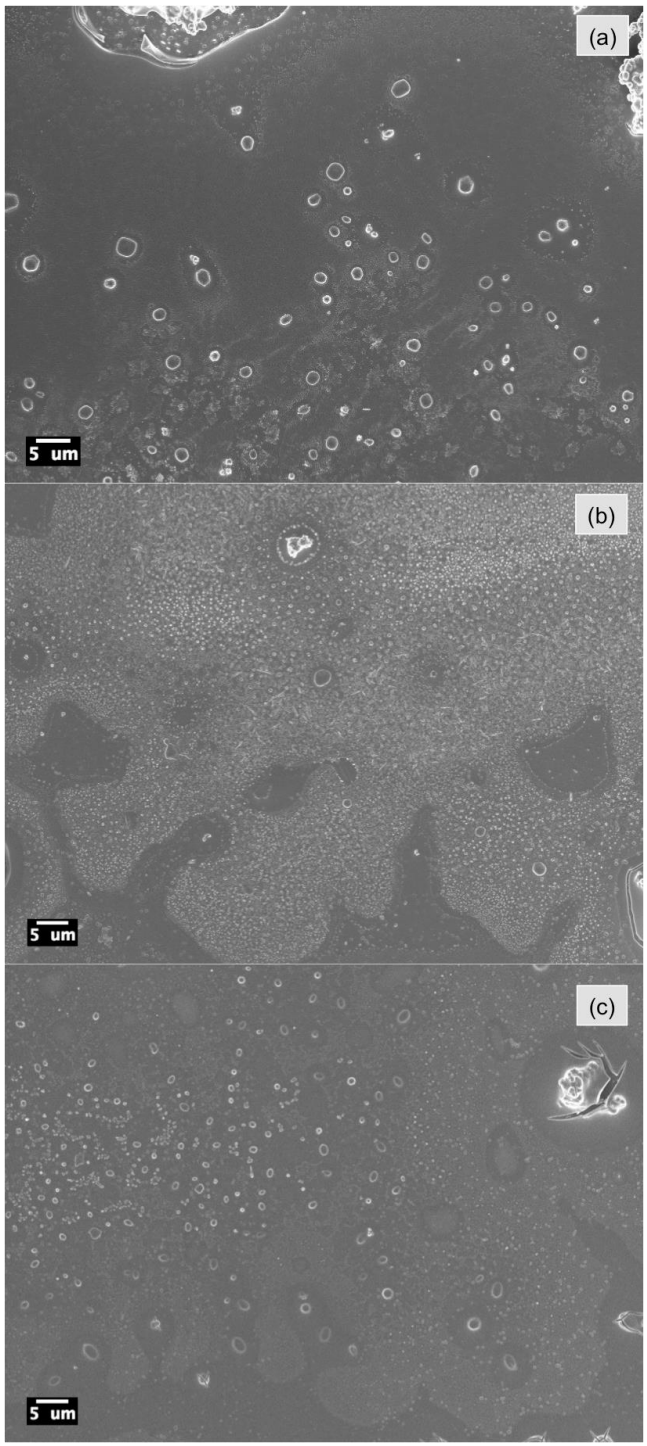

Figure 5-27 TiF_4 reactions in IPA and water mixture at a I: W ratio of 1:1 for (a) 2 hours, (b) 4 hours, (c) 6 hours.

Transmission electronic microscopy (TEM):

As Figure 5-28 (a) and (c) show, porous titania film were composed of particles with size ranging 10-20 nm and pore size ranging in 10-40 nm, attributed to the removal of cellulose fibers. Particles were observed to be agglomerated due to the thickness of the film and incompetence of sonication and dispersion. Figure 5-28 (b) SAED ring patterns confirm that the TiO_2 was made of polycrystalline anatase TiO_2 with the Debye-Scherrer concentric rings (101), (004) and (200). The 0.35 nm lattice fringe spacing (Figure 5-28 (d)) further implied the existence of anatase (101) facet (JCPDS No. 21-1272). Titania film has (101) the most exposed face in the nanocrystal forms.

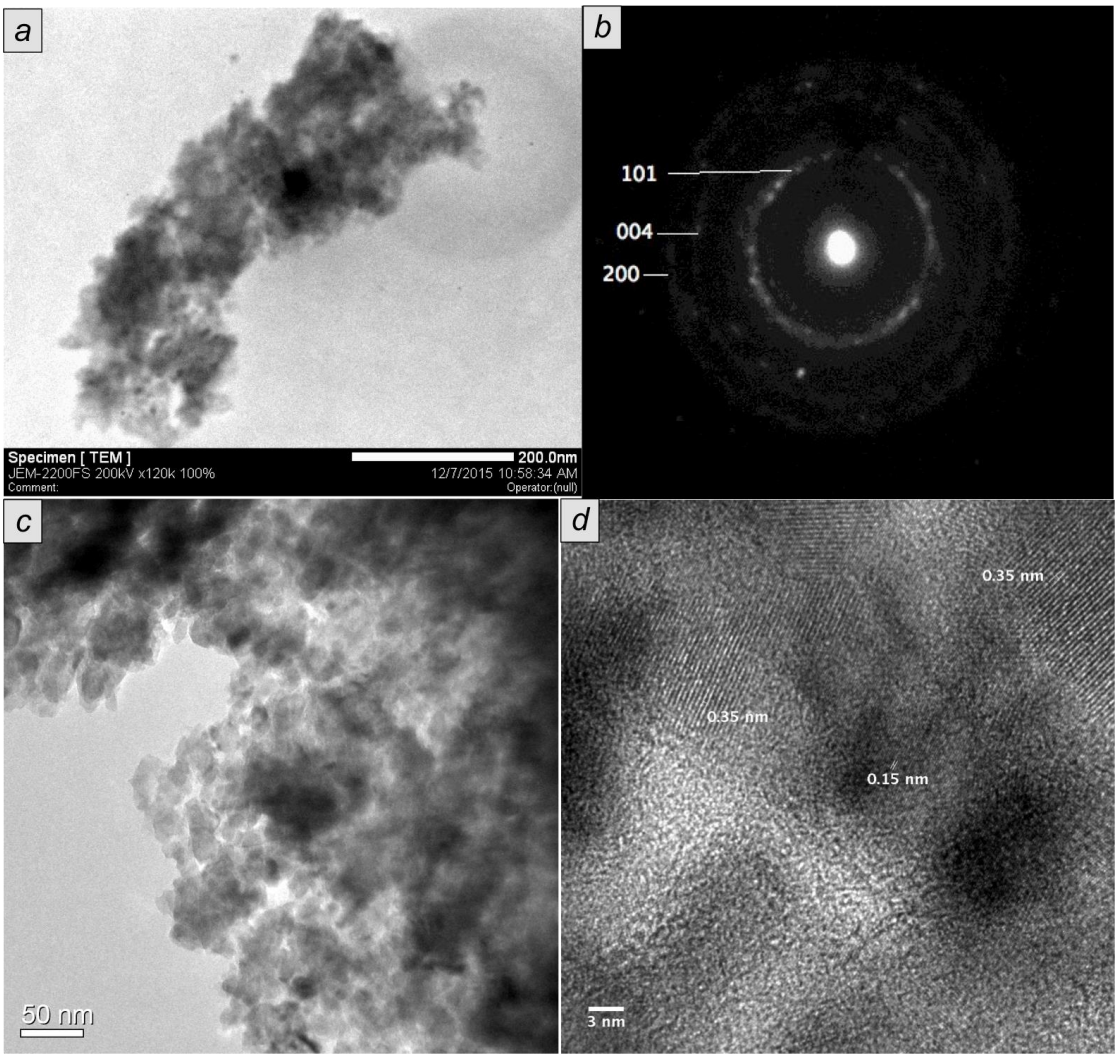

Figure 5-28 TEM images of anatase TiO_2 film generated by TiF_4 liquid phase deposition, with a solvent ratio of IPA/H_2O =0:1. (a) and (c) porous structure, at low and high magnification. (b) SAED diffraction pattern and (d) HRTEM image noted with anatase lattice spacing ~0.352 nm of facet (101) and 0.148 nm of (213)

As Figure 5-29 shows, nanotubular titania with diameter ranging 10-35 nm were found and it was due to the removal of nano-size MFCs. As discussed before, even after homogenization, different level of aggregation still existed in the cellulose suspension. Some of them remained at the finest size, becoming ideal template for nanotubular titania structures. Figure 5-29 (a-c). The 0.355 and 0.24 nm lattice fringe spacing (Figure 5-29 (d)) implied the existence of anatase (101) and (004) facets (JCPDS No. 21-1272).

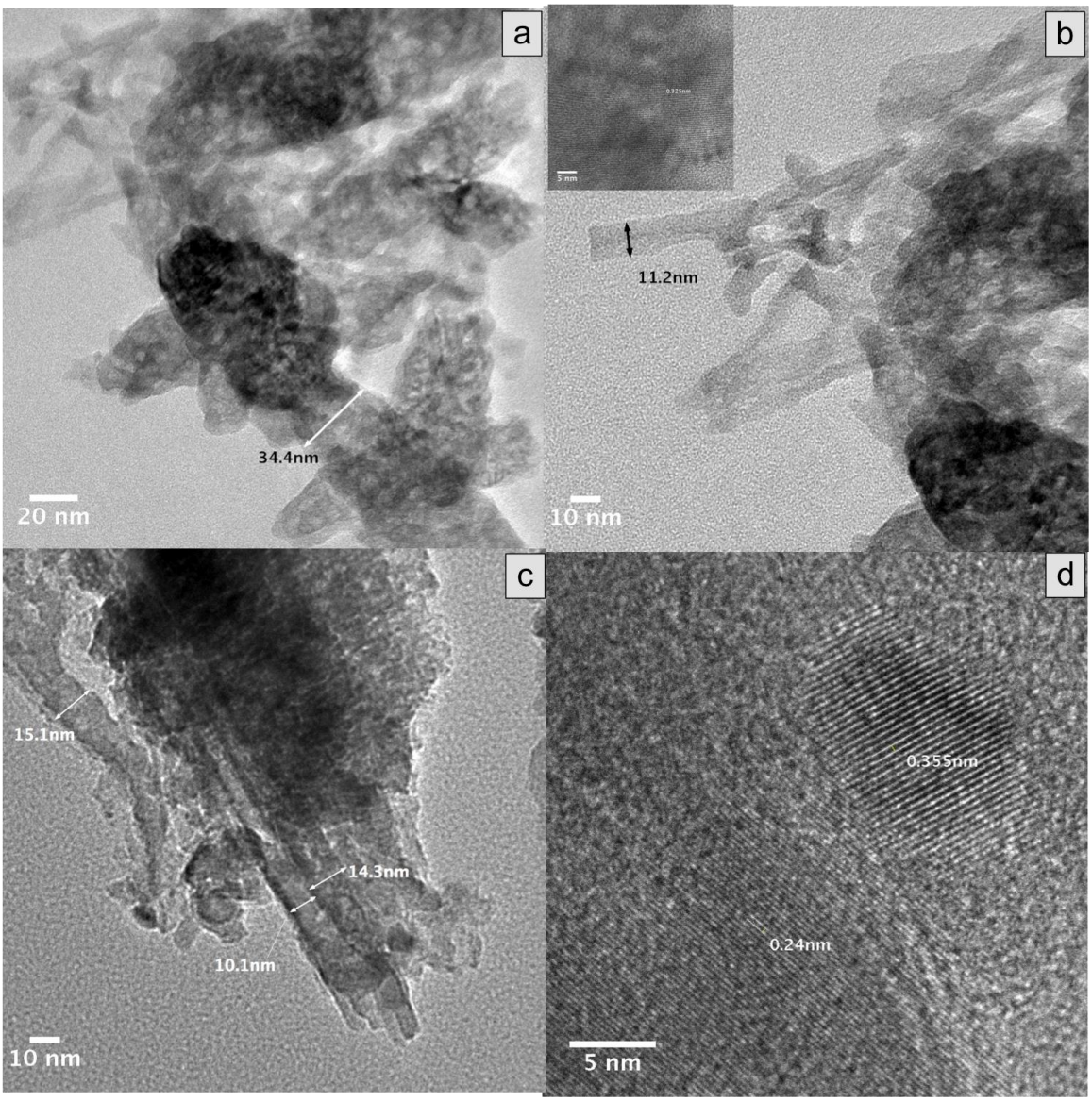

Figure 5-29 TEM images of anatase TiO_2 film generated by TiF_4 liquid phase deposition, with a solvent ratio of IPA/H_2O =0:1. (a-b) tangled tubular-shaped TiO_2, at low and high magnification. (b) another TiO_2 tube showing the hollow inner and outside wall, lattice spacing is 0.352 nm in the inset image (d) corresponding HRTEM image of (c) highlighting the anatase lattice spacing of facet (101) with spacing 0.355 nm and (004) with spacing 0.24 nm.

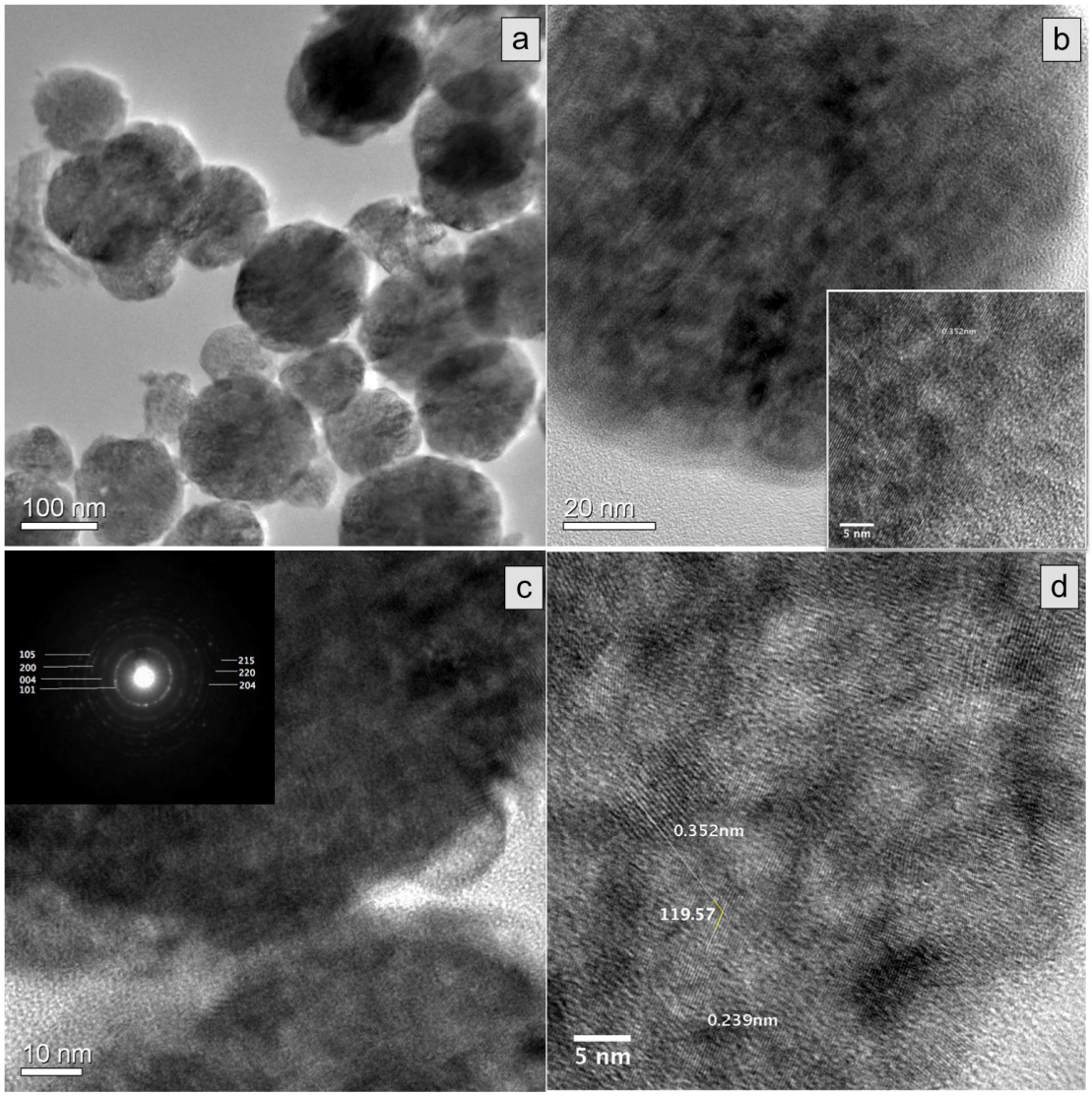

Figure 5-30 TEM images of anatase TiO_2 film generated by TiF_4 liquid phase deposition, with a solvent ratio of IPA/H_2O =4:1. (a-b) spherical TiO_2, at low and high magnification. (c) interface between two spherical particles, and the SAED pattern (inset) labeled (d) corresponding HRTEM image of (c) highlighting the anatase lattice spacing of facet (101) and (004), and the lattice angle between is 119.6°

When the IPA to water ratio was increased to 4:1, the morphology of the film changed dramatically. As shown in SEM images previously, uniform sphere grew along the chain and crossed over, resulting in a porous interconnected network. TEM images in Figure 5-30 (a) illustrate the neighboring particles with diameter around 150 nm. The inset image in (b) revealed the anatase phase, corresponding to the SAED rings (105) (200) (004) (101) (215) (220) (204) of inset image in Figure 5-30 (c). Similarly, the lattice space shown in (d)

confirmed the anatase planes of (101) and (004) again, with the lattice angel measured as around 120°.

5.3.2.2 Surface and elemental properties of TiO_2 films

Elemental analysis:

Energy-dispersive x-ray spectroscopy (EDS) was utilized with SEM for elemental analysis. It is elucidated in Figure 5-31 that after calcination, no carbon was left in the film. And the sodium, silicon, and calcium were from glass substrate background based on the comparison of two inset quantitative results.

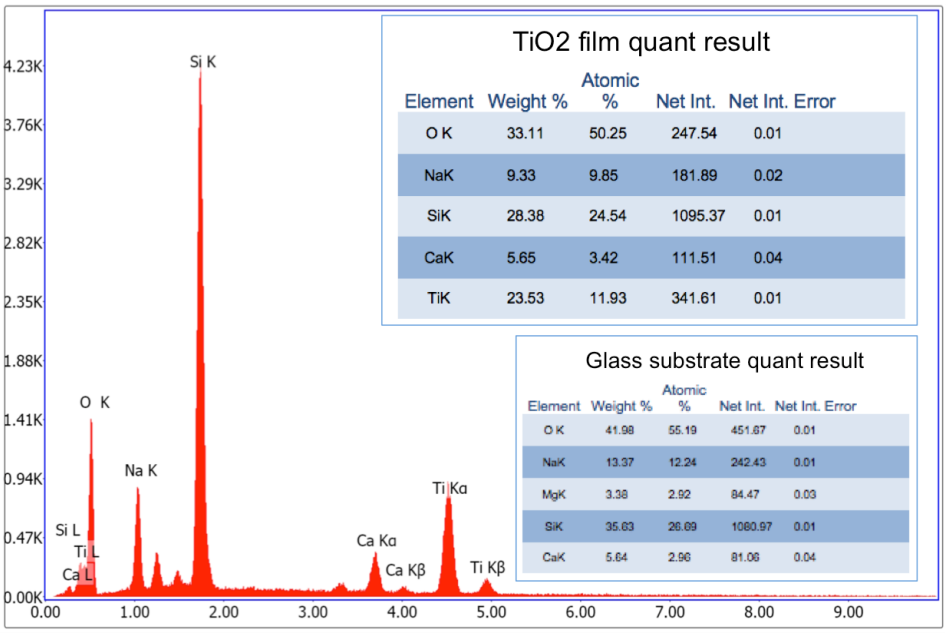

Figure 5-31 EDS information of a calcined TiO_2 film (with MFCs in suspension of I: W =1:1) on a glass substrate. The inset tables explained the atomic composition of oxygen and titanium, and the background elements from the glass substrate.

Table 5-2 is a summary of the element percentages, corresponding to the full scan in Figure 5-32. Before calcination, C 1s has a much higher atomic ratio in the film, indicating organic composition in the film before calcination counted around 30%, and C 1s in all other calcined films came from carbon contamination from atmosphere. The highest Ti 2p

concentration came from precursor without any IPA, which possibly was due to the highest level of precipitation of titania. When IPA was added to adjust the polarity of the precursor, hydrolysis and precipitation were slowed down, resulting in less TiO_2, higher porosity on the top surface of the film. Na and Si had been detected with repeating experiments, and they were suspected to be from the chemical reactants contaminations, water used, or glass substrates.

Table 5-2 Atomic concentration of related elements in TiF_4- MFCs induced films detected by XPS.

	Sample: TiF_4 with or without cellulose MFCs	**C1s**	**O1s**	**F1s**	**Na1s**	**Si2p**	**Ti2P**
1	0.5% w.t., 1 water + 4 IPA	25.3	50.5	0.5	6.3	7.8	9.5
2	0.5% w.t., 1 water +1 IPA	23.9	50.8	0.5	7.3	10.4	7.2
3	0.5% w.t., 0 water +1 IPA	25.7	49.2	0.4	8.5	2.9	13.3
4	sample (1), non calcined	54.1	39.9	3.8	0.4	-	1.8
5	0.5% w.t., 1water+0 IPA	23.0	50.4	0.5	7.7	4.1	14.3
6	water 10 mL, w/o cellulose	26.4	49.5	0.5	7.1	8.4	8.1

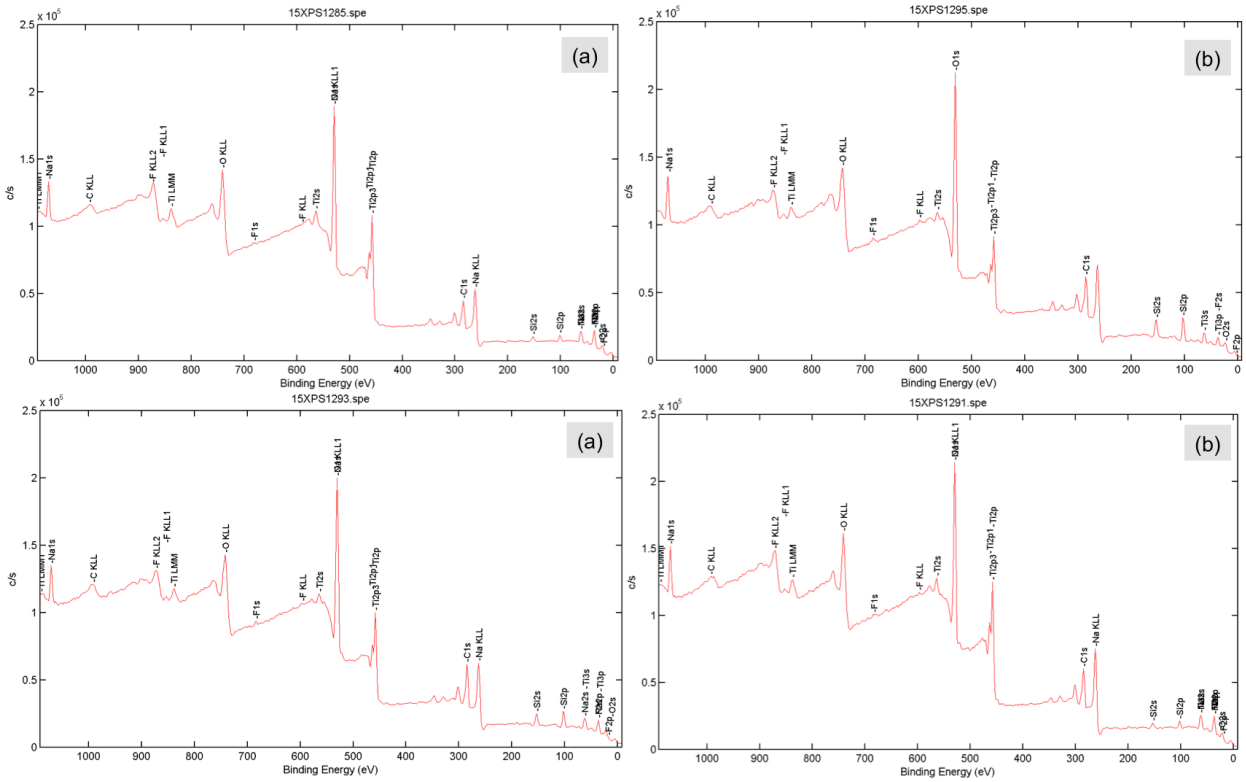

Figure 5-32 XPS spectra of thin titania films made with TiF_4 precursors with MFCs, at different solvent compositions: (a) IPA: water= 0:1, (b) IPA: water=1:1, (c) IPA: water= 4:1, (d) IPA: water= 1:0.

Table 5-2 is a summary of the element percentages, corresponding to the full scan in Figure 5-32. Before calcination, C 1s has a much higher atomic ratio in the film, indicating organic composition in the film before calcination counted around 30%, and C 1s in all other calcined films came from carbon contamination from atmosphere. The highest Ti 2p concentration came from precursor without any IPA, which possibly was due to the highest level of precipitation of titania. When IPA was added to adjust the polarity of the precursor, hydrolysis and precipitation were slowed down, resulting in less TiO2, higher porosity on the top surface of the film. Na and Si had been detected with repeating experiments, and they were suspected to be from the chemical reactants contaminations, water used, or glass substrates.

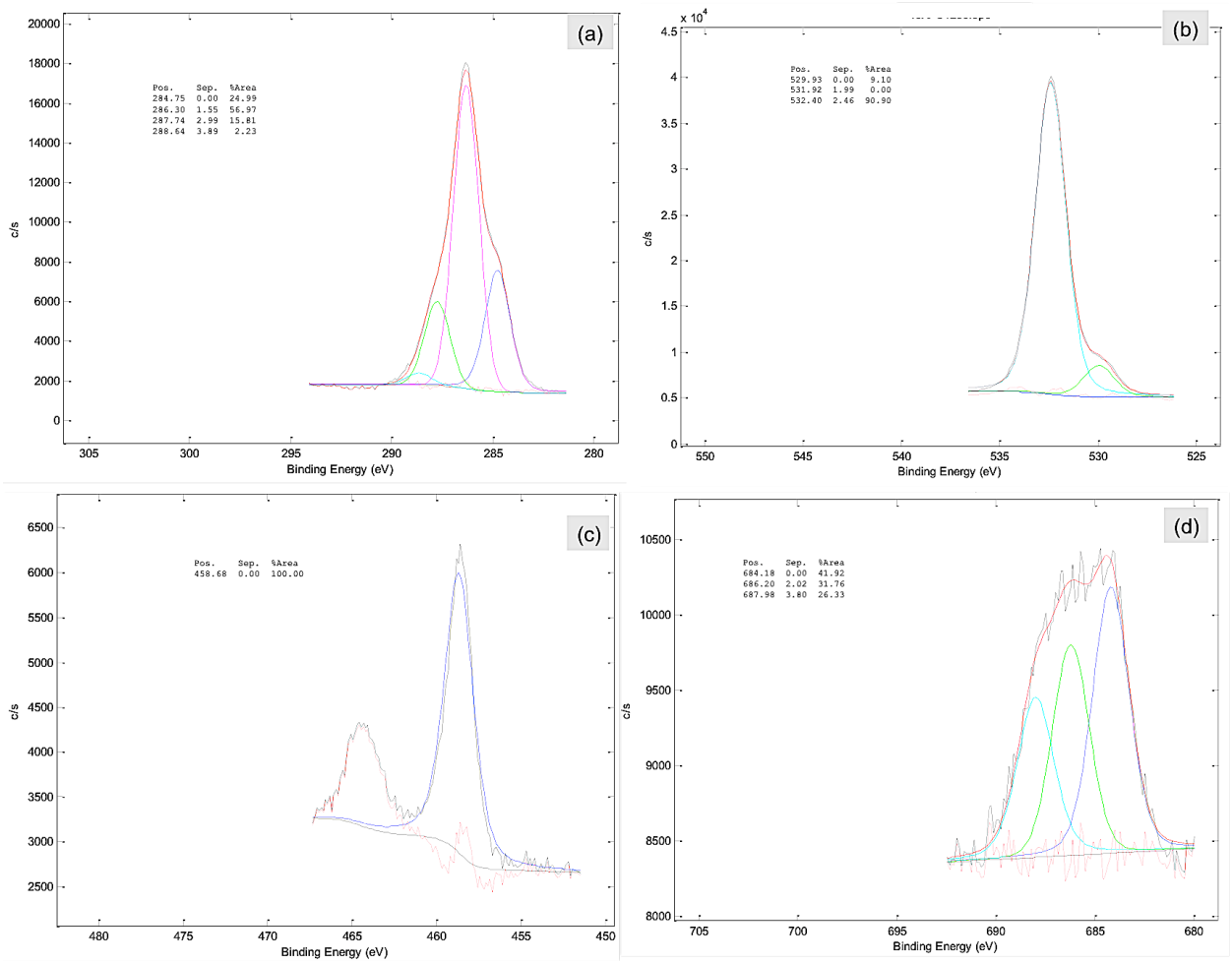

Figure 5-33 XPS convolution results of thin titania dried films without calcination, made with TiF_4 precursors with MFCs at IPA: water= 4:1. (a) C 1s, (b) O 1s, (c) Ti 2p, (d) F 1s.

Further surface chemical states of each element within the TiO_2 films were obtained via XPS peak fitting as shown in Figure 5-33 and Figure 5-34. C 1s distributed its chemical states bonding energy as 284.8 eV (25%), 286.3 eV (57%), 287.7 eV (15.8%), and 288.6 eV (2.2%) in Figure 5-33 (a). While for calcined titania films (Figure 5-34 (a)), the composition is 284.8 eV (71.2%), 286.4 eV (12.7%), 288.4 eV (10.3%), and 289.9 eV (5.8%). The change from uncalcined to calcined, corresponding to

Table 5-2 is a summary of the element percentages, corresponding to the full scan in Figure 5-32. Before calcination, C 1s has a much higher atomic ratio in the film, indicating organic composition in the film before calcination counted around 30%, and C 1s in all other calcined films came from carbon contamination from atmosphere. The highest Ti 2p concentration came from precursor without any IPA, which possibly was due to the highest level of precipitation of titania. When IPA was added to adjust the polarity of the precursor,

hydrolysis and precipitation were slowed down, resulting in less TiO_2, higher porosity on the top surface of the film. Na and Si had been detected with repeating experiments, and they were suspected to be from the chemical reactants contaminations, water used, or glass substrates.

Table 5-2, is also similar when compared to other calcined titania films synthesized at other IPA: water ratios. When the precursor was not calcined, the contribution of C-C (~284.8 eV), C-O (~286.0 eV), O-C=O (~288.5 eV), C=O (~289 eV) was characteristic of cellulose.

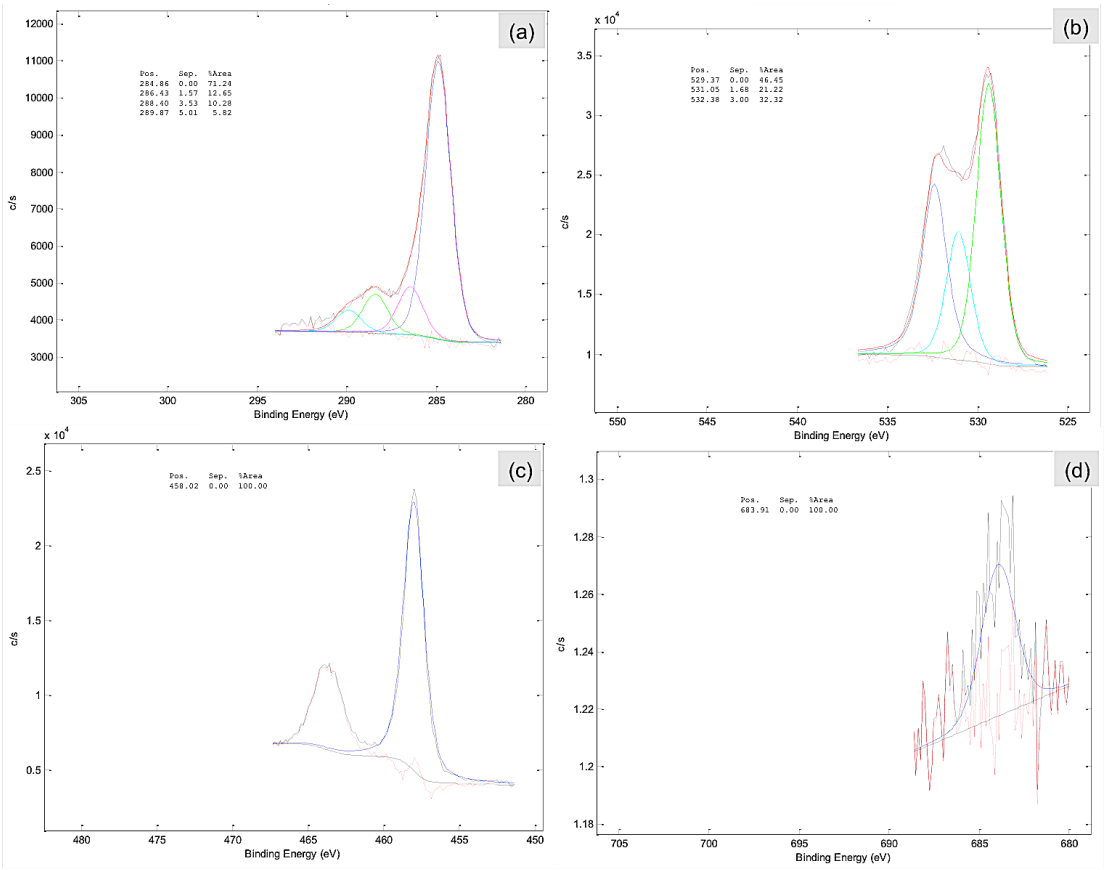

Figure 5-34 XPS convolution results of thin titania films after calcination, made with TiF_4 precursors with MFCs at IPA: water= 4:1. (a) C 1s, (b) O 1s, (c) Ti 2p, (d) F 1s.

After calcination, the ratio of each bond was changed, because it came from adventitious carbon on the surface. O 1s had dramatic change as demonstrated in Figure

5-33 (b) and Figure 5-34 (b). The peak at ~529.9 eV increased from 9 % to 46.5 % after calcination, implying that metal oxide bond was formed. And the peak at 531-532 eV dropped from 90.1 % to 30.0 % due to the removal of C-O bonds from the degradation of cellulose at elevated temperatures. Ti 2p bonding energy transformed from 457.8 eV to 458.0 eV and maintained a similar Ti(IV) state. As for F 1s, after calcination, the chemical state turned from organic fluorine (~686-688 eV) to metal fluoride (~684 eV), as shown in in Figure 5-33 (d) and Figure 5-34 (d).

Crystallinity analysis:

Raman spectroscopy, as an easy quick way to detect the crystallinity of TiO_2, was utilized to compare two parallel samples, thin films with IPA: water = 0: 1 and 4: 1. Both films reveal anatase crystallinity. The Raman spectra of the calcined film clearly show that titania is anatase by the characteristic peaks at 144, 197, 399, 513, 519, 639 cm^{-1}.[16]

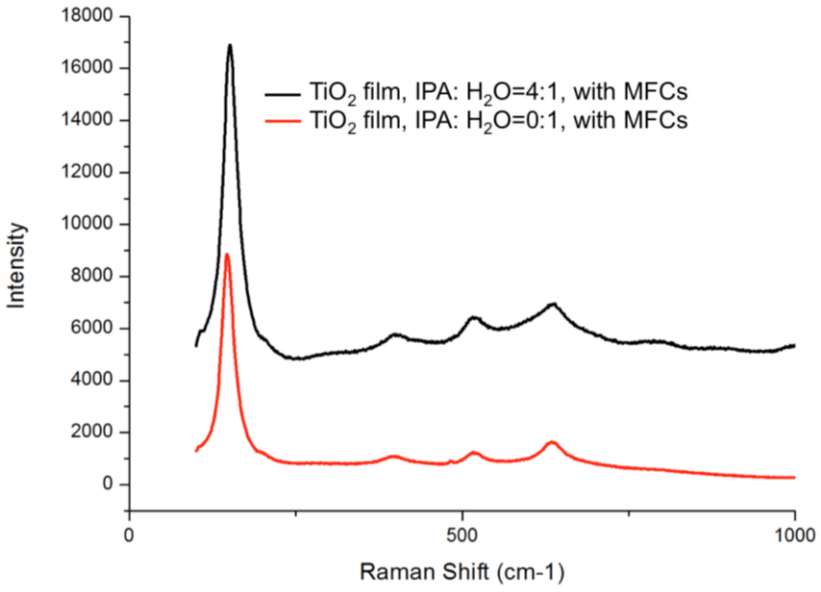

Figure 5-35 Raman spectra of two thin titania films, made from TiF_4-MFCs precursor with different solvent compositions: IPA: water= 0:1 and IPA: water= 4:1.

All samples were detected with peaks at around 25.3, 38.3, 48.3, 54.0, 55.2 and 63.0 °, which represented plane (101), (004), (200), (105), (211) and (204) [JCPDS 78-2486]. Anatase phase could be obtained by appropriate annealing at 450-500 °C.

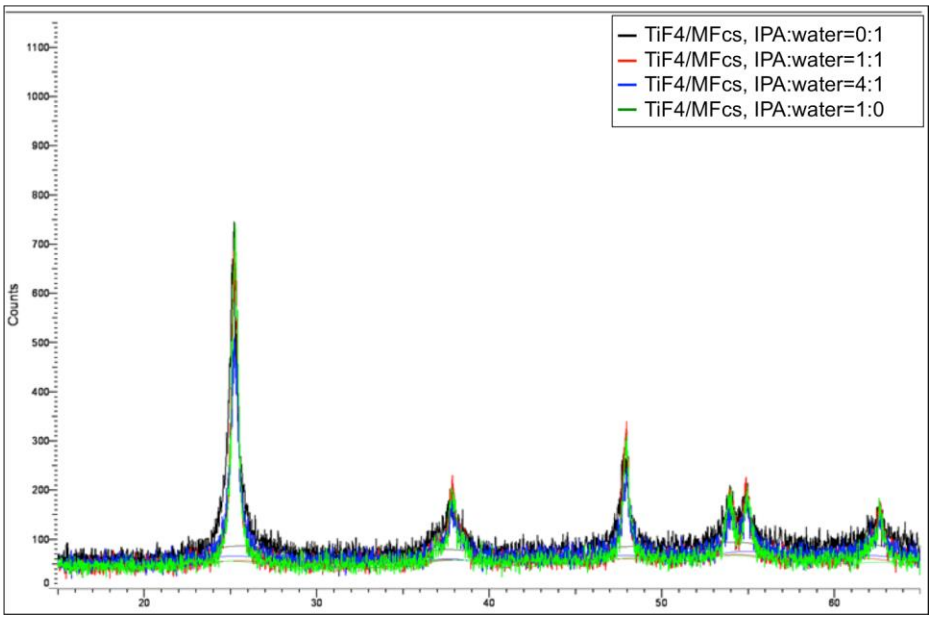

Figure 5-36 XRD of titania films made with TiF_4/ MFCs templates, with different IPA: water solvent compositions

Thermal analysis:

The thermal stability of both MFCs, uncalcined TiF_4 with MFCs were studied to explore the degradation of MFCs at elevated temperatures. Figure 5-37 shows several stages of the calcination of cellulose. Between room temperature and 100 °C, the residue water content not removed from drying process was evaporated, giving a major peak in the derivative weight change curve. The following weight loss before the temperature reached around 200 °C was attributed to the detachment of the absorbed water on the surface of the porous cellulose structure. At 300 °C, a large derivative weight change peak showed up, resulting from the rapid loss of weight due to oxidation of cellulose. During this stage, dehydration

and decarboxylation will produce anhydrocellulose and combustible gases like aldehydes, ketones, ethers, and so on. From 360 °C to 450 °C, the carbonaceous residues were oxidized and resulted in CO_2, CO and H_2O. Around 0.2% w.t. char was left after heating process till 500 °C.

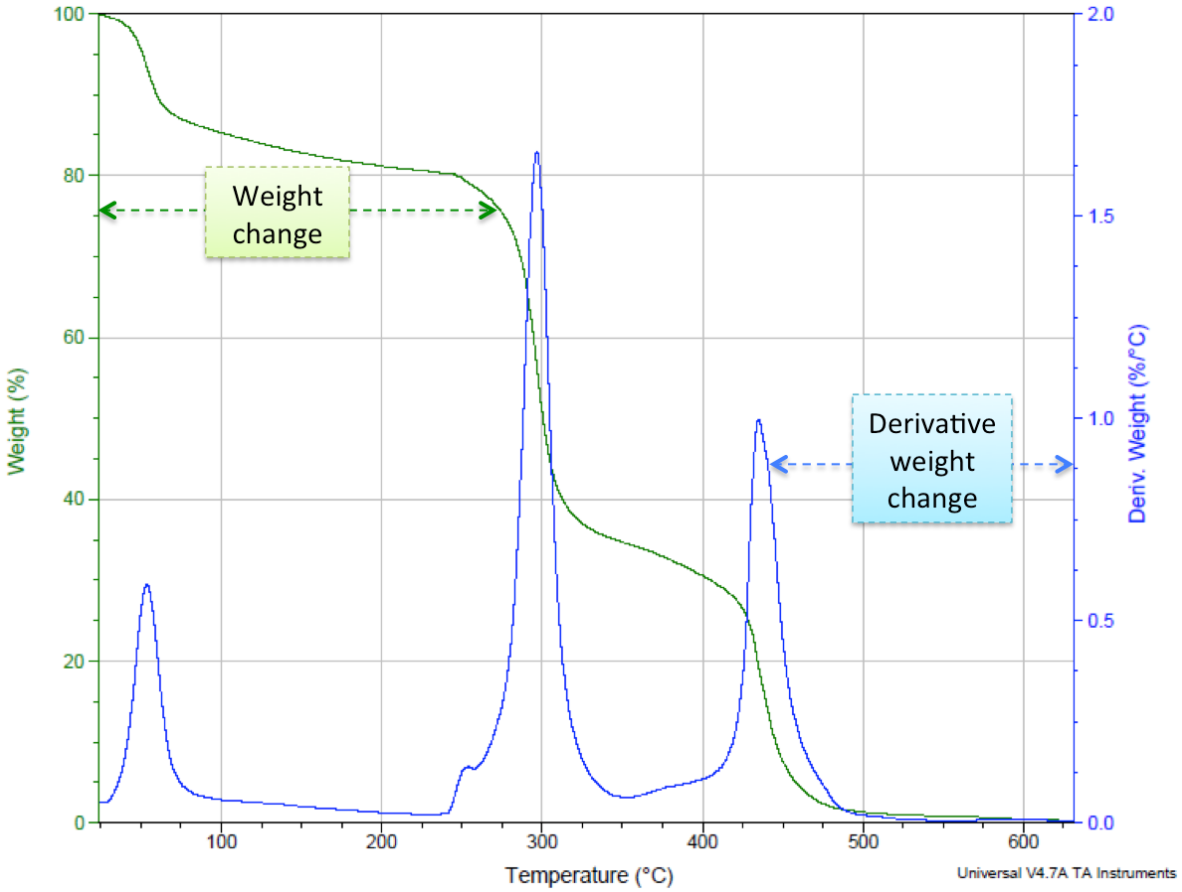

Figure 5-37 TGA of dried MFCs. To eliminate the water evaporation step during thermal analysis, sample was dried in vacuum oven overnight at 80 °C before the test. TGA was conducted in air through a high resolution ramp program at a heating rate of 25 °C/min.

The thermal stability of MFCs combined with Ti precursor showed the degradation during the heating process very well. In Figure 5-38, the weight loss from room temperature to ~100 °C was from the major evaporation of solvents, in which a small peak at around 70 °C indicated the existence of organic solvent. Then the weight loss continued till around 250 °C, during which the absorbed water was removed, and the shrinkage of the

TiO_2 cross-linked structure started, eventually, the oxidization of cellulose began. At around 274 °C, dehydration and decarboxylation of cellulose reached the highest rate and produced anhydrocellulose and combustible gases like aldehydes, ketones, ethers, and so on. From 360 °C to 450 °C, the carbonaceous residues were oxidized and resulted in CO2, CO and H_2O , while at the same time, titania was further crystallized. After 500 °C, around 46% w.t. residue was left and that was the weight of TiO_2 if the 0.2% w.t. cellulose was neglected.

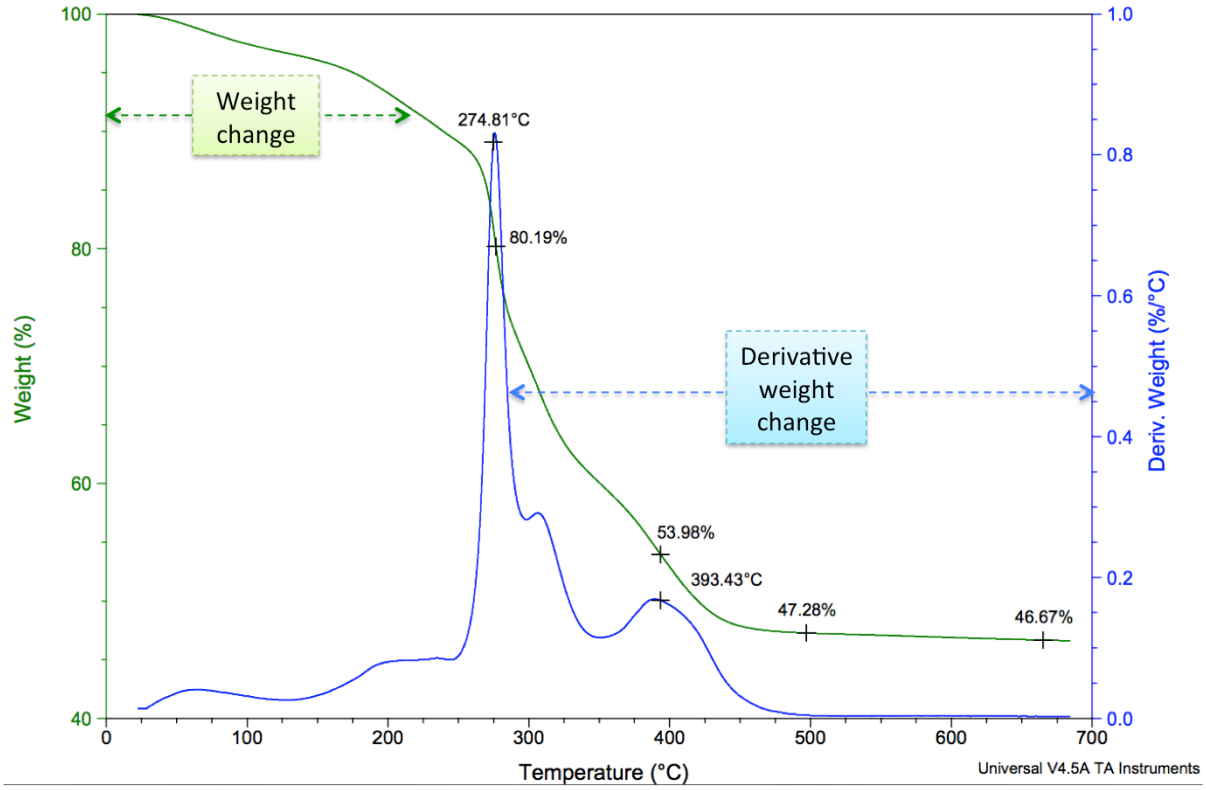

Figure 5-38 TGA of uncalcined TiF_4 precursor with template MFCs in a solvent of I: W at ratio 1: 1. To eliminate the solvent evaporation step during thermal analysis, sample was dried in vacuum oven overnight at 80C before the test. TGA was conducted in air through a high-resolution ramp program at a heating rate of 25 °C/min

When the solvent was simplified to water only for TiF_4 precursor, the preliminary stage slightly differed from Figure 5-37. As Figure 5-38 shows, at 163 °C, around 8% w.t. weight loss was observed. Although the weight loss percentage of both I: W = 1: 1 and 0 : 1

samples were similar, a steep drop of latter might be due to the difference in solvent composition, or inadequate drying process of the tested sample. Two more peaks in derivative weight change curve occurred at similar temperatures (310 °C and 400 °C) when compared with Figure 5-37 due to cellulose degradation and TiO_2 crystallization. The weight maintained constant after 500 °C and resulted in 45% w.t. TiO_2 crystals.

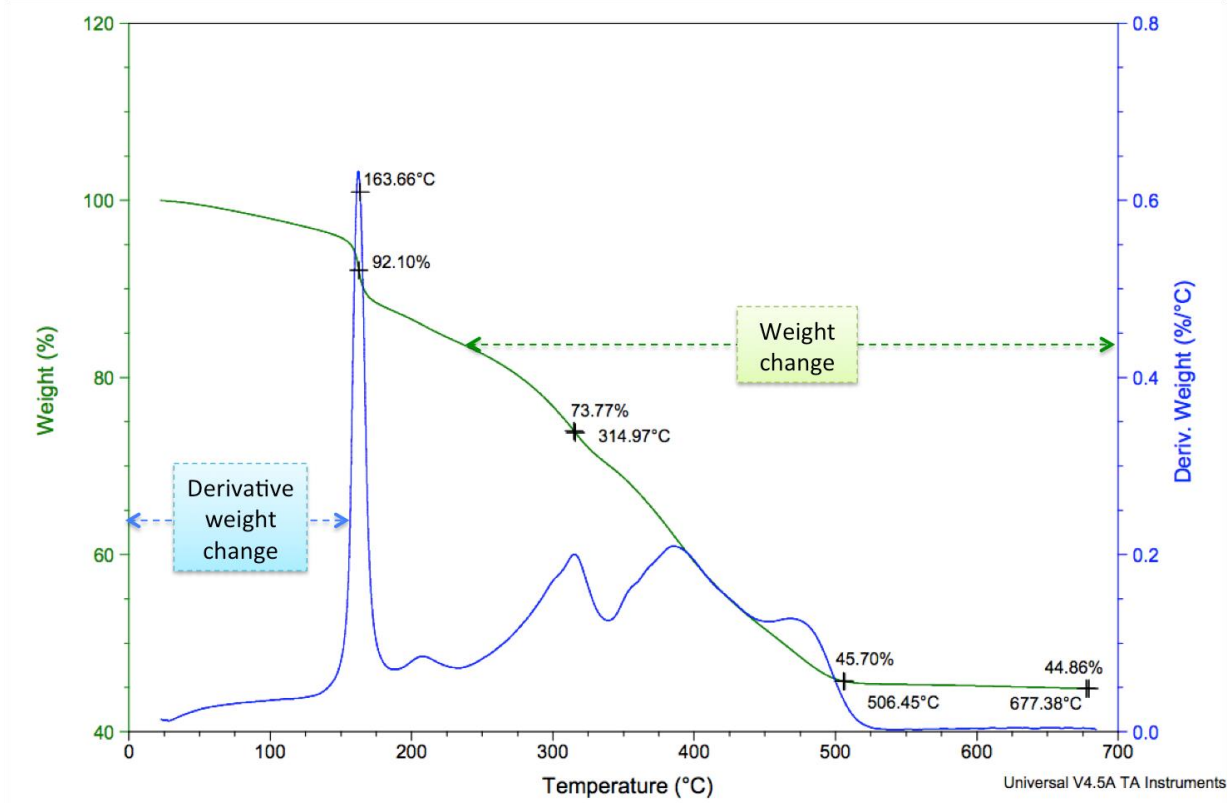

Figure 5-39 TGA of uncalcined TiF_4 precursor with template MFCs in a solvent of I: W at ratio 0: 1. To eliminate the solvent evaporation step during thermal analysis, the sample was dried in vacuum oven overnight at 80C before the test. TGA was conducted in air through a high-resolution ramp program at a heating rate of 25 °C/min.

The thermal stability of calcined TiF_4- induced films was further measured with TGA and Figure 5-40 shows the weight loss curves of two samples in different ratios of organic and water solvent. The first drop before 200 °C was due to the removal of free-standing water and adsorbed water molecules. There was an average of 1.2% w.t. weight loss

between 500 °C and 600 °C which should be from either the further degradation of cellulose char or the transition of titania particles at much higher temperatures.

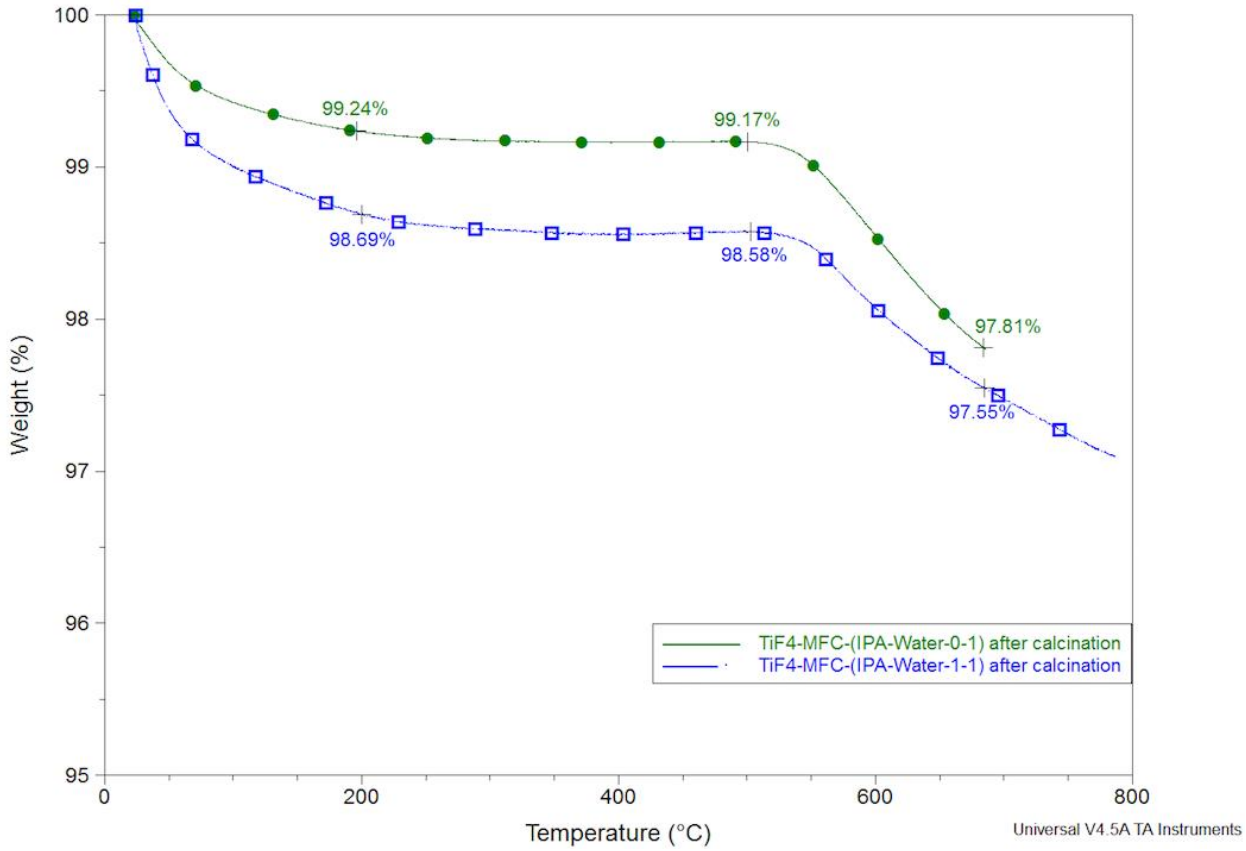

Figure 5-40 TGA of calcined TiF_4 precursor with template MFCs in two different solvent systems: (1) top curve with • was prepared in I: W at ratio 0: 1; (2) bottom curve with □ was prepared in I: W at ratio 1: 1. TGA was conducted in air through a high-resolution ramp program at a heating rate of 15 °C/min.

XRD, Raman, UV-Vis, AT-IR, BET and TGA measurements on titania-coated silicone nanofilaments did not provide additional insight beyond the results reported.[14] We attribute this to the thin film nature and to the low absolute amount of material which was deposited on the glass slides. Similar situations applied for this work as well, the materials were collected not in the original form of the film, instead, it was scraped from the substrates, and the amount of materials had limitations for ideal results as we predicted.

As for thin films, especially nanoscale thin films, Raman signals could be covered by the substrate information. To get improved signals, one should consider accumulating the spectra for more time until getting an appropriate intensity. A general method is to increase the integration time and number of running cycles. Changing the configuration of the measured film might also help by turning the film surface 90 degrees, from vertical to the laser beam, to parallel to the laser beam. In addition, if possible, subtracting the signals of background substrate from the whole thin film could yield a relatively accurate spectrum of the film itself as well.

5.3.3 Photocatalysis performance of tunable titania thin films

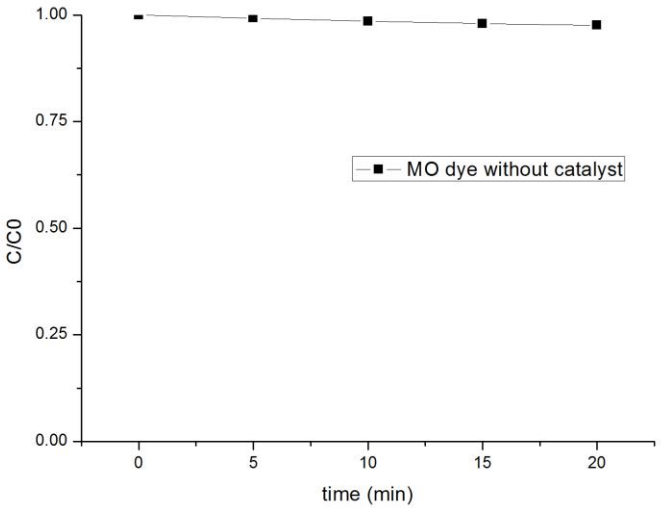

Figure 5-41 Concentration change of the MO solution on glass substrate measured by UV-Vis absorbance, over a 20-minute UV lamp irradiance, without any catalyst.

Before the photocatalytic degradation test, 1×10^{-5} M MO solution was tested with no catalyst applied at the beginning. Absorbance data from UV-Vis were taken every five minutes and converted to concentration change. Figure 5-41 clearly shows that over UV irradiation, the concentration of MO solution has minimum change of ~2%, which also

corresponds to the literature.[17] Besides of the UV degradation to MO, one of the possible reasons for the change might be the trace evaporation of the solution volume.

The ideal concentration of the MO solution should no be too low or too high. When 1×10^{-5} M concentration was used, the extent of change was too small to be well observed and compared. When the concentration was too high, the coverage of MO on TiO_2 surface was too saturated to ensure adequate conversion of photons. Similarly, the volume of solution cast on the TiO_2 film matters too. An optimum concentration and volume combination was set to be 5×10^{-4} M and 10 uL for an 1 inch by 1 inch titania film.

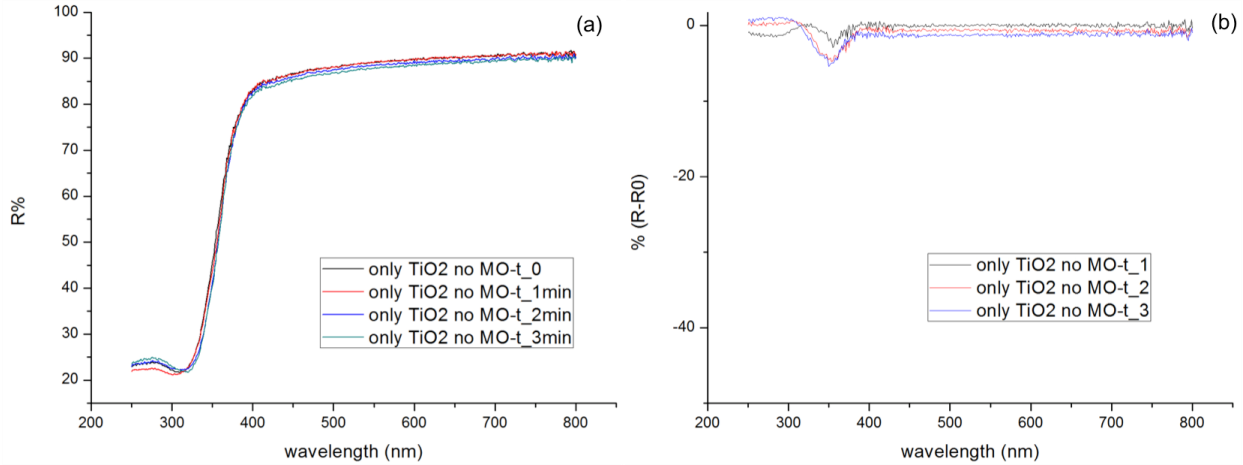

Figure 5-42 Reflectance measurement of TiO_2 film made from TiF_4/MFCs illuminated by UV lamp over time. (a) the reflectance of initial TiO_2, UV treated by 1 min, 2 min, and 3 min. (b) Subtracted from initial reflectance, v.s wavelength.

One set of titania blank films were tested with UV lamp illumination for 1-minute interval each. From Figure 5-42 (a), the reflectance of the TiO_2 film was scanned after each UV treatment, and the reflectance change based on initial pristine TiO_2 was shown in (b), where a 5% drop was observed from time 0 to 3 minutes at wavelength around 350 nm. The change is likely caused by the band gap difference brought in from UV radiation.

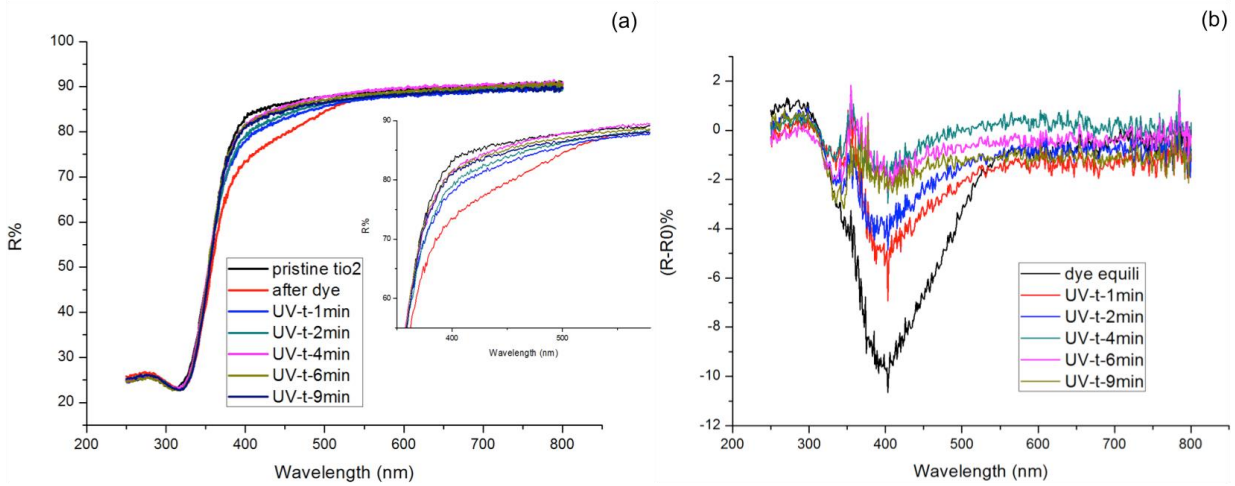

Figure 5-43 Reflectance change over time of UV-illuminated TiO_2 film with 1×10^{-5} M MO solution adsorbed. Titania film was made with TiF_4/ MFCs and IPA: water = 1: 1. (a) Reflectance change from clean TiO_2, MO solution adsorbed (after dye), and treated with UV lamp for a total time of 1 min, 2 min, 4 min, 6 min, and 9 min. Inset image showed details of the same curves. (b) Reflectance difference over time, from dye adsorption, to photocatalytic degradation.

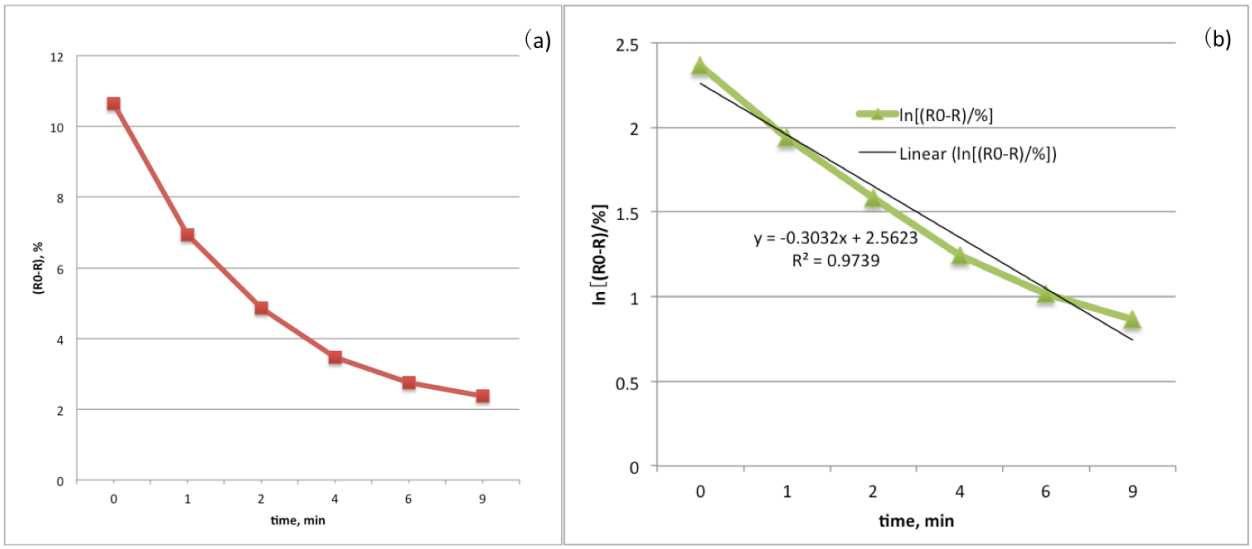

Figure 5-44 For film made with TiF_4/ MFCs and IPA: water = 1: 1. (a) Reflectance difference change at wavelength 395 nm v. s. time. (b) pseudo-first-order kinetic model of ln(reflectance) v. s. time.

Before MO solution was adsorbed onto titania films, the reflectance data is shown by the black curve in Figure 5-43 (a), while after dye equilibrium, the red curve represented the change. Once photocatalytic degradation started, the curve moved back to the original pure TiO_2 stage gradually over time, as shown in the inset image in Figure 5-43 (a). Another

way to illustrate the degradation change is shown in Figure 5-43 (b) where the reflectance difference for dye elimination at 395 nm was calculated and plotted. Further calculations in Figure 5-44 explain the relationship between dye decomposition amount (R_0-R) and time, then generated the pseudo-first-order kinetic model in Figure 5-44 (b). The rate constant was calculated as 0.30 min^{-1}, and the degradation was completed to 77.7% of the original dye concentration, for the films made with TiF_4/ MFCs and IPA: water= 1:1 solvents.

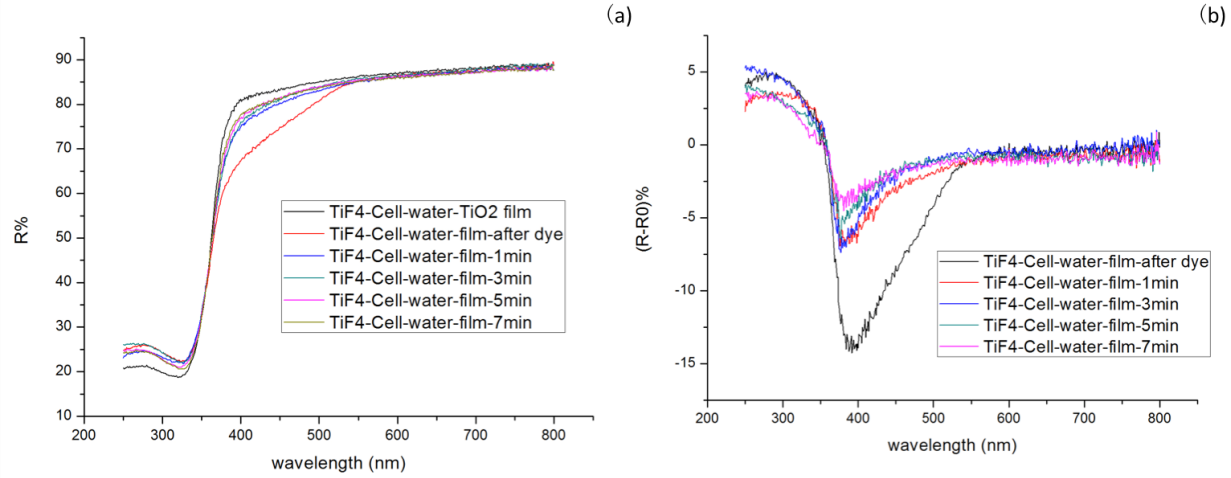

Figure 5-45 Reflectance change over time of UV-illuminated TiO_2 film with 1×10^{-5} M MO solution adsorbed. Titania film was made with TiF_4/ MFCs and IPA: water = 4: 1. (a) Reflectance change from clean TiO_2, MO solution adsorbed (after dye), and treated with UV lamp for a total time of 1 min, 3 min, 5 min, and 7 min. Inset image showed details of the same curves. (b) Reflectance difference over time, from dye adsorption, to photocatalytic degradation.

Similarly, Figure 5-45 and Figure 5-46 show the degradation of MO by the films made with TiF_4/ MFCs and IPA: water = 4:1 solvents. The rate constant was calculated to be 0.52 min^{-1}, and the degradation was improved to 97%.

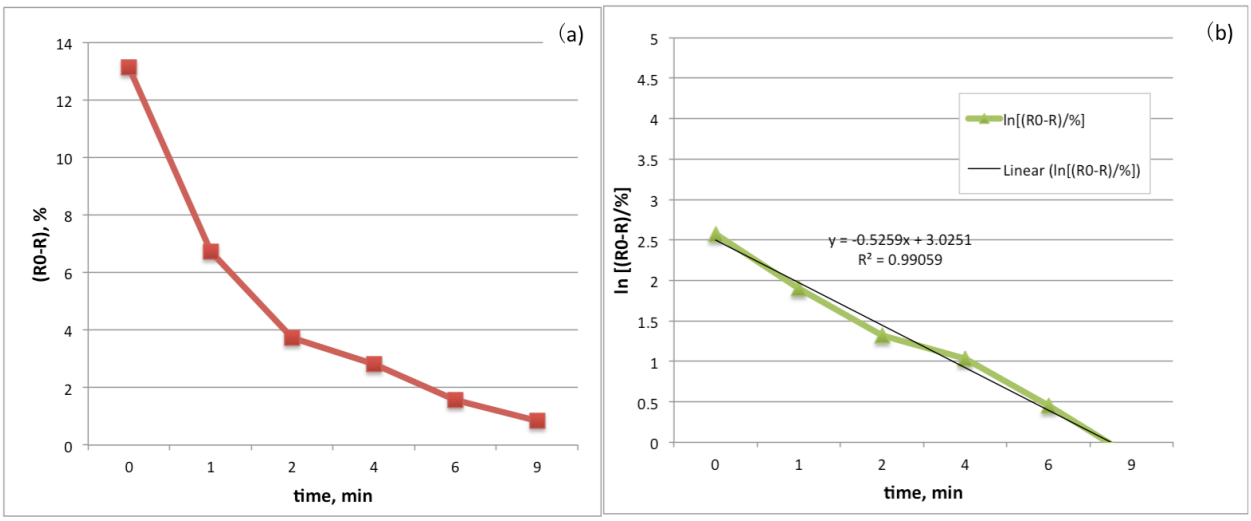

Figure 5-46 For film made with TiF_4/ MFCs and IPA: water = 4: 1. (a) Reflectance difference change at wavelength 395 nm vs. time. (b) pseudo-first-order kinetic model of ln(reflectance) vs. time.

Table 5-3 Summary of kinetics of photocatalytic degradation of MO by variable TiF_4- induced TiO_2 films

y=-k+b	TiF_4-water-1	TiF_4-water-2	TiF_4-cellulose-1IPA-1Water-1	TiF_4-cellulose-1IPA-1Water-2	TiF_4-cellulose-4IPA-1Water-1	TiF_4-cellulose-4IPA-1Water-2	TiF_4-cellulose-4IPA-1Water-3
Rate constant (k, min^{-1})	0.25	0.25	0.32	0.34	0.61	0.78	0.76
Intercept (b)	2.33	2.25	2.84	2.66	3.08	3.13	3.28
R^2	0.9417	0.9374	0.956	0.9402	0.9887	0.9877	0.9786
Degradation percentage(%)	56	63	72	76	92	96	97

Photocatalytic performance of TiO_2 films made with TiF_4 and water only without cellulose templates, and with cellulose but variable IPA: water solvent composition are shown in Figure 5-47. Table 5-3 summarized the rate constants and linear modeling R-squared values, as well as the degradation percentage. The average rate constant and degradation percentage was, 0.25 min^{-1}, 60% for TiF_4- no cellulose films, 0.33±0.01 min^{-1},

74% for TiF_4- cellulose-1IPA-1Water films, and 0.72±0.09 min^{-1}, 95% for TiF_4- cellulose-4IPA-1Water films.

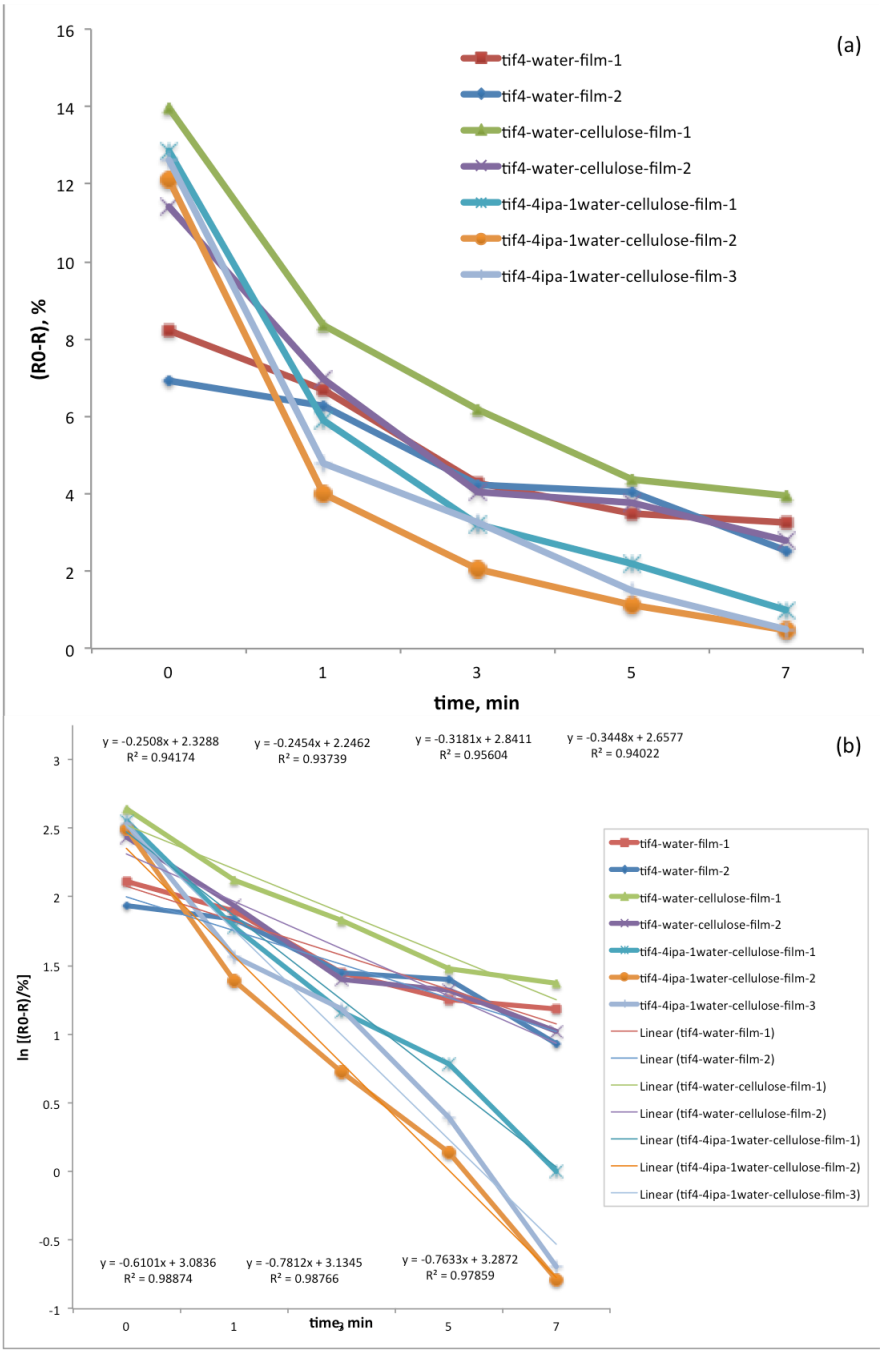

Figure 5-47 Variable films (a) reflectance change (b) kinetics with linear modeling and equations.

5.3.4 Porous titania network via ammonium hexafluorotitanate and boric acid method

A liquid phase deposition method was used to apply the aqueous titanium precursor to the cellulose/water suspension. In the acidic environment, the solution supersaturation is low. The stepwise hydrolysis and dehydration of $(NH_4)_2TiF_6$ produce TiO_2 nanoparticles coated along the hydrophilic cellulose fiber surface through heterogeneous nucleation.

Figure 5-48 presents the transformation of titanium precursor with cellulose before and after calcination. Ratios of BA to AHFT varied and directly had an influence on the product. A growing BA ratio resulted in more cracks within the film surface, while more AFHT led to dense and non-porous anatase titania films. Specific shaped amorphous TiO_2 were formed before calcination. From (a) to (b), primary nucleation was annealed into a fine web-like film; Particle size shrunk from (c) to (d), and (e) to (f) had a shape change from cubic to spherical (g) and (h) showed a denser layer of titania probably due to increased Ti concentration. When boric acid is fixed at 0.15M, by increasing the Ti concentration from 0.05M- 0.15M-0.30M, different morphologies formed. Higher resolution SEM images in Figure 5-49 reveal fiber-like titania materials, duplicating the size of the cellulose templates at ~30 nm. Flower-like TiO_2 also surrounded these TiO_2 fibers.

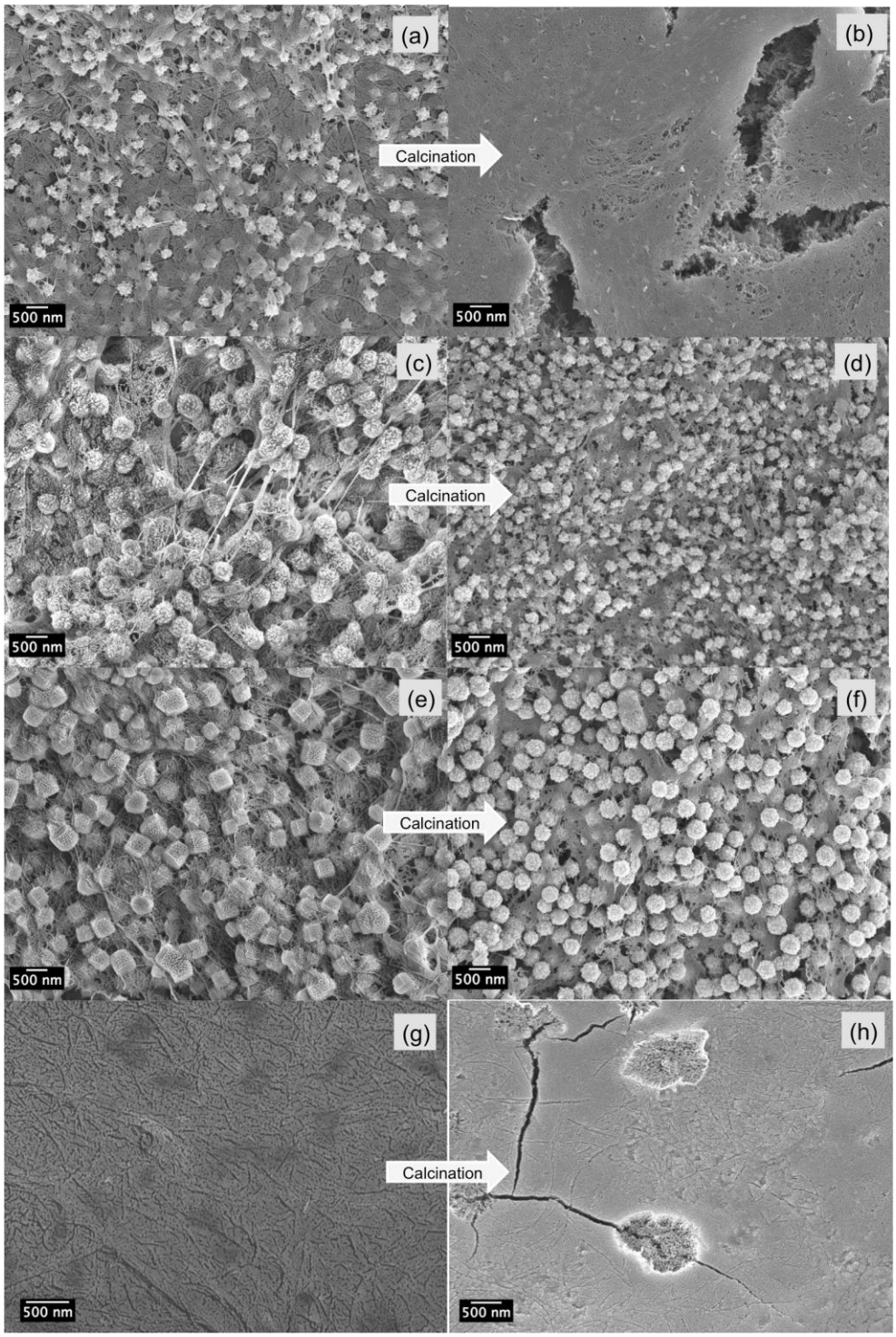

Figure 5-48 Comparison between "before calcination" and after calcination of AHFT and BA with MFCs composite. (a, c, e, g) are before calcination while (b, d, f, h) are calcined. (a,b) has a molar ratio of BA: AHFT= 0.15:0.05. Similarly, (c,d)'s BA: AHFT= 0.30:0.05; (e,f)'s BA: AHFT= 0.30:0.30; (g,h)' BA: AHFT= 0.15:0.30.

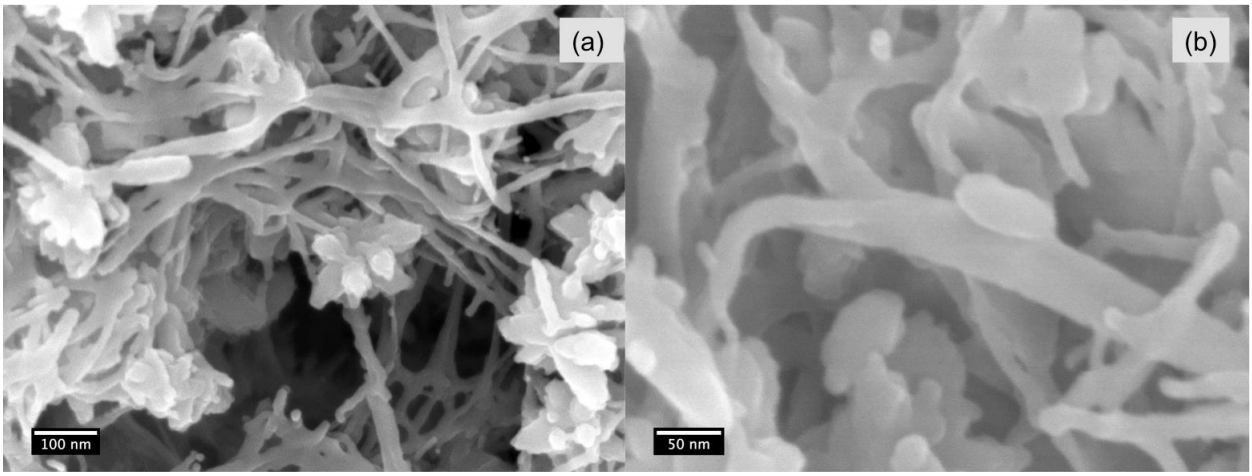

Figure 5-49 Calcined titania film from AHFT and BA with MFCs precursor, and the molar ratio of BA: AHFT is 0.15:0.05.

To study the parameters influencing the morphology, a series of experiments were conducted at different reaction temperature, time, concentration and binder content. For example, the results from set BA: AHFT = 0.15 M: 0.15 M were compared between temperatures kept at 50 °C or just room temperature. White precipitates appeared after 30 min in 50 °C reaction, while suspension looked the same after 10 h for room temperature. (Figure 5-50)

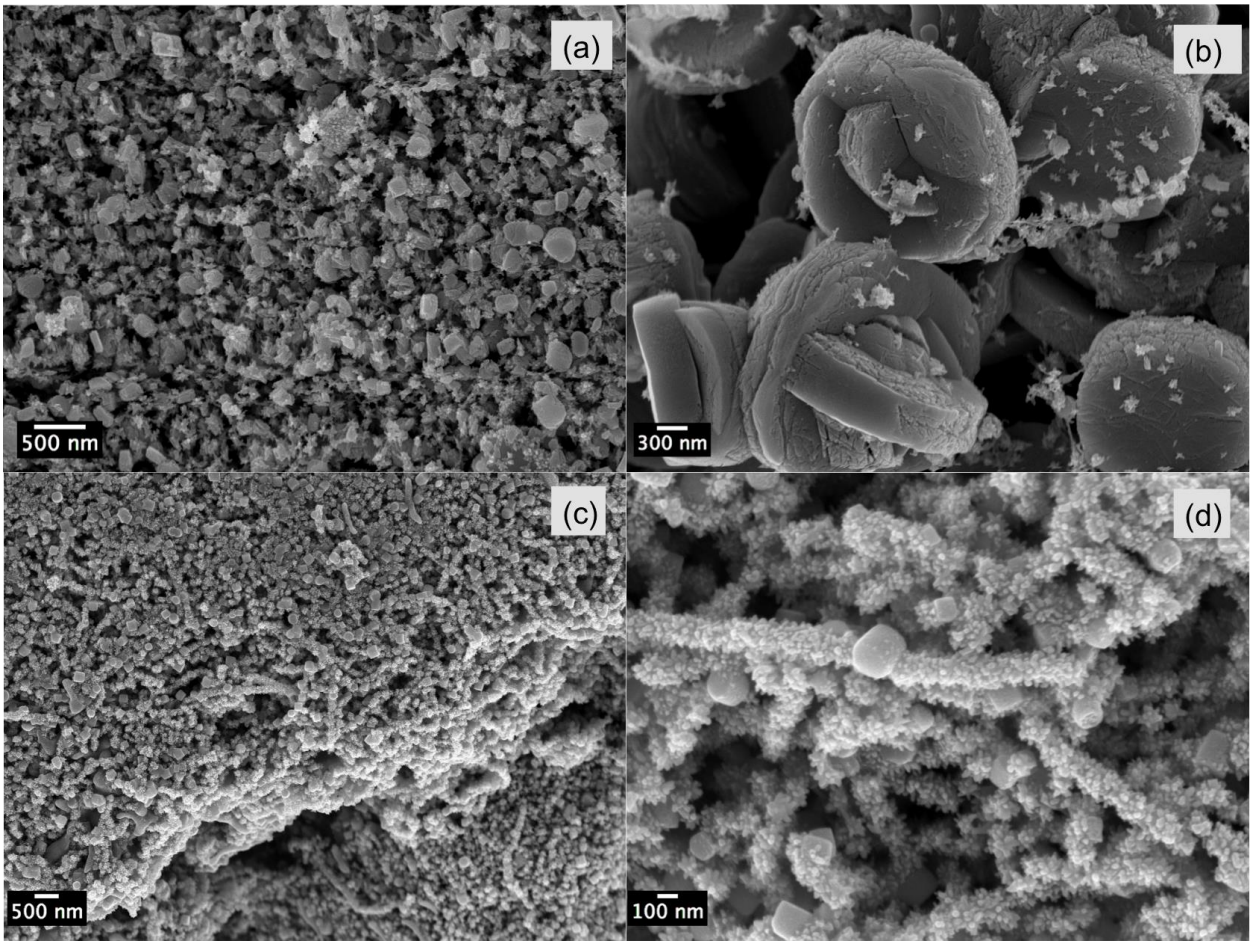

Figure 5-50 BA: AHFT= 0.15:0.15 films, calcined. (a-b) low and high magnification SEM images of 24h-reaction at room temperature; (c-d) low and high magnification SEM images of 24 h-reaction at 50 °C.

Increasing the mass percentage of binder PEG caused the change of morphologies for the film deposited from 1: 1 precursor with MFCs, as shown in Figure 5-51. The ratios of BA: AHFT were lowered to 0.075 M: 0.025 M, or 0.025 M: 0.008M. For the 0.075: 0.025 ratio, no obvious difference was observed for 6 hours and 15 hours reaction times. However, in general lowering the concentrations adopted an evolution of morphology from SEM images (Figure 5-52). The addition of binder PEG created more porous structures when BA: AHFT = 3: 1.

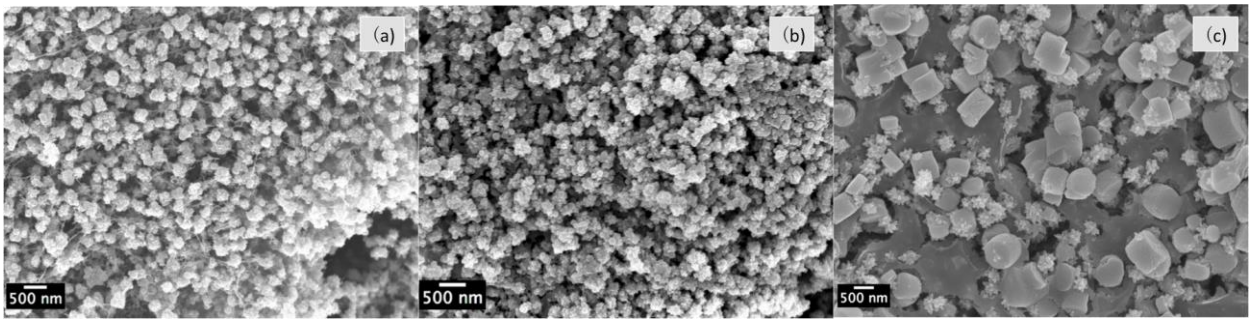

Figure 5-51 SEM images of titania films prepared from BA-AHFT/MFCs precursor with BA: AHFT = 0.15M: 0.15M. From (a) to (c), PEG weight percentages were 1%, 5%, and 10%.

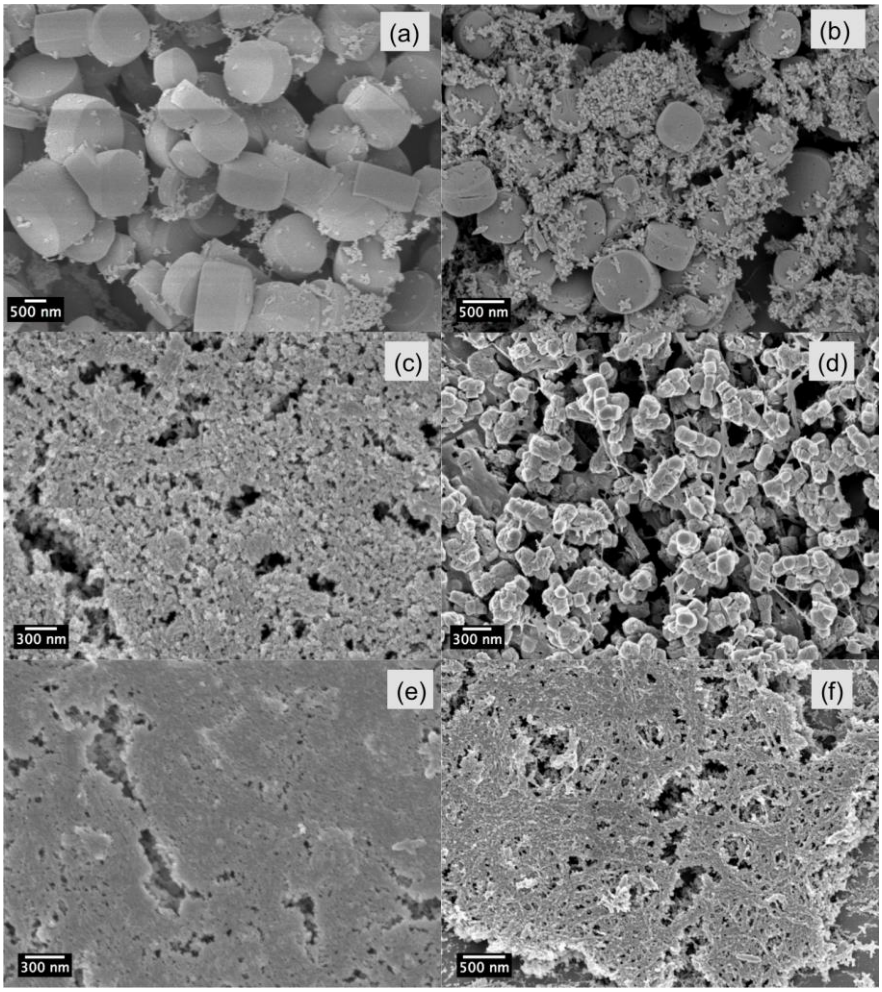

Figure 5-52 SEM images of titania films prepared from BA-AHFT/MFCs precursor with low concentrations. (a-b) BA: AHFT=0.075 M: 0.075 M, (c-d) BA: AHFT=0.025 M: 0.025 M, (e-f) 0.025 M: 0.008 M. (a, c, e) was recorded without addition of binder, while (b, d, f) was taken with addition of PEG.

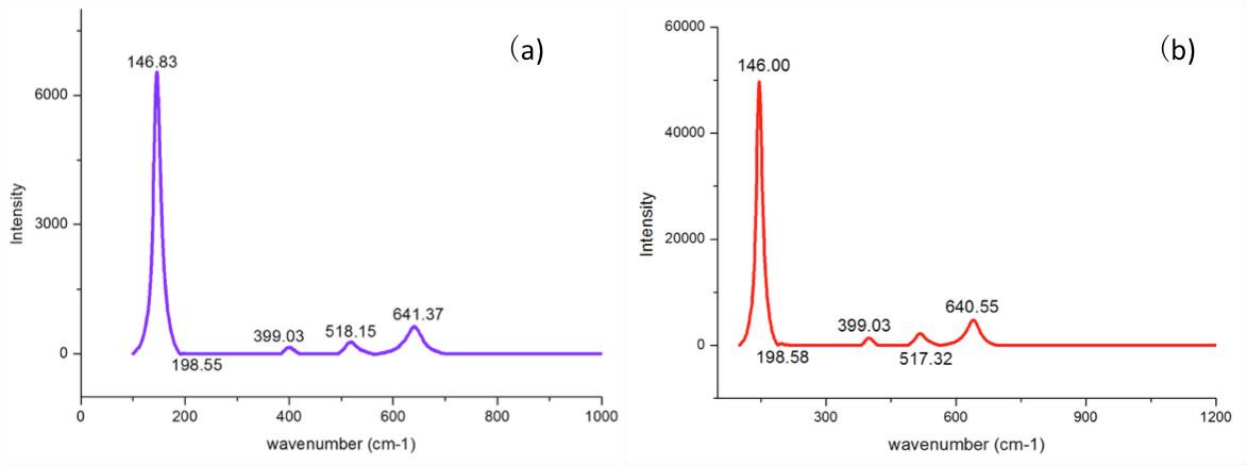

Figure 5-53 Raman spectrum of titania films made from AHFT-BA/MFCs precursor: (a) BA:AHFT = 0.15: 0.05 (b) BA:AHFT = 0.15:0.15

Figure 5-53 shows the characteristic peaks for anatase phase at wavenumber around of 149, 199, 399, 519, 639 cm^{-1}, while the peaks at 513 cm-1 were weaker to be observed. Anatase is tetragonal with two TiO_2 units per primitive cell. The six Raman modes are related to symmetries A1g+2B1g+3Eg. Both 1:1 and 3:1 ratios of 0.15 M base Ti(IV) were tested and confirmed anatase.

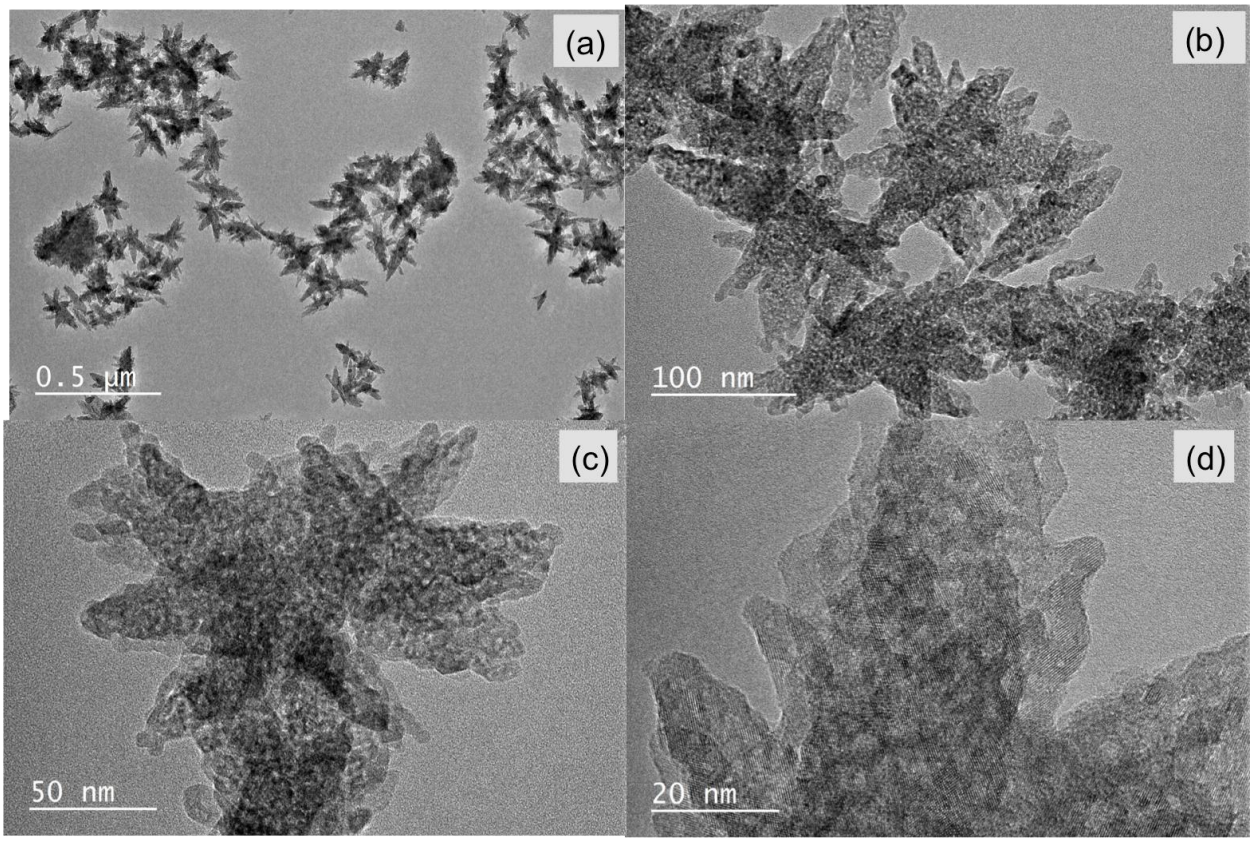

Figure 5-54 TEM images of the titania films made from AHFT-BA/MFCs precursor, and the ratio of BA: AHFT = 0.15M : 0.05M. From (a) to (d) magnification increased. Measurement of lattice (d) shows the lattice space of 0.35 nm and 0.24 nm, respectively referred to plane (101) and (004).

5.4 Conclusions and Future Work

Liquid phase deposition was utilized as a simple and effective method to prepare TiO_2 nanomaterials with tunable morphologies and porosities. Preliminary experiments successfully prepared TiO_2 coatings on cotton rounds fibers and filter paper with titanium tetrafluoride precursor and ammonium hexafluorotitanate/boric acid, creating hollow ribbon materials after the removal of cellulose templates. However, the dimensions of these titania materials were much larger than nanoscale. To further improve the surface area, porosity, and potential applications, home-made micro/nano-fibrillated cellulose fibers were combined with liquid phase deposition method.

TiF_4 system has generated bulk materials and thin films. For bulk materials, reaction time, pH level, surface properties and the effects of MFCs templates were studied. For thin film materials, an optimized solvent composition of isopropanol/water ratio of 4 to 1 was found to yield coatings with uniform sphere-shaped TiO_2 possessing a chain-like morphology oriented along the axis of the heat-removed cellulose fiber templates. Effects of cellulose and reaction time were studied as well.

Photocatalytic activity of the nano-chained titanium dioxide was investigated by monitoring the degradation of methyl orange (MO) with the use of quantitative diffuse reflectance UV-Vis spectroscopy. The enhancement in photocatalytic performance was explained regarding the surface area, pore size, and the unique morphology. The three-dimensional web structure with pseudo one-dimensional sphere-chain could retard the recombination of photogenerated electron-hole pairs and improve the charge transport. An increase of decomposition rate was found when the sample was compared with the traditional water-based precursor. The average rate constant and degradation percentage were 0.72 ± 0.09 min^{-1}, 95% for TiF_4- cellulose-4IPA-1Water films, increased by 1.88 times of the film prepared without cellulose templates.

Ammonium hexafluorotitanate and boric acid system was prepared. Reaction time, temperature, reactant concentration and ratio, and binder addition were investigated for the titania formation. The morphology evolved from aggregated particles to spheres, and flower-shaped, with increased surface area, compared to non-hydrolytic methods.

To remove cellulose fibers, heating was required in our work. The crystallinity from liquid phase deposition alone has been proved to be excellent, for photocatalytic activities

from others' work.[8] Future directions could be focused on the photocatalytic woven structures with MFCs as the substrates, thus no additional high-temperature annealing will be required.

Based on the completed results, it was concluded that the surface chemistry of nano-sized MFCs is different from the traditional large-scale (μm to cm range) cellulose or other natural fibers reported on in the literature. It is important to understand what differences exist in the surface chemistry of the cellulose, either in water or isopropanol, or even dried paper form.

BIBLIOGRAPHY

BIBLIOGRAPHY

(1) Yu, J.; Fan, J.; Cheng, B. Dye-Sensitized Solar Cells Based on Anatase TiO2 Hollow Spheres/Carbon Nanotube Composite Films. *Journal of Power Sources* **2011**, *196*, 7891–7898.

(2) Yu, J.-G.; Yu, H.-G.; Cheng, B.; Zhao, X.-J.; Yu, J. C.; Ho, W.-K. The Effect of Calcination Temperature on the Surface Microstructure and Photocatalytic Activity of TiO 2Thin Films Prepared by Liquid Phase Deposition. *J. Phys. Chem. B* **2003**, *107*, 13871–13879.

(3) Maeda, M. Preparation of Titania Films with Cohered Nanosized Particles Using Improved Liquid Phase Deposition Process. *international journal of electrochemical science* **2015**, *10*, 2988–2996.

(4) Malvadkar, N.; Dressick, W. J.; Demirel, M. C. Liquid Phase Deposition of Titania Onto Nanostructured Poly-P-Xylylene Thin Films. *J. Mater. Chem.* **2009**, *19*, 4796–4799.

(5) Li, S.; Liu, J.; Feng, T. Low Temperature Coating of Anatase Thin Films on Silica Glass Fibers by Liquid Phase Deposition. *J. Wuhan Univ. Technol.* **2007**, *22*, 136–139.

(6) Lee, M.-K.; Fan, C.-H.; Wang, H.-C.; Chang, C.-Y. Fluorine Passivation of Titanium Oxide Films on ITO/Glass Grown by Liquid Phase Deposition for Electrochroism. *J. Electrochem. Soc.* **2011**, *158*, D511.

(7) Maki, H.; Okumura, Y.; Ikuta, H.; Mizuhata, M. Ionic Equilibria for Synthesis of TiO2 Thin Films by the Liquid-Phase Deposition. *J. Phys. Chem. C* **2014**, *118*, 11964–11974.

(8) Shimizu, K.; Imai, H.; Hirashima, H.; Tsukuma, K. Low-Temperature Synthesis of Anatase Thin Films on Glass and Organic Substrates by Direct Deposition From Aqueous Solutions. *Thin Solid Films* **1999**, *351*, 220–224.

(9) Imai, H.; Takei, Y.; Shimizu, K.; Matsuda, M.; Hirashima, H. Direct Preparation of Anatase TiO2 Nanotubes in Porous Alumina Membranes. *J. Mater. Chem.* **1999**, *9*, 2971–2972.

(10) Pourmand, M.; Taghavinia, N. TiO2 Nanostructured Films on Mica Using Liquid Phase Deposition. *Materials Chemistry and Physics* **2008**, *107*, 449–455.

(11) Imai, H.; Matsuta, M.; Shimizu, K.; Hirashima, H.; Negishi, N. Preparation of TiO2 Fibers with Well-Organized Structures. *J. Mater. Chem.* **2000**, *10*, 2005–2006.

(12) Yu, H.; Yu, J.; Cheng, B.; Lin, J. Synthesis, Characterization and Photocatalytic Activity of Mesoporous Titania Nanorod/Titanate Nanotube Composites. *Journal of*

Hazardous Materials **2007**, *147*, 581–587.

(13) Yu, H.; Yu, J.; Cheng, B.; Liu, S. Novel Preparation and Photocatalytic Activity of One-Dimensional TiO 2hollow Structures. *Nanotechnology* **2007**, *18*, 065604.

(14) Meseck, G. R.; Kontic, R.; Patzke, G. R.; Seeger, S. Photocatalytic Composites of Silicone Nanofilaments and TiO2 Nanoparticles. *Adv. Funct. Mater.* **2012**, *22*, 4433–4438.

(15) Dozzi, M.; Selli, E. Specific Facets-Dominated Anatase TiO2: Fluorine-Mediated Synthesis and Photoactivity. *Catalysts 2013, Vol. 3, Pages 455-485* **2013**, *3*, 455–485.

(16) Phase-Pure TiO2 Nanoparticles: Anatase, Brookite and Rutile. **2008**, *19*, 145605.

(17) Li, Y.; Li, X.; Li, J.; Yin, J. Photocatalytic Degradation of Methyl Orange by TiO2-Coated Activated Carbon and Kinetic Study. *Water Research* **2006**, *40*, 1119–1126.

6 Nanoporous TiO_2 Films Templated with Micro/nano-fibrillated Cellulose and Applications in Dye-Sensitized Solar Cells

6.1 Background

6.1.1 Nano-structuring of the photoanode of DSSCs

As introduced in Chapter 1, The design of nanocrystalline semiconductor electrode is significantly important because of its responsibility in the loading of dyes, transport of electrons, and diffusion of electrolytes but also the suppression of recombination reactions.

Natural templates have been researched as promising candidates to create tunable titania structures for applications in DSSCs. Nanostructured hollow TiO_2 fibers were prepared via fibers from cotton rounds, and used as porous photoanode for DSSCs,[1] resulting in enhanced electron transport properties, compared to randomly packed spherical nanoparticle photoanode. The transport of photoinjected electrons in the oxide network got 3-4 times of lifetime, due to the faster travel within fiber morphology. The efficiency of the cell reached 7.2% under simulated AM 1.5 solar illumination. However, the fiber size was large still with ~2 um diameter and ~100 um length. The preparation process was complicated due to the fact that materials had to be prepared, thermally treated, washed, and then mixed with other chemicals to form a paste.

Another interesting approach was through a virus, in a similar mechanism.[2] Highly interconnected and nano-channeled titania films were fabricated with the M13 virus as a template. After calcination, viruses were decomposed and left trace channel structure

inside TiO_2 particles. This not only provided access to electrolyte but also increased surface area and porosity. The efficiency of the DSSC generated was 6.32%. Commercial TiO_2 particles were used in the film with binder PEG for better slurry thickness.

A modified sol-gel based template-controlling approach is proposed to assist the formation of micro/nano channels in the original random nanoparticle network, to optimize the dye loading, interfacial contact with the electrolyte, and the electrical contact efficiency.

6.1.2 Controlled hydrolysis in a sol-gel process for MFCs templating

Chapter 1 has discussed sol-gel to synthesize metal oxide materials and the specialty of titanium precursors as transition metal source. Sol-gel derived materials can be prepared by tailoring parameters for high surface area, controlled porosity, and desired electric and optical properties. A controlled hydrolysis is crucial for manipulation of materials size, morphology, and chemical properties. Chapter 3, 4, and 5 comprehensively demonstrated how cellulose fibers worked as soft templates for inorganic materials fabrication in non-hydrolytic and hydrolytic media and the enhancement in photocatalysis. To further the exploration of cellulose templating and titania film applications, the combination of MFCs-templated titania and the DSSCs anode will be discussed in this chapter.

MFCs will be combined with the titanium precursor in modified sol-gel systems, resulting in the encapsulation of the MFCs in the growing direction of the TiO_2 crystalline nanoparticles. After calcination, the MFCs will cleanly decompose leading to the formation of micro/nano channels in the TiO_2 nanoporous film. Other systems such as TiF_4 and ammonium hexafluorotitanate and boric acid will be illustrated by similar means as Figure

4-1 shows. The benefits are expected to be a more ordered interconnection and less aggregation with nano/micro channels.

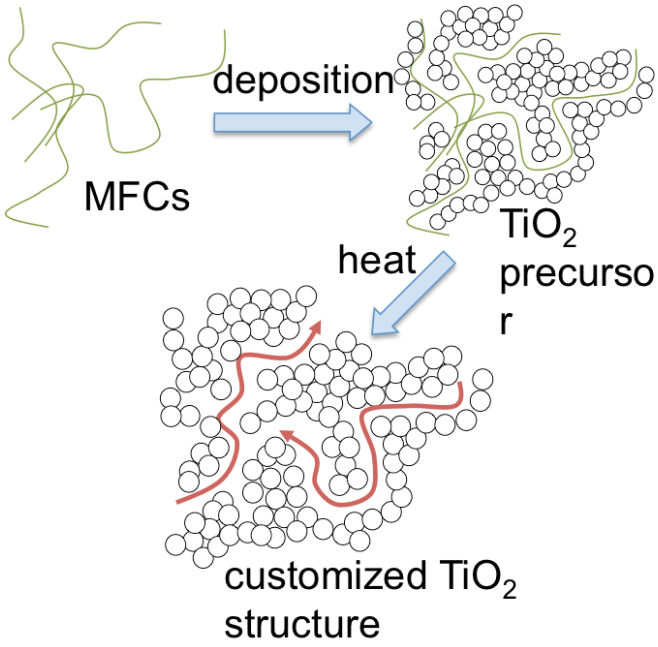

Figure 6-1 Scheme of applying MFCs as a template for porous TiO_2 network synthesis

6.2 Experimental

6.2.1 Materials and equipment

Materials:

All chemicals were used without pre-treatments unless noted. MFCs in isopropanol (IPA) were processed by Mini DeBEE ultrahigh-pressure homogenizer as Chapter 3 described. Titanium(IV) isopropoxide (≥ 97%), valeric acid (≥ 99%), ethanol (≥ 99.5%, A.C.S. reagent), 2-propanol (A.C.S. grade, ≥ 99.5%), Lithium iodide (99.9% trace metal basis), iodine (≥ 99.99%), acetonitrile (≥ 99.99%), and anhydrous 2-propanol were purchased from Sigma Aldrich. Hydrochloric acid (analytical reagent grade) was from Mallinckrodt. Commercial titania paste Ti-Nanoxide T (transparent, 11% w.t.)，25μm-thick Surlyn and N,N'-bis(4,4'-dicarboxylate-2,2'-bipyridine)ruthenium(II) (N3 dye) were

purchased from Solaronix. Ethanol (200 proof, 99.5% ACS grade) and isopropanol (99.5 %) were purchased from MSU university stores. Hydrogen hexachloroplatinate (IV) hydrate (40% Pt) was purchased from Acros Organics. 4-*tert*-butylpyridine was purchased from TCI America Inc. The silver conductive epoxy (8331G) was purchased from Fulton Radio Supply Co. Tapes for the mask frame were 3M Scotch 810 & 811, and the microscope cover glasses at a thickness of 0.14 mm were from Corning. Plain, pre-cleaned micro glass slides were purchased from VWR International, in a size of 1 inch by 3 inches, with a thickness of 1.2 mm. TEC-15 (15 Ω/mm^2) fluorine-doped tin oxide (FTO) glass was purchased from Hartford Glass Co.

Equipment and Characterizations:

Details of sample preparation have been stated in previous chapters, and most of the material characterization methods used in this chapter have been described. Thus, only a brief description is provided here.

The structure of the cellulose (MFCs) templates and titania porous thin films were characterized by scanning electron microscopy (Carl Zeiss Auriga CrossBeam SEM-FIB). Thickness of films were characterized after milling into the cross section of the film by focused ion beam (FIB). The transmission electron microscopy (TEM) images, high-resolution transmission electron microscopy (HRTEM) images, and selected-area electron diffraction (SAED) patterns were taken on a JEOL 2200FS equipment. UV-Vis spectrophotometer (Perkin Elmer Lambda 900 UV Spectrometer) was applied for TiO_2 films absorption and transmission characterizations. UV-vis absorption spectra of the TiO_2 films were recorded in the range of wavelength 300-800 nm. Fourier transform infrared

(FTIR) absorption spectra were collected with Perkin Elmer 2000 Spectrum One FT-IR spectrometer at room temperature. The spectra of the composites were scanned from 4000 to 400 cm^{-1}. Thermogravimetric analysis (TA instruments Q500) used a high-resolution ramp of 25 °C/min to ~800 °C in air was conducted on TiO_2 samples. X-ray photoelectron spectroscopy (XPS) was carried out on Perkin Elmer Phi 5400 using Kα line of Mg (1254 eV) X-ray source with a beam voltage of 15 kV and current of 20 mA for the survey spectra scan (pass energy 187.85 eV, and 1 eV step size). A HIMONT Plasma Science PS 0500 Plasma Surface Treatment System was used to clean the glass substrates for ~0.5h. The oxygen pressure was 0.270 Torr and the power was 300 W. Photoelectrochemical measurements were performed with a JV-EQE solar cell testing station with an AM 1.5 solar filter used to simulate sunlight at 100 mW cm^{-2}. Atomic layer deposition was finished with Savannah 100 instrument (Cambridge Nanotech, Inc.).

6.2.2 Synthesis of porous TiO_2 network as thin film

To moderate the hydrolysis and precipitation rates during the sol-gel reactions, valeric acid was used as a chelating agent for the non-aqueous environment. Valeric acid (v-acid) was added to titanium isopropoxide (TTIP) followed by water as shown in Figure 4-3, The atomic ratio of v-acid: water: TTIP is 9: 1.5: 1 respectively.[3] The mixture was vigorously stirred in capped vials at room temperature for 1 h. Then the as-prepared titanium valerate was combined with MFC/isopropanol suspension at a ratio of 2: 1 and kept in a 50 °C oil bath for 14 h. The mixture turned from a colorless, transparent solution to cloudy.

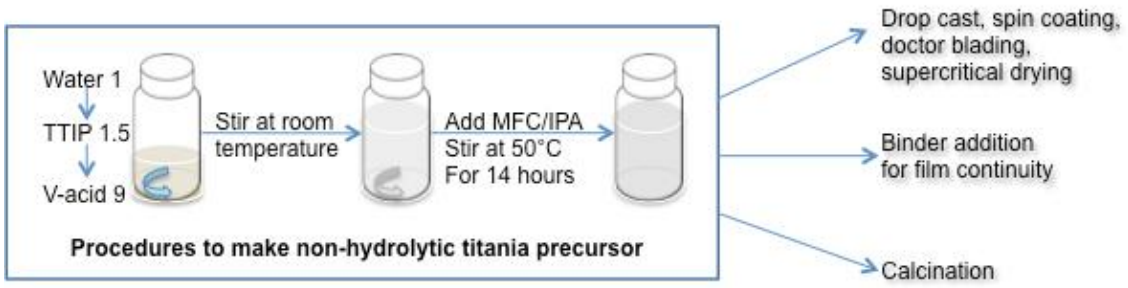

Figure 6-2 Scheme of MFCs-templating slow sol-gel method

Films were then dried in vacuum oven for 0.5 h without heating to avoid moisture, followed by a step-wise annealing at 200 °C, 300 °C, 350 °C, 450 °C for 0.5 h, 0.5 h, 0.5 h, and 1 h.

6.2.3 DSSC assembly and measurements

To investigate the potential of MFC-templated TiO_2 as a DSSC photoanode material, a series of solar cells were assembled and current density vs. voltage (*J*-*V*) measurements were conducted. Using a commercial titania paste and lab-made Ti(IV) precursors as examples, the procedure of assembling a test-ready DSSC is described as below:

Cleaning:

Fluorine-doped tin oxide (FTO) glasses were cut into 0.75 inches by 1 inch (or 0.5 inches), and 1 inch by 1 inch slides for anode and cathode use. A cleaning procedure is essential to remove dirt and oil from the original packaging. First FTO was cleaned with soap water (Alconox Powder Detergent) and then rinsed in acetone, isopropanol, and ethanol in the sonication bath for 20 minutes each. After dried in air, FTO glass slides were located in a glass or metal petri dish ready for a 30-minute oxygen plasma treatment where the oxygen pressure was 0.270 torr and the power was 50% of 600 W. Thus, most of the contaminants were removed and hydroxyl groups were exposed as well. At the same time,

tools for the coating step such as glass pipets, razor blades etc. should be cleaned with acetone and let dry in the hood. Based on previous experience, the furnace used for titania annealing should be purified at 600 °C for 1 hour to ensure no cross contamination from materials of other users.

Coating:

A coating frame was made simply by weighing paper and Scotch 810 tape with the dimensions of 1 cm by 1 cm (or 0.6 cm by 0.6 cm), which would serve as the mold for the tape mask every time. To make a tape mask, overlay the removable Scotch 811 tape onto the coating frame, apply pressure, and then cut precisely along the 1 cm by 1 cm edges with a sharp razor blade. The tape mask was attached onto the conductive surface of the FTO glass and no ridges or bumps should be created along the tape.

A small amount of commercial titania paste was applied to the bottom edge of the tape mask, and then doctor-bladed across the 1 cm by 1 cm area using a cleaned glass pipet. For lab-synthesized titania, the precursor was either doctor-bladed in the same way, or by drop casting and tilting for accumulating layers. The TiO_2 photoanode film was made by drop casting 20 uL Ti/cellulose (2:1) precursor and spread evenly within the tape mask. After the film was dried for 10 min, accumulating layers could be applied and dried again when necessary. The coated slides went through a two-stage calcination. Note that different procedures were followed when the film was lab-synthesized with or without templates, or by different systems. After titania coating was dried in air for more than 15 minutes, the tape mask was carefully peeled off.

The coated slides were annealed in air in the furnace at 450°C for 30 minutes for commercial paste. Different procedures were followed when the film was lab-synthesized with or without templates, or by different systems. Details about these can be reached in previous chapters.

Dye loading:

0.3 mM N3 dye in ethanol was prepared and bath-sonicated for 20 minutes. The annealed TiO_2-FTO glass was treated in oxygen plasma chamber again to remove possible contaminants and quickly heated up to 90 °C on a hot plate. Slides were immersed in a 10 mL beaker with as-prepared dye solution covering at least the top of the titania area. Beakers were also covered with paraffin films to prevent evaporation. All the slides were immersed in dye solution for 20-24 h in the dark.

Cathode fabrication:

Pre-cut FTO slides were drilled with two 1 mm-in-diameter holes. The holes should be aligned in the diagonal direction located at the corner of the active TiO_2 area to ensure a smooth percolation of the electrolyte. To save time, cleaning of the cathode substrates should be followed after drilling for cathode. Deposition of a thin layer of Pt catalyst was performed in the following steps: 32.3 uL of 5 mM H_2PtCl_6 in IPA solution was applied to the conductive side of FTO and spread on the surface by tilting. It is important to avoid leaking of solution into drilled holes. After dried for 5-10 min on a flat surface in the hood, cathode slides were calcined at 400 °C for 15 min (for commercial paste) in a furnace and then cooled down.

Wire electrodes can be applied using 2'' copper wires and silver epoxy. The polymer sheathing of copper wires was removed and the wires were cleaned with acetone and ethanol. Silver epoxy was prepared by mixing double tubes quickly and let set till it was sticky. Then a string of copper wire was attached to the farther edge away from holes on FTO slide with a dollop of silver epoxy. The epoxy can be cured by heating at 65 °C for 15 min or at room temperature for five hours.

Cell assembly and electrolyte injection:

When the dye loading process was finished, the assembly could be started. The dyed photoanode was washed with ethanol to remove the excess dye, and dried with nitrogen. Pieces of surlyn were cut 0.5'' by 0.5'' with the center cut out leaving a 2-3 mm thick frame. The surlyn frame was placed around the dyed area with no ridges and then covered with the platinized counter electrodes with the conductive surface facing down. The assembly was pressed sealed for 20-30 seconds with another piece of thick glass on a 120 °C hot plate. A well-sealed surlyn between both electrodes should become translucent with no bubbles or open channels seen by naked eyes.

Before the electrolyte percolation, another piece of copper wire was attached to the conductive side of the photoanode, and cured for 15 minutes at 65 °C. The standard electrolyte consists of 0.3 M lithium iodide, 0.03 M iodine, 0.2 M 4-*tert*-butylpyridine in acetonitrile. A 1-mL volumetric flask was used to prepare the fresh solution for each single time use. The solution was dispersed in sonication bath minimally (both iodine and acetonitrile easily vaporize) and transferred into a tightly capped vial.

The as-prepared cell was placed photoanode-side down, and a 0.1 mL droplet of the electrolyte was placed close to one hole using a syringe or micropipette. To prevent bubble formation, the cell could also be vertically positioned so that the electrolyte was drawn in with the help of gravity. After the excess electrolyte solution was wiped off, immediately a soldering iron should be used to melt the surlyn beneath the cover glass to seal the holes. Sometimes, the electrolyte emerges under the surlyn and will cause it not to melt properly. Re-wipe the glass and dry the contact surface sufficiently if necessary.

Characterization of solar cells was conducted with a JV-EQE solar cell testing station with an AM 1.5 solar filter used to simulate sunlight at 100 mW cm^{-2}. Voltage was applied in a two-electrode arrangement, where the working electrode lead was the photoanode, and the reference and counter electrode leads were the cathode. The solar cell under evaluation was secured onto an irradiation port, and the solar-simulated light beam could be adjusted regarding intensity, angle, and position. The same position has been located for the beam source to ensure the irradiation created was maintained at the same level. A mask with an open area in the center was also made to apply to the solar cell before testing so that only the aimed TiO_2 area was interacting with the beam source.

6.3 Results and Discussions

6.3.1 Applications of cellulose-templated TiO_2 as photoanode in DSSC

SEM images in Figure 6-3 showed the morphology and cross-sectional view of the calcined 4-layer film. TEM images further demonstrated the particle size of ~20 nm at higher magnification and resolution, and the diffraction pattern shows an anatase phase.

Solar-to-electricity performance was tested on a series of cells made with different numbers of layers of TiO_2 (Figure 6-4).

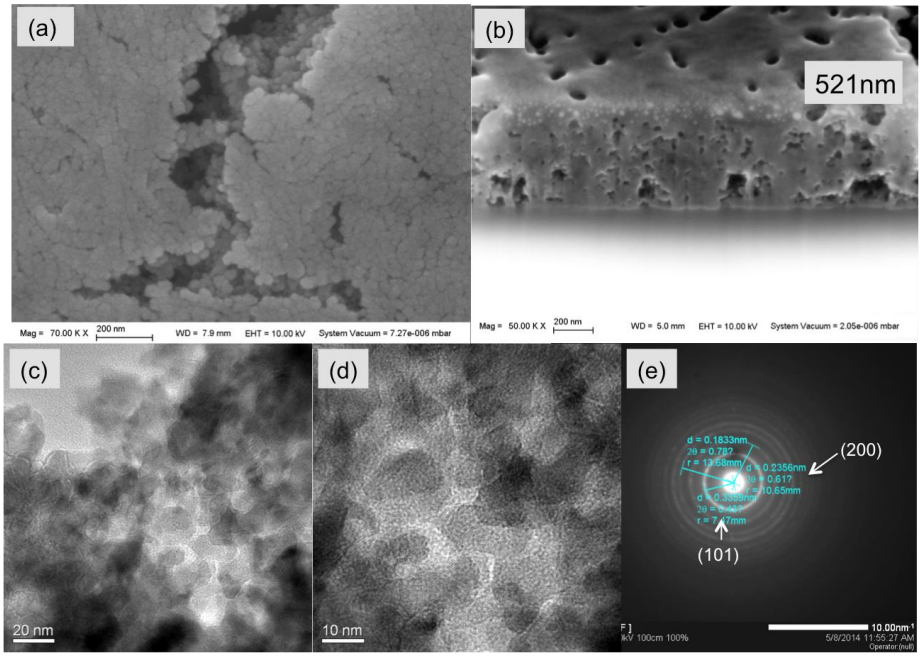

Figure 6-3 Four-layer TTIP-cellulose precursor, calcined, for DSSCs. SEM images: (a) top view, (b) cross section view. TEM images: (c-d) at higher magnifications and resolutions, lattice plane measured 0.3 nm (e) selected area diffraction pattern.

6.3.2 Photovoltaic performance test with ttip-vacid films and other films

Based on Figure 6-4 and Table 6-1, the efficiency of the solar-to-electricity transformation increased with the increasing number of layers at first and then decreased for thicker films. Both photocurrent and photovoltage increased first and then decreased when the thickness went up.

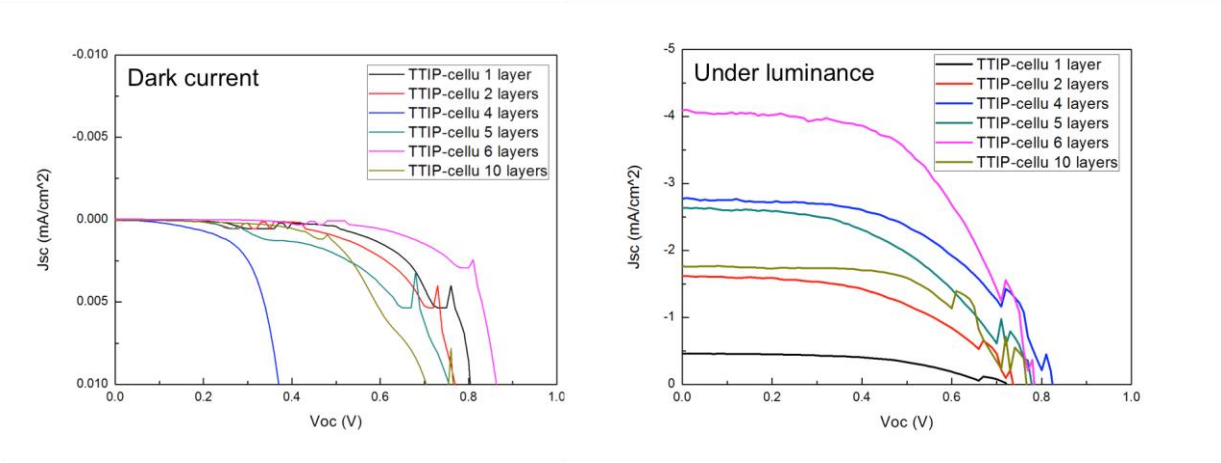

Figure 6-4 J-V curves of TTIP-cellulose deposited DSSCs in dark and luminance

Table 6-1 Photocurrent, photovoltage, fill factor and efficiency of TTIP-cellulose cells

Device	Photoanode material	Photoanode thickness (nm)	J_{sc} (mA/cm^2)	V_{oc} (V)	FF	Efficiency **η**
1	1 layer	-	-0.50	0.72	0.51	0.17 %
2	2 layers	-	-1.90	0.63	0.40	0.49 %
3	4 layers	644	-2.77	0.82	0.52	1.20 %
4	5 layers	-	-2.60	0.78	0.48	0.98 %
5	6 layers	727	-4.09	0.78	0.55	1.75 %
6	10 layers	1435	-1.76	0.75	0.60	0.80 %

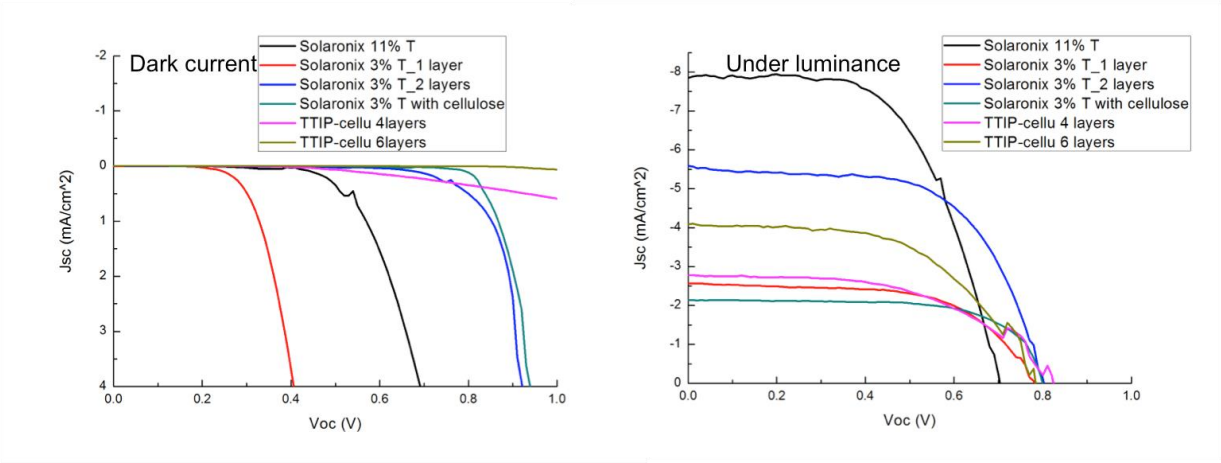

Figure 6-5 J-V curves of commercial Solaronix paste deposited photoanode for DSSCs in dark and luminance

Solaronix 3% w.t. TiO_2 as a photoanode material:

A commercial paste Solaronix Ti-Nanoxide T (11% w.t.) was applied by the doctor blade with microscope cover glass and calcined, forming a 4.1 μm thick film. To normalize

the thickness influence, Ti-Nanoxide T was diluted to 3% w.t. and sonicated thoroughly with ethanol in a capped vial. Solaronix 3% T 1 layer and 2 layers were made by doctor blade as well. Solaronix 3% T with cellulose was prepared by adding cellulose/isopropanol suspension into the original paste and sonicating. Figure 6-5 indicates that at the approximately same thickness, homemade 6-layer TTIP-cellulose TiO_2 photoanode had higher J_{sc} increased by ~59% and efficiency improved by ~44% (Table 6-2). While when the thickness exceeded the TTIP-cellulose films, the performance of the whole cell was further behind commercial anodes assembly. The addition of cellulose/isopropanol suspension did not improve the overall efficiency.

Table 6-2 Photocurrent, photovoltage, fill factor and efficiency of Solaronix TiO_2-cellulose cells

Device	Photoanode material	Photoanode thickness (nm)	*Jsc* (mA/cm^2)	*Voc* (V)	*FF*	Efficiency η
1	Solaronix 3% T_1 layer	717	-2.57	0.78	0.60	1.21 %
2	Solaronix 3% T_2 layers	1350	-5.59	0.80	0.61	2.73 %
3	Solaronix 3% T with cellulose	-	-2.14	0.8	0.68	1.17 %
4	Solaronix 11% T	4100	-7.90	0.73	0.59	3.26 %

Compact blocking layer (CBL) influence on different cells:

Before any photoanode material deposition, a thin CBL was applied on FTO with 500 atomic layer deposition (ALD) cycles using TTIP and water as precursors. TiO_2 was grown at 225 °C using reactant exposure times of 0.3 s and 0.015 s, respectively, and nitrogen purge times of 5 s between exposures. Then 4 layers, 6 layers of TTIP-cellulose precursor and Solaronix 3% TiO_2 were used as photoanodes and tested, as Figure 6-6 shows below.

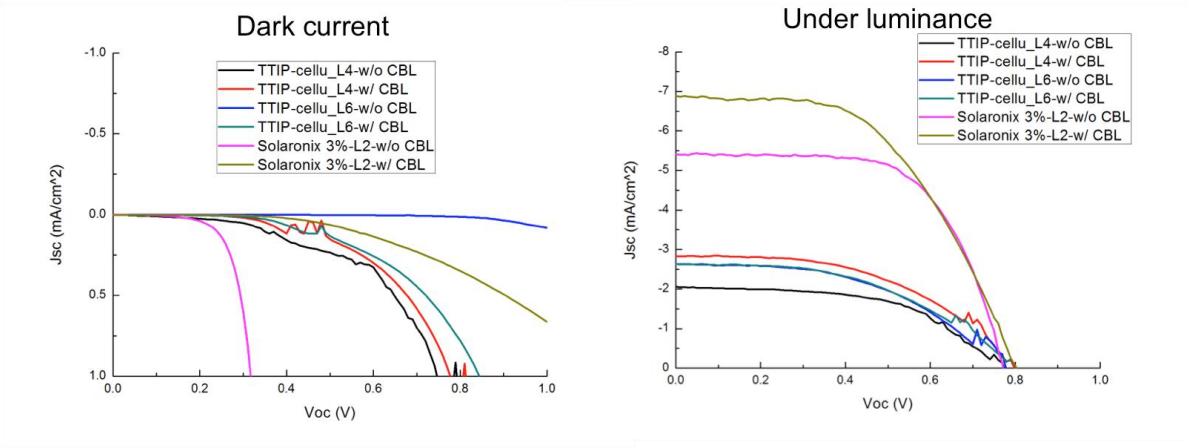

Figure 6-6 J-V curves of different DSSCs in dark and luminance, with compact block layer deposited or without.

As stated above, back reactions suppressed the solar-to-electricity efficiency, especially the one where photogenerated electrons from anode reacted with the liquid electrolyte. When illumination is not sufficient, the FTO/electrolyte back reaction is more dominant. An increase of V_{oc}, J_{sc} and efficiencies was attributed to the compact pinhole-free thin barrier layer between FTO glass and the nanoporous titania layer application, which blocked the loss pathway and retarded the charge recombination.

Table 6-3 Photocurrent, photovoltage, fill factor and efficiency of DSSCs w/ or w/o compact layers

Device	Photoanode material	J_{sc} (mA/cm^2)	V_{oc} (V)	*FF*	Efficiency η
1	TTIP-cellulose 4 layers, without CBL	-2.06	0.77	0.54	0.87 %
2	TTIP-cellulose 4 layers, with 500 cycles of ALD CBL	-2.83	0.8	0.49	1.12 %
3	TTIP-cellulose 6 layers, without CBL	-2.60	0.78	0.48	0.98 %
4	TTIP-cellulose 6 layers, with 500 cycles of ALD CBL	-2.63	0.8	0.47	1.01 %
5	Solaronix 3% T_2 layers, without CBL	-5.41	0.77	0.63	2.69 %
6	Solaronix 3% T_2 layers, with 500 cycles of ALD CBL	-6.89	0.8	0.52	2.91 %

Photoanodes made with hydrolytic-induced TiO_2 films: Two types of cells made with anodes deposited by TiO_2 from the aqueous system were briefly investigated as well, respectively, the (BA: AHFT = 0.15M: 0.05M) with binder 2-hydroxyl ethyl cellulose (HEC)

precursor, and the (TiF_4-cellulose) precursor. The performance of these two cells couldn't exceed the TTIP-cellulose system, probably due to the larger particle and pore sizes limiting the effective dye adsorption and photon-to-electron conversion.

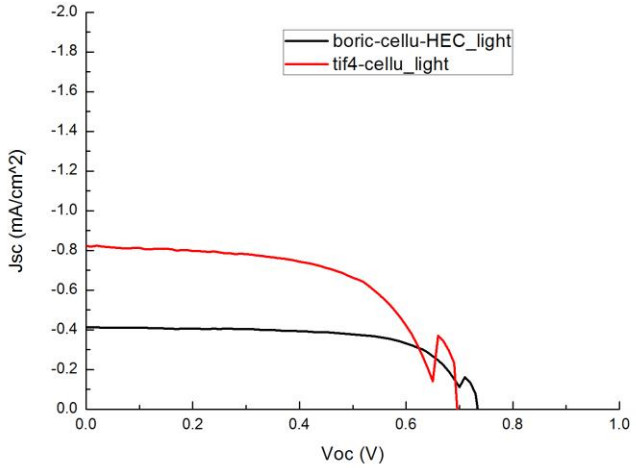

Figure 6-7 J-V curves of boric-cellu and TiF4-cellu-induced DSSCs under luminance

Table 6-4 DSSCs trials on alternative TiO_2 films prepared from aqueous systems

Device	Photoanode material	J_{sc} (mA/cm^2)	V_{oc} (V)	*FF*	Efficiency $\boldsymbol{\eta}$
1	(BA: AHFT = 0.15M: 0.05M) with binder 2-hydroxyl ethyl cellulose (HEC)	-0.41	0.74	0.66	0.20 %
2	TiF_4-cellulose	-0.82	0.67	0.60	0.33 %

Cell lifetime: Another study on how storage time influenced the cell performance was conducted on a series of cells. Storage conditions are light-free, water-free desiccator, and tests were made at 1 h, 22 h, 52 h and 166 h after electrolyte injection. Figure 6-8 indicates that as time went by, the performance was significantly influenced, since an 80% decease was observed for efficiency after 166 h. The degradation is possibly caused by the electrolyte evaporation during the storage time and sealing defects.

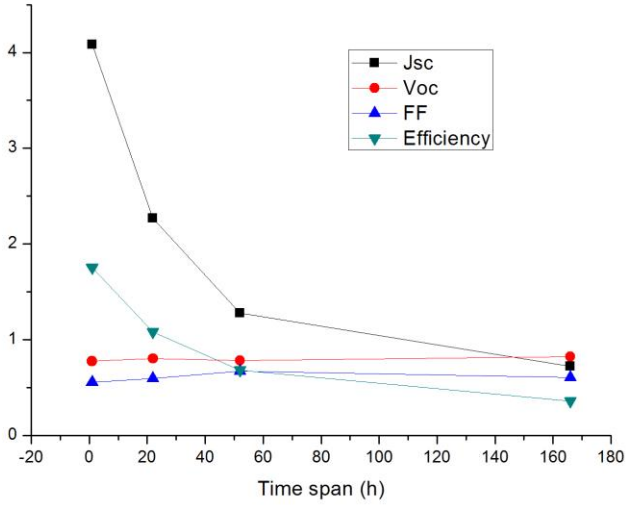

Figure 6-8 Cell performance over the time span. This is a TTIP-cellulose based 6-layer photoanode cell.

6.4 Conclusions and Future Work

6.4.1 Conclusions

To summarize, a facile approach to synthesize nanoporous titania films via micro-fibrillated cellulose templating and an *in-situ* coating has been developed to be applied in dye-sensitized solar cells. As for TTIP-cellulose precursor, the thickness of the anode film is a dominant factor for the overall performance and efficiency. The 6-layer cell showed a ~40% increase in solar-to-electricity efficiency (1.75%) compared to commercial paste at the same thickness level under a simulated solar light irradiation of 100 mW cm^{-2} (AM1.5).

6.4.2 Future Work

Work that has been completed for DSSCs is still at preliminary stage, and the solar cells could be enhanced in many more aspects, such as adding barrier layer on FTO by titanium tetrachloride ($TiCl_4$, Aldrich) coating at 70 °C, and increasing the thickness of the titania anode coating.

In order to improve the capacity of cellulose-templating photovoltaic films, one could manipulate the template in various ways. For example, 3D free-standing cellulose template will work as a dry scaffold for further coating, especially with methods that have been developed in previous chapters. Dehydration methods such as freeze drying, supercritical drying could be combined and new design on the template structures will be worth researching too.

In terms of flexible and transparent electrode substrates, liquid phase deposition method will offer low-temperature deposition technique without destroying the flexible electrode.

BIBLIOGRAPHY

BIBLIOGRAPHY

(1) Ghadiri, E.; Taghavinia, N.; Zakeeruddin, S. M.; Grätzel, M.; Moser, J.-E. Enhanced Electron Collection Efficiency in Dye-Sensitized Solar Cells Based on Nanostructured TiO 2Hollow Fibers. *Nano Lett.* **2010**, *10*, 1632–1638.

(2) Lee, Y. M.; Kim, Y. H.; Lee, J. H.; Park, J. H.; Park, N.-G.; Choe, W.-S.; Ko, M. J.; Yoo, P. J. Highly Interconnected Porous Electrodes for Dye-Sensitized Solar Cells Using Viruses as a Sacrificial Template. *Adv. Funct. Mater.* **2011**, *21*, 1160–1167.

(3) Askeland, P. A. Preparation and Characterization of Sol-Gel Derived Metal Oxide Thin Films and Powders for Coatings and Catalysts, 1997.